School of Physics and Astronomy
University of Glasgow
Glasgow
G12 8QQ

PhD Thesis

Pixel Detector with Exotic Sensors:

Device Characterisation, Analysis, & Application

Lojius Lombigit

March 17, 2024

Submitted in fulfilment of the requirements for the
Degree of Doctor of Philosophy

Abstract

The detection of charged particles is an integral part of several scientific endeavours. To detect a charge particle, it must interact with a sensing volume and produce charges within it that can be read out. In hybrid pixel sensor, the sensor and readout electronics can be optimised separately, and this property makes them highly desirable for future applications.

University of Glasgow and Micron Semiconductor Ltd collaboration produces 50 µm thick LGAD and a 250 µm thick iLGAD sensors. The LGADs are envisaged as fast-timing detectors for particle physics experiments, while the iLGADs were developed as a technological solution to solve issues with the low fill factor in the conventional LGAD. These detectors are produced as pad detectors of various pixel sizes and doping concentrations for testing. The pixelated version of the 250 µm thick iLGAD and an earlier iteration of a 200 µm LGAD are bonded to Timepix3 readout ASICs as one-of-a-kind hybrid pixel detector prototypes. In addition to these detectors, the University of Glasgow also produced hybrid pixel detectors with high-Z sensors.

The electrical properties of the (i)LGAD pad detectors are explored via IV and CV measurements. Some LGAD pad detectors are also evaluated for their gain using the TCT with a 1040 nm infrared laser source. The doping concentration in the multiplication region dictates the electrical characteristics of (i)LGADs. The 50 µm thick LGADs achieve full depletion at voltages between 26 V to 31 V. Breakdown voltages were 5 to 9 times higher than full depletion voltage, indicating a wide dynamic range for operation. The

JTE width or, collectively, the device's active area restricts the achievable gain and fill factor in the 50 µm thick LGAD. The 1.0 mm × 1.0 mm LGAD achieves a 6.75 gain at 30 °C, with a 74 % increase in gain for a 50 °C temperature drop.

The hybrid pixel detectors with (i)LGAD sensors are calibrated for energy and corrected for time-walk with XRFs and γ-ray sources. Subsequently, their pixel responses and signal gains are investigated with a micro-focused synchrotron beam at Beamline B16, Diamond Light Source. No signal gain was observed in the hybrid pixel detector with 55 µm pitch LGAD, but this is expected and fully understood—however, the 110 µm pitch variant performed with a limited fill factor as expected, with a gain of around 5 at −350 V bias voltage. The iLGAD is a viable solution to overcome the low-fill factor of an LGAD. A gain of around 5 at 250 V bias voltage with a fill factor of more than 80 % was obtained in the hybrid pixel detector with 55 µm pitch iLGAD.

The thesis also discussed the application of a hybrid pixel detector with a high-Z sensor as a single-layer Compton camera. Proof of concept was demonstrated in a very thin (1 mm thick), 55 µm pitch CdTe bonded to a Timepix3 readout ASIC. Despite limited data, an image depicting the origin of a gamma-ray source was fully reconstructed just by utilising the Compton scattering kinematics.

Kunsikahan dii ouh ogina-gina kumaa dii kooduo molohing ku **Abel Lombigit Bolukis** om **Rubeca Ladom** - RIP.

Sawo om tambalut ku **Rollyne Alip** om nogi tanak ku **Luke Ryan Lombigit** - Kounsikou sokodung diikoyu ngoduo.

Acknowledgements

I would like to thank my supervisors Prof. Valentine O'Shea and Dr. Dima Maneuski for their support and guidance during my time as a PhD student at the University of Glasgow. An immeasurable thank to my family (Rollyne & Luke Ryan) for their continued support, love, motivation and prayers especially during and after the pandemic. A special thank also to Dr. Richard Bates for giving me the opportunity to work on the Low-Gain Avalanche Detectors (LGAD) project.

Not forgetting fellow PhD colleagues in room 328b (Niel Moffat, Dwayne Spiteri, Lluis (Don Simon), later Laurynas Mince, and ERASMUS students from DIT and Turkey) and ATLAS Phd students office. You guys helped me integrate into the group and help this "OLD MAN"during his struggles against physics and coding. Also big thank you to Mr. Calum Gray and Rory McFeely for helping me with the IV/CV measurement, wire-bonding and TCT measurements.

I would like to acknowledge the Public Service Department of the Malaysian Government for sponsoring my PhD study under the Federal Training Grant (HLP). Not forgetting my employer the Malaysian Nuclear Agency for granting me three and a half year study leave. I also would like to thank Dr. Benedikt Bergmann of the Institute of Experimental and Applied Physics (IEAP), Czech Technical University (CTU) in Prague for accepting me as a fellow for one month and allowing me to use their facilities to enable me to complete the Compton camera chapter.

Lastly, how could I ever escape by not mention the legendary “Bean On Roast Coffee Club ” especially the founding members; Niel (the clown) Moffat, Laurynas (cassanova) Mince, Dean Spiteri (sorry for giving you a hard time in Badminton court), Dima Maneuski, Adam Rennie, Connor Harkin and Lluis (Don Simon). I had an unforgettable time of my life attending house parties, culinary heritage sharing and pub life with you guys.

Contents

List of Figures

List of Tables

Declaration

I declare that the materials presented in this thesis is solely my own work other than where I have clearly indicated that it is the work of others and that the thesis has not been edited by a third party beyond what is permitted by the University's PGR Code of Practice.This work is not been submitted to any degree at the University of Glasgow or other institutions.

Lojius Bin Lombigit

CHAPTER 1

Introduction

1.1 Pixel detectors

Radiation pixel detectors can track the trajectories of charged particles produced during high-energy collisions in particle physics experiments. Thus they are used as imaging detectors in particle physics, medical, and industrial applications. A typical pixel detector consists of individual microscopic sensors, each with readout electronics and arranged in a 2D grid pattern called a *pixel* [1]. Monolithic and hybrid pixel detector architectures are two different approaches to building pixel detectors, each with their own advantages and disadvantages. In a monolithic pixel detector architecture, the sensor and readout electronics are integrated into the same chip, offering compactness and scalability. Monolithic pixel detectors are known for their low power consumption, high pixel density, excellent noise performance, and are cheaper to produce. Currently, the monolithic pixel detector is restricted to silicon materials, where the sensor and readout electronics are fabricated using the complementary metal-oxide semiconductor (CMOS) technology.

In a hybrid pixel detector, the sensor and readout electronics are separate components

that are bonded together. The sensor can be picked from various semiconductor materials, and the readout electronics are CMOS chips. The sensor and readout chip are bonded using bump bonding, allowing for a high-density connection between the two components. Despite being more expensive to fabricate, the hybrid pixel detector offers greater flexibility where the sensor and readout electronics can be optimised independently. The sensor can be designed for high radiation tolerance and detection efficiency. At the same time, the readout electronics can be optimised for low noise, low power, and high-speed data acquisition.

The hybrid pixel detectors based on the CERN[1] Medipix/Timepix families of readout application-specific integrated circuits (ASICs) have been used in particle physics experiments and other fields such as education, space, and weather dosimetry, synchrotron imaging, studies of sensor materials, spectroscopic imaging (X-ray, γ-ray & particles) and electron microscopy[2]. The event-driven architecture introduced in Timepix3[3, 4] presents a significant improvement in the readout architecture that permits immediate data transfer whenever a pixel hit occurs. The Timepix3 has become the flagship readout ASIC of the Medipix Collaboration in the past decade and has been successfully transferred to many applications. The prototype readout for the LHCb[2] upgrade, VELOpix ASIC[5], is the latest ASIC variant based on the Timepix3.

Interest in the hybrid pixel detectors based on the Timepix3 readout ASIC continues to grow despite being a decade old; recent studies and applications include fast neutron detection [6], 3D charged particle momentum mapping in Free Electron Laser (FEL) facility [7], dose monitoring in FLASH radiotherapy[3] [8, 9] and Ion Microscope Imaging Mass Spectrometry [10]. The advancement of integrated circuit process technology and sensor materials continues to push the limit of pixel detectors in the future, where pix-

[1] Conseil Européen pour la Recherche Nucléaire or European Council for Nuclear Research
[2] Large Hadron Collider beauty
[3] A novel radiotherapy method that delivers an ultra-high dose ($\geq 40\,\mathrm{Gy/s}$) in milliseconds irradiation.

els will become smaller and more sophisticated. Recently, Through-Silicon Vias (TSV) technology [11] became available and has already been implemented in the upcoming Medipix4/Timepix4 readout ASIC currently under development within the Medipix4 collaboration. This technology enables further miniaturisation of ASIC and the development of larger area pixel detectors via edgeless tiling. Spectroscopic and colour-discriminating imaging based on single-quantum processing became crucial for future X-ray imaging systems [12–14]. Hence, pixel detectors remain relevant today and will play more significant roles in the future. The proceeding sections describe the motivation for undertaking the projects described in this thesis, the aims and novelty of said approach, and an overall thesis overview.

1.2 The motivation

The ATLAS[4] and LHCb VELO Upgrade II proposed future silicon detectors with $\leq 30\,\text{ps}$ time resolution to mitigate the expected signal pile-up in the upcoming High-Luminosity LHC (HL-LHC) accelerator[15, 16]. The Low Gain Avalanche Detector (LGAD) [17] was identified as one of the technologies for such detectors. These proposals sparked interest in LGAD, and such detectors have been explored by diverse institutions such as CNM[5] [18, 19], FBK[6][20], Hamamatsu Photonics (Japan) [21, 22] and Brookhaven National Laboratory (USA)[23] in recent years.

The University of Glasgow, collaborating with Micron Semiconductor Ltd, has expanded on previous LGAD research in [24] to develop two LGAD prototypes. The first is a thin $50\,\mu\text{m}$ pad LGAD with a Junction Termination Extension (JTE) structure produced in various sizes across three wafer batches. This LGAD is envisaged as an ultra-fast detector detection with sub-30 ps time resolution, meeting the ATLAS and LHCb VELO Upgrade

[4] A Toroidal LHC Apparatus
[5] The Institute of Microelectronics of Barcelona (IMB-CNM-CSIC), https://www.imb-cnm.csic.es/en
[6] Fondazione Bruno Kessler, Trento, Italy. https://www.fbk.eu/en/

II requirements. The second is a 250 µm thick inverse-LGAD (iLGAD), available in both pad device and pixelated configurations, produced on two wafers. This prototype builds on earlier findings that revealed limitations in conventional LGAD designs, particularly the inability to produce substantial gain at 55 µm pixel pitch[25]. The development of the iLGAD specifically aims to overcome these gain limitations at small pixel pitches.

Multiple sizes of pad devices were cut from the LGAD and iLGADs wafers and were delivered to the University of Glasgow. The electrical properties and gain of the 50 µm thick LGAD are investigated—however, time resolution measurement is a subject of another work and was excluded from this thesis. The iLGAD is a very recent addition to the LGAD variants. Their electrical properties and radiation response are not fully understood. Understanding their fundamental properties helps optimise the operation of the detectors and enables developers to design applications that utilise their capabilities effectively.

This thesis also examines the performance of hybrid pixel detectors with (i)LGADs sensors under radiation exposure. Initially, 300 µm thick pixelated LGADs with 55, 110, and 220 µm pixel pitches were bonded to Timepix3 ASICs in 2019. These pioneering devices, being the first of their kind, were characterised using synchrotron radiation at the Beamline B16 facility of Diamond Light Source (DLS) in late 2019 to assess their previously unknown radiation response. Following this, pixelated iLGADs with identical pixel pitches were cut from the iLGAD wafer and bonded to Timepix3 ASICs. These new hybrid pixel detectors underwent identical testing conditions at the same synchrotron facility during a second beam session in 2021.

The University of Glasgow also produced hybrid pixel detectors with high-Z semiconductor detectors. These detectors are 5 mm thick with highly pixelated 110 µm-pitch CZT bonded onto a Timepix and Timepix3 readout ASICs. This technology is mature, and both

detectors are fully characterised, but their potential applications are yet to be explored. The single-layer Compton camera (SLCC) based on the hybrid pixel detector with high-Z semiconductors recently gained popularity following the work in[26]. Thus, it was decided to revisit and reanalysed data acquired with both detectors to explore its potential for an SLCC system.

1.2.1 Aims and novelty of thesis work

This thesis seeks to explore the following subjects;

(i) To characterise the thin LGAD (50 µm thick) and the iLGAD pad devices produced within the University of Glasgow - Micron Semiconductor Ltd collaboration.

(ii) To characterise the hybrid pixel detector with 300 µm thick LGAD with radioisotope and X-ray fluorescence (XRF) sources. Also reanalysed the radioisotope and XRF data previously acquired with the hybrid pixel detector with 5 mm thick 110 µm-pitch CZT.

(iii) To characterise the two hybrid pixel detectors with LGAD and iLGAD sensors with micro-focus synchrotron radiation.

(iv) To explore the potential of the Hybrid pixel detectors with high-z semiconductors for a single-layer Compton camera system.

The LGAD and iLGAD pad devices and the hybrid pixel detectors with LGAD sensors are produced using Micron Semiconductor's process technology. The hybrid pixel detectors characterised in this thesis are the world's first small-pixel LGAD and iLGAD bonded to Timepix3 readout ASIC. Characterisation of such hybrid pixel detectors with a micro-focus synchrotron beam has not been reported in any publication. The CZT sensors used in this study are grown with different manufacturing processes and differ from recent studies in [27–29]. Additionally, it is noteworthy that one of the CZT sensors in this study has

been affixed to the most recent high-performance Timepix3 readout ASIC.

Moreover, this thesis also contributes to the development of analysis code to process the hybrid pixel detector's data. The analysis code is based on the Python 3 IDE and is compatible with the ADVACAM Pixet Pro software[7] data format. It has been used successfully in characterising the hybrid pixel detectors and the single-layer Compton camera system. The single-layer Compton camera demonstrated in this thesis uses a much thinner (1 mm thick) high-Z Cadmium Telluride (CdTe) sensor which also uses bespoke code to process data with additional Compton kinematics criteria. Therefore, it aslo differs from other published works. In conclusion, cumulative findings from this thesis are valuable additions to the existing knowledge in this field.

1.3 Thesis overview

This thesis is divided into 9 chapters; the first 4 chapters describe the background of the subject, fundamental theories of semiconductor detectors, an overview of the Medipix Collaboration's Timepix3 readout ASIC, and detector's characterisation techniques. Chapters 5, 6, 7 and 8 are the core chapters of this thesis.

Chapter 5 presents the characterisation of the 50 µm thick LGAD and 250 µm thick iLGAD pad devices. Both of which are characterised electrically by IV and CV measurements. Additionally, the signal gain in the 50 µm thick LGAD is characterised by Transient Current Techniques (TCT) with a 1040 nm infrared laser. Results of the electrical characterisation and gain measurements as a function of doping concentration, pixel sizes and temperatures are presented and discussed. Characterisation of the hybrid pixel detectors with XRF and radioisotopes is presented in Chapter 6, with detailed descriptions of the experiment setup, analysis scripts, energy calibration and time-walk correction in hybrid pixel

[7]The acquisition software used with the ADVACAM (https://advacam.com/) readout system.

detector with LGAD sensor and the response of the hybrid pixel detector with 5 mm thick CZT to radioisotopes with higher energy.

Chapter 7 describes the two synchrotron test beam campaigns involving two hybrid pixel detectors with LGAD and iLGAD sensors conducted at the Beamline B16, Diamond Light Source (DLS), in 2019 and 2021. The synchrotron test beam setup is explained, and the key findings are presented and discussed. Chapter 8 explores the viability of a hybrid pixel detector with a high-Z semiconductor sensor for an SLCC system. A proof-of-concept of a SLCC with a 1 mm thick CdTe bonded to a Timepix3 readout ASIC is shown with 122 keV γ-ray. Lastly, the conclusion and outlook are given in Chapter 9.

CHAPTER 2

Theoretical background

This thesis uses two types of semiconductor materials as detector elements: Silicon and high-Z compound semiconductors, Cadmium Telluride (CdTe) and Cadmium Zinc Telluride (CZT). The LGAD and iLGADs detector elements are fabricated with p-type silicon and produced as test devices in pad detectors and pixelated form. The pixelated LGAD and iLGAD are then bump-bonded to Timepix3 readout ASICs. The detector elements are characterised and calibrated by various photon sources, X-ray fluorescence (XRF), γ-ray from radioisotope decay, and the synchrotron radiation from the particle accelerator.

It is essential to fathom the fundamental properties and operation of semiconductor detectors, the interactions and energy loss of charged particles and photons and the signal generation and formation in semiconductor detectors. It is also necessary to understand the basic principles of the readout electronics used to process the semiconductor detectors' signals and the uncertainties that influence the detector performance.

This chapter is divided into four sections. The first section briefly overviews the fundamental properties of semiconductor materials, focusing on silicon and high-Z compound semiconductor (CdTe & CZT) materials. The second section describes the operation prin-

ciples and the semiconductor detector's basic structures. The energy loss mechanisms of charged particles and photons are introduced in the third section. The last section discussed signal generation and formation. Also, briefly introduce the readout electronics.

2.1 Semiconductor physics

Semiconductor detectors use semiconductor materials to detect and measure charged particles and photons. Semiconductors are a good medium to detect charged particles and photons since they are a high-density medium (as opposed to a gaseous medium) and, most importantly, produce higher ionisation yields with lower charge generation fluctuations that guarantee excellent spectroscopic resolution. The most commonly used semiconductor material for radiation detectors is silicon. However, other materials, such as germanium (Ge) and compound semiconductors, are also utilised, depending on the application's specific requirements. This section reviews the semiconductor physics relevant to this thesis, including the properties of semiconductor materials, intrinsic and extrinsic semiconductors, charge transport, charge multiplication in silicon sensors, and carrier loss in CdTe/CZT materials.

2.1.1 Energy band and semiconductor materials

Solid materials are defined by energy bands called *valence* and *conduction* bands. Figure 2.1 shows the energy band structure of insulators, semiconductors and conductors. A conductor may have overlapping valence and conduction bands or a partially filled conduction band. In contrast, an insulator has all its electrons in the valence band while the conduction band is empty, and both energy bands are widely separated. The semiconductor has a narrow energy gap between the valence and conduction bands and a balanced number of charge carriers in their respective energy bands. The energy level at the top of the valence band is referred to as the *valence energy* (E_V), while the bottom of the conduction band is the *conduction energy* (E_C). The energy differences, E_V - E_C is called the *bandgap energy*

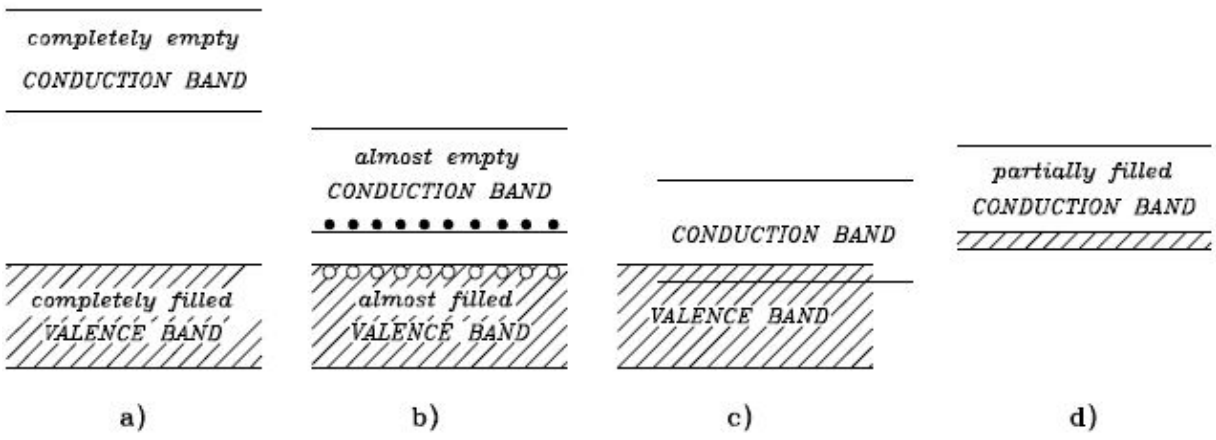

Figure 2.1: The energy band of solid. (a) An insulator has empty electrons in the conduction band. It is filled with the electron in the valence band, (b) semiconductors with almost full of electrons in the valence band but almost empty of electrons in the conduction band, and (c) (d) conductors with partially filled conduction band or overlapping valence-conduction band [30]

.

(E_G). The E_G is the energy required to free an electron from valence to the conduction band. This energy is temperature-dependent and defines the electrical properties of the material. The E_G is considered non-existent in conductors, very narrow in semiconductors (typically between 0.4 eV to 4 eV) and significantly large in insulators (> 5 eV) [31, 32].

Silicon is an elemental semiconductor from group IV(B) with four electrons in its outermost orbital shell. The silicon used for detector construction is made from a single crystal with a diamond structure[30]. Silicon has low bandgap energy (≈ 1.12 eV) with a modest atomic number (Z=14) and density ($2.33\,\mathrm{gcm}^{-3}$), which makes it unsuited for room-temperature operation and measuring high-energy photons ($>$ a few hundred keV). Silicon is typically fabricated as thin semiconductor detectors ($\approx$ a few hundred microns) for particle tracking in particle physics experiments or charged particle detectors (α & β particles) in nuclear science applications.

There is a demand for semiconductor detectors capable of absorbing high-energy photons and operating in room-temperature environments, especially as imaging detectors in medical and industrial applications. Work in [33] (and references therein) proposed

requirements of such a detector where the semiconductor material should have an $E_G > 1.4\,\text{eV}$ for room-temperature operation and high effective atomic number (Z > 30) to provide adequate absorption of high-energy photons. The latter requirement suggests that such detectors must be made with a combination of elements.

Table 2.1: Physical properties of Si, Ge, CdTe and CZT (adapted from [34] [33])

Material	Si	Ge	CdTe	CZT
Crystal structure	Cubic	Cubic	Cubic (ZB)	Cubic (ZB)
Atomic number	14	32	48, 52	48, 30, 52
Density (g/cm^3)	2.33	5.33	6.2[34], 5.85[33]	5.78
Bandgap, E_G (eV)	1.12	0.67	1.44[34], 1.5[33]	1.57[34], 1.48[33]
Pair creation energy, E_i (eV)	3.62	2.96	4.43	4.6[34], 4.64[33]
Resistivity, ρ (Ω·cm)	10^4	50	10^9	10^{10}
$\mu_e\tau_e(cm^2/V)$	> 1	> 1	10^{-3}	$10^{-3} - 10^{-2}$
$\mu_h\tau_h(cm^2/V)$	~ 1	> 1	10^{-4}	10^{-5}
$\mu_e\tau_e(cm^2/V)$	> 1	> 1	10^{-3}	$10^{-3} - 10^{-2}$
$\mu_h\tau_h(cm^2/V)$	~ 1	> 1	10^{-4}	10^{-5}
Fano Factor, F	0.06[35]	0.06[35]	0.06[35]	0.10[35]

Cadmium Telluride (CdTe) and Cadmium Zinc Telluride (CZT) are two wide-bandgap compound semiconductor materials that have been extensively explored as room-temperature imaging detectors in medical and industrial applications[34][33][36][37]. The physical properties of the CdTe and CZT compared to silicon and germanium are shown in Tab. 2.1. The CdTe and CZT are compound semiconductor derived from the group - IIB metal (Cd) and group - VIA cation (Te). The CdTe is a binary, while CZT ($Cd_{1-x}Zn_xTe$) is considered as a pseudo-binary which contain more than two elements but only made of two elements (Cd and Te). The CZT can be ideally regarded as CdTe crystal with the introduction of Zn atoms for a fraction x of the Cd atoms. Both CdTe and CZT compound semiconductor have a cubic zinc blende crystal structure with high atomic numbers (> 30), wide bandgap energies ($E_G > 1.4\,\text{eV}$), and high density, which guarantees room-temperature operation and good absorption of low to mid-energy photons. CZT has at least one order of magnitude greater bulk resistivity than CdTe. Therefore, CZT has a smaller leakage current, enabling it to be biassed at higher voltages and operated at higher temperatures.

The CdTe and CZT semiconductor materials currently available today are far from perfect. They mainly suffer from material defects and impurities during crystal growth and manufacturing. Material defects and impurities act as trap centres, causing poor charge transport and significant disparity between the electron and hole mobility-lifetime ($\mu\tau$) properties. The CdTe, in particular, suffers from a *polarisation effect* that causes a reduced count rate and charge collection efficiency (CCE) during a prolonged operation. This effect is mainly due to the trapping and de-trapping of charge carriers, which affect the detector's space charge distribution and electric field profile[34]. The effect can be minimised by operating the CdTe at lower temperatures and higher biassed voltage[38].

2.1.2 Intrinsic & Extrinsic Semiconductors

An *intrinsic semiconductor* is a semiconductor with a lower impurity concentration than the thermally generated carrier concentration. The thermally generated carrier concentration for holes (p) and electrons (n) is deduced from the Fermi-Dirac occupation probability function ($F_n(E)$) and given as [30]

$$p = N_V \exp \frac{E_V - E_F}{kT} \tag{2.1}$$

$$n = N_C \exp \frac{E_C - E_F}{kT}\,, \tag{2.2}$$

where the N_C and N_V are the effective density states of conduction and valence bands, k is the Boltzmann constant, T is the temperature in Kelvin, and E_F is the Fermi level. The product of electron and hole concentration ($n \cdot p = N_C N_V \exp \frac{E_C - E_V}{kT}$) depends only on the bandgap energy E_G. The Fermi level for intrinsic semiconductors, E_i is the energy level close to mid-bandgap where the number of electrons and holes are equal : $n = p = n_i$, thus the E_i and the intrinsic carrier concentration, n_i are defined as

$$E_i = \frac{E_C + E_V}{2} + \frac{3kT}{4} \ln \left(\frac{m_p}{m_n} \right) \tag{2.3}$$

$$\begin{aligned} n_i &= \sqrt{N_C N_V} \exp -\frac{E_C - E_V}{2kT} \\ &= \sqrt{N_C N_V} \exp -\frac{E_G}{2kT}\,, \end{aligned} \tag{2.4}$$

with m_n and m_p are the mass of electrons and holes, respectively.

Intrinsic semiconductors have limited use as semiconductor devices, and obtaining high purity in semiconductors is extremely challenging. In most cases, the intrinsic semiconductor is deliberately doped with impurity atoms to alter the property of the semiconductor. A doped intrinsic semiconductor is called an *extrinsic semiconductor*. Depending on the number of electrons in the outer shell of these dopants, impurity atoms either donate or accept electrons to or from the lattice. For example, if silicon is doped with phosphorus, as phosphorus has five valence electrons, it "donates"one electron to the conduction band to form a covalent bond with four electrons. The phosphorus acts as a *donor* atom, producing an n-type semiconductor. In another scenario, boron with three valence electrons "accepts" one electron from silicon to form the covalent bond and generate a positively charged hole in the valence band. The boron acts as an *acceptor* atom, producing a p-type semiconductor. The proceeding subsection discussed the important charge transport processes that are relevant to the scope of this thesis.

2.1.3 Carrier transport and resistivity

A diverse range of transport processes collectively governs the operation of a semiconductor device. For simplification, only the *drift, diffusion and charge multiplication* that are relevant to the context of this thesis are discussed. The electron in thermal equilibrium (in non-zero temperature) moves in all directions by thermal motion. Their motion is due to random scattering after collisions with the lattice atoms, impurity atoms or other electrons. However, the net displacement is zero when no bias voltage is applied. The average *time* and *distance* between collisions is called the *mean free time* and the *mean free path*. Given that the mean kinetic energy of free charge carriers at room temperature is $\frac{3}{2}kT$, a typical *mean free path* is 10^{-5} cm and *mean free time*, $\tau_c \approx 10^{-12}$ s[30].

In the presence of an electric field, the charge carriers experienced force and accelerated in

the direction determined by the electric field. The net average drift velocity for electrons are

$$v_n = -\left(\frac{q \cdot \tau_c}{m_n}\right) E \tag{2.5}$$

and similarly, for holes,

$$v_p = -\left(\frac{q \cdot \tau_c}{m_p}\right) E\,, \tag{2.6}$$

where q is the elementary charge and E is the electric field. Equation 2.5 and equation 2.6 show that the drift velocity is proportional to the magnitude of the electric field, E. The drift velocity rises linearly at low E, becomes non-linear at high E, and saturates at very high E. It would be worth noting that the semiconductor detector operates at saturated drift velocity. The proportionality factor $\left(\frac{q\cdot\tau_c}{m_n} = \mu_n \text{ or } \frac{q\cdot\tau_c}{m_p} = \mu_p\right)$ is called the *mobility*. It describes how strongly the electric field determines motion. The charge carrier mobilities (μ_n, μ_p) are dependent on temperature and doping concentration [30]. Equation 2.5 and equation 2.6 now can be simplified to

$$v_n = -\mu_n E \tag{2.7}$$

$$v_p = -\mu_p E\,. \tag{2.8}$$

Besides the *drift* mechanisms, the free charge carriers also experience *diffusion*. Upon creation, electron-hole pairs experience a random thermal motion that spreads from the origin point with time. The charge spread distribution is approximated by a Gaussian function with σ given by [39] [32]

$$\sigma = \sqrt{2Dt}\,, \tag{2.9}$$

where D is the diffusion coefficient, and t is the elapsed time. According to the Einstien equation, the D is related to the mobility, μ as [30]

$$D_{n,p} = \frac{kT}{q}\mu_{n,p}\,. \tag{2.10}$$

Resistivity also holds significant importance in the context of semiconductor detectors. Materials with high resistivity are desirable because they can achieve full depletion at lower

biassed voltages. Typical values used in high energy physics detectors are $\approx 2 \times 10^5\,\Omega$cm. The doping concentration controls the resistivity, ρ, defined as [40].

$$\rho = \frac{1}{(n\mu_n + p\mu_p)} \tag{2.11}$$

2.1.4 Charge multiplication

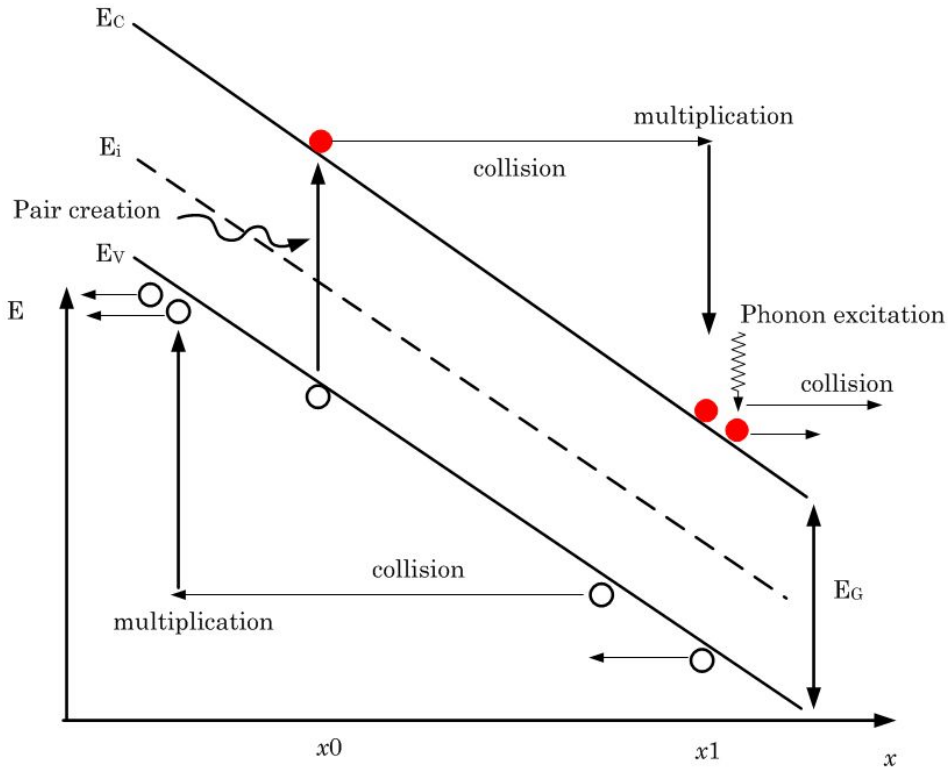

Figure 2.2: Illustration of charge multiplication in the high-field region of a semiconductor (adapted from [30])

In semiconductor detectors, charge carriers acquire kinetic energy as they travel between collisions with lattice atoms. When subjected to sufficiently strong electric fields, these carriers may gain enough energy to trigger secondary ionisations during collisions. This phenomenon, impact ionisation, is analogous to the Townsend avalanche in gas-filled proportional counters. Figure 2.2 demonstrates this charge multiplication process in a silicon detector's high-field region. Consider a primary ionisation event at position x_0, which produces an electron-hole pair. The electron, accelerated by the electric field, accumulates kinetic energy between collisions. Upon impact, a portion of this energy creates a new

electron-hole pair (depicted by a solid downward arrow), whilst the remainder is transferred to lattice vibrations. Consequently, charge multiplication occurs, resulting in two electrons and one hole reaching position x_1. This process significantly amplifies the initial charge, enhancing the detector's sensitivity.

Gain due to impact ionisation of one type of charge carrier within a length d is described as

$$G_q = e^{\alpha_q d}, \tag{2.12}$$

where α_q is the ionisation coefficient of the charge carrier[18]. This coefficient, conveniently described separately for electrons and holes, is the reciprocal of the mean distance between successive ionisation events (in cm^{-1}). It is highly dependent on the electric field (E) and is defined in terms of two coefficients as

$$\alpha_q = \alpha_{q0} \cdot e^{-\frac{E_q}{|E|}} \tag{2.13}$$

The α_q also depends on the material and temperature[41]. The terms α_{q0} and E_q increase with temperature, but since the exponential term in Equation 2.13 dominates, the α_q decreases with temperature[42]. Thus, higher gain is obtained at lower temperatures. In silicon, the impact ionisation rate ratio of electrons (α_n) to holes (α_h) exceeds unity. This ratio varies with the electric field strength, approaching one as the field intensifies. When the electric field becomes sufficiently strong, holes generate secondary charges through impact ionisation. This process initiates additional avalanches, ultimately leading to device breakdown.

2.1.5 Charge carrier loss in CZT and CdTe

The average time the charge carriers remain free before recombine is called *mean lifetime*, τ . The mean lifetime depends on the "deep impurities", which act as *traps* or *recombination centres* [32]. The trap and recombination centres contribute to the charge carrier loss and reduce the mean lifetime. The carrier drift length λ is the mean distance of charge

carrier drifts before recombining under the electric field. The λ is related to the mobility, μ and lifetime, τ as

$$\lambda_{n,h} = (\mu\tau)_{n,h} E. \tag{2.14}$$

The term $\mu\tau$ called *mobility-lifetime product* is a crucial parameter reflecting the semiconductor detector's quality. The hole trapping is significant in CdTe and CZT detectors due to its lower hole mobility, affecting charge collection efficiency. The charge collection efficiency (CCE) is the ratio of charge collected, Q, to charge generated, Q_0. For a planar detector with thickness, L assuming uniform electric field and neglecting the charge de-trapping, the CCE is calculated according to the Hecht equation [43]

$$\begin{aligned} CCE &= \frac{Q}{Q_0} \\ &= \left[\frac{\lambda_h}{L} \left(1 - \exp^{-\frac{x}{\lambda_h}} \right) + \frac{\lambda_n}{L} \left(1 - \exp^{-\frac{L-x}{\lambda_n}} \right) \right], \end{aligned} \tag{2.15}$$

where x is the depth of interaction from the biased electrode.

2.2 Principle of detector operation

Semiconductor detectors operated under a reversed biassed. For silicon detectors with a p-n junction structure, a space charge region called the *depletion region* exists between the junctions. In the depletion region, the carrier density is zero [40], and this region becomes the sensitive volume for p-n junction detectors. On the other hand, a high-purity n or p-type semiconductor (close to intrinsic) is generally used as material for the CdTe/CZT detectors construction [32]. So, the bulk becomes the sensitive volume of the detectors. Photons or charged particles interact within the sensitive volume, creating electron-hole pairs that move under an electric field's influence and induce an electrical signal at their respective electrodes.

2.2.1 Reverse biassed p-n junction

A p-n junction is created by joining n-type and p-type semiconductors. Upon reaching thermal equilibrium, a space charge region is formed between the p and n junction. A potential difference called *built-in* potential, V_{bi} exists between the edges of the depletion region defined as

$$V_{bi} = \frac{kT}{q} \ln\left(\frac{N_A N_D}{n_i^2}\right), \tag{2.16}$$

with N_D, N_A, and n_i are the donors, acceptors, and intrinsic carrier concentrations. If an external voltage is applied in the same direction as the built-in voltage (*reverse biassed*), the depletion region expands and its depth (W) becomes

$$W = x_n + x_p = \sqrt{\frac{2\epsilon}{q}\left(\frac{1}{N_A} + \frac{1}{N_D}\right)(V_{bi} + V)}, \tag{2.17}$$

where the x_n and x_p are part of the depletion region on the n- and p-side, respectively, V is the externally applied voltage, and ϵ is the permittivity of semiconductor material.

In practice, one side of the p-n junction is heavily doped and thinner than the other. Thus, the term $\frac{1}{N_A}$ is negligible, which means the depletion region extends much deeper into the lower doped side. Moreover, the built-in voltage is much smaller ($\approx 0.5\,\mathrm{V}$ in silicon) than the applied voltage. These assumptions lead to

$$W \approx x_n \approx \sqrt{\frac{2\epsilon}{qN_D}V} \tag{2.18}$$

.

The N_D is usually replaced with the term N, which is the dopant concentration of the bulk. The voltage required to extend the depletion region over the device thickness d is called the *full depletion voltage*, V_{FD}. This quantity is an essential parameter that defines the minimum operating voltage of a detector. The V_{FD} is calculated from equation 2.18 with $W = d$ as

$$V_{FD} = \frac{qNd^2}{2\epsilon} \tag{2.19}$$

The full depletion capacitance C_{FD} is another essential parameter of semiconductor detectors. The detector capacitance influences the noise of the readout electronic system, whilst pixel-to-pixel capacitance influences the cross-talk between pixels [44]. For a planar p-n junction detector, the total capacitance is estimated according to the parallel plate capacitor equation as

$$C_D = \epsilon\frac{A}{d} = A\sqrt{\frac{q\epsilon N}{2V_{FD}}}. \tag{2.20}$$

2.2.2 Basic structures of silicon detectors

The basic structure of a p-n junction in figure 2.3a is the most common structure for silicon detectors. The junction is formed by a shallow, highly doped n^+ implant on a low-doped, high-resistivity p-type silicon substrate. In practice, the p-n junction detector is biassed at a much higher voltage than its V_{FD}. This condition creates a uniform electric field of $\frac{V - V_{FD}}{d}$ between the electrodes. An incident particle interacts in the depletion region, creating electron and hole pairs. The uniform electric field presents allow these free charges to move to their respective electrodes, inducing an electrical signal that can be detected by a readout system.

A Low Gain Avalanche Detector (LGAD) is an example of a silicon detector with an internal gain (typically gain of a factor 5 to 10)[17]. Figure 2.3b shows a typical structure of an LGAD that is based on a p-type silicon substrate. The main structural difference in the LGAD structure is the additional moderately doped p-type multiplication layer diffused under the n^+. The doping profile of the p-type multiplication layer is designed to create a high electric field region in this layer (see the electric field profile of the LGAD in figure 2.3b). The free charge generated by incident particles may gain sufficient kinetic energy to create a secondary electron-hole pairs via impact ionisation once they enter the high field

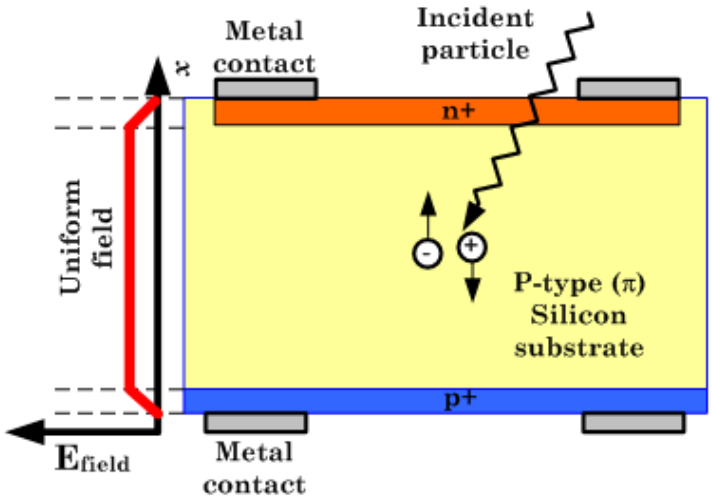

(a)

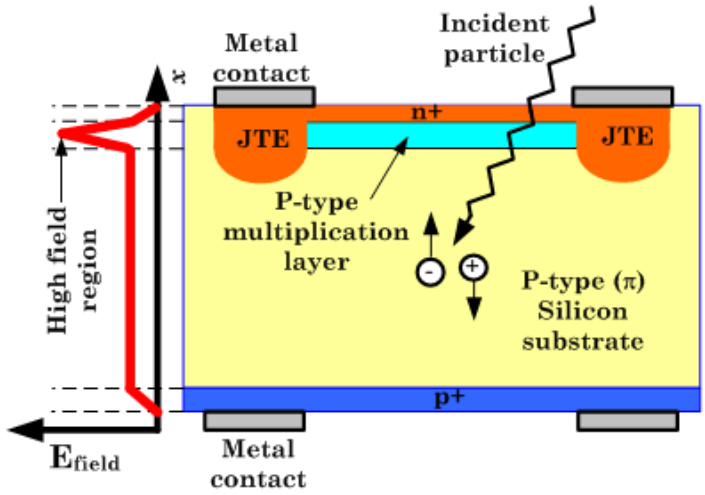

(b)

Figure 2.3: Basic structure of (a) p-n junction silicon detectors and (b) the Low Gain Avalanche Detectors (LGAD) based on a p-type silicon substrate. The p-n junction is normally biassed higher than their V_{FD} to get a uniform electric field between electrodes. The LGAD has a multiplication layer with a higher electric field.

region ($E_{field} > 200\,kV/cm$) in the multiplication layer. A traditional LGAD typically incorporates a deeper extension of the n^+ called the Junction Termination Extention (JTE) structure. The JTE weakens the electric field at the edges so that the high field is concentrated in the multiplication layer. The LGAD usually multiplies a single carrier, i.e., only the electrons, and the charge multiplication follows the exponential law [45]

$$N(x) = N_0 \cdot G, \tag{2.21}$$

where N_0 is the number of electrons generated from the primary ionisation, and G is the gain due to impact ionisation described in equation 2.12.

LGADs can provide excellent time resolution compared to a standard p-n junction diode because the signal generated in LGAD is much higher. Therefore, the LGAD was identified as one of the candidates for the *High-Granularity Timing Detector* detector for the ATLAS Phase-II upgrade [15]. A few variants of LGAD exist, namely the inverse LGAD (iLGAD), Trench Isolated LGAD (TI-LGAD), and AC-coupled LGAD (AC-LGAD)[46].

2.2.3 Basic structures of CdTe and CZT

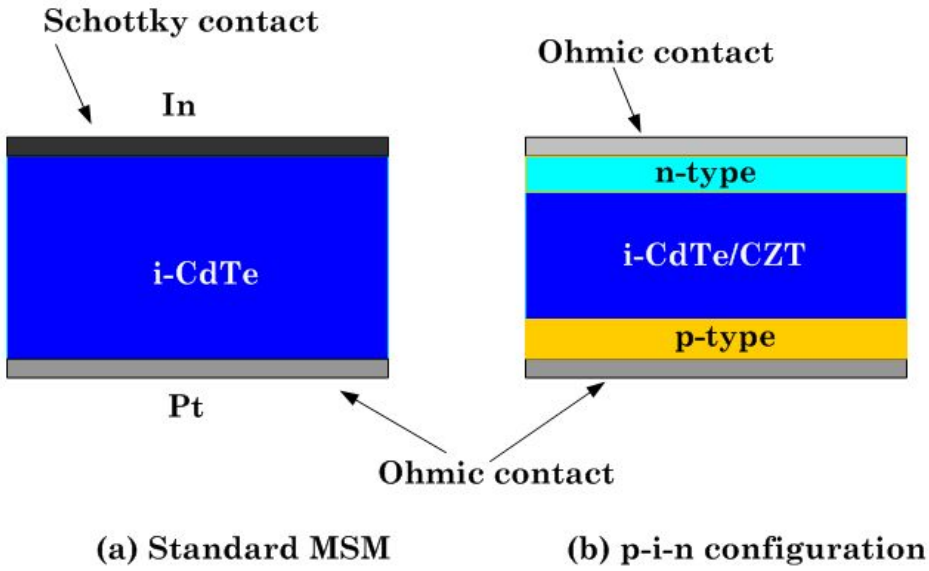

Figure 2.4: Two detector configurations for CdTe and CZT detectors (adapted from [34]). The standard metal-semiconductor-metal (MSM), a pure substrate with Pt/In metal contacts which is typical for CdTe detectors (a) and (b) the p-i-n configuration with a pure substrate, two n-/p-type homo-epitaxial layers and two ohmic contacts

.

The metal-semiconductor-metal (MSM) and p-intrinsic-n (p-i-n) structures (figure 2.4) are two common structures for CdTe/CZT detectors. The latter will not be discussed here since the CdTe/CZT detectors used in this thesis are made with MSM structures. A high-resistivity, detector-grade (high purity) CdTe/CZT substrate is sandwiched between two

metal contacts in an MSM structure. The work function of the metal (Φ_M) and the type of semiconductors (n- or p-type) used are two parameters that decide the type of contact that will form on the metal-semiconductor interface. The work function (Φ) is the energy required to remove an electron from its Fermi level to a reference energy level outside the metal. It determines charge carriers' flow across the metal-semiconductor interface.

Suppose the work function of the metal (Φ_M) is higher than the semiconductor (Φ_S). In that case, the contact becomes Schottky on an n-type semiconductor but Ohmic on a p-type semiconductor, whilst vice versa if $\Phi_M < \Phi_S$. In Schottky contact, the charge carriers move from semiconductor to metal (unilateral transfer) until the Fermi levels on both sides of the junction are equal and this charge transfer creates a depletion region at the semiconductor's surface that acts as a charge barrier [47]. In contrast, the charge carriers move from metal to semiconductor in an Ohmic contact, but the charge transfer did not create a depletion region [48]. Gold and platinum are an example of metals with higher work functions, while aluminium has a lower work function. Detectors with MSM structure are difficult to fabricate since the electrical characteristics of the metal are over-relying on the fabrication conditions. Moreover, they require significantly higher bias voltage to obtain good charge collection and therefore generate higher dark current ($10 \times 10^{-7}\,\mathrm{A/cm^2}$ to $10 \times 10^{-8}\,\mathrm{A/cm^2}$) [34].

2.3 Interactions and energy loss mechanisms of charged particles and photons

The LGAD and iLGAD sensors are designed for detecting soft X-rays in synchrotron applications or charged particles in particle physics experiments, while the 5 mm thick CZT and 1 mm thick CdTe are for γ-ray imaging below 1 MeV range. Three types of photon sources are used to characterise these detectors; the XRF, γ-rays, and a micro-focused monochromatic (15 keV) synchrotron beam. Despite being tested only with photons, the

semiconductor detector remains first and foremost a charged particle detector. Hence, discussion on the charged particles and photons interactions is relevant. This section briefly reviews the interactions of charged particles and photons and their energy loss mechanisms in semiconductor detectors.

2.3.1 Interactions of charged particles

Charged particles are particles that possess either positive or negative charge. Their origins can be natural, such as cosmic rays, or artificial, e.g. particle accelerators. Charged particles interact simultaneously with many *bound electrons* in the atom via Coulomb interactions, and depending on the proximity of their encounter, they lose their *kinetic energy* continuously either by *excitation* or *ionisation* [32, 49]. The energy loss by excitation is where Coulomb impulsion raises the electron to the higher energy shell within the absorber atom. In another scenario where the charged particle passes close to an electron, the Coulomb impulsion ejects the electrons from the atom leaving the atom in an ionised state (ionisation). The ejected electrons, called δ-rays, are highly energetic and may have sufficient kinetic energy to create further ionisations. Under typical conditions, the δ-ray is the primary mode in which charged particles lose energy [32]. The range of the δ-ray is short compared to the incident charged particle, so it forms ionisation tracks close to the primary track.

As the charged particle transfers energy to the electrons and the lattice, its velocity decreases. Interactions continue until the charged particle exhaust their energy and are stopped in the absorber. The rate of energy loss dE per unit length dx [MeV/(g/cm^2)] of charged particles in an absorber medium is described by the Bethe-Bloch equation

$$-\frac{dE}{dx} = \frac{4\pi e^4 z^2}{m_0 v^2} NZ \left[ln\frac{2m_0 v^2}{I} - ln\left(1 - \frac{v^2}{c^2}\right) - \frac{v^2}{c^2}\right], \tag{2.22}$$

where e is the elementary charge, m_0 electron rest mass, and v, z are the velocity and charge of the incident particles[32]. The Z and N are the atomic number and number

density of the absorber atom. The I is the absorber's average excitation and ionisation potential in eV. A few conclusions can be drawn from the Bethe-Bloch equation in 2.22:

i. For non-relativistic particles ($v \ll c$), only the first logarithmic term is significant. Hence, $\frac{dE}{dx}$ varies with $\frac{1}{v^2}$ or inversely with particle's energy.

ii. For relativistic particles ($v \approx c$), $\frac{dE}{dx}$ depends only on the incident particle's charge (z). Particles with a higher z have a greater rate of energy loss.

iii. For different absorber materials, the $\frac{dE}{dx}$ depends on the product of NZ. Therefore, absorbers with high density and atomic numbers have greater energy loss (higher linear stopping power).

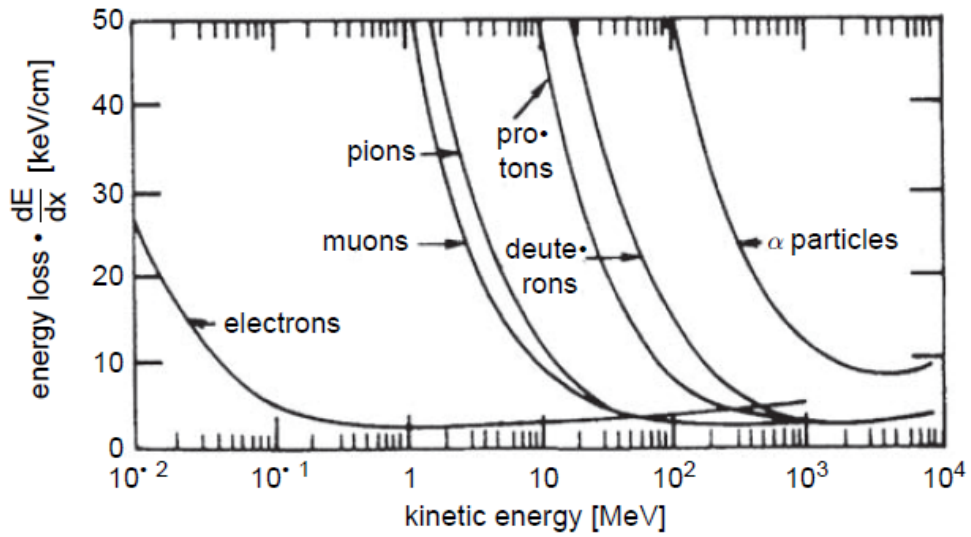

Figure 2.5: The rate of energy loss for several charged particles in air [49].

Figure 2.5 shows the $\frac{dE}{dx}$ of several charged particles in the air. This figure indicates that as the particles' velocity approaches the speed of light, their $\frac{dE}{dx}$ approaches a constant minimum value. A particle with enough kinetic energy to be in this regime is referred to as a *minimum-ionising particle* (MIP). MIPs have fixed energy loss that varies with materials; for silicon, MIPs will have energy loss $\approx 3.87\,\mathrm{MeV/cm}$ [50]. The distribution of energy losses by MIPs in a thin absorber is characterised by a *Landau distribution*, where the energy loss is determined by the *most probable* (MP) value of the distribution.

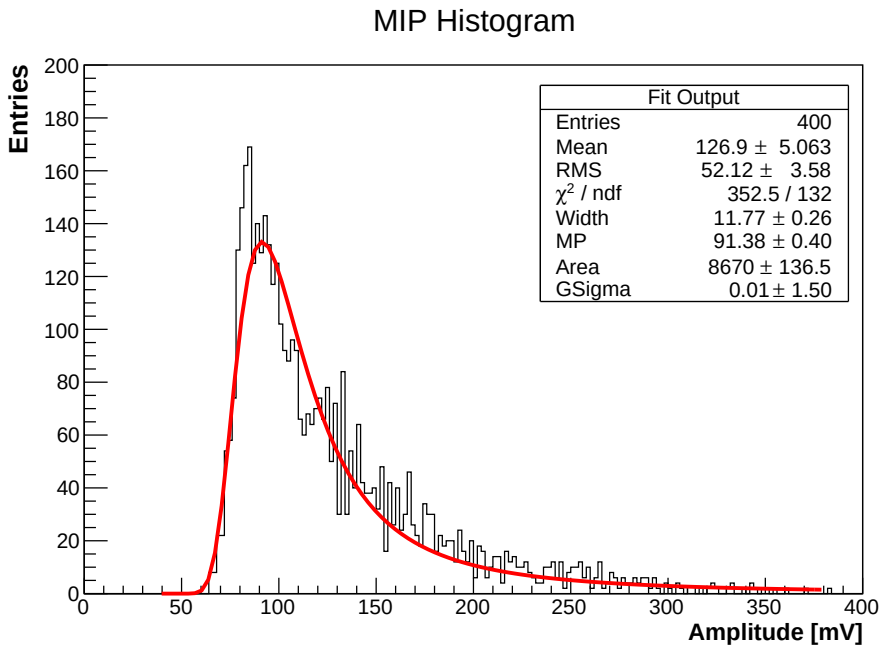

Figure 2.6: Distribution of minimum-ionising particles (MIP) of β-particles from ^{90}Sr decay in LGAD silicon sensor.

Figure 2.6 shows a Landau distribution of MIPs of β-particles in a 50 µm thick LGAD silicon sensor. For a very thick absorber, the energy loss of MIPs begins to approximate a Gaussian [49, 50].

The Bethe-Bloch equation only describes the energy loss due to ionisation and excitation, and only valid for moderately relativistic heavy charged particles. The energy lost due to radiative effects (Bremsstrahlung, direct pair-production or photonuclear interactions) becomes significant for particles with higher energy. The total energy loss of a heavy charged particle in matters is generally given as

$$\begin{aligned} -\left.\frac{\mathrm{d}E}{\mathrm{d}x}\right|_{\text{Total}} &= -\left.\frac{\mathrm{d}E}{\mathrm{d}x}\right|_{\text{Ionisation}} - \left.\frac{\mathrm{d}E}{\mathrm{d}x}\right|_{\text{Bremss.}} - \left.\frac{\mathrm{d}E}{\mathrm{d}x}\right|_{\text{pair}} - \left.\frac{\mathrm{d}E}{\mathrm{d}x}\right|_{\text{photonuclear}} \\ &= a(Z,A,E) + b(Z,A,E).E, \end{aligned} \tag{2.23}$$

where the term $a(Z, A, E)$ is the energy loss according to equation 2.22 and $b(Z, A, E).E$ is the summed energy losses due to breamsstrahlung, direct electron-pair production and photonuclear interactions.

The energy loss describes in equation 2.22 requires corrections for incident particle electrons or positrons as they have the same mass as the target. Furthermore, the breamsstrahlung process significantly influences the energy loss even at a low energy range ($\approx$ MeV range) for electrons or positrons cases. The average energy loss of electrons and positrons can be approximated as [39]

$$\left(\frac{\mathrm{d}E}{\mathrm{d}x}\right) \simeq \left(\frac{\mathrm{d}E}{\mathrm{d}x}\right)_{\text{radiative}} + \left(\frac{\mathrm{d}E}{\mathrm{d}x}\right)_{\text{ionisation}} \tag{2.24}$$

2.3.2 Interactions of photons

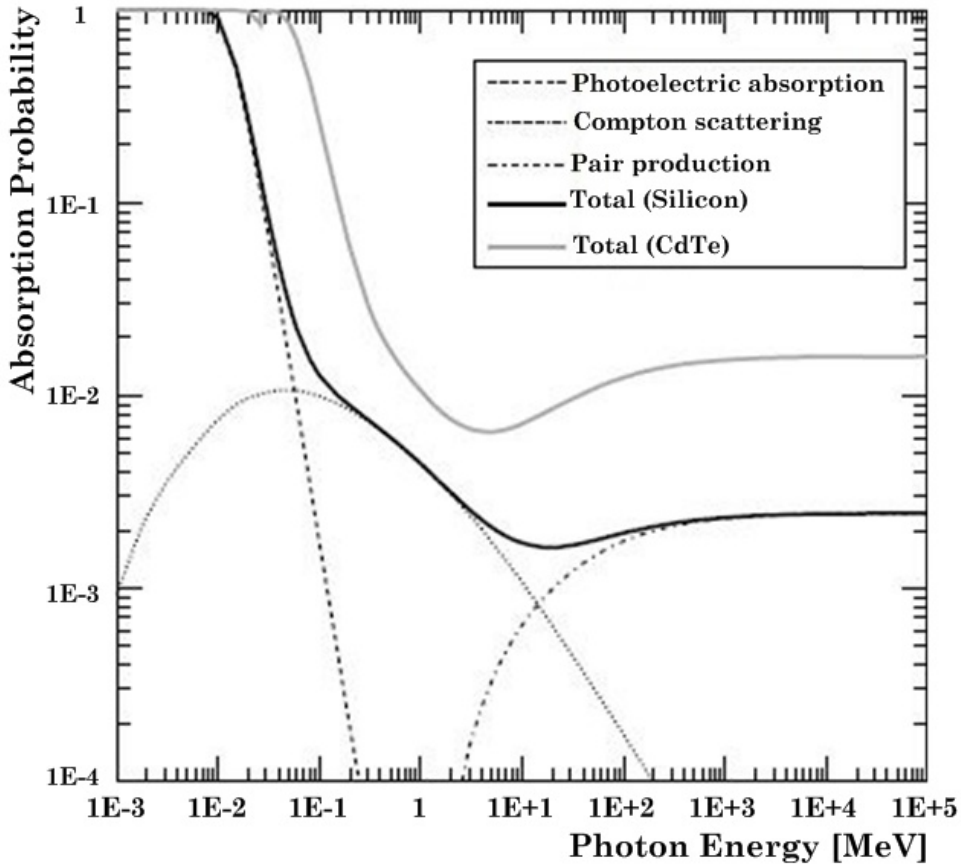

Figure 2.7: Probability of photon absorption as a function of energy in 300 μm *thick silicon. Contributions from photoelectric absorption, Compton scattering and pair production processes are indicated, and the total absorption in* 300 μm *thick CdTe is given for comparison. [44]*

The XRF, γ-rays and synchrotron radiation collectively categorised as *photons* are highly energetic electromagnetic waves of different origins. The XRF is a mono-energetic X-ray

emitted from the atomic shell due to the rearrangement of shell electrons in an excited atom. The XRF is produced either from radioisotope decay by electron capture or interactions of external radiation via photoelectric absorption. As the XRF energy is related to the binding energy of the shell, the energy range for the XRF is low (typical laboratory XRF sources $< 50\,\text{keV}$). The γ-rays are photons emitted from the excited nuclei during a β decay of radioisotopes or nuclear reaction. Additionally, it is also produced during the annihilation of electrons and positrons. The γ-ray has a broad energy range from a few keV to a few MeV. When a beam of relativistic electrons is bent into a circular orbit, a fraction of their energy is radiated as photons, called synchrotron radiation. Synchrotron radiation produces an intense photon beam with a broad energy spectrum. An optical device called a monochromator utilises Bragg's Law to obtain a specific wavelength (or energy). After this selection process, a focusing mirror can further refine the monochromatic beam, concentrating it into specific focal spots as required for various experimental setups.

For photons with energy below 2 MeV, only photoelectric absorption, Compton scattering, and pair production lead to complete or partial energy transfer to bound electrons that produce an electrical signal. Figure 2.7 shows the probability of photon absorption as a function of energy in 300 µm thick silicon. The contributions from the three processes are included to highlight the dominant processes in specific energy ranges. The total absorption probability of photons in a similar thickness CdTe is also included to indicate the advantage of high-Z materials. The photoelectric absorption is dominant at energy below 100 keV, between 100 keV to 1 MeV Compton scattering is dominant, and above 1.022 MeV, the pair-production becomes dominant.

2.3.2.1 Photoelectric absorption

Figure 2.8 shows an illustration of the photoelectric absorption. One of the shell electrons completely absorbs the photon, followed by the emission of a highly energetic electron called the *photoelectron*. The absorption of photon energy by shell electrons is made

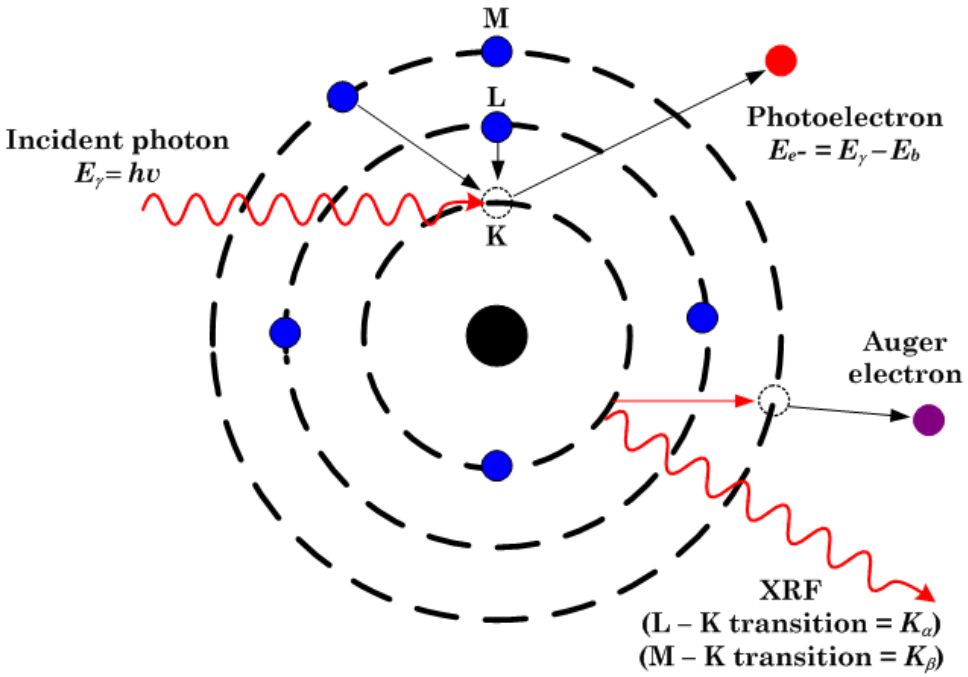

Figure 2.8: An illustration of photon interaction by photoelectric absorption. The incident photon is absorbed, and the subsequent emission of photoelectrons. The atom becomes ionised with one vacancy in its shell. The vacancy is filled by an electron from other shells. The excess energy is liberated as XRF photons or Auger electrons.

possible by the atomic nucleus, which acts as a third collision partner to satisfy momentum conservation. The main interactions primarily involve K-shell electrons, which have a high interaction cross-section of around 80% due to their proximity to the atomic nucleus [49]. The relationship between the energy of photoelectron, E_{e^-} and the incident photon $E_\gamma = hv$ is

$$E_{e^-} = E_\gamma - E_\mathrm{b}, \tag{2.25}$$

where E_b is the binding energy of the photoelectron from its original shell.

Photoelectron emission leaves the atom in an ionised state with one vacancy in its shell. The vacancy is quickly filled by electrons from other shells, and the energy difference (ΔE_b) between those shells is liberated as an XRF photon (characteristics X-ray). The transition from L-shell to K-shell produces K_α XRFs, and M-shell to K-shell produces a higher energy XRF (K_β) is also possible but with a lower probability. The energy of the

XRF emitted in this process is given by Mosley's law,

$$E = Ry\,(Z-1)^2\left(\frac{1}{n^2}-\frac{1}{m^2}\right), \tag{2.26}$$

where Ry ($= 13.6\,\text{eV}$) is Rydberg's constant while n and m are the shell's quantum number. The XRF energy for L - K shell transition ($m = 2$, $n = 1$) is

$$E(K_\alpha) = \frac{3}{4}Ry(Z-1)^2. \tag{2.27}$$

The XRFs produced in this process eventually lose their energy via further photoelectric absorption to produce even more photoelectrons.

Sometimes the energy difference is not converted into a photon but transferred to an electron from an outer shell, ejecting it from the atom. This ejected electron is called an *Auger electron*[1]. The energy of the Auger electron is quite small compared to the photoelectron.

2.3.2.2 Compton scattering

First observed by Arthur Holly Compton in 1925, Compton scattering is an inelastic scattering between the incident photons and the absorber's quasi-free electron. The incident photon transfers a fraction of its energy to the electron, then is scattered at an angle θ from their initial direction (see figure 2.9). The electron hit by the photon is called the *recoil electron* and is scattered at an angle ϕ during the interaction. The recoil electron loses its energy via the mechanisms described for charged particles in subsection 2.3.1.

The amount of energy transferred to the recoil electron varies upon the scattering angle.

[1]Electrons with characteristics energies emitted through Auger effect - Electrons from the upper shell fill the vacancy in the inner shell by transferring its energy to the outer shell electron and ejecting it from the atom

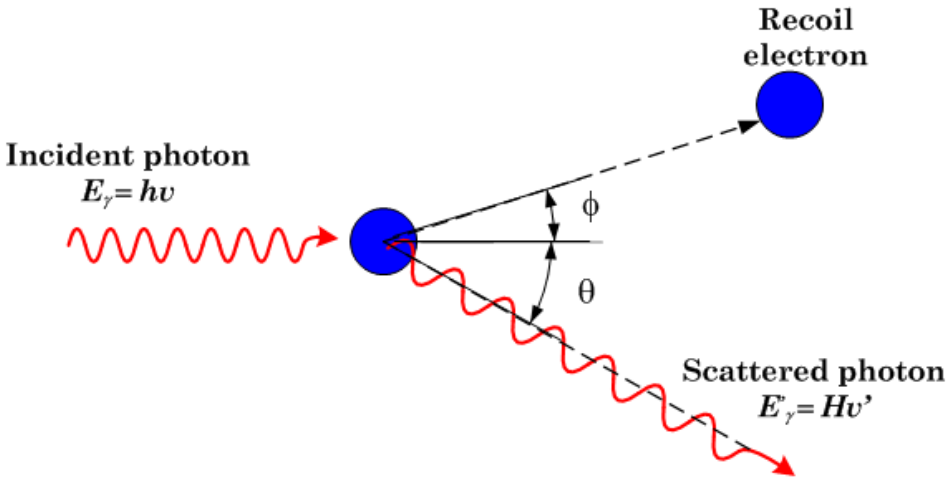

Figure 2.9: An illustration of photon interaction by Compton scattering. The incident photon transferred a fraction of its energy to an electron (recoil electron), then scattered at an angle θ.

The energy of the scattered photon is given by

$$\begin{aligned} E'_\gamma &= \frac{E_\gamma m_e}{m_e + E_\gamma\,(1 - cos\theta)} \\ &= \frac{E_\gamma}{1 + \frac{E_\gamma}{m_e}\,(1 - cos\theta)}. \end{aligned} \tag{2.28}$$

Depending on its energy, it may undergo photoelectric absorption or another Compton scattering, producing photoelectrons or Auger electrons.

2.3.2.3 Pair-Production

The electron-positron *pair production* is possible when an incident photon with energy exceeding twice that of a rest-mass electron ($\geq 2m_ec^2$) interacts with the Coulomb field of the nucleus. The pair-production in the Coulomb field of an electron is also probable but strongly suppressed; the threshold energy for this to occur is $E_\gamma \geq 4m_ec^2$ [49]. Upon creation, the positron and electron move in opposite directions with a separation angle of 180°. The positron subsequently annihilates with an electron in the absorbing media, thus producing two *annihilation photons* of 511 keV. The kinetic energy (E_k^{pp}) transferred to the electron-positron pair is

$$(E_k^{pp}) = E_\gamma - 2m_ec^2 \tag{2.29}$$

The annihilation photons may undergo photoelectric absorption or Compton scattering, eventually imparting their energy into various charged particles.

2.3.3 Summary of charged particles and photons interaction

The interactions of charged particles and photons within the semiconductor sensitive volume have been reviewed. The charged particles undergo a continuous Coulomb interaction with the atomic electrons and lose their energy by excitation and ionisation. The Bethe-Bloch equation describes the energy loss of charged particles. For relativistic charged particles, a minimum energy loss dubbed the MIP exists, which becomes the basis of detection for relativistic charged particles in particle physics experiments. Photon interactions produce highly energetic charged particles (photoelectrons, Auger and recoil electrons), eventually losing their energy through the same ionisation and excitation mechanisms described earlier in the charged particle interactions subsection. In conclusion, the semiconductor detector is a charged particle detector. The next section discusses the signal generation and formation in semiconductor detectors.

2.4 Electron-hole generation and signal formation

Charged particles generate electron-hole pairs directly via ionisation along their travelling path. Photons must first produce various charged particles that generate the electron-hole pairs via ionisation. The mean generated electron-hole pairs, N_{pair}, are given as

$$N_{pair} = \frac{E}{E_i}, \tag{2.30}$$

where E is the energy absorbed and E_i is the average energy for electron-hole pair creation. Energy absorbed must be greater than the E_G to excite an electron to the conduction band, thus forming an electron-hole pair. Silicon has a band gap energy of 1.12 eV, so photons with wavelengths shorter than 1100 nm can be detected. Energy absorption requires en-

ergy and momentum conservation, transferring the latter to lattice vibration, quantised as *phonons*. The momentum, $p = \frac{E}{c}$ absorbed in the lattice is very small for photons with $E \approx E_G$. However, for photons with $E \gg E_G$ and charged particles, a significant portion of the energy is used for phonons excitation[2]—explains why the E_i for silicon (3.6 eV) in Table 2.1 is higher than their E_G [41].

If a Poisson distribution governs the number of pair generations, the variance of N_{pair} in equation 2.30 would be

$$(\Delta N_{pair})^2 = N_{pair} = \frac{E}{E_i}. \tag{2.31}$$

In reality, the variance in the detected signal is smaller than the value predicted by the Poisson statistics in equation 2.31. The assumption for Poisson distribution is valid for an individual energy loss event, but the entire event is collectively correlated by energy conservation. Thus, the variance in the mean generated pair in equation 2.31 is modified according to [51, 52] as

$$\sigma^2 = F N_{pair} = F\frac{E}{E_i}, \tag{2.32}$$

where F is the *Fano factor* that has values between zero and unity. The Fano factor is material-dependent and expected to be energy-dependent at low energy ($\sim$ a few eV) [30]. The value of F in Si, Ge, CdTe, and CZT is between 0.06 to 0.10 [35], but $F \approx 0.10$ is a good approximation for all semiconductor detectors.

Upon generation, the electron-hole pair moves under the influence of the electric field towards its respective electrodes. Movements of electron-hole pairs induce an instantaneous current on the electrodes, which is described by the Shockley-Ramo theorem [53, 54]. Despite the term "charge collection" being more popular, the signal that appears in the front-end electronic is not generated by the collection of charge but rather by the

[2]The phonon excitation refers to the process where the lattice vibration gains energy and becomes more energetic

movement of the electron-hole pairs. The instantaneous current on an electrode induced by a moving charge q is

$$i = qv \cdot E_{wf}\,, \tag{2.33}$$

where q is elementary charge, v the carrier velocity and E_{wf} is the *weighting field* in m^{-1}. The E_{wf} is calculated by solving Poisson's equation for unity potential on the sensing electrode and zero to other electrodes [55], which in turn introduce the new unitless quantity with zero to unity values called the *weighting potential* (φ_{wp}). The total induced charge Q on an electrode is calculated by multiplying the moving charge q with the difference in the weighting potential between the generation point and the electrode:

$$Q = q\Delta\varphi_{wp}\,. \tag{2.34}$$

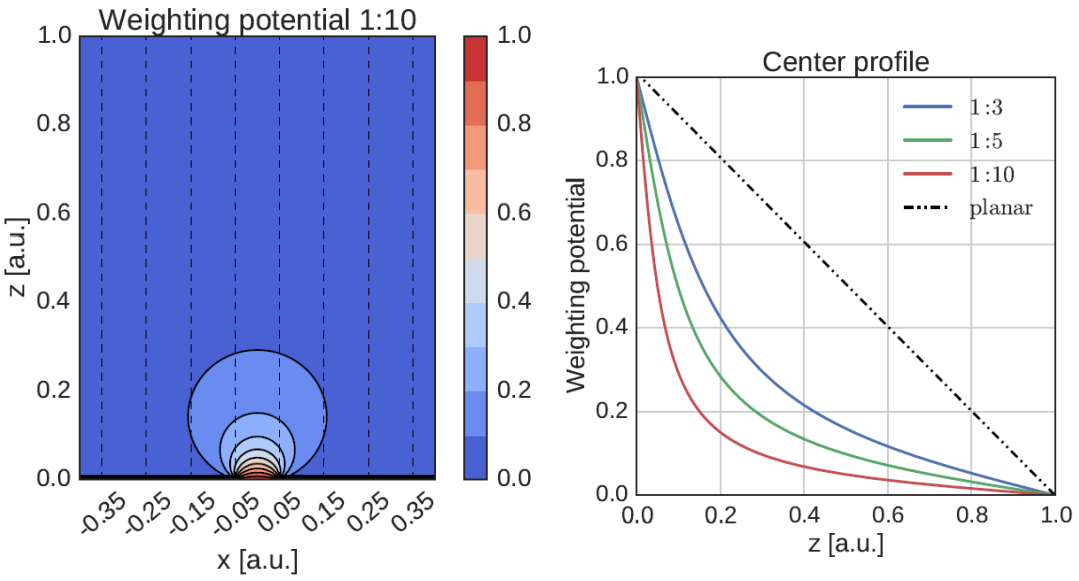

(a) *(b)*

Figure 2.10: An example of weighting potential in pixelated detectors [56]. (a) The weighting potential for a pixel with a ratio of width (w) to detector thickness (L) of 1:10. (b) the weighting potential calculated at a centre pixel (x = 0) for a pixel with 1:3, 1:5, and 1:10 w/L ratios and in a planar detector.

The φ_{wp} depends on the detector's geometry and defines how the charge moves in a specific electrode. As shown in figure 2.10a, the φ_{wp} is stronger closer to the pixel in the pixelated detector and becomes a lot stronger for pixels with smaller width to thickness (w/L) ratio

(see Figure 2.10b). These figures indicate that the carrier that moves towards the pixel contributes the most to the induced charge Q (according to equation 2.34). This type of electrode design is called a *unipolar* sensing electrode, which is important for CdTe and CZT detectors due to the significant disparity between their electron and hole mobility. In contrast, the φ_{wp} in the planar detector is linear, where the induced charge Q is sensitive to the movement of both electrons and holes.

2.5 Readout electronics and system resolution

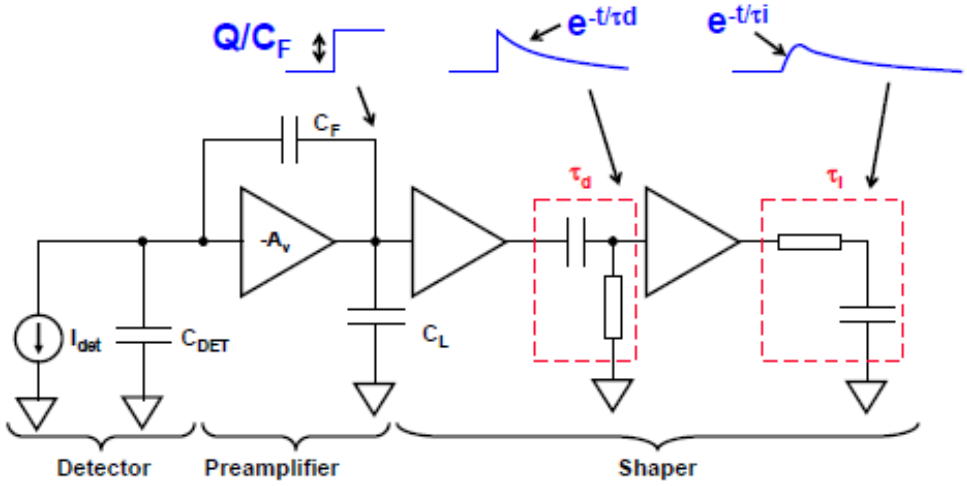

Figure 2.11: Basic schematics of front-end electronics for semiconductor detectors [57]. The reset mechanism is not included in this schematic as this can be achieved through various configurations (feedback resistor, constant current sources of an optical link, etc.)

A minimum-ionising particle (MIP) generates about 22 000 electron-hole pairs ($\approx 4\,\text{fC}$) in 300 µm thick silicon detectors. The induced signals are extremely small and mixed with electronic noises. An amplifying and noise-filtering circuit is required to process the signal. Figure 2.11 shows the basic schematics of a typical detector's front-end electronics (FEE). The FEE comprises a charge sensitive preamp followed by a pulse shaping network (*Shaper*). The charge sensitive preamp is designed to have a high input impedance R_i and high voltage gain $-A_v$. Therefore detector current, I_{det}, is not flowing into the preamp but rather charging the feedback capacitor (C_F).

Assume the induced charge from the detector is Q_i, and the voltage across C_F is $V_F = (A_v + 1)V_i$. The charge integrated in C_F is $Q_F = C_F V_F = C_F\,(A+1)\,V_i$ which equal the detector's induced charge $Q_i = C_i\,V_i$. The preamp input becomes a dynamic input capacitance expressed as

$$C_i = \frac{Q_i}{V_i} = C_F\,(A_v + 1) \tag{2.35}$$

The voltage at the input preamp $V_i = \dfrac{Q_i}{C_{DET} + C_i}$, and if the FEE has very high input capacitance ($(A_v + 1)C_F \gg C_{DET}$), the output voltage of the preamp would be

$$V_o = -A_v\,V_i = -\frac{A_v Q_i}{(A_v + 1)C_F} \approx -\frac{Q_i}{C_F} \tag{2.36}$$

Equation 2.36 indicates that system gain only depends on the feedback capacitor C_F, which makes this system robust and insensitive to technology or temperature variations [57]. The charge sensitive preamp produces a voltage step output with maximum amplitude equal $\dfrac{Q_i}{C_F}$. A reset mechanism, typically a high-value resistor, is added in parallel to the C_F to prevent the C_F from being saturated. Hence, the preamp output has an exponential tail defined by the time constant of the C_F and reset resistor. Only the amplitude is important since it represents the energy of the incident particles ($V_{amplitude} \propto E$), and the long tail is undesirable. The shaper shapes the signal into a semi-gaussian pulse (typical for ASIC readout). The shaper also has a band-pass filter composed of both high- and low-pass filters, which provides noise filtering.

Electronic noise is an important parameter which affects the system resolution. It is defined as the electrical interference from current noise sources (*parallel noise*) or voltage noise sources (*series noise*) generated by the electronic components. The origin and contribution of the parallel and series noise in the detector-readout system are well-discussed in the literature. They will not be discussed here (detailed discussion can be found in [55, 58]). The input noise of the preamp dominates the total noise in the system. Hence, the preamp's input transistor must be a low-noise transistor with an input impedance

matching the detector input impedance for full charge transfer [30, 58].

The shaper only filters the low and high frequency components of the noise, keeping the signal from worsening. Electronic noise is still present, propagated along the electronic chain, and superimposed on the signal at the FEE output. The magnitude of the electronic noise is expressed as "Equivalent Noise Charge"(ENC) in a detection system. The ENC is defined as noise referred to the amplifier input that yields a signal-to-noise (SNR) of 1 at the output and expressed in r.m.s electron (or Coulomb) [55, 58, 59]. The noise contributes to the uncertainty in radiation measurement. The total uncertainty for an energy measurement with radiation detectors can be expressed as

$$\sigma^2_{Total} = \sigma^2_{Fano} + \sigma^2_{CC} + \sigma^2_{ENC}, \tag{2.37}$$

where σ^2_{Fano}, σ^2_{CC} are the uncertainties due to carrier generation (*Fano Factor*) and charge collection, and σ^2_{ENC} is the uncertainty due to the electronic noise. The uncertainty due to *Fano Factor* sets the fundamental limit for energy resolution in semiconductor detectors. The ENC usually becomes the dominant contributor to the total uncertainty in the detection system and must be kept to a minimum when designing the FEE for radiation detectors. The energy resolution of the detector-readout system is expressed as full-width half maximum (FWHM) in energy unit (eV) given as FWHM $= 2\sqrt{2\ln 2}\sigma_{Total} \approx 2.355\sigma_{Total}$.

CHAPTER 3

The Timepix3 readout ASIC

The hybrid pixel detectors are comprised of pixelated semiconductor detectors and readout ASICs. The semiconductor detectors are introduced in the previous chapter, and this chapter will focus on the readout ASICs. Understanding both components allows users to master hybrid pixel detector operation and understand their characteristics, performance and limitations. This chapter presents an overview of the Timepix3 readout ASIC, developed by the Medipix Collaboration at CERN. The chronological development of the ASIC is presented in the first section, starting from the first one, Medipix1, to the Timepix3 readout ASIC. The second section gives an in-depth overview of the technical aspects and the pixel's operation in Timepix3. The proceeding section elucidates the fundamental operation of a Timepix3-based hybrid pixel detector, focusing on equalising the detector's response and masking the noisy or dead pixels. The last section describes the energy calibration and time-walk correction of Timepix3-based hybrid pixel detectors.

3.1 From Medipix1 to Timepix3

The *Medipix1* or Photon Counting Chip (PCC) was introduced in 1997 as a single photon counting ASIC for the Large Hardon Collider (LHC) experiments at CERN[2]. The

Medipix1 consist of 64 × 65 square pixels with 170 µm pixel pitch. The bottom row consists of dummy pixels for leakage current compensation, leaving only 64 × 64 pixels for readout. Each pixel is connected to the preamp-discriminator-counter readout chain. The preamp provides gain of $\approx 30\,\mathrm{mV/ke^-}$, but only accepts positive input charge. The discriminator is controlled by a single threshold that could be set for individual pixels. The counter has a 15-bit counter depth that guarantees a high dynamic range. The hybrid pixel detector of Medipix1 combined with gallium arsenide (GaAs) detectors attracts some interest in medical imaging primarily due to the Medipix1's high dynamic range [60–62]. However, it achieved limited success because its spatial resolution (170 µm) is too large for this application. The Medipix1 readout has significant limitations. The uniform current measured in the dummy cell compensates for the detector leakage current. Therefore it is not suitable for detectors that have a non-uniform leakage current. Moreover, building a large area detection system via tiling this type of detector is not possible because it has a large dead area (guard ring) around the ASIC[63].

The Medipix2 collaboration introduced the *Medipix2* readout ASIC in 2002 primarily to explore spectroscopic X-ray imaging with a small detector pitch. The chip has 256 × 256 square pixels on 55 µm pitch fabricated using 250 nm CMOS technology. The preamp is based on the Krummenacher type charge sensitive amplifier that provides $\approx 10.5\,\mathrm{mV/ke^-}$ signal gain. The Medipix2 has two discriminators, each with an independent threshold for window discrimination. A few versions have been fabricated mainly to improve its performance, with the MPIX2MXR2.0 being the final version. The Krummenacher-type preamp provides improved leakage current compensation, allowing compensation in both polarities. Medipix2 has a smaller pixel-pitch (55 µm), which gives a better spatial resolution. Moreover, building a large area detector is now feasible via tiling on three sides. It has been extensively bonded with High-Z compound semiconductors for spectroscopic imaging of hard X-rays and high energy γ-rays. The Medipix2 ASIC has one significant drawback: it has no mechanism to deal with the charge sharing issues, which are severe

in small pixels when detecting high-energy photons.

The *Timepix* introduced in 2006 is a modified version of the MPIX2MXR2.0 as an answer to the request made by EUDet consortium for a 3D particle tracking ASIC in their gaseous detector system[2, 63]. The number of pixels and pixel size are the same as Medipix2, but the functionality of the pixel was extended. Besides the *Event Counting (PC) mode* that already had in Medipix2, two more modes are introduced: the *Time-over-Threshold (ToT) mode* for charge measurement, and the *Time-of-Arrival (ToA) mode* to measure the arrival time of the signal. The front-end architecture is identical to the Medipix2 but with a single discriminator. The preamp provides a signal gain of $\approx 14.7\,\mathrm{mV/ke^-}$ with a peaking time of $\approx 100\,\mathrm{ns}$, and dynamic range of $\pm\, 55\,\mathrm{ke^-}$. The discriminator is controlled by a 4-bit adjustable single threshold that provides a minimum threshold of $\approx 600\,\mathrm{e^-}$[64].

The Timepix readout ASIC has been quite successful but has several limitations. Timepix employs a frame-based readout method for data acquisition, which has two significant implications: ToT measurement errors from multiple particles hitting the same pixel becoming one ToT value and dead time from pixel inactivity during readout. Moreover, the ToA relies on the shutter's opening time, which is limited by the clock period and the counter depth, which leads to an overall precision of $\approx 10\,\mathrm{ns}$ [63, 65]. These limitations, combined with the emergence of the latest 130 nm CMOS process technology, led to the development of the Timepix3 readout ASIC.

3.2 The Timepix3 readout ASIC

The Timepix3 readout ASIC introduced in 2015, consist of 256 × 256 square pixels with a size of 55 × 55 µm fabricated using 130 nm CMOS process technology [3]. It has two main novelties with respect to Timepix: the *zero suppression data-driven* readout and simultaneous acquisition of ToT and ToA. Table 3.1 shows the comparison of the technical

Table 3.1: Comparison of technical specifications between Timepix and Timepix3 readout ASICs[3, 63, 65–67].

	Timepix	Timepix3
Pixel arrangement	256 × 256	
Pixel size	55 × 55 µm^2	
Acquisition modes	1. ToT 2. ToA 3. Event counting (PC)	1. ToT & ToA 2. ToA 3. Event counting (PC) & Integral ToT (iToT)
Readout type	Frame-based	Frame-based or Data-driven
Zero suppression readout	No	Yes
Dead time per pixel	> 300 µs (Readout time per frame)	> 475 ns (Pulse measurement + packet transfer time)
ToA resolution	10 ns	1.562 ns
ToT resolution	Standard setting: ≈ 300 e$^-$ to 600 e$^-$ (FWHM) Note: Timepix3 can use 4-bit fToA to improve ToT resolution	
Minimum detectable charge	> 750 e$^-$	> 500 e$^-$
Collection polarity	e$^-$ and h$^+$ (Leakage current compensation up to ≈ 2 ns/pixel	

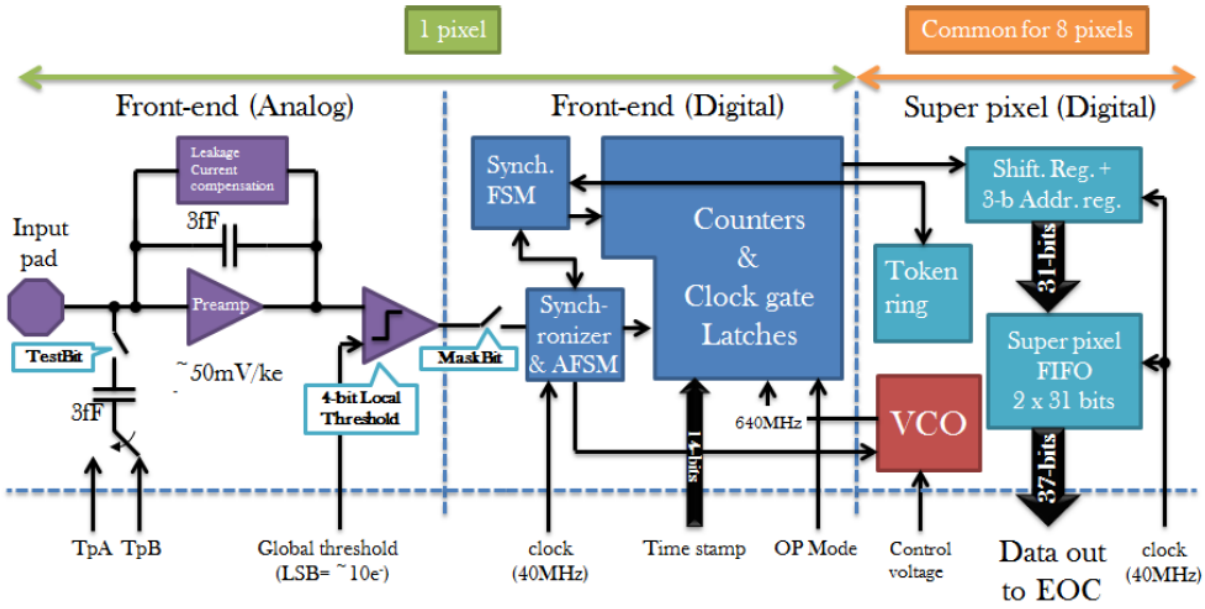

Figure 3.1: A Schematic of the front-end of Timepix3 ASIC[3]

specifications of Timepix and Timepix3. The Timepix3 addressed most of the limitations identified in the Timepix readout ASIC. Introducing the data-driven readout architecture reduces the dead time per pixel to 475 ns, mostly due to the pulse measurement and data packet transfer time. The introduction of the 4-bit fast ToA (fToA) with a 640 MHz clock

improved the ToA resolution to $\approx 1.56\,\text{ns}$. It is also worth highlighting that the 4-bit fToA can also be used to improve the ToT resolution. Moreover, the on-chip zero suppression architecture in Timepix3 increases the maximum per pixel hit rate to 1.2 kHz, which is equivalent to $40\,\text{Mhits/cm}^2\text{/s}$. This maximum output rate is limited by the periphery, which has a bandwidth of 5.12 Gbps[68].

Figure 3.1 shows the front-end section of the Timepix3 readout ASIC. Each Pixel is connected to an analogue and digital front-end circuitry, and every 8 pixels (2×4 pixels) share one common digital circuitry called the *super-pixel* structure. The analogue front-end consists of a preamp and a single threshold discriminator. The Krummenacher-type preamp has 3 fF feedback capacitor, providing signal gain of $50\,\text{mV/ke}^-$ with peaking time of around 25 ns[67]. The preamp compensates for the leakage current of the detector in both polarities and is designed to accommodate the detector's capacitance ranging from 25 fF to 100 fF. The discriminator has a 4-bit local threshold adjustment to adjust the lower threshold level (THL) set by the 4-bit digital-to-analogue converter (DAC) global threshold. This configuration provides a minimum detectable charge of $\approx 500\,\text{e}^-$. The total noise of the analogue front-end is expected to be in the order of $90\,\text{e}^-$ r.m.s.

The front-end of the digital section is the building block for a larger structure of 2×16 pixels, which is repeated to form the full matrix. It receives an incoming pulse from the discriminator, starts the 4-bit fine time stamp counter, and latches the 14-bit time stamp provided by the 40 MHz on-chip ramp counter. The 10-bit pseudorandom counter running at 40 MHz for ToT measurement is also part of the digital front-end. The back-end of the digital is part of a super-pixel formed by 8 pixels (2×4). Each super-pixel is controlled by a single voltage-controlled oscillator (VCO), oscillating at 640 MHz. The data originating from each pixel is systematically transmitted to the super-pixel through round-robin arbitration. A token ring scheme transmits hit information from the super-pixel to the periphery at the bottom of the pixel's column via a double-column data bus with a speed

of 40 MHz. The transmitted off-chip data includes the pixel address (16-bit), the course Time of Arrival (ToA) (14-bit), the fine Time of Arrival (fToA) (4-bit), the Time over Threshold (ToT) (10-bit), and a 4-bit header.

The Timepix3 can be read out in the data-driven Zero suppression or frame-based Zero suppression readouts. Data transmission does not depend on the shutter operation in data-driven zero suppression readout. As long as the shutter is open, only the data from pixels that are being hit are immediately sent off-chip. This approach helps to optimise data bandwidth and reduce processing time and data size. The shutter open/close operation controls the frame-based Zero suppression readout. However, unlike the frame-based readout used in Timepix readout ASIC, only data from pixels that are being hit are included in the frame data and transmitted off-chip. The pixels can be programmed in either acquisition mode (taking data) or configuration mode (testing). The configuration mode is used to program the 6-bit pixel configuration mask for threshold equalisation and test pulse operation[66]. The pixel acquisition modes available in Timepix3 readout ASIC are discussed in the following subsections.

3.2.1 Acquisition modes in Timepix3 readout ASIC

Table 3.2 shows three available pixel acquisition modes in Timepix3 depending on the super-pixel Voltage-Control Oscillator (VCO) states. The pixel in Timepix3 can be operated in combined ToT & ToA mode, ToA only mode, and combined Event counting & Integral ToT (iToT) mode. The Timepix3 produces different output data depending on the VCO super-pixel states. Only the first and the last modes, both with VCO super-pixel in the ON states, are used for data acquisition in this thesis. Hence, the other mode is not discussed here.

The Event Count and Integral ToT mode is designed specifically for photon counting applications. The acquisition time is defined by the opening and closing operation of the

Table 3.2: Pixel acquisition modes depend on the VCO super-pixel states in Timepix3.

Acquisition mode	VCO super-pixel state (ON = Fas_lo_en = 1) (OFF = Fast_lo_en = 0)	Output data
ToT + ToA	ON	ToT = 10-bit ToA = 14-bit fToA = 4-bit @ 640 MHz (1.562 ns)
	OFF	ToT = 10-bit ToA = 14-bit Hit counter = 4-bit
ToA	ON	ToA = 14-bit fToA = 4-bit @ 640 MHz (1.562 ns)
	OFF	ToA = 14-bit Hit counter = 4-bit
Event counting + Integral ToT (iToT)	ON	Integral ToT = 14-bit Hit counter = 10-bit
	OFF	Integral ToT = 14-bit Hit counter = 10-bit Hit counter = 4-bit

shutter. When the shutter opens, the pixel hit is incremented into 10 bits of ToA data. Additionally, the combined deposited energy of all hits is measured as 14 bits of iToT data.

Most of the data in this thesis are taken in the ToT + ToA mode with the data-driven zero suppression readout. In this mode, ToT and ToA data from pixels that are being hit are transmitted off-chip immediately. This acquisition mode is crucial when energy and arrival time are needed for the experiment. The combined ToT and ToA data contain the following information:

- 16-bit pixel address is the pixel coordinate of the hit (x, y).
- 14-bit coarse ToA and 4-bit fToA are the arrival time of the hit.
- 10-bit ToT is the measured charge.

Figure 3.2 shows a snippet from the ASCII file output form measurement using the data-driven ToT + ToA acquisition mode. The ASCII data contains 6 columns corresponding

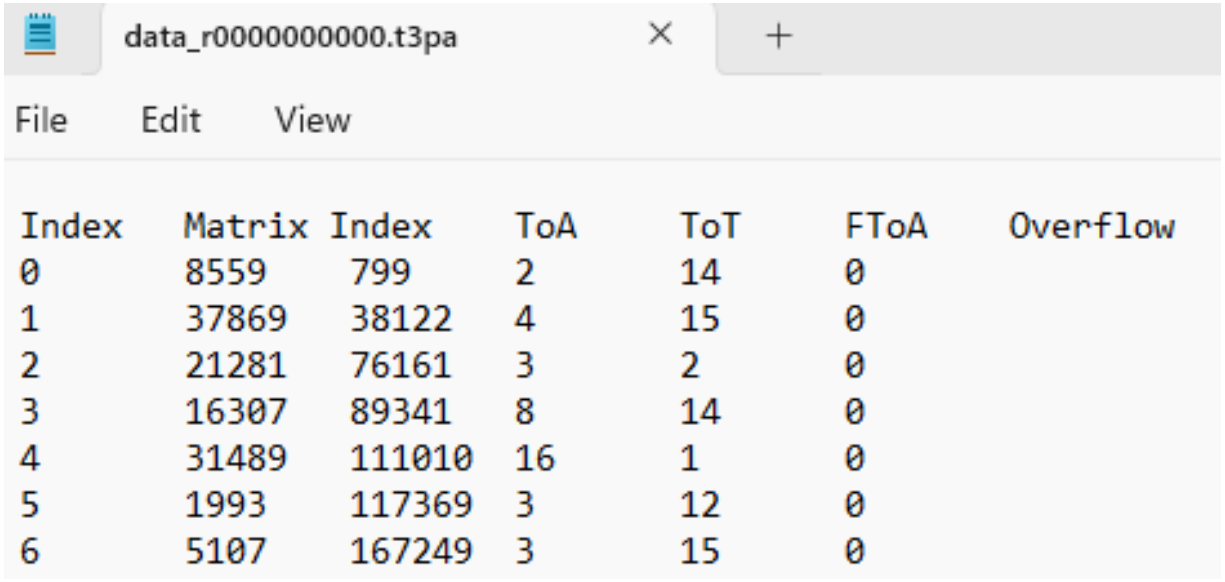

Figure 3.2: A snippet from the output file of the data-driven ToT + ToA acquisition mode.

to the *Index, Matrix Index, ToA, ToT, FToA,* and *Overflow values*. The column *Index* indicates the logged event number starting from 0. The *Matrix Index* represents the pixel coordinate given as 16-bit integer numbers (0 to 65535). The y and x coordinates of a particular pixel are obtained as $y = \frac{\text{Matrix Index}}{256} - \text{remainder}$ and $x = \text{remainder} * 256$. The ToA and ToT values represent 14-bit and 10-bit integer numbers corresponding to the number of clock edges count of the 40 Mhz clock, one count each equals 25 ns. The next subsection describes how the ToT, ToA and fToA are defined in Timepix3.

3.2.2 ToT and ToA information

Figure 3.3 shows how the ToT, ToA, and fToA information are defined in Timepix3. When the signal is above the discriminator's threshold level (THL), the 10-bit ToT is counted on the first rising edge of the 40 MHz ToT clock, and one ToT count is 25 ns. The ToT depends on the width of the pulse that is above the THL. As shown in Figure 3.3, the ToT value will change when the THL value or Krummenacher current (I_{Krum}) is varied. The I_{Krum} is set at the beginning of the measurement, and for a fixed THL value, the pulse width is proportional to the energy deposition. Hence, the ToT value is related to the energy deposition.

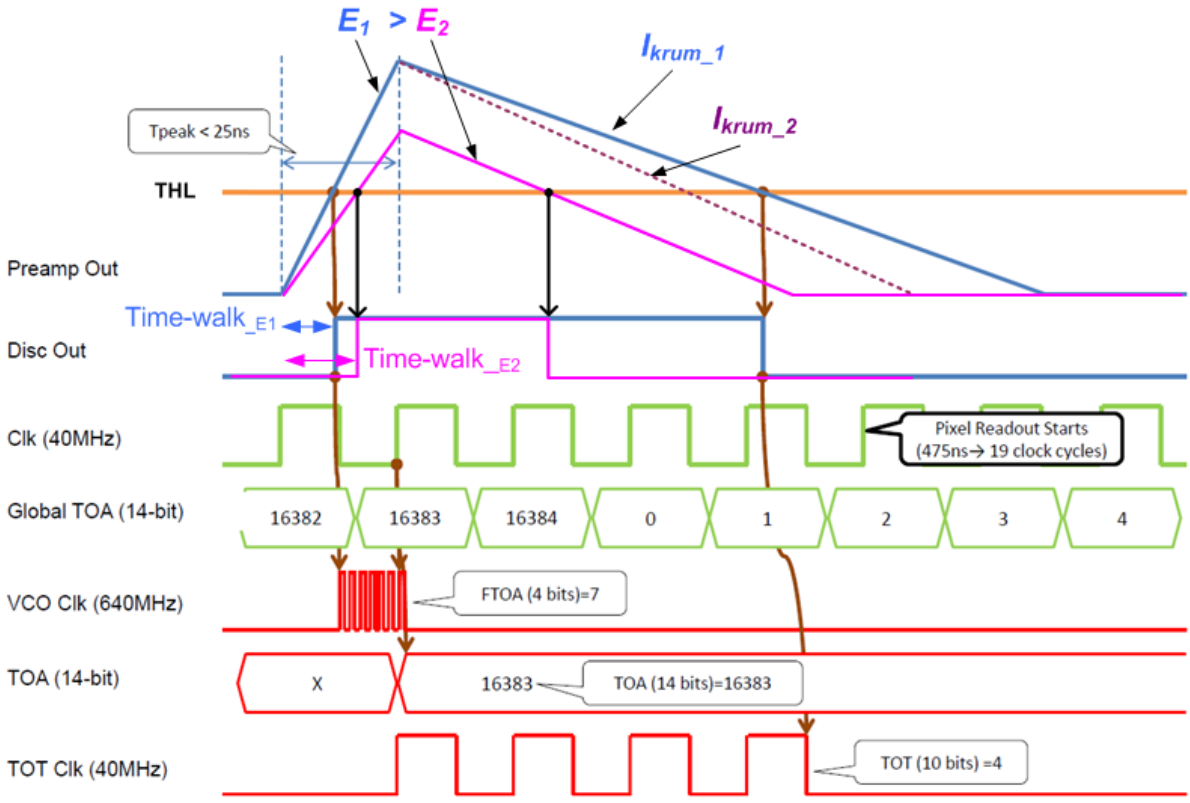

Figure 3.3: The definition ToT and ToA in Timepix3. The ToT count is incremented as long as the signal is over the THL and is influenced by the THL and the Krummenacher current(I_{krum}) settings. The peaking time of the pulse is 25 ns *independent of the pulse amplitude. The VCO clock starts at a much earlier time stamp for the signal with a large amplitude (E_1) since it crosses the THL earlier than the signal with a smaller amplitude.*

The definition of the ToA in Timepix3 is different from the ToA defined in Timepix. In Timepix3, the ToA is obtained from the fToA and coarse ToA time stamps. A 640 MHz VCO clock starts a time stamp at 1.562 ns resolution right after the pulse crosses the THL and stops at the next rising edge of the 40 MHz clock. This timestamp is assigned as the fToA value. After the VCO clock stops, the 40 MHz clock starts another time stamp at 25 ns resolution. This timestamp is assigned as the coarse ToA value. The fToA and coarse ToA determine the final value of the ToA as ToA (ns) = (coarse ToA $*$ 25 ns) $-$ (fToA $*$ 1.562 ns).

Data in this thesis are taken with the AdvaDAQ USB 3.0 interface readout and PIXet

pro software [69] except for the per pixel ToT calibration and time-walk correction in the hybrid pixel detector with LGAD sensor (Section??) and single-layer Compton camera (Chapter 8). The next section describes pixel equalisation and masking procedures for hybrid pixel detectors connected to the AdvaDAQ USB 3.0 interface readout system.

3.3 Device equalisation and pixel masking

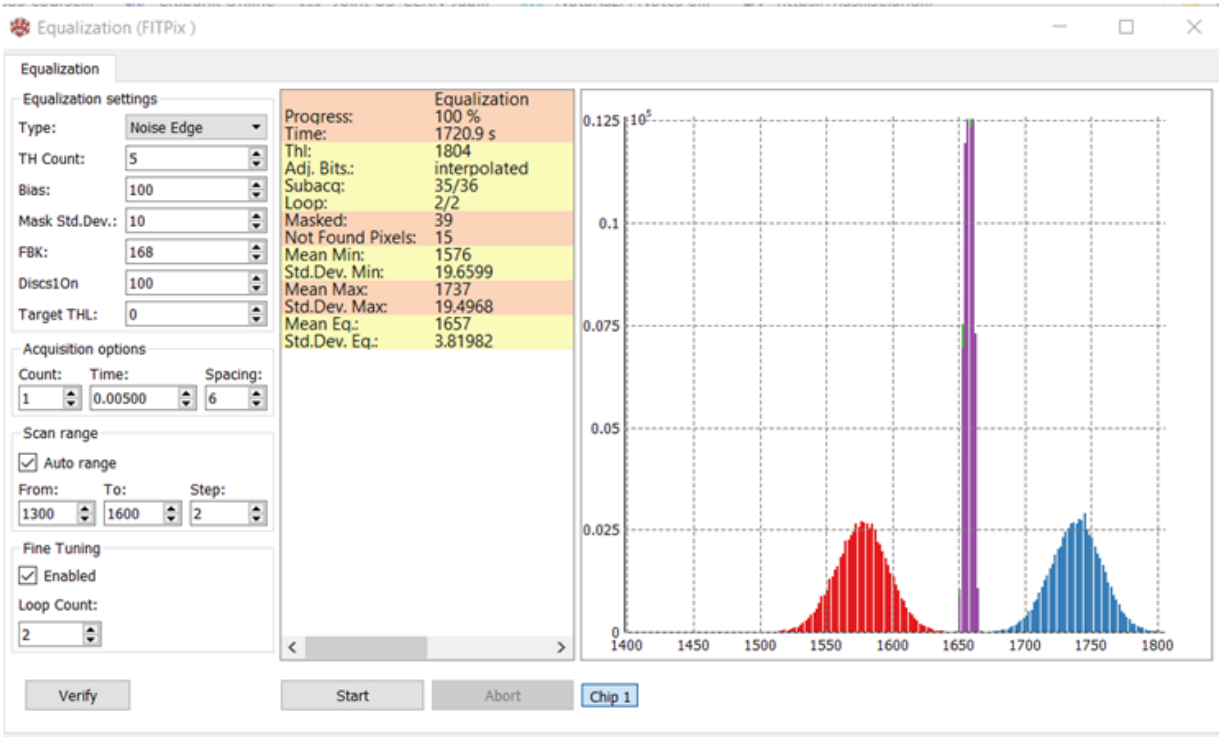

Figure 3.4: Pixel equalisation of Timepix3-based hybrid pixel detectors with the AdvaDAQ USB 3.0 interface readout and PIXet Pro software.

Pixel equalisation aims to compensate for pixel-to-pixel threshold variations due to current mismatches and transistor threshold voltages[64]. Figure 3.4 shows an example of threshold equalisation on Timepix3. The 4-bit local threshold adjustment in the discriminator is used for this purpose, and it is done using the noise equalisation procedure as follows [63];

- The 4-bit local threshold adjustment is set to minimum (DAC = 0), and a threshold scan for the noise edge. Repeat the procedure at a maximum 4-bit local threshold

value (DAC = 16). The results are two broad Gaussian distributions (red and blue) representing the noise edge position in units of the global threshold for all pixels (Figure 3.4).

- The 4-bit local threshold in every pixel is then tuned to the midpoint between the two broad Gaussian. The narrow Gaussian in the middle is the distribution of the tuned thresholds.

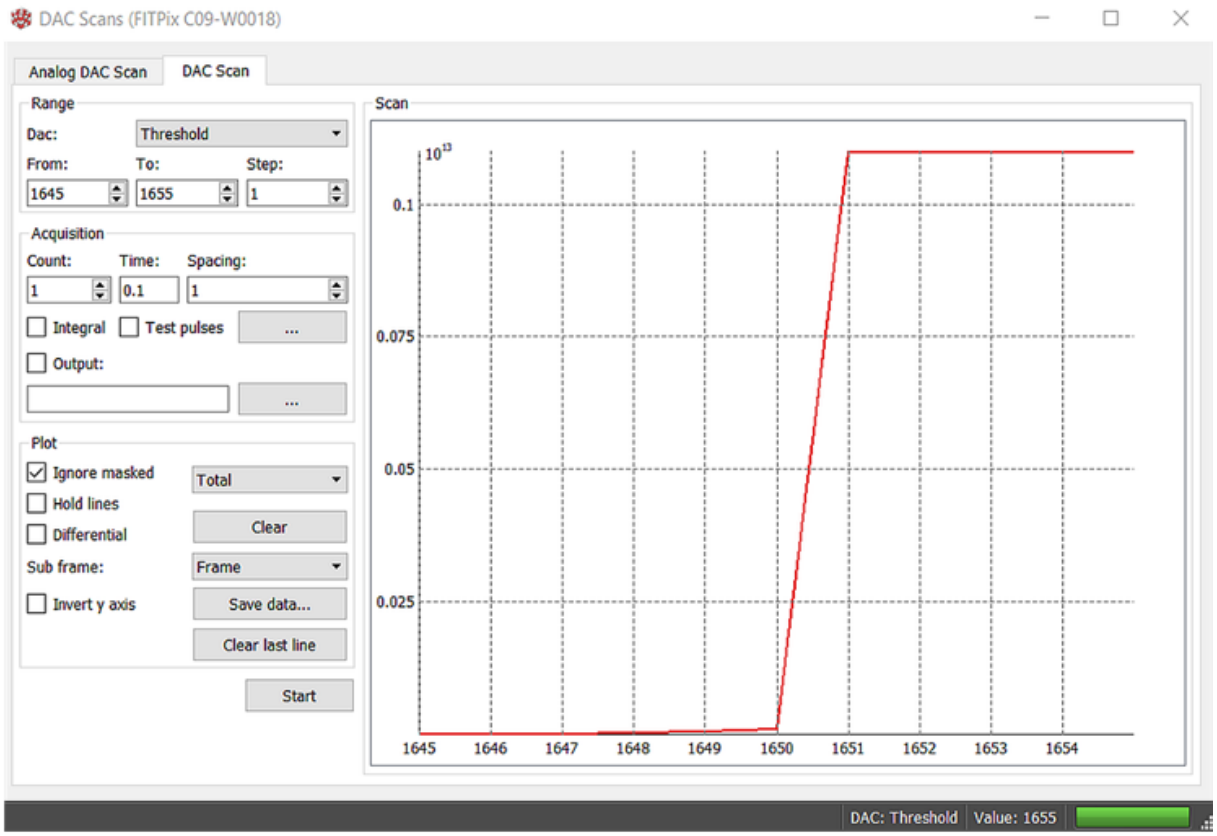

Figure 3.5: Fine adjustment of the global threshold with the DAC scan function.

A global threshold is found after a successful threshold equalisation. It is common practice in Timepix3 operation to verify and make fine adjustments to the newly found global threshold. The *DAC scan function* is used in this procedure by scanning the threshold for a specific range of the threshold while monitoring the detector response. An example of such a scan is shown in Figure 3.5. The global threshold is typically set to the corresponding threshold value before the pixel count rises. After equalisation, some pixels might still

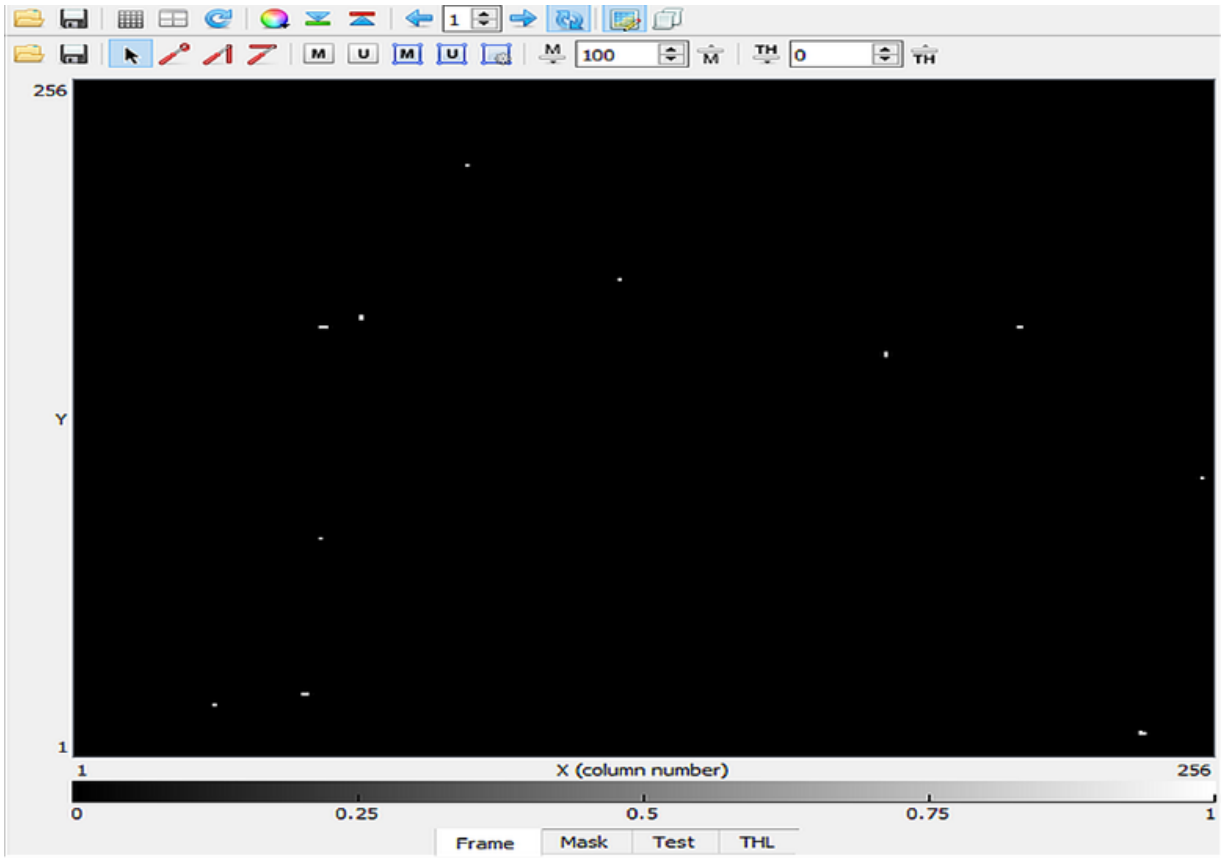

Figure 3.6: Masking the noisy pixels.

produce high responses (noisy pixels). They must be disabled or "masked" to exclude the noisy pixel in the proceeding measurement. A background measurement is required for the pixel *masking* procedure (see Figure 3.6), where a few frames of data are acquired with Event counting + iToT mode ($\approx$ 200 frames). Noisy pixels are then masked individually or by using a global mask value.

3.4 ToT calibration

In particle detectors, charge clusters generated by particle interactions spread during collection and are gathered by adjacent pixels. The total collected charge correlates linearly with the particle's energy loss. A charge preamplifier converts these charges into asymmetric pulses with amplitudes proportional to the incident particle energy, characterised by a rapid rise and prolonged decay. Whilst conventional setups use ADC circuits to digitise

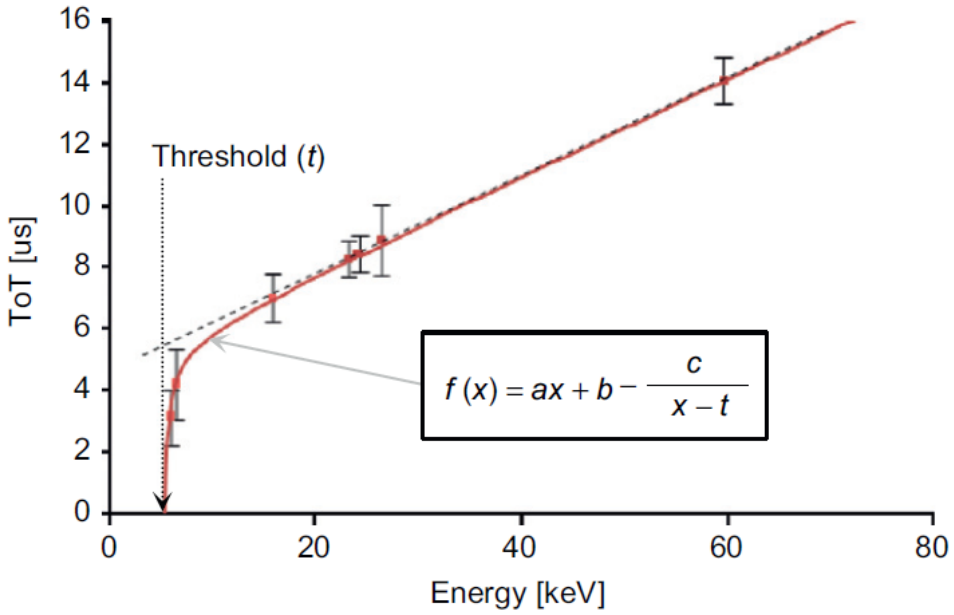

Figure 3.7: The Time-over-Threshold (ToT)—Energy conversion for silison sensor bonded to Timepix3 readout ASIC. The relationship (red line) is modelled after a a surrogate function, $f(x)$ [70].

the pulse peak and relate it to energy via calibration, the Timepix3 readout ASIC employs Time-over-Threshold (ToT), measuring energy based on the pulse's duration above a preset threshold. Although ToT simplifies the electronics, it suffers from non-linearity, particularly in the energy range close to the threshold, due to the pulse's asymmetry. This non-linearity arises because low-energy events have a significant portion of their pulse below the threshold, whilst higher-energy pulses spend disproportionately more time above it, owing to the long decay tail.

Figure 3.7 shows an example of ToT to energy conversion for silicon sensor bonded to Timepix3 readout ASIC. The relationship is modelled after a surrogate function, $f(x)$, described as

$$f(x) = ax + b - \frac{c}{x - t}\,, \tag{3.1}$$

where a, b, c, and t are four calibration constants obtained by a least-square fit. The

calibration curve is composed of linear ($ax + b$ above $\approx 20\,\text{keV}$) and non-linear ($\frac{c}{x-t}$) regions. The sharp fall off transition is set by the threshold level, the minimum detectable enargy of the said pixel detector. The threshold level depends on the minimum threshold of the Timepix3 ($500\,\text{e}^- \approx 2\,\text{keV}$), and also factoring the contribution of Fano noise ($\sigma_F^2 = \frac{FE}{E_i}$), and total electronic noise (detector + ASIC). Threshold value of around 3 – 4 keV is typical for a Timepix3-based pixel detector depending on the type of detector used[3, 4].

The ToT calibration for pixel detectors employs a combination of radioisotopes and X-ray fluorescence sources, as detailed in [70–72]. For each pixel, sufficient data are collected at various calibration energies. The ToT value corresponding to each photopeak energy is extracted and plotted against energy. A surrogate function is then fitted to these data points using least-squares minimisation, yielding calibration coefficients. This process is repeated for every pixel, ensuring per-pixel calibration. Kroupa et al. (2017)[73] enhanced this method by incorporating Monte Carlo simulations to account for inter-pixel charge sharing effects.

3.5 Time-walk correction

The time-walk (see Figure 3.8a) is an anomaly in the time of arrival (ToA) that occurred in Timepix3. This anomaly occurs when a particle deposits a large charge cloud spread over several adjacent pixels. Each pixel collects a fraction of the total charge and produces four pulses of different amplitudes. These four pulses are supposed to belong to the same interaction but produce different ToAs. If this time-walk is not corrected, it introduces errors in the ToA measurement. The work in [69] introduces a method for correcting the time-walk in Timepix3. They use the 59.6 keV photon decay of the radioisotope ^{241}Am and only consider charge clusters that have pixel sizes between 3 and 4 pixels with one of the pixels carrying half the total energy deposited(in this case, $\approx 30\,\text{keV}$). The ToA

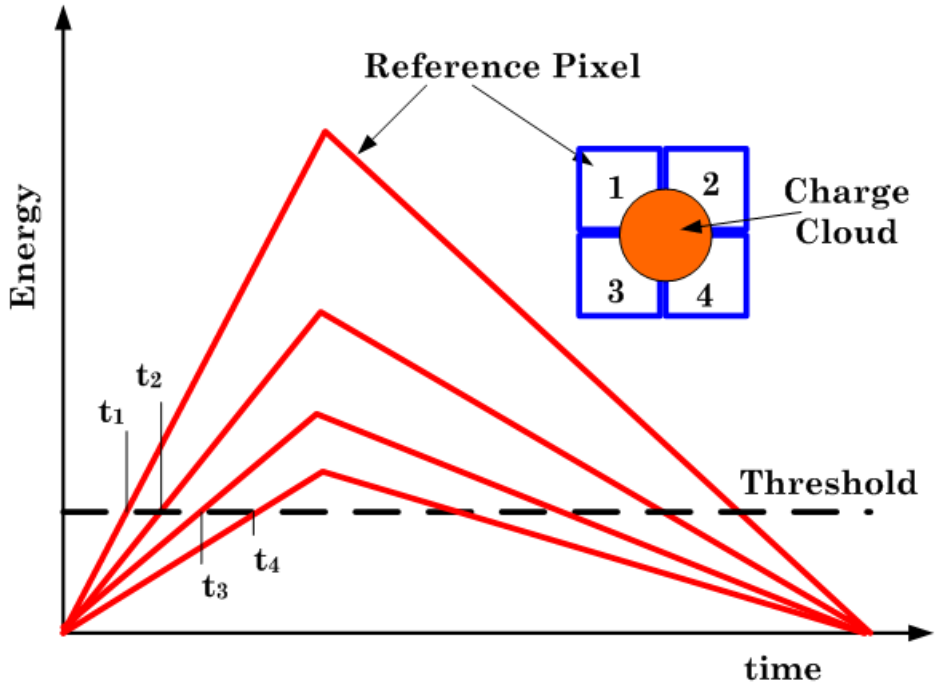

(a)

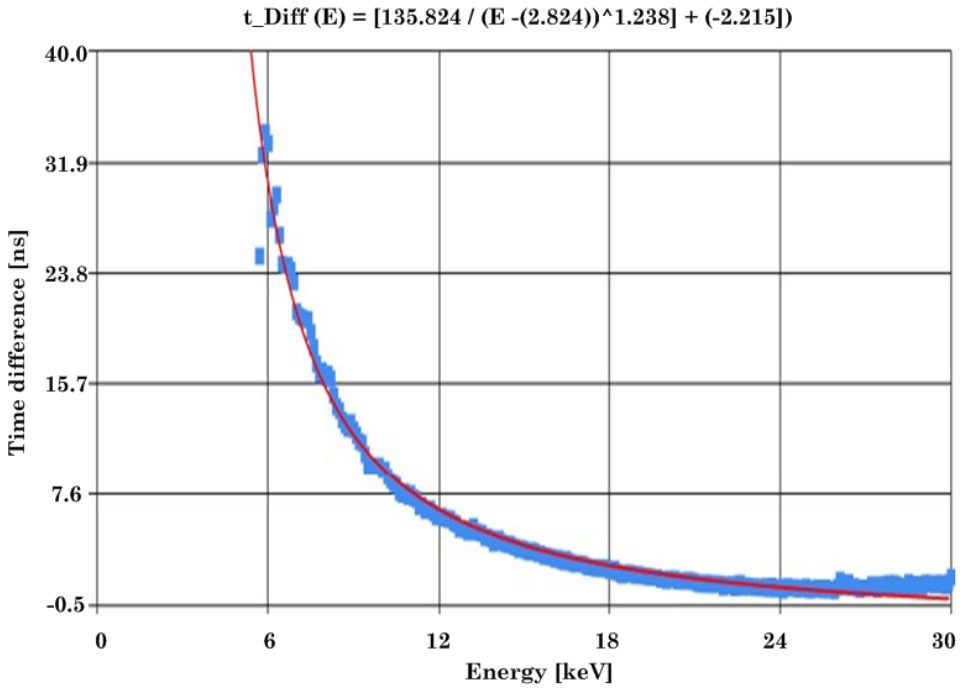

(b)

Figure 3.8: Time-walk anomaly in Timepix3. (a) Four pixels collecting fractional charges from one charge cluster produce four different ToAs, and (b) an example of a time-walk correction curve.

in the pixel carrying half the total energy is used as the reference ToA (denoted as t_1 in figure 3.8a). The other pixels randomly share half of the remaining energy, and the ToA for these pixels are assigned as t_2, t_3, and t_4. The time differences (t_1 - t_i) for all identified charge clusters are calculated and plotted as a function of their energies. Figure 3.8b shows an example of such a plot, clearly showing that the time difference is higher at lower energy. The relationship between the time difference and energy is described by a non-linear surrogate function $\triangle T$ as:

$$\triangle T = \frac{a}{(E - E_0)^b} + c\,, \tag{3.2}$$

where $\triangle T$ is the time-walk in ns, E is energy in keV, and E_0 the detector's threshold in keV. The three free parameters c, b, and c correspond to the curvature, the asymptote, and the offset of the function determined by a least-square fit. The ToA value for subsequent measurement is corrected according to: $ToA_{\text{corrected}} = ToA - \triangle T$.

The Time-walk correction using the Timepix3 onboard test-pulse is explored in [4]. They use the onboard *analogue test-pulse* at the preamp while pulsing the digital circuit with the onboard *digital test-pulse*. The time-walk is computed as the difference in the arrival time between the two pulses. The onboard test pulses are scanned over a range of energies, and their response is fitted with a non-linear function, $f(x)$ defined as

$$f(x) = P_0 + \frac{P_1}{x - P_2} \tag{3.3}$$

where P_0 is the latency of the pixel, P_1 is the threshold, and P_2 is the time-walk. A shortcoming of this method that is the dominant contributing factor to the error in time-walk, the homogeneity of the detector, is excluded in the calculation.

3.6 Chapter summary

The Medipix collaboration at CERN produced the first Medipix1 readout ASIC in 1997, designed as a single-photon counting ASIC for the LHC experiment. The Medipix2 readout ASIC with 65K pixels and 55 µm pixel pitch was introduced in 2002 and designed to explore spectroscopic X-ray imaging with a High-Z sensor. The Timepix readout ASIC was the Medipix2 collaboration's answer to the request made by the EUDet consortium as ASIC for their Time Projection Chamber project in 2007. This ASIC is modified from the MPIX2MXR2.0 by extending pixel functions to measure particle energy (ToT) and their arrival time (ToA). The emergence of the 130 nm CMOS technology and the need to improve the Timepix drove the Medipix collaboration to produce the Timepix3 readout ASIC in 2015. This ASIC has two main novelties to Timepix: simultaneous ToT and ToA acquisition and the data-driven with zero suppression readout architecture. The ToA resolution is improved from 10 ns to 1.562 ns thanks to the new 640 Mhz fToA clock. Also, the data-driven with zero suppression readout improved the dead time from 300 µs to 475 ns. The Timepix3 has been successfully transferred to many applications. Furthermore, work is ongoing within the collaborative successor to Medipix3, Medipix4, to produce an ASIC with better performance.

CHAPTER 4

Detector characterisation techniques

The detectors investigated in this thesis are LGADs and iLGADs in pad device forms and hybrid pixel detectors, i.e., the pixelated detectors (LGAD, iLGAD, and CZT/CdTe) bonded to the Timepix3 readout ASICs. Test versions of the LGAD and iLGAD pad devices are produced to study their electrical characteristics and signal gain. Electrical characteristics of the detectors, depletion voltage, breakdown voltage and leakage current are important since they define the fundamental operation of the detector. Additionally, both detectors need to have their signal gains investigated since they are designed to produce signals with gain. The electrical characteristics of the detectors are probed through current-voltage (IV) and capacitance-voltage (CV) measurements, and their gain is evaluated with the Transient Current Technique (TCT).

Characteristics such as pixel-to-pixel charge sharing and diffusion and the homogeneity of their response and gain are collectively referred to as pixel response. The pixel response of the hybrid pixel detectors with LGAD or iLGAD sensors is not fully understood since they are a relatively new technology. These properties are best probed with parallel beams with a fine beam spot size and high-intensity monochromatic photon sources. A synchrotron beam fulfils said requirements, and it has been widely used to probe the pixel

responses of microscopic pixel detectors. The hybrid pixel detector with a CZT sensor is a mature technology. Its pixel response is fully understood, so it only requires pixel calibrations (energy and time-walk) for operation. The calibration is accomplished by using radioisotopes or XRF sources. However, the calibration of the hybrid pixel detectors is described in a separate chapter (see Chapter 6) and will not be discussed here. This chapter describes the characterisation techniques used to characterise the pad and hybrid pixel detectors, discusses the fundamentals of said techniques, and outlines the experiment setups.

4.1 Electrical characterisation via IV and CV measurements

A reverse biassed detector produces a small magnitude of *leakage current* or *dark current* even in the absence of incident photons or charged particles. The leakage current arises from various factors: thermally generated electron-hole pairs at the generation-recombination centres at the surface of the detector and in the depleted volume; diffusion current due to concentration gradient (from the undepleted to the depleted region); and the high electric field effect[24, 44]. In unstructured p-n junction detectors, the thermally generated current in the depleted volume normally dominates. This current is proportional to the square root of the applied bias voltage and can be expressed as follows[44]:

$$J_{vol} \approx -q\frac{n_i}{\tau_g}W \approx -q\frac{n_i}{\tau_g}\sqrt{\frac{2\epsilon}{qN_D}V}\ , \tag{4.1}$$

with J_{vol} is the volume generation current per unit area, while τ_g and n_i are the carrier generation lifetime and intrinsic carrier concentration, respectively. Additionally, the temperature influences the leakage current through intrinsic carrier concentration and the generation lifetime. The leakage current is a noise source which degrades the detector's performance.

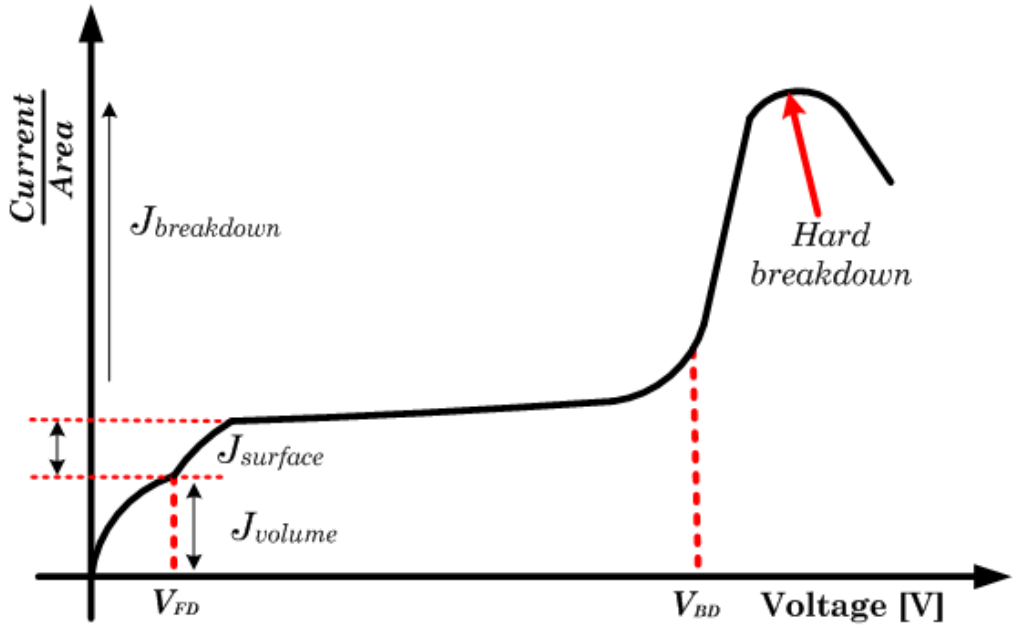

Figure 4.1: The typical current-voltage curve of a p-n junction silicon detector and the contribution of various current sources to the total leakage current. Adapted from [44].

The IV curve is an invaluable tool for detector testing as it elucidates the relationship between the detector's current and the applied biassed voltage. Figure 4.1 shows a typical IV curve of a reverse biassed p-n junction silicon detector, which also indicates the contribution of different current components to the total leakage current. Below full depletion, the volume generation current is dominant. The surface generation current contribute to the slight increase in leakage current when the depletion region reaches the backside of the detector. At full depletion, the IV curve shows a plateau region with a very small current increase before experiencing a sharp increase at high biassed voltage. The voltage at which the IV curve goes from the plateau to the sharp rise is called the *breakdown voltage* (V_{BD}), and increasing the voltage further causes a hard breakdown that will eventually destroy the detector.

In theory, the breakdown voltage is the maximum operating voltage of a detector. However, in practice, the detector is typically operated well below this value, i.e., in the plateau region. The breakdown voltage of detectors tends to be higher for larger junction areas

but lower for higher doping levels. The *full depletion voltage* (V_{FD}), which is the required voltage to fully deplete the detector, is another important property that can be obtained from the IV curve. This property is extracted from the transition where the current is proportional to the square root of voltage to the plateau region. However, the precise measurement of the transition is difficult and better measured with the CV measurement.

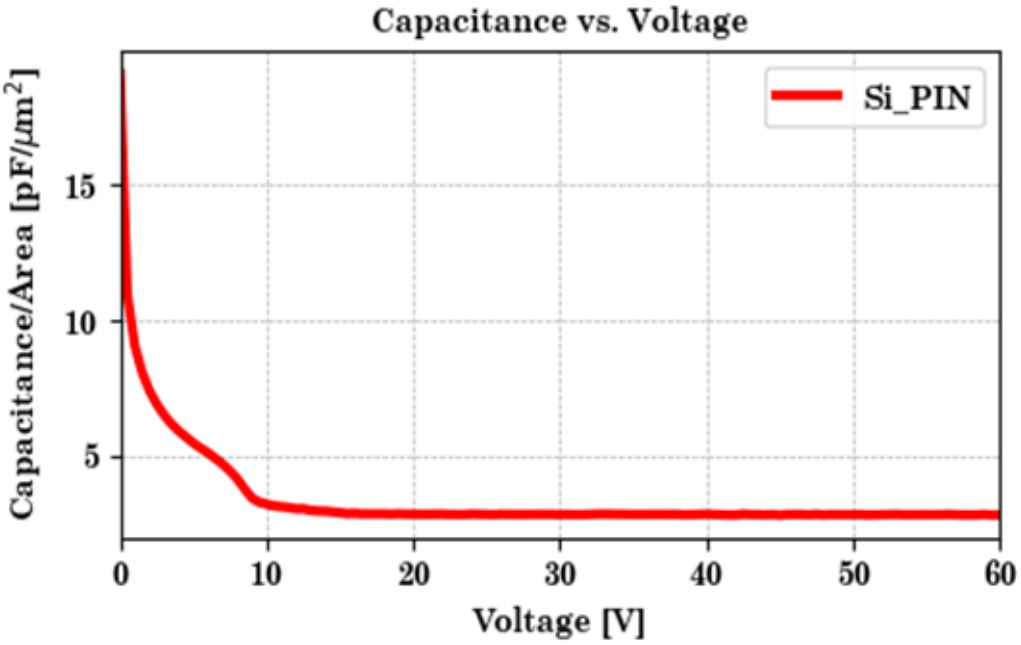

Figure 4.2: Current-voltage (CV) curve of a typical p-n junction silicon detector.

The capacitance-voltage (CV) characteristics of a reverse biassed semiconductor detector describe the relationship between the capacitance of the detector and the applied biassed voltage. The depletion region widens as the biassed voltage increases. Before full depletion, the capacitance per unit area decreased with increasing voltage (see Figure 4.2) and becomes constant when the detector is fully depleted at higher voltages. The CV measurement provides information about a detector's characteristics, including the V_{FD}, the full depletion capacitance and width W, and the doping concentration. For abrupt p-n junction detectors, the capacitance at a given biassed voltage is

$$C(V) = A\sqrt{\frac{q\epsilon N_{eff}}{2V}}\,, \tag{4.2}$$

where the N_{eff} is the effective doping concentration.

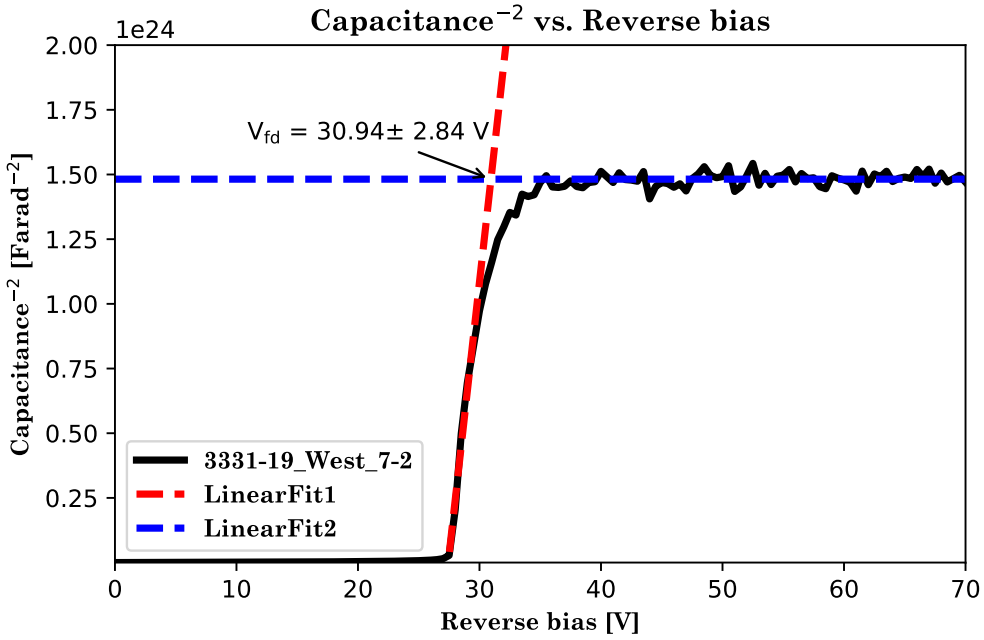

Figure 4.3: Obtaining the full depletion voltage (V_{FD}) from the $\frac{1}{C^2}$ as a function of voltage plot.

As stated earlier in the IV measurement, the V_{FD} can be obtained from the transition between the region where the current is proportional to the square root of voltage and the plateau region. It is difficult to extract the V_{FD} directly from the CV curve in Figure 4.2, but by rearranging and squaring equation 4.2 leads to

$$\frac{1}{C^2} = \frac{2}{q\epsilon N_{eff} A^2} V \,, \tag{4.3}$$

which links the $\frac{1}{C^2}$ to the voltage. Figure 4.3 shows an example of the $\frac{1}{C^2}$ as a function of the biassed voltage plot. The full depletion voltage (V_{FD}) can be extracted from the intersection point of the linear (red dash trace) and plateau (blue dash trace) regions[18, 74]. The width of the depletion region W can also be obtained from the CV measurement as

$$W = \frac{\epsilon A}{C} \,. \tag{4.4}$$

Using the relation between the W and capacitance in equation 4.4 and by rearranging 4.3

leads to the effective doping concentration at a given depletion region width:

$$N_{eff}(W) = \frac{2}{q\epsilon A^2}\left(\frac{d(\frac{1}{C^2})}{dV}\right)^{-1}. \tag{4.5}$$

Equation 4.5 shows that the effective doping concentration at a given depletion region width is proportional to the inverse of the first derivative of $\frac{1}{C^2}$ with respect to voltage. Therefore, the effective doping concentration profile across the width (or depth) of the depletion region can be obtained from this equation by using data from CV measurements, which is the first derivative of $\frac{1}{C^2}$ with respect to voltage. The peak doping concentration at the multiplication layer, an important parameter for LGAD detectors, can be extracted from the plot of effective doping as a function of depletion width (depth). The next subsection outlines the setup of IV and CV measurements in the Glasgow Laboratory for Advanced Detector Development (GLADD) clean room.

4.1.1 IV/CV measurement set up at GLADD

Table 4.1: GLADD Wentworth Probe Station IV/CV Operation Parameters

Measurement	LabVIEW program	Parameters
Current-Voltage (IV)	CurrentVoltageMeasurer_K237_v1.3.2 K2700_T_RH_Monitor_v1.0.1 SensorMarketSurvey_GUI_Assist_v1.3.1	$I_{compl.}$ = 100 nA Start = 0 V, End = 250 V Δ = 5 V
Capacitance-Voltage (CV)	CurrentVoltageMeasurer_K237_v1.3.2 K2700_T_RH_Monitor_v1.0.1 SensorMarketSurvey_GUI_Assist_v1.3.1 CapacitanceMeasurer_v1.1.0	$I_{compl.} > 10\,\mu$A Start = 0 V, End = - 100 V ΔV = - 0.5 V Correction: OPEN & CLOSE circuit f_{range} = 1 kHz, 10 kHz, 100 kHz Measurement f = 10 kHz

The IV and CV measurements are performed at the Wentworth Probe Station in the GLADD clean room. Figure 4.4 shows the schematic diagram for the IV measurement. The Keithley 237 is a voltage source and simultaneously measures the device under test (DUT) inverse leakage current. For a standard p-type LGAD, the DUT is biassed with a positive voltage at the n^+ contact on the front side of the DUT, and the back side

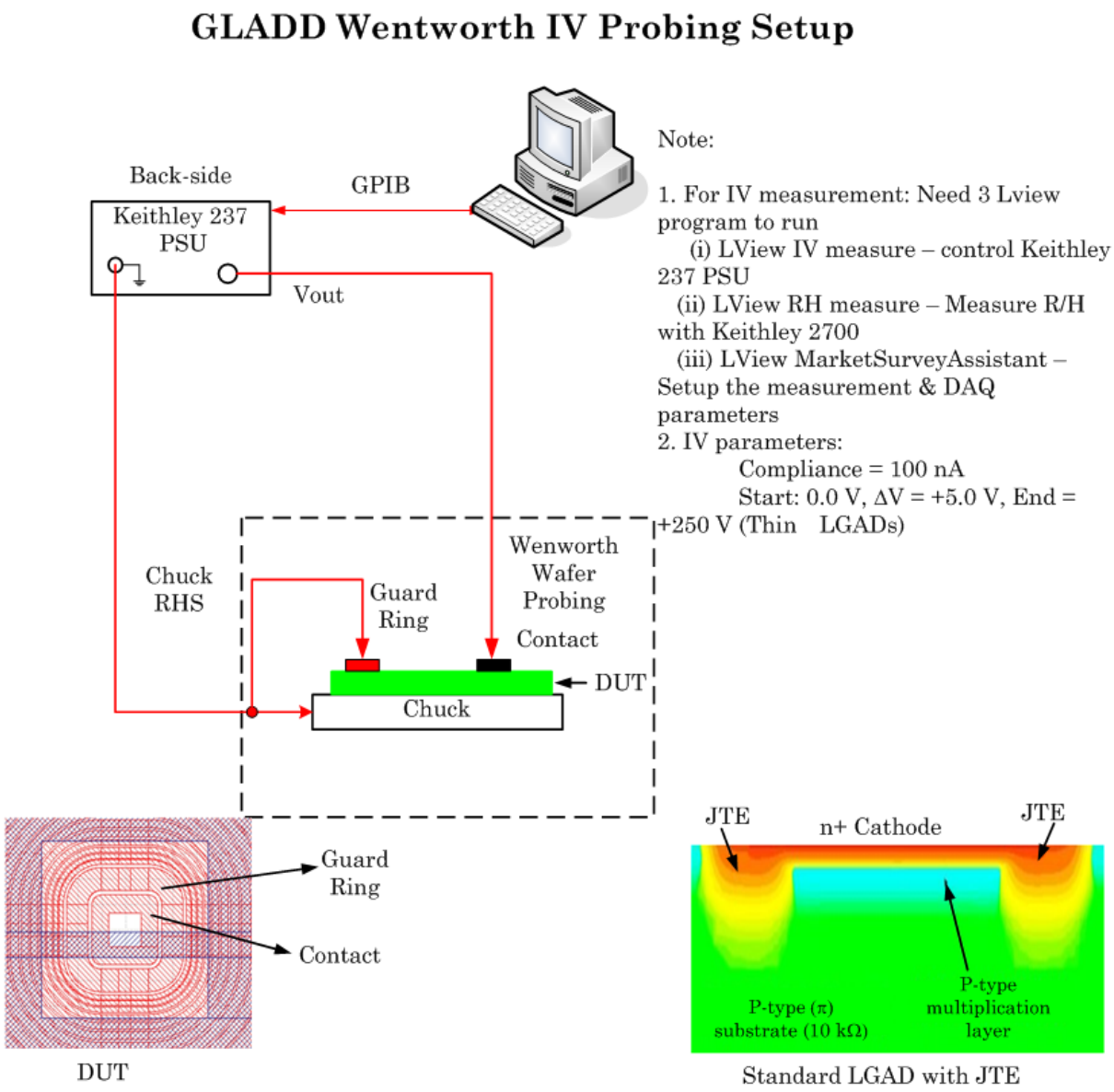

Figure 4.4: Schematic diagram for the Current-Voltage (IV) measurement at the GLADD Wentworth probe station.

is in contact with the chuck. Both chuck and the first guard ring are grounded. The temperature and relative humidity inside the Wentworth Probe Station are monitored and recorded during the measurement with a Keithley 2700 multimeter. The IV measurement is controlled by three custom-written LabVIEW programs, running on a PC (see Table 4.1). The DUT is biassed with voltage from 0 V to 250 V at +5.0 V interval with the compliance current set at 100 nA. The temperature and relative humidity are also recorded as part of the IV data for each voltage change.

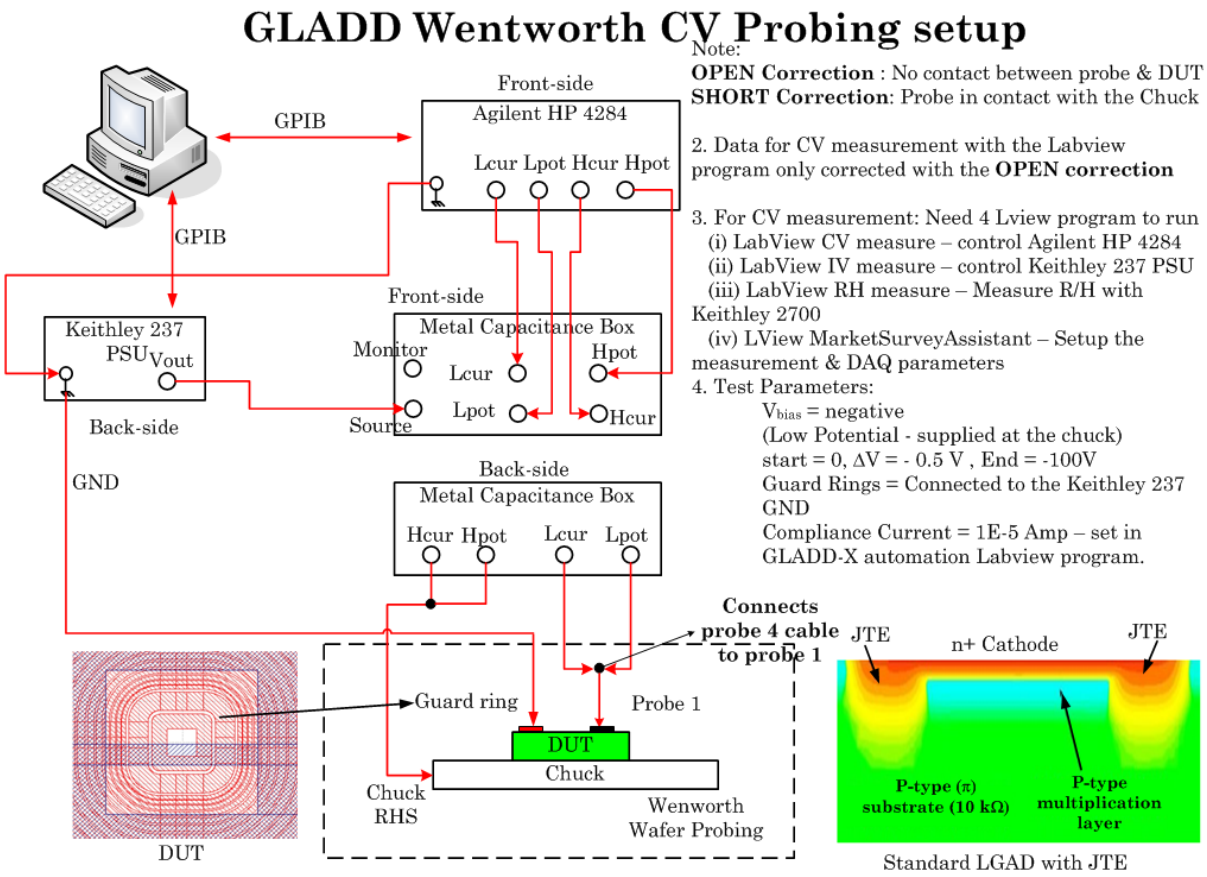

Figure 4.5: Schematic diagram for the Capacitance-Voltage (CV) measurement at the GLADD Wentworth probe station.

The setup for the CV measurement is shown in Figure 4.5. The low potential and low current probes (L_{pot} & L_{cur}) are connected to the DUT contact (where the gain implant layer is) while the chuck is connected to the high potential and high current probes (H_{pot} & H_{cur}). The voltage source is supplied by the Keithley 237 via the capacitance reference network (denoted as metal capacitance box in Figure 4.5), and the capacitance is measured as a complex impedance with a precise HP4284A Inductance, Capacitance, and Resistance (LCR) meter. The HP4284A offers parallel and series RC equivalent circuit models for measuring capacitance. The parallel RC model was used in this study as it considers the fluctuations in surface current caused by surface resistance and aligns with the model of a fully depleted diode [75].

Before CV measurement, the HP4284A LCR meter is calibrated at three frequency ranges

stated in Table 4.1 to consider the effect of the decoupling capacitance and resistance in the system. The calibration is done by performing the *OPEN* and *CLOSE* circuit corrections at the known load provided by the metal capacitance box. As shown in Table 4.1, the CV measurement is controlled by four custom-written LabVIEW programs. A negative bias at -0.5 V interval is supplied to the chuck, and the measurement was performed at 10 kHz frequency. This frequency offers a good compromise between the signal and noise for this CV measurement setup[75]. The leakage current, temperature and relative humidity are also recorded as part of the CV data for each voltage change.

4.2 The transient current technique (TCT)

The Transient Current Technique (TCT) is one of the essential tools for studying semiconductor radiation detectors. In a TCT system, a laser pulse generates free charge carriers (electron-hole pairs). According to the Shockley-Ramo theorem, charge carriers induce current while moving under the electric field towards their respective electrodes. For a simple two-electrode pad detector with thickness d, the induced current is $I_{e,h}$ given by [76]

$$I_{e,h}(t) = N_{e,h} exp\left(\frac{-t}{\tau_{\text{eff}_{e,h}}}\right)\frac{1}{d}\mu_{e,h}E \tag{4.6}$$

where the $N_{e,h}$ is the number of electron-hole pairs generated, $\tau_{\text{eff}_{e,h}}$ is the effective trapping time of carriers, $\frac{1}{d}$ the weighting field, $\mu_{e,h}$ carrier mobility, and E is the electric field. Several key parameters can be extracted from the TCT measurement: the sign and concentration of the space charge, the full depletion voltage, the induced charge $Q = \int_0^{t_{int}} I(t)dt$, mobility measurements and the correction of charge trapping.

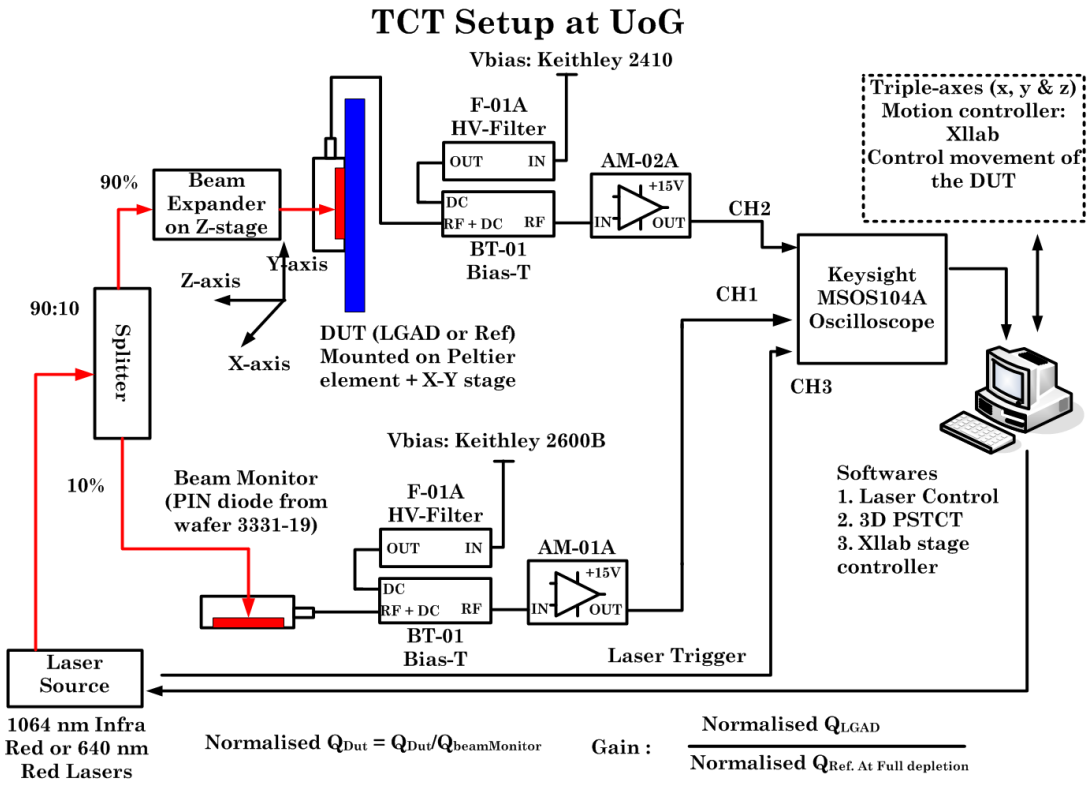

(a)

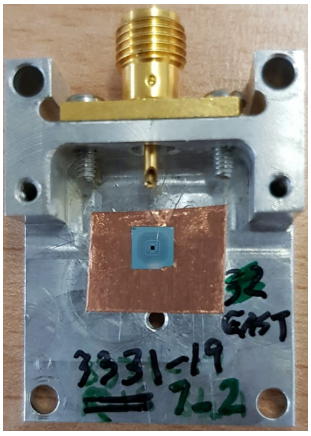

(b)

Figure 4.6: (a) Schematic diagram for the Transient Current Techniques (TCT) setup at University of Glasgow, and (b) The DUT assembly; The pad LGAD is glued onto an Aluminium metal.

4.2.1 The TCT setup and data analysis

Figure 4.6a shows the set-up of the scanning TCT system supplied by Particulars[1] at the University of Glasgow. The detector is biassed with a high voltage supply through a high

[1]Particular, Advanced Measurement System, Dragomelj 154, SI-1230 Domazle, Slovenia/Tel:+386 41 423 469, https://particulars.si/index.php

voltage (HV) filter and a Bias-T network. A fast wide-band current amplifier (AM-02A) amplifies the detector's output signal, and the amplified signal is digitised and recorded by an oscilloscope. The device under test (DUT) assembly (see figure 4.6b) is in contact with a Peltier element and is mounted on a dual-axis motion stage. The Laser source is split at a 90:10 ratio with a beam splitter; 90% goes to the DUT, and 10% goes to the beam monitor. The beam monitor is a standard PIN diode that acts as a reference to normalise the DUT against instability in the laser output during the measurement. Only 10% of the laser output is used as input for the beam monitor to limit the number of incident photons, thereby preventing the beam monitor from early saturation.

The TCT is controlled by a LabVIEW program (3D PSTCT) running on a PC. The laser output signal triggers the DUT pulse acquisition, and the oscilloscope is configured in high-resolution acquisition with 500 analogue averaging modes to get reliable and stable pulses. The TCT data is stored in binary form and analysed by a custom-written C++ program which uses features from the ROOT (root.cern.ch) library.

4.2.2 Laser focusing, alignment and MIP calibration

Focus-finding and laser alignment are essential procedures to be conducted before any TCT measurements are taken. The focus-finding procedure (see Figure 4.7) is performed by scanning the laser (in the x or y-axis) from the metallised to the non-metallised part of the detector while moving the optical along the z-axis. Data is analysed with a macro written in C++ called *GetFocus.cpp*, which calculates the FWHM of the laser spot, and finds the focus position and misalignment between the detector and the optical axis. Figure 4.8a shows the plot of the induced charge as a function of scanning position in the x-axis for a given optical distance. An error function fit extracts the FWHM of the laser spot for a given optical distance (the red traces in Figure 4.8a). Figure 4.8b shows the plot of the FWHM of the laser spot as a function of the optical distance (z-axis); the focus is defined as the optical distance with the smallest FWHM value. The misalignment angle, θ (see

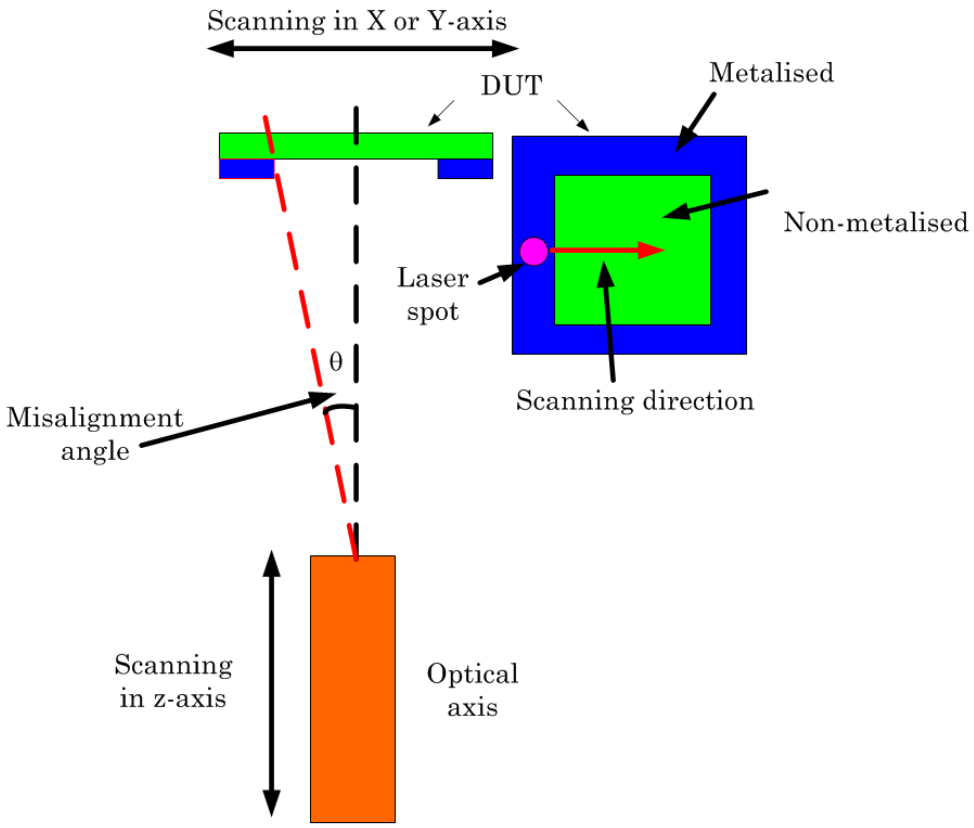

Figure 4.7: The setup for the laser focus finding and alignment

Figure 4.7) between the x-axis and optical axis occurs if the transition between metallised and non-metallised is dependent on the position of the optical axis. This angle can be measured by measuring the position of the edge in x-axis at a different optical distances (see Figure 4.9). If the misalignment angle θ is small (Tan $\theta \approx \theta$), θ is equivalent to the slope of the curve (see Figure 4.9).

In order to determine the electron-hole pairs produced by a laser, the TCT system is first calibrated with MIPs. The experiment setup for the MIPs calibration (see Figure 4.10) is arranged to allow coincidence detection of the β^- particle from ^{90}Sr in the LGAD and scintillation detector. If the β^- particle is a MIP, it will lose energy in the LGAD, penetrate through and be detected in the scintillation detector. The scintillation detector's output signal is used as a trigger to ensure that only the MIP events are recorded on the LGAD. Figure 4.11a shows the energy-loss spectra of 400 MIPs. The most probable value (MPV),

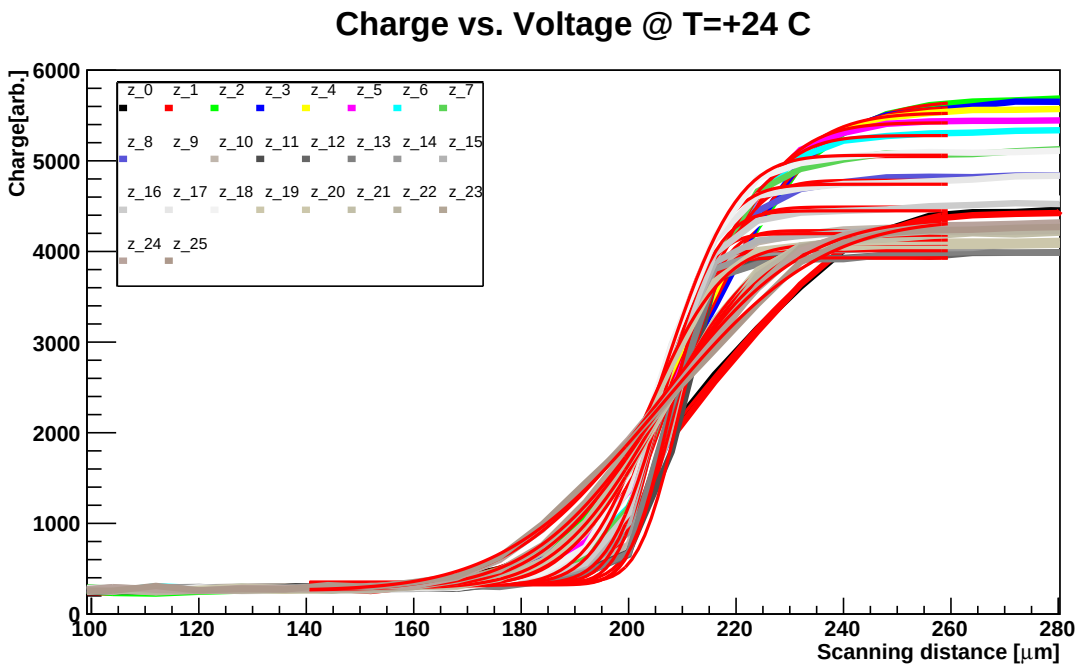

(a)

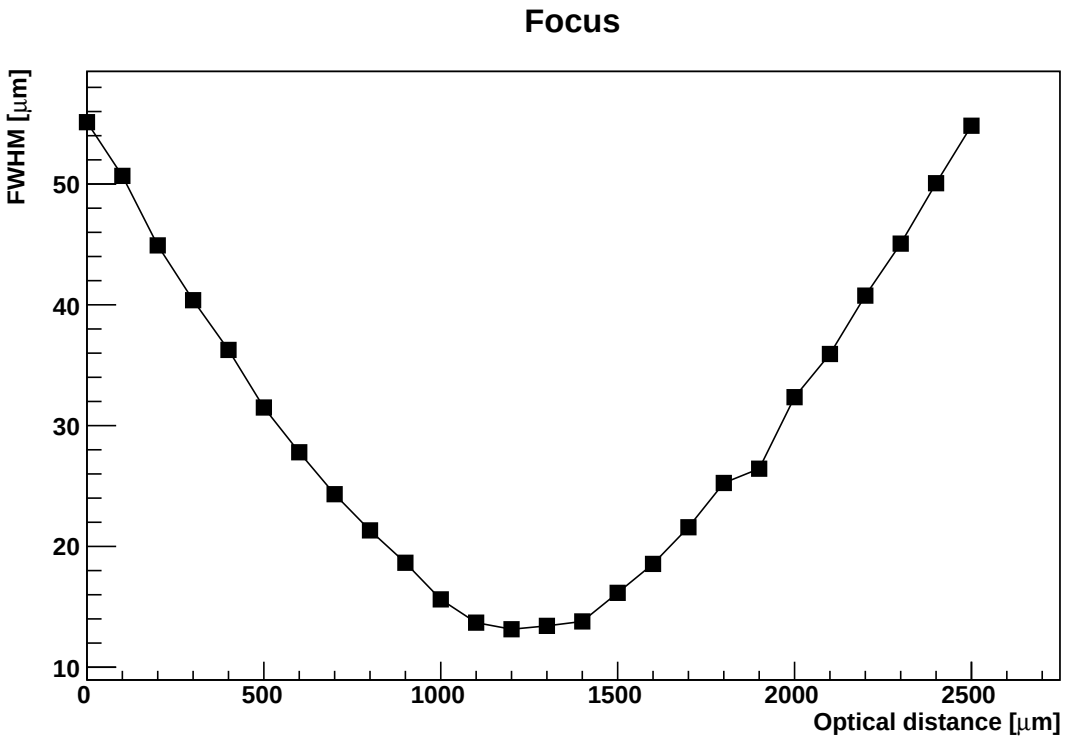

(b)

Figure 4.8: (a) Plot of the induced charge as a function of x or y-axis; FWHM of laser is extracted by an error function, (b) FWHM as a function of the optical distance plot; smallest FWHM indicates laser at optimum focus.

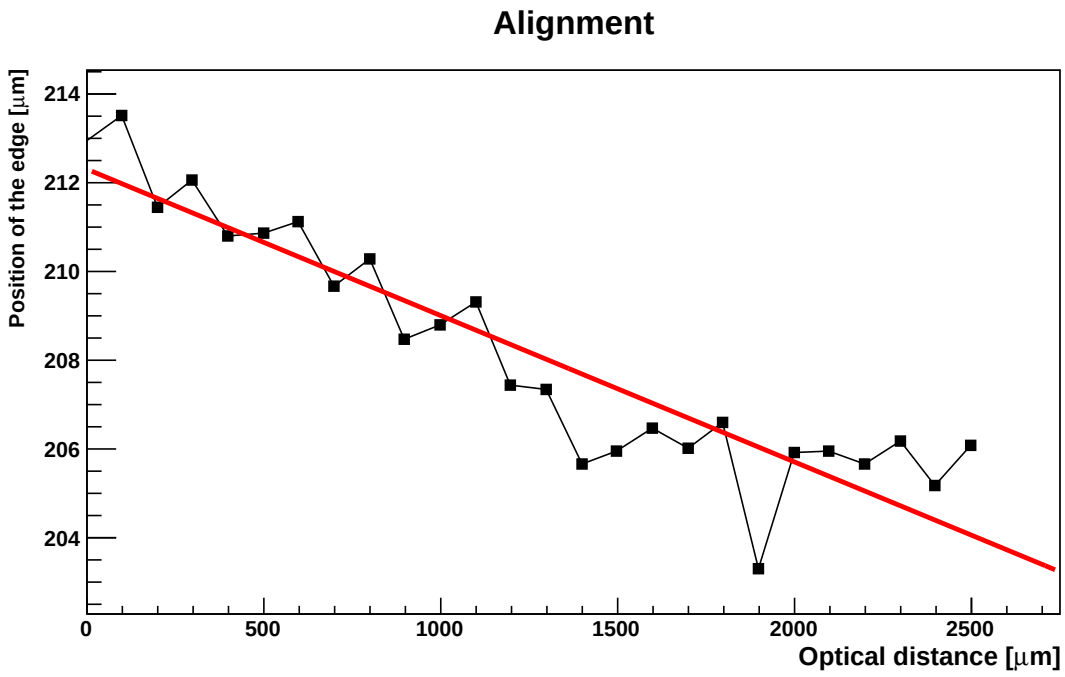

Figure 4.9: The plot of the Position of the edge as a function of the optical distance; misalignment angle θ between the detector and optical axis is given by the slope of the linear fit (red line)

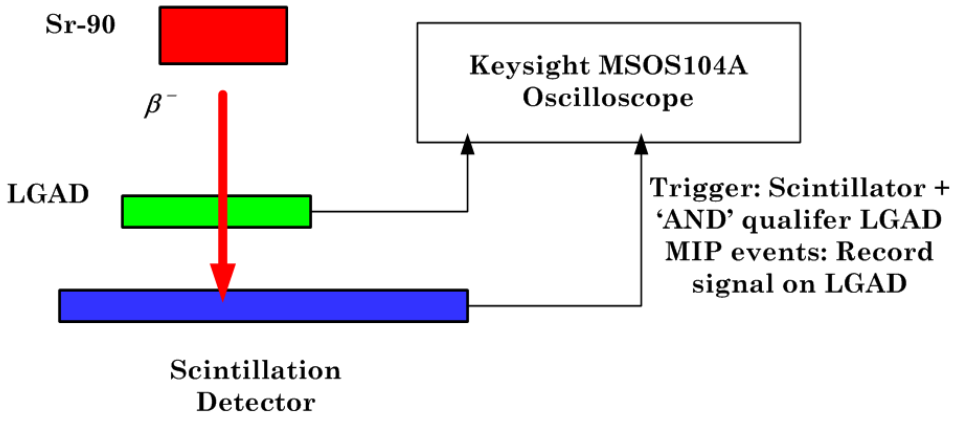

Figure 4.10: The setup for the TCT calibration using MIP from ^{90}Sr.

extracted using a convoluted Landau-Gauss fit (red line), is $\approx$ 91 mV. An equivalent number of entries are recorded for laser pulses at various laser power (LP) settings. A histogram of pulse amplitudes versus entries is plotted, and the peak value is extracted with a Gaussian fit. Figure 4.11b shows the histogram of pulse amplitudes at laser power setting (LP) = 55.8%, equivalent to 1 MIP. This laser power setting is used as laser pulse output for the later gain measurement.

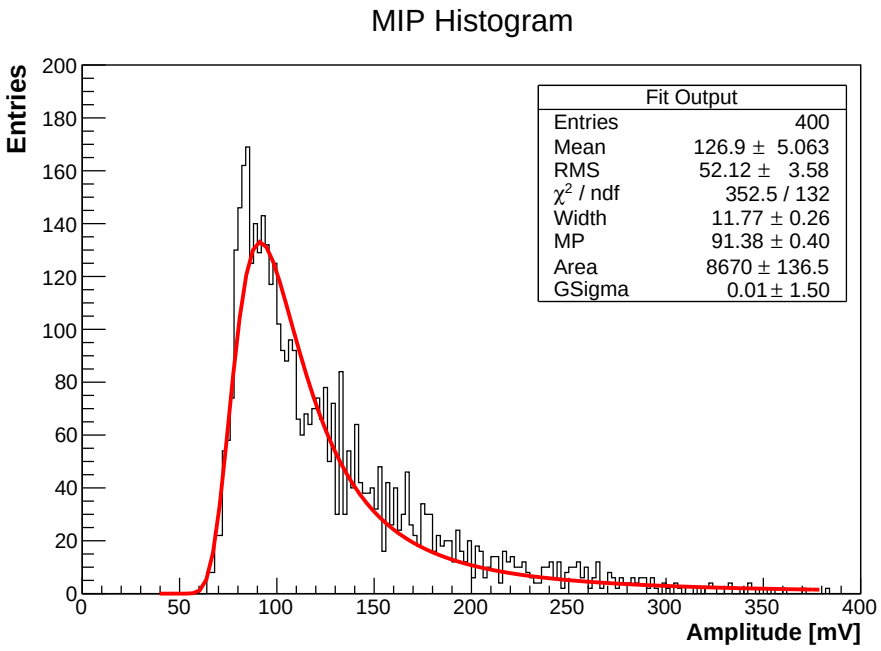

(a) Energy-loss spectrum of MIP in LGAD.

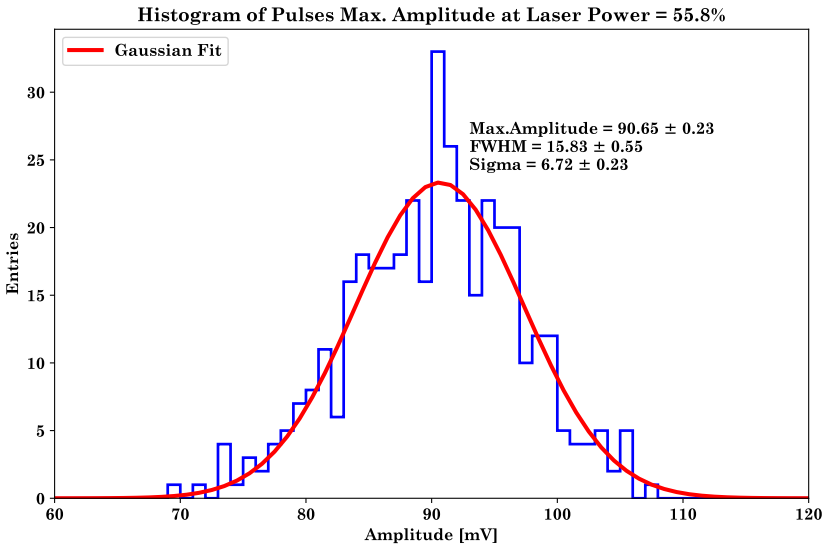

(b) Histogram of pulse amplitude acquired with laser source at laser power (LP) 55.8 %.

Figure 4.11: MIP calibration in TCT system. The energy-loss of a MIP is used to determine the number of electron-hole pairs generated from the laser pulse.

4.2.3 Measurement of signal gain in LGAD devices

The signal gain of LGAD detectors is assessed through TCT measurements using a 1064 nm infrared (IR) laser and is calculated as the ratio of the measured charge in an LGAD to

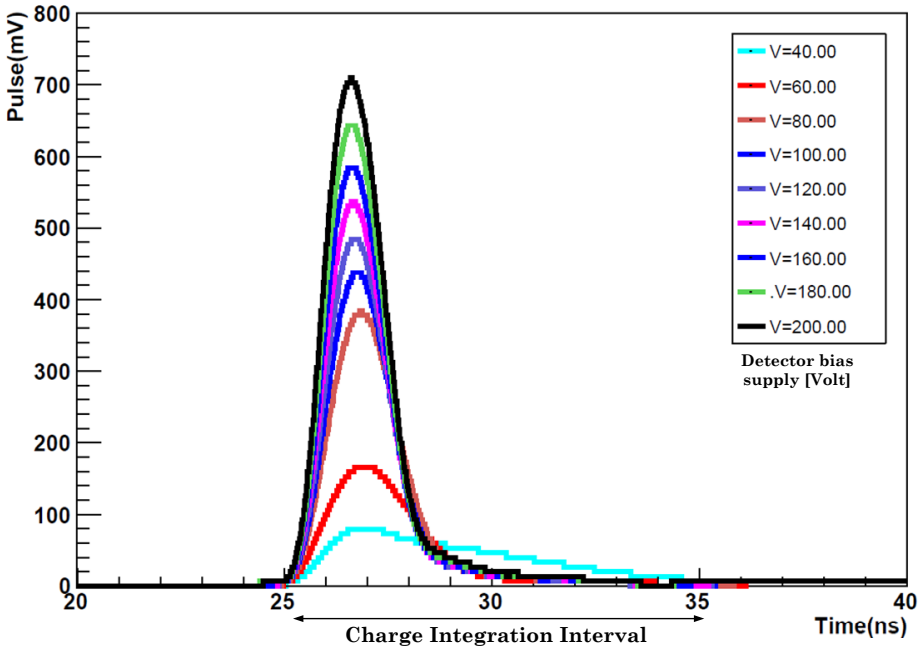

Figure 4.12: An example of TCT pulses at various bias voltage from an LGAD devices. The induced charge is calculated by integrating the pulse between their start and end times.

the measured charge in a PIN reference. The PIN reference used in the TCT setup at the University of Glasgow is a 50 µm thick, 1.0 × 1.0 mm^2, p-n junction silicon pad detector from wafer 3331-19. The measurement is also performed at various temperature settings (30, 10, 0, -10, -20, and -24 °C) since the gain in LGAD and the infrared (IR) absorption in silicon are temperature-dependent. The data is analysed with a custom-written C++ macro called *VoltageScanGlasgow.cpp*. Figure 4.12 shows an example of LGAD output pulses at various bias voltages acquired with a TCT system. The induced charge Q is the integral of the pulse over its lifetime.

The pulse integration is corrected for baseline variations by taking into account the baseline values of 0 ns to 20 ns prior to the starting of the pulse. A total of 20 to 50 pulses per voltage step are taken to ensure statistically sufficient data for the gain measurement. The average induced charge for n number of pulses for the DUT and beam monitor (BM) are given as

$$\overline{Q_{\mathrm{DUT}}} \pm \frac{\sigma_{\mathrm{DUT}}}{\sqrt{n}} \quad \text{and} \quad \overline{Q_{\mathrm{BM}}} \pm \frac{\sigma_{\mathrm{BM}}}{\sqrt{n}} \tag{4.7}$$

where the $\frac{\sigma}{\sqrt{n}}$ is the standard error of the mean (SEM). The normalised charge of the DUT (LGAD or PIN reference) is calculated as follows

$$Q_{\mathrm{DUT}}^{\mathrm{norm}} = \frac{\overline{Q_{\mathrm{DUT}}}}{\overline{Q_{\mathrm{BM}}}} \tag{4.8}$$

and the normalised charge error $\sigma_{\mathrm{DUT}}^{\mathrm{norm}}$ is calculated according to error propagation based on ratio as

$$\sigma_{\mathrm{DUT}}^{\mathrm{norm}} = \frac{\overline{Q_{\mathrm{DUT}}}}{\overline{Q_{\mathrm{BM}}}} \left(\sqrt{\left(\frac{\frac{\sigma_{\mathrm{DUT}}}{\sqrt{n}}}{Q_{\mathrm{DUT}}} \right)^2 + \left(\frac{\frac{\sigma_{\mathrm{BM}}}{\sqrt{n}}}{Q_{\mathrm{BM}}} \right)^2} \right) . \tag{4.9}$$

The gain of an LGAD device is calculated as follows

$$\mathrm{Gain} \pm \sigma_{\mathrm{Gain}} == \frac{Q_{\mathrm{LGAD}}^{\mathrm{norm}}}{Q_{\mathrm{PIN}}^{\mathrm{norm}}} \pm \frac{Q_{\mathrm{LGAD}}^{\mathrm{norm}}}{Q_{\mathrm{PIN}}^{\mathrm{norm}}} \left(\sqrt{\left(\frac{\sigma_{\mathrm{LGAD}}^{\mathrm{norm}}}{Q_{\mathrm{LGAD}}^{\mathrm{norm}}} \right)^2 + \left(\frac{\sigma_{\mathrm{PIN}}^{\mathrm{norm}}}{Q_{\mathrm{PIN}}^{\mathrm{norm}}} \right)^2} \right) ,$$

where $Q_{\mathrm{PIN}}^{\mathrm{norm}}$ and $\sigma_{\mathrm{PIN}}^{\mathrm{norm}}$ are the average normalised charge and SEM measured in a fully depleted PIN reference device.

4.3 Synchrotron test beam

Synchrotron radiation is high-energy electromagnetic radiation emitted when charged particles travel near the speed of light in curved paths or circular accelerators. It is characterised by its continuous spectrum, polarisation, and intense brightness, making it invaluable for applications in materials science, biology, and medical imaging. Monochromators and focusing mirrors produce a monochromatic, focused, and parallel synchrotron beam, simplifying data analysis by eliminating the need to deconvolute interaction depth. These properties make synchrotron beams ideal for investigating charge sharing, homogeneity response, and material defects in pixel detectors, offering insights that other techniques

cannot accurately measure.

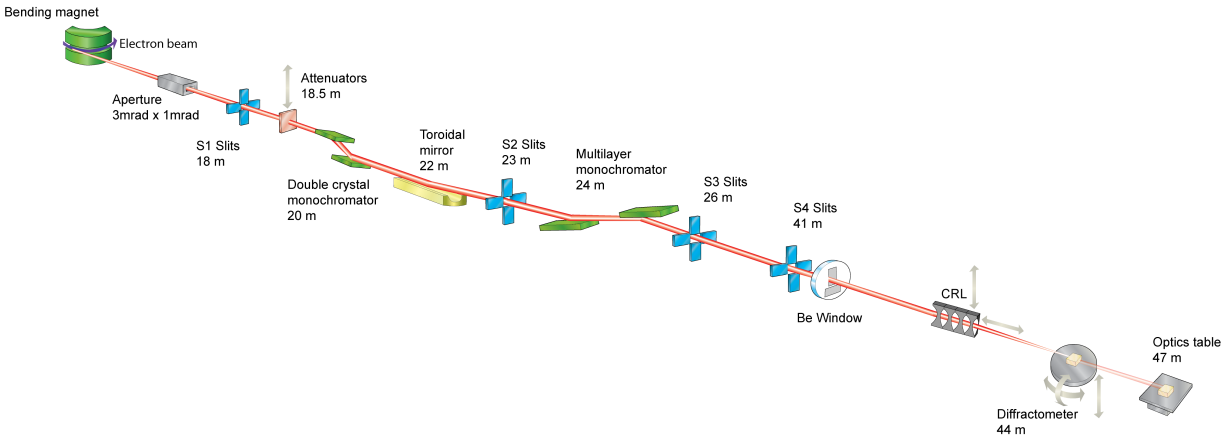

Figure 4.13: Beamline layout at the Beamline B16, Diamond Light Source(DLS) [77].

Two synchrotron test beam campaigns were conducted at Beamline B16, Diamond Light Source (DLS), to evaluate highly pixelated (i)LGADs bonded to the Timepix3 Readout ASIC. Figure 4.13 shows the schematic of Beamline B16, where both experiments took place on the optical table following the diffractometer. Beamline B16 offers high-intensity, low-divergence beams that can be monochromatic or white, with adjustable photon energies ranging from 4 keV to 20 keV for focused to 4 keV to 45 keV for unfocused modes. These capabilities are tailored to accommodate specific user requirements, making Beamline B16 ideal for studying microscopic samples like highly pixelated detectors (Reference: [78]).

4.3.1 Test beam setup

Figure 4.14 illustrates the experimental setup used in two synchrotron test beam campaigns at Beamline B16, Diamond Light Source. The hybrid pixel detector is housed within a high-density polyethylene (HDPE) casing and placed inside an Aluminium box (Figure 4.14a). This box features a small window for beam access and sits on a 6-axis alignment stage (Figure 4.14b), allowing precise adjustments in positional axes (x, y, z) and tilt angles (Ψ, Θ, Φ). The synchrotron beam, tuned to ≈ 15 keV and micro-focused by

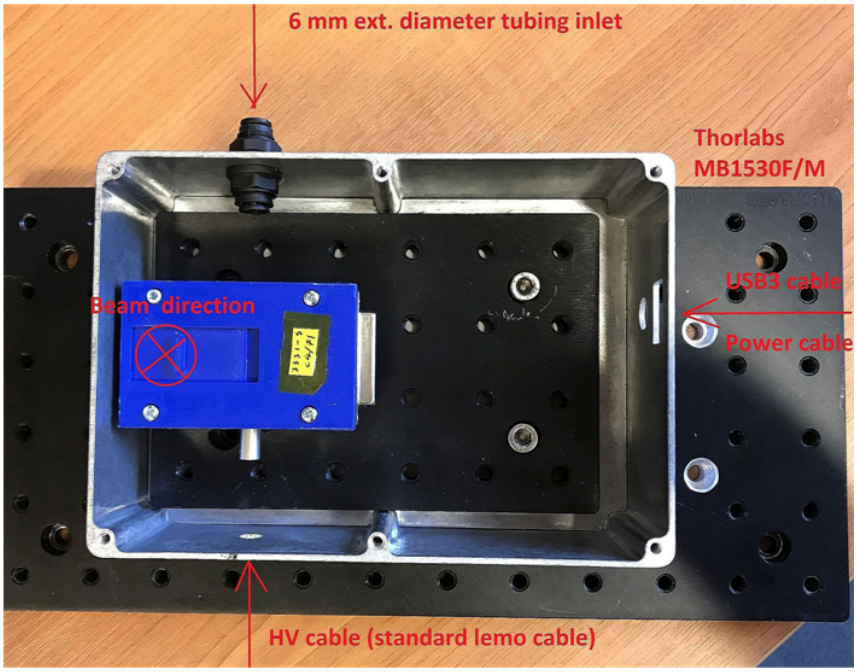

(a)

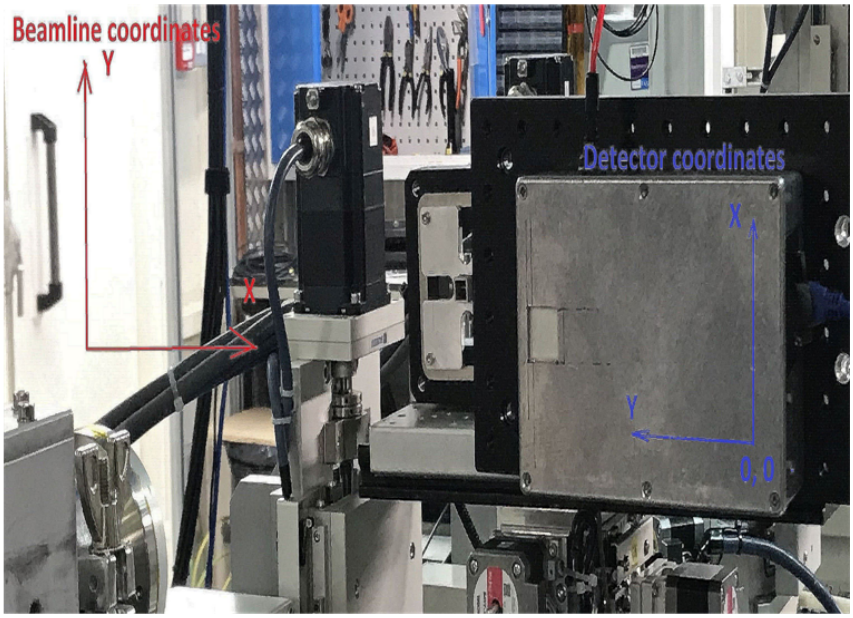

(b)

Figure 4.14: The experiment setup used during the two synchrotron test beam campaigns at the Beamline B16, Diamond Light Source (DLS). (a) The hybrid pixel detector under test, and (b) the Al box mounted on 6-axis alignment stage.

a Beryllium compound refractive lens (CRL), undergoes horizontal and vertical transmission scans using a 200 µm diameter gold wire. Gaussian fitting of the transmission data extracts the beam's horizontal and vertical spot sizes, measured to be $\approx 2\,\mu$m FWHM (see

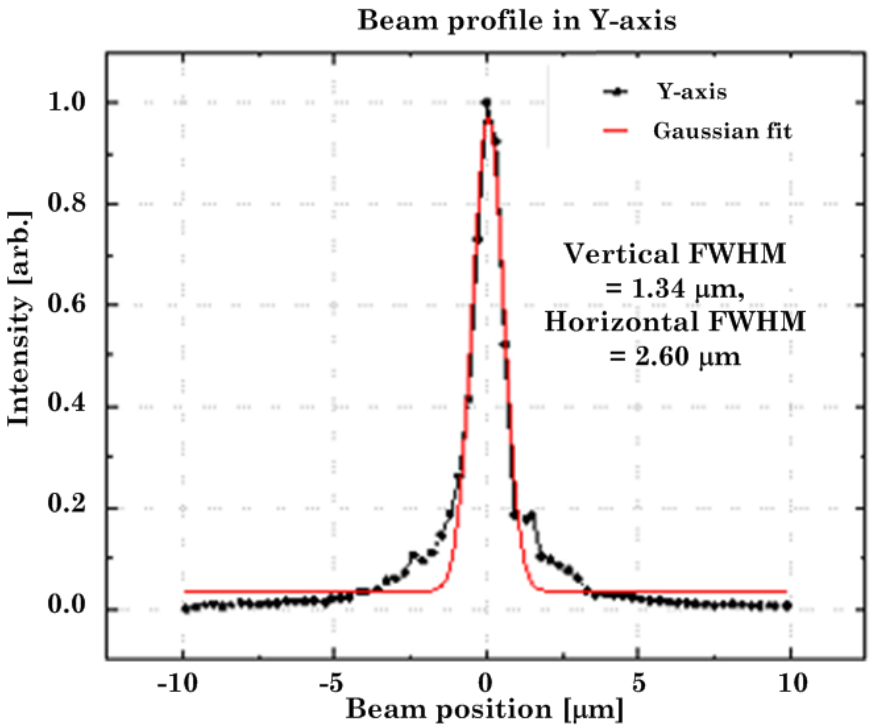

Figure 4.15: The vertical profile of the synchrotron beam used during synchrotron test beam.

Fig. 4.15). This setup was chosen to utilise the smallest achievable beam size at 15 keV mono-energy synchrotron beam available at Beamline B16, ensuring precise localised interaction within the detector to map small pixel detectors accurately.

The choice of 15 keV for this study is motivated by several factors. Firstly, it ensures a high signal-to-noise ratio, as the Timepix3 minimum threshold is approximately 2 keV (500 e^-), which could increase a few keV when coupled to a detector. Secondly, the $\frac{1}{e}$ probability of interaction for 15 keV in silicon is $\approx$ 400 µm, guaranteeing a high probability of interaction within a 300 µm thick silicon detector[79]. Additionally, there is a historical rationale: the University of Glasgow began working with the hybrid pixel detector with Medipix/Timepix ASICs around 15 years ago, initially using a 15 keV synchrotron. Continuity at this energy allows for consistent performance tracking and comparison with historical data, facilitating long-term research and analysis.

The 6-axis stage where the detector was mounted was precisely adjusted using a laser for

vertical alignment to ensure the synchrotron beam was perpendicular to the detector. This alignment was confirmed by checking the laser reflection on white paper approximately 5 m from the detector. Aluminium attenuators of various thicknesses, ranging from 1.0 mm to 5.0 mm, were tested to balance beam intensity, aiming for a high rate of pixel hits without significant signal pile-ups. Ultimately, the 5 mm thick aluminium attenuator proved the most effective choice in both test beams, achieving an optimal balance between beam intensity and maintaining signal clarity.

4.3.2 Test beam scanning methods

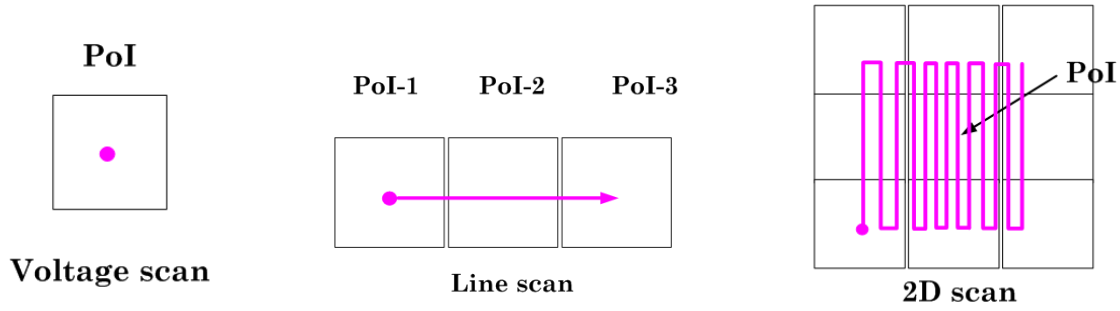

Figure 4.16: The three scanning methods used during the two synchrotron test beam campaigns at the Beamline B16, Diamond Light Source (DLS). (a) Voltage scan: Measurements at various biassed voltages with the beam positioned at the centre of the pixel-of-interest (PoI), (b) Line scan: Beam is scanned across 3 PoIs, and (c) 2D scan: 2D raster scan covering the PoI.

Three scanning methods characterise hybrid pixel detectors in synchrotron test beam campaigns: *Voltage scan, Line scan*, and *2D scan*. The Voltage scan (Figure 4.16a) assesses pixel performance by varying bias voltages at the centre of the PoI. The Line scan (Figure 4.16b) evaluates pixel response, signal gain, charge sharing, and diffusion by scanning the beam across three PoIs at optimal bias voltage. Voltage and Line scans are conducted on pixels expected to produce signal gain and on control pixels. The 2D scan employs a fine-step (2 µm) raster across the PoI to assess pixel response homogeneity and signal gain. Chapter 7 provides further details on scan locations. This comprehensive approach enables thorough characterisation of detector performance and pixel-level behaviour.

In both test beams, data are collected using Timepix3's data-driven ToT + ToA mode, but only ToT data are analysed. Two key measurements are extracted: the summed ToT pixel value and the over-threshold pixel count. The latter indicates total photon interactions, while the summed ToT pixel value represents total collected charges corresponding to energy loss from synchrotron radiation (assuming 100 % charge collection). Both measurements are used to determine pixel response, with the summed ToT pixel value being particularly crucial for deriving important detector characteristics. Signal gain is quantified by comparing summed ToT pixel responses from the Line scan in control (no gain) and gain pixels. The spectral distribution of summed ToT values reveals charge sharing and diffusion properties. Finally, the 2D scan's summed ToT data directly indicate pixel response homogeneity and gain distribution across the hybrid pixel detectors.

CHAPTER 5

Characterisation of low gain and inverse low gain avalanche pad detectors

The Low Gain Avalanche Detector (LGAD) is a new concept in silicon detectors with moderate *gain* between 5 to 10 [80]. The University of Glasgow and Micron Semiconductor Ltd collaboration produced two prototypes of silicon detectors with an internal gain characterised in this thesis. The first types of prototypes are 50 µm thick devices, which are one of three different types of gain doping implants. The primary motivation for the thin LGAD is to explore its potential as a fast-time resolution detector for the upcoming ATLAS and LHCb phase-II upgrades [15, 81]. The previous iteration of much thicker LGAD (250 µm) achieved moderate gain at around a factor of 5 and time resolution of ≈ 85 ps at 250 V reverse bias voltage and $-30\,^{\circ}$C, respectively. The 50 µm thick LGAD is expected to achieve a sub-50 ps timing resolution, the minimum requirement proposed in the LHCb phase-II upgrade. However, the measurement of timing resolution in this 50 µm thick LGAD device is the subject of another study and will not be discussed in this

thesis. The conventional design of LGAD with a Junction Termination Extension (JTE) suffers from a severe reduction in fill factor, as explained in [25]. In LGAD detectors, the fill factor is defined as $\frac{\text{Gain area}}{\text{Total area}}$ [24]. The inverse LGAD (iLGAD) is produced as the technological option to overcome the low fill factor issue. The initial work of the iLGAD device is completed in [24], which includes the devices' design, simulation and fabrication.

A *pad detector* is a sensor element with coarse segmentation and has a shape more or less equal in both directions on the sensor's surface [44]. The pad device exhibits different electrical characteristics and radiation responses than its pixelated counterparts. The leakage current and capacitance in pad devices are free from the readout system-induced effects, which normally occur in the hybrid pixel detector. A pad device also exhibits a true characteristic of an individual detector, free from pixel-to-pixel charge sharing and diffusion. Therefore, the LGAD and iLGAD are first characterised in their pad form for electrical characteristics and radiation response in a controlled environment in a laboratory.

This chapter describes the characterisation of the (i)LGAD pad detectors. Both detectors are characterised by Current-Voltage (IV) and Capacitance-Voltage (CV) measurements. The gain measurement in both devices is also planned, but only the gain measurement for the 50 µm thick LGAD was completed in this thesis. The signal gain as a function of temperatures in the 50 µm thick LGAD is evaluated using the TCT method with a 1040 nm infra-red laser. The key findings of the electrical characterisation and gain measurement are presented, discussed and summarised here.

5.1 The LGAD & iLGAD pad devices

The main structural difference between the LGAD and the iLGAD is shown in figure 5.1. The LGAD has a deeper extension of n^+ structure at the edges called the JTE. The pixelation is on the n^+ layer, and pixels are separated by a $\approx$ 20 µm to 30 µm wide no-gain

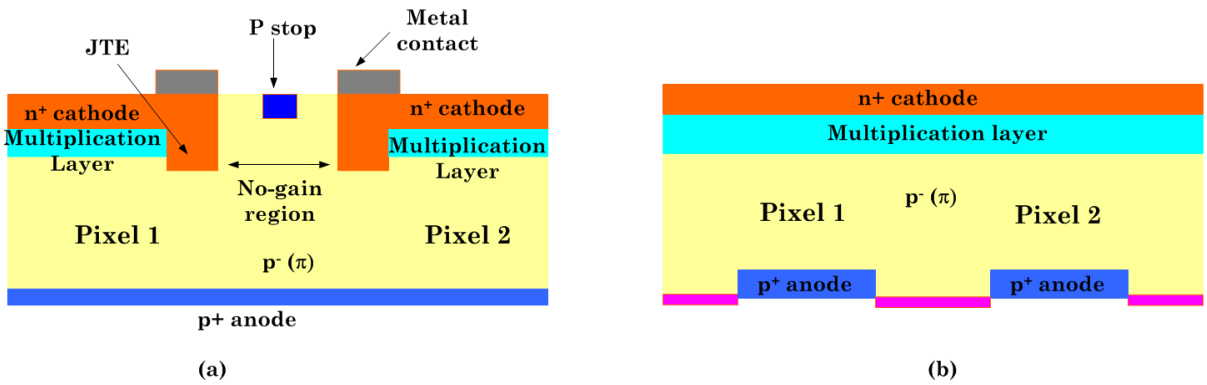

Figure 5.1: Structural difference between the LGAD and iLGAD. Pixelation is done on the n^+ layer for the LGAD (a), while for an iLGAD, the pixelation is on the p^+ layer for iLGAD.

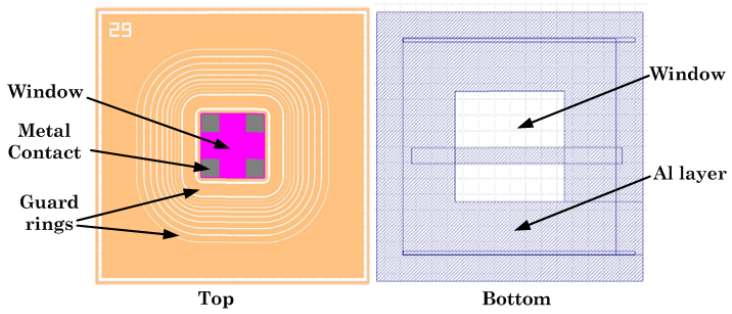

(a) LGAD

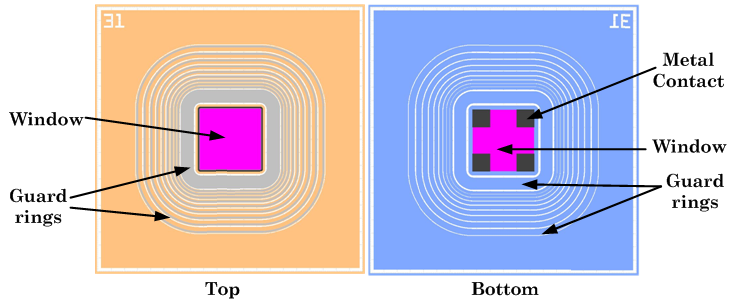

(b) iLGAD

Figure 5.2: Samples of fabrication mask of the LGAD and iLGAD devices. (a) The LGAD is fabricated with gain layer, metal contact and guard rings at the front-side while the back-side is just an Al metallisation with windows. (b) The iLGAD is fabricated with identical guard rings structures at the front and back-side, the gain layer is on the front-side but the metal contacts is on the back-side

region. In contrast, for the iLGAD, the pixelation is on the p^+. Both devices are configured for electron collection where the LGAD is biased with a negative voltage at the n^+ layer, while the iLGAD is biased with a positive voltage at the p^+ layer.

Figure 5.2 shows two examples of fabrication masks of the (i)LGAD detectors. The LGAD has a multiplication layer, metal contacts, and guard rings structure on the top and an aluminium metallisation with windows on the bottom. The iLGAD was fabricated with double-sided processing with identical guard rings on the top and bottom sides. The multiplication layer is on the top, whilst the p^+(pixel) and metal contacts are at the bottom. Both devices were fabricated using Micron Semiconductor Ltd process technology.

5.1.1 Electrical characteristics of 50 µm thick LGAD

Table 5.1: Electrical characterisation of the 50 µm thick LGAD showing the: Device list, their specifications, measurement methods and environment conditions

Device's Naming Convention:
3331-W_X_Y-Z = LGAD variant_Device ID
LGAD variant: 3331-W : W = 13, 16 & 19
Gain Implant Doping Concentration: 3331-19 (HIGH), 3331-16 (INTERMEDIATE) & 3331-13 (LOW)
Device ID : X_Y-Z : X = Location of the pad device on the wafer (North, South, East & West)
Y = Pad device number (1, 2, 4, 7, ...etc.)
Z = Index Number - Identifier for the same device number
Example: 3331-19_West_2-2 :
LGAD variant = 19 (HIGH doping concentration)
Location = West side of the wafer
Device number = 2 , Pixel size = 220 × 220 µm^2, JTE width = 10 µm JTE)
Index No = 2

LGAD variant	**Device ID**	**Device Description**	**Specifications: Pixel Size [mm^2], JTE width [μ m]**	**Measurement Methods & Environment Condition**
3331-19	West_2-2	LGAD	[0.22 × 0.22], 10	Current-Voltage (IV), Capacitance-Voltage (CV) Temperature [°C] = 24 ± 2 RH [%] = 40 ± 5
	West_7-2	LGAD	[0.50 × 0.50], 10	
	East_39-2	PIN (Control)	[1.00 × 1.00], 20	
3331-16	North_2	LGAD	[0.22 × 0.22], 10	
	North_4	LGAD	[0.50 × 0.50], 10	
	North_7-1	LGAD	[0.50 × 0.50], 10	
3331-13	2	LGAD	[0.22 × 0.22], 10	
	4	LGAD	[0.50 × 0.50], 10	
	7	LGAD	[0.50 × 0.50], 10	

Table 5.1 shows the device list and specifications of the 50 µm thick LGADs, testing methods and environment conditions used during the electrical characterisation of the LGADs. Figure 5.3 shows selected pad devices' current-voltage (IV) characteristics of the three LGAD variants. LGADs with the highest gain implant doping concentration (3331-19) breakdown at voltages ≈ 200 V, while the LGAD with the lowest gain implant doping concentration (3331-13) breakdown at higher voltages (≈ 280 V). This measurement makes sense since a higher doping concentration in the multiplication layer increases the electric

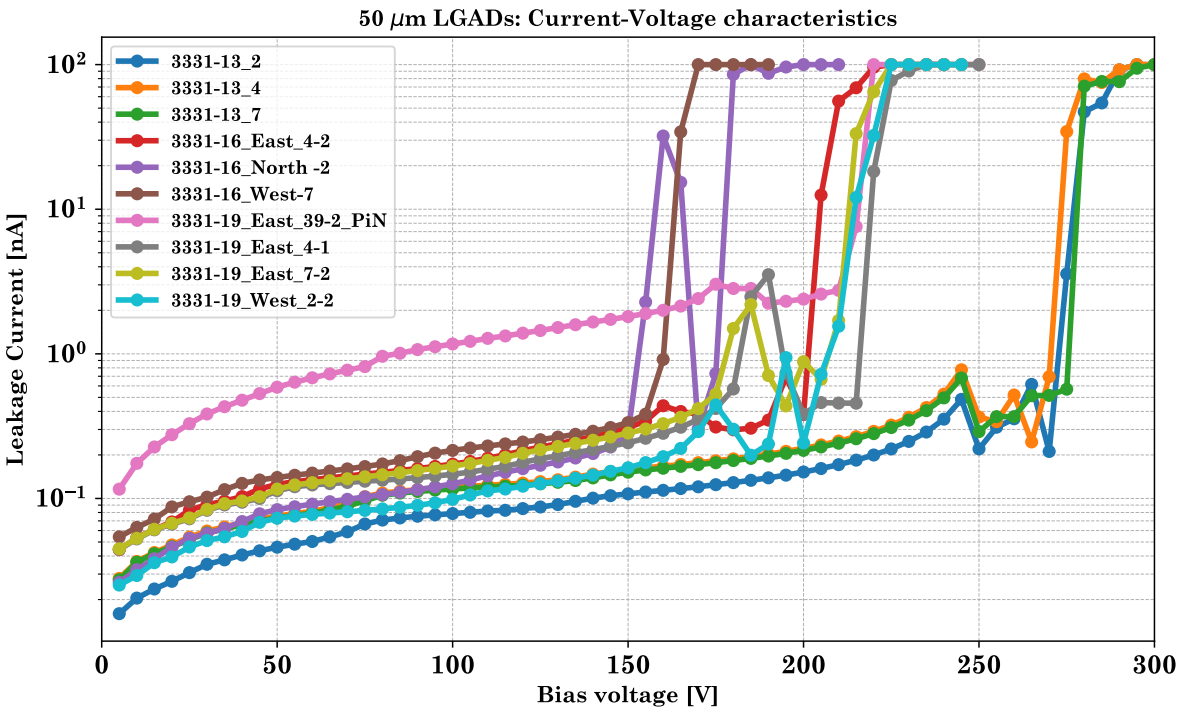

Figure 5.3: Current-Voltage (IV) characteristics of the 50 μm *thick LGAD devices. The LGAD with lower doping concentration in the multiplication layer (3331-13 variant) exhibit higher breakdown voltage compared to the other variants.*

field around this region. Hence, a lower bias voltage is required for the electric field to reach a critical value where the junction breaks down.

Micron Semiconductor Ltd process technology produced devices with a consistent breakdown voltage for these two variants. However, the intermediate gain implant doping concentration variant (3331-16) has inconsistent breakdown voltages ($\approx 150\,\mathrm{V}$ to $200\,\mathrm{V}$). This irregularity shows that precision control of the doping process is challenging. The IV measurement is conducted at room temperature; therefore, all variants show a characteristic *bump* in their IV curve just before the device breaks down. The characteristic bump in the IV curve is understood due to a localised breakdown that occurs prematurely because of the temperature effect. An IV measurement on the same devices by a group from the University of Birmingham showed that this bump disappeared when the IV was measured at lower temperatures ($< 10\,^{\circ}\mathrm{C}$).

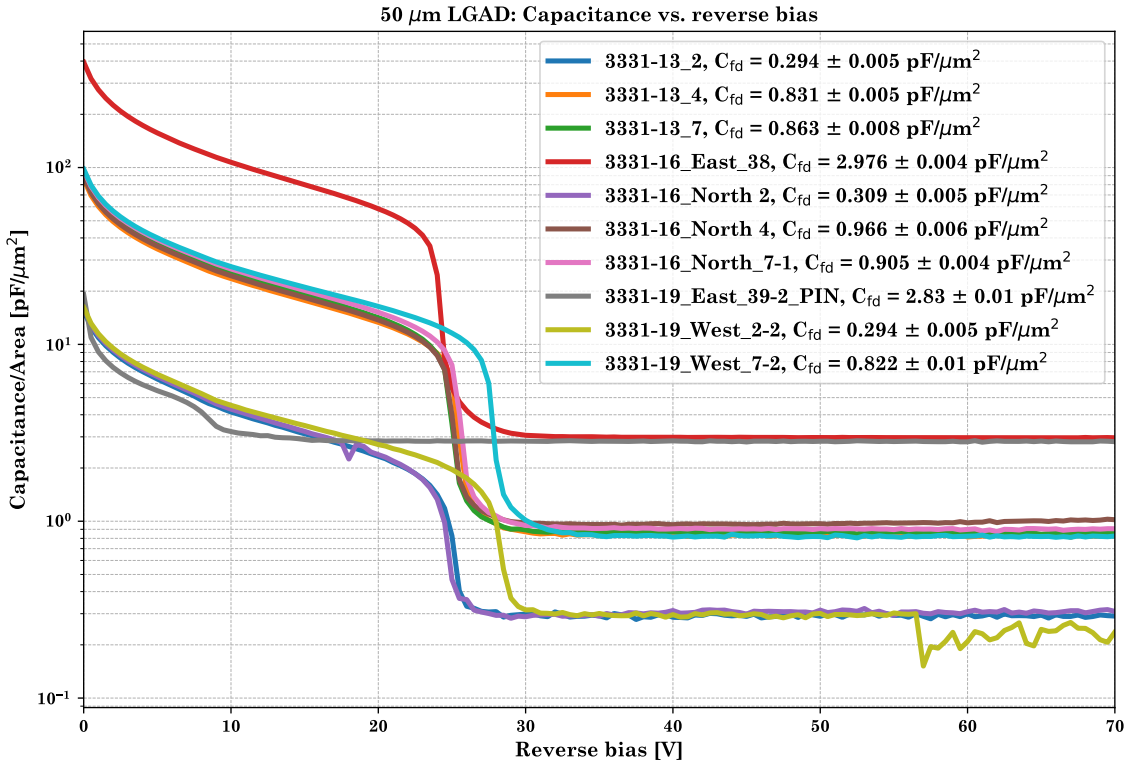

Figure 5.4: Capacitance-voltage (CV) characteristics of the three 50 μm *thick LGAD variants. Abrupt changes in capacitance at certain bias voltages were observed in LGADs. The voltage that triggers these changes, the V_{GL} depends on the gain implant doping concentration; LGADs with higher gain implant doping concentration require higher bias voltages.*

Figure 5.4 shows the plot of capacitance per unit area as a function of reverse bias for all LGAD variants. The depletion region starts to grow as the applied bias increases; thus, capacitance drops as the bias voltage increases. Since the multiplication region does not exist in PIN devices, a low applied voltage was sufficient to deplete the detector fully. Therefore, the capacitance in the PIN device (3331-19_East_39-2) quickly becomes stable when the device is fully depleted at voltage > 10 V. In contrast, the capacitance in LGADs gradually drops until the bias reaches the voltage that fully depletes the multiplication layer, V_{GL}. An abrupt capacitance change occurs when the multiplication layer is fully depleted, and the capacitance becomes invariant after the bulk is fully depleted. As seen from figure 5.4, the voltage that fully depletes the multiplication layer, V_{GL}, depends on

the gain implant doping concentration; the 3331-19 variant needs a higher voltage than the other two variants. The full depletion capacitance (C_{FD}) of the LGAD was estimated by finding the mean value of capacitances once the capacitance starts to plateau.

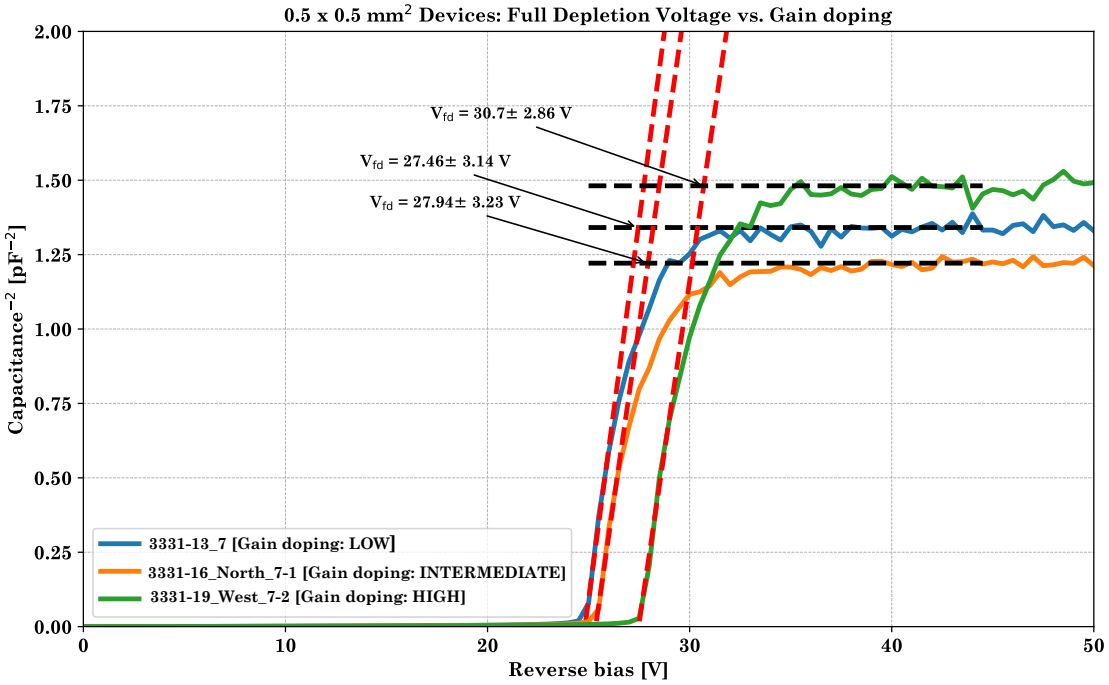

Figure 5.5: An example of the measured full depletion voltage (V_{FD}) in the 0.5 × 0.5 mm², 10 µm JTE three LGAD variants. The V_{FD} is scale up with the gain implant doping concentration.

Figure 5.5 shows an example of the measured V_{FD} in the 0.5 × 0.5 mm², 10 µm JTE LGAD from three LGAD variants using the method described in section 4.1. The LGAD variant with the higher implant doping concentration (3331-19) shows a higher V_{FD} than the other two variants. The effective doping concentration, N_{eff}, as a function of the depletion depth of three 0.5 × 0.5 mm², 10 µm JTE LGAD variants is shown in figure 5.6a. The peak doping concentration extracted from these plots for the 3331-19, 3331-16, and 3331-13 variants are 2.70E+16 cm^{-3}, 2.56E+16 cm^{-3}, and 2.37E+16 cm^{-3} respectively.

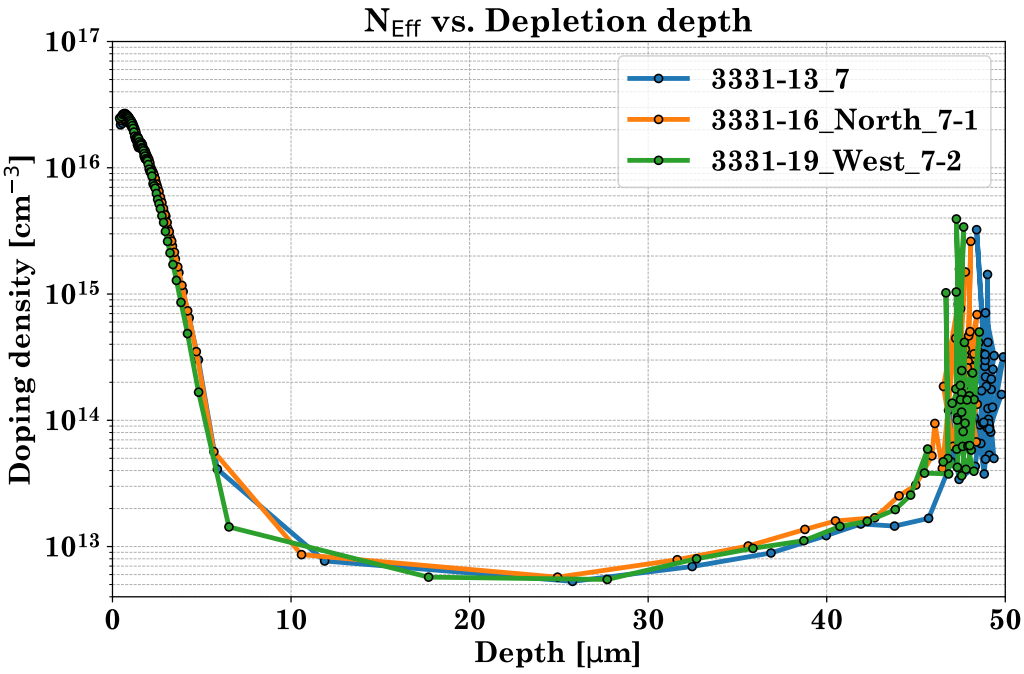

(a)

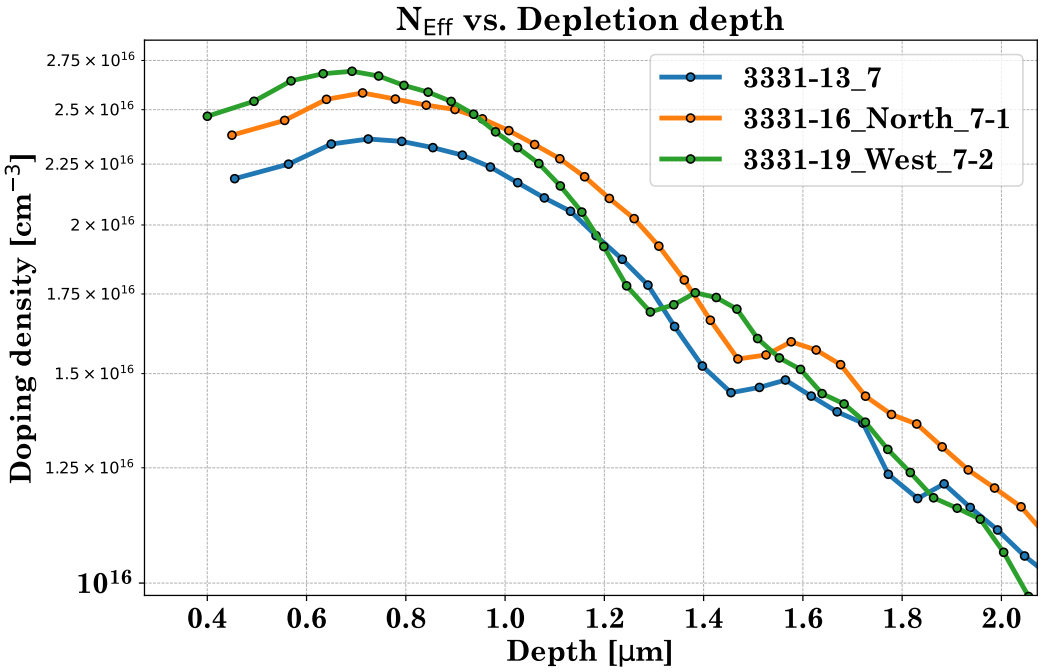

(b)

Figure 5.6: (a) The effective doping concentration, N_{eff}, as a function of depletion depth for three 0.5 × 0.5 mm^2, 10 μm JTE LGAD variants. (b) Zoomed section showing the peak of the doping concentration at the multiplication layer.

5.1.2 Electrical characteristics of 250 µm thick iLGAD

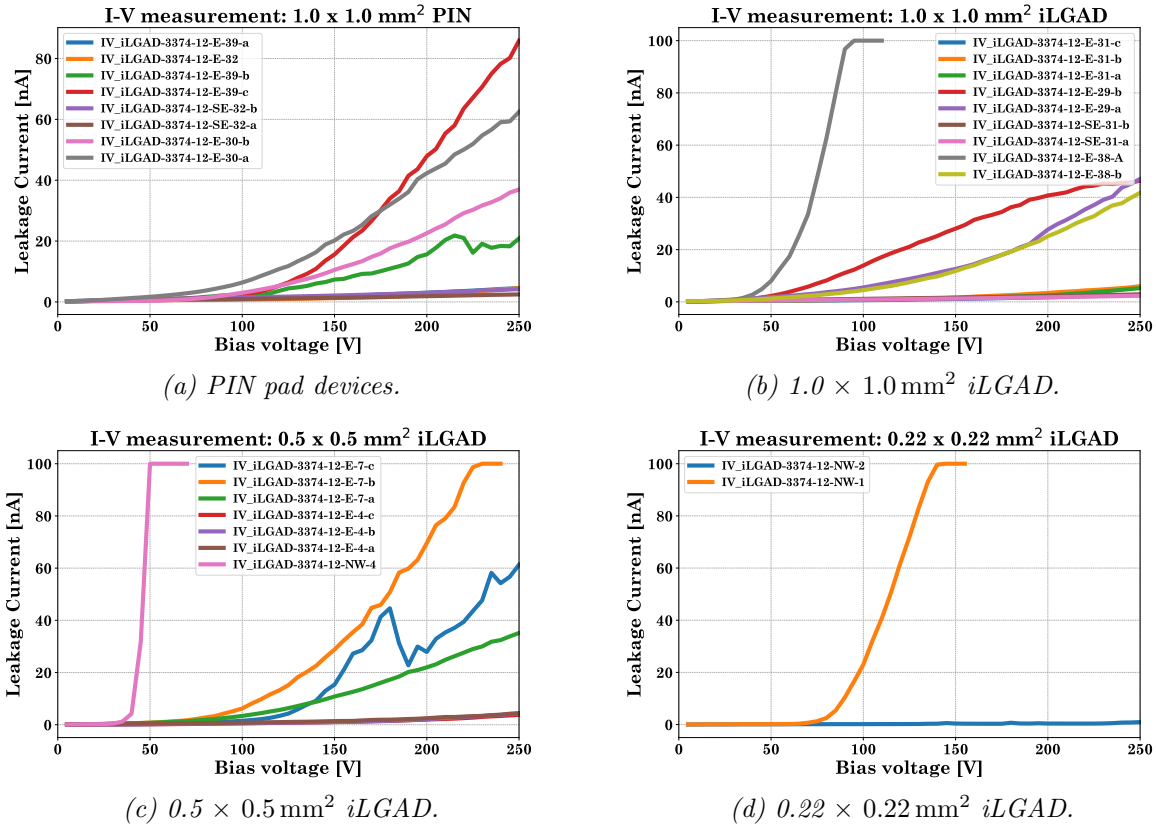

(a) PIN pad devices.

(b) 1.0 × 1.0 mm² iLGAD.

(c) 0.5 × 0.5 mm² iLGAD.

(d) 0.22 × 0.22 mm² iLGAD.

Figure 5.7: IV characteristics of pad devices from 3374-12 iLGAD wafer. The pad devices exhibit inconsistent breakdown voltage. A few devices break down below 100 V, some around 150 V, and some exhibit low and flat leakage currents despite being biased above 250 V.

Figure 5.7 shows the IV curves of the PIN and iLGAD pad devices from the 3374-12 wafer. Most tested pad devices demonstrate poor and sporadic IV characteristics that diverge from the typical IV characteristics of p-n junction devices. As shown in figure 5.7a, only four PIN devices demonstrate satisfactory IV characteristics. The leakage current in these four devices is low when the bias voltage is below 100 V, then steadily increases as bias increases but remains below the pre-set current limit of 100 nA at 250 V. The leakage current in the other three PIN devices remains unchanged despite being biassed up to 250 V.

The IV curves in figure 5.7b show that only three out of nine 1.0 × 1.0 mm² iLGAD devices

show satisfactory IV characteristics. One of the devices breaks down at around 50 V, while the other five show a flat IV curve up to 250 V bias voltage. Similar IV characteristics are observed for the $0.5 \times 0.5\,\mathrm{mm}^2$ iLGAD device (see figure 5.7c). Only two $0.22 \times 0.22\,\mathrm{mm}^2$ iLGAD devices were available for testing. Unfortunately, neither produced satisfactory IV characteristics. In general, it can be concluded that PIN devices or iLGAD pads from 3374-12 wafers start to show signs of breakdown at a bias voltage of around 100 V but do not enter full breakdown even when biassed to 250 V.

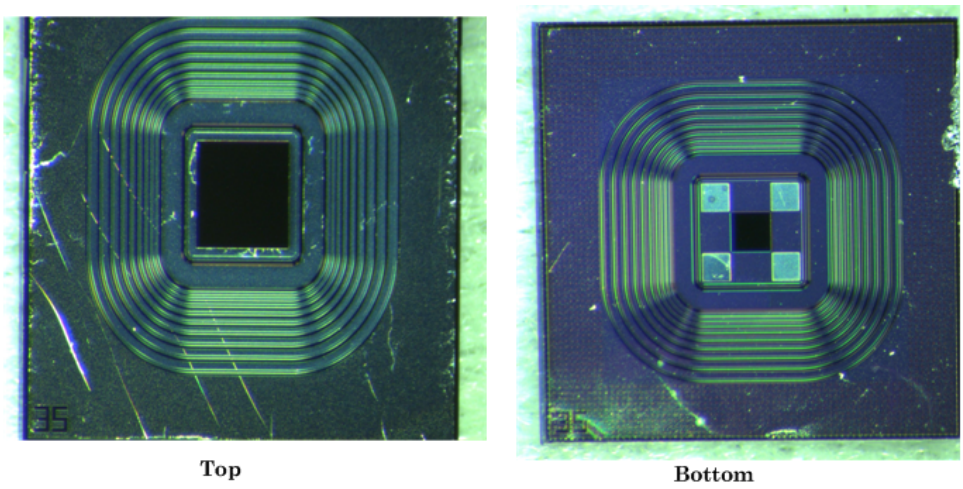

Figure 5.8: Photograph showing the glue residue covers the top and bottom of the iLGAD device.

Several tested devices demonstrated an abnormal IV characteristic, wherein the magnitude of the leakage current remains unchanged even when subjected to a high bias voltage. This anomaly is understood and is believed to be caused by insufficient electrical contact when the IV measurement is performed. A photograph of one of the iLGAD pad devices in figure 5.8 shows a greenish coating covering the top and bottom of the device. Upon investigation, it was found that the 3374-12 wafers had been coated with adhesive glue during an under-bump metallisation work on the pixelated iLGAD device that happened to be fabricated on the same wafer. The adhesive glue residue is difficult to remove. Despite being washed for 30 minutes each in an ultrasonic bath with acetone, isopropyl alcohol (IPA), and reverse osmosis water; residual glue remains. This non-conductive residual layer prevents good electrical contact during IV measurements. In general, the number of

devices with satisfactory IVs is low. Therefore, only a handful of devices are worth testing further with CV measurements.

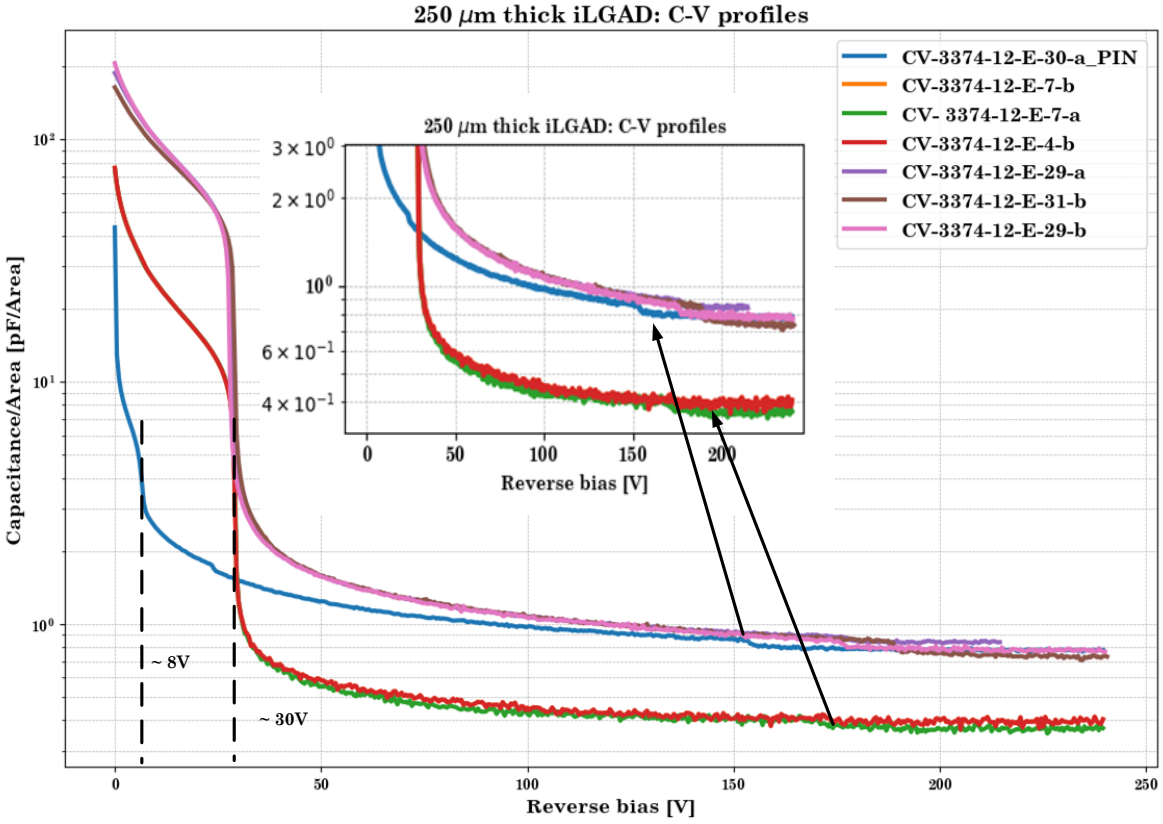

Figure 5.9: Capacitance-voltage (CV) characteristics of the 250 μm *thick iLGAD devices.*

Figure 5.9 shows the CV curves of the PIN and iLGAD pad devices with acceptable IVs. As the applied bias increases, the depletion grows, causing a decrease in the capacitance. The PIN device (3374-12-E-30-a) exhibits a double drop in its CV curve, one at around 8 V and another at around 150 V. The first drop is due to the depletion of the detector's bulk. The n^+ contact is fully depleted at a bias voltage of around 8 V. The abrupt drop in the capacitance occurs because the bulk quickly depletes to the edges of sensor thickness. The CV curve gradually decreases until it experiences another slight drop around a bias voltage of 150 V before finally stabilising at 250 V.

A similar trait is also observed in the CV curves of the iLGAD devices. However, the first

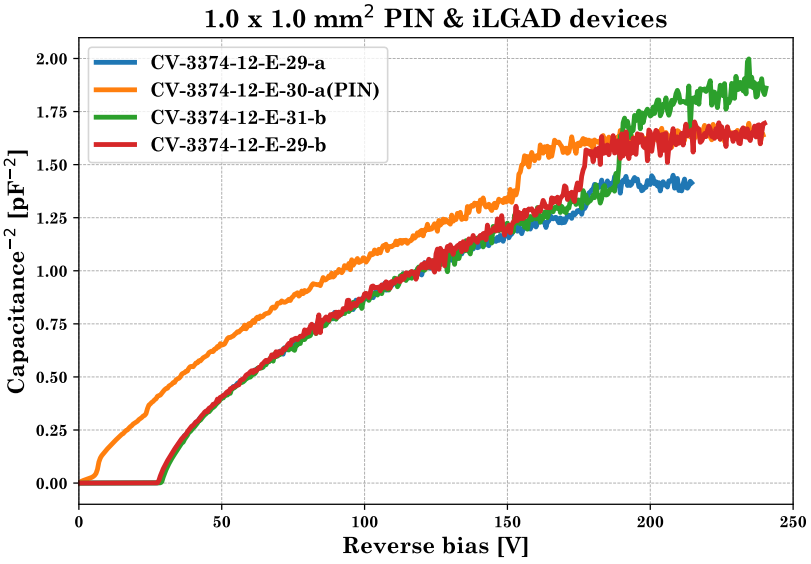

(a) 1.0 × 1.0 mm^2 PIN & iLGAD devices.

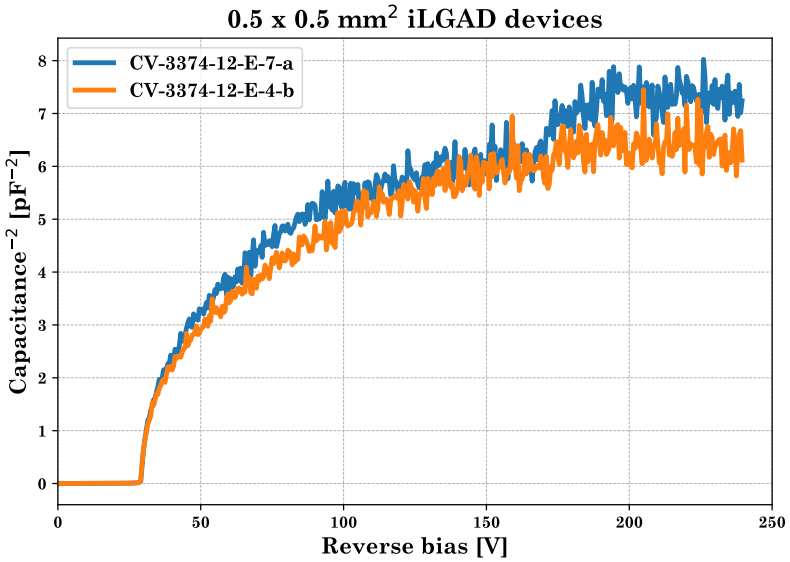

(b) 0.5 × 0.5 mm^2 iLGAD.s

Figure 5.10: A collection of C^{-2} as a function of bias voltage plots of the the PIN and iLGAD devices from the 3374-12 wafer. The $\frac{1}{C}$ increases with voltages after the applied bias reaches ≈ 30 V (≈ 8 V in PIN case), followed by another sharp increase around 170 V to 180 V (≈ 150 V in PIN case) before becoming constant. No clear linear region were observed in all plots.

capacitance drops appear at higher bias voltages of around 30 V, because the multiplication layer requires additional voltage to be depleted. Henceforth, the second capacitance drop is shifted to a higher bias voltage at around 170 V to 180 V. The nature of the second drop is unknown, as the double-drop feature in a CV curve is not typical of p-n junction

devices. The depletion area A calculated using the equation 4.4 with the capacitance value derived from the CV measurement and physical sensor thickness of 250 µm is larger than the specified pixel area. This discrepancy indicates that the depletion area expands beyond the active pixel of the device.

Figure 5.10 depicts $\frac{1}{C^2}$ as a function of the reverse bias for PIN and iLGAD devices from 3374-12 iLGAD wafer. The curves shown in figure 5.10 deviate from the $\frac{1}{C^2}$ curve of an ideal LGAD device, as no linear regions were observed. Hence, it was impossible to extract V_{FD} with the method described in 4.1. Nonetheless, based on the $\frac{1}{C^2}$ curve of the 0.5 $\times$ 0.5 mm^2 and 1.0 $\times$ 1.0 mm^2 devices, V_{fd} is roughly assumed to be above 170 V. This assumption is validated since the hybrid pixel detector with iLGAD sensor tested at the Diamond Light Source (DLS) synchrotron facility (see section 7.3) from the same wafer batch start producing signals around a bias voltage of 160 V.

5.1.3 Summary of the electrical characterisation of (i)LGAD pad detectors

Table 5.2: Summary of the IV and CV measurement of the 50 µm thick pad LGAD devices.

LGAD Variants	Pixel size, JTE [μm^2], [μm]	Breakdown Voltage [V]	Full Depletion Voltage [V] V_{FD}	Full Depletion Capacitance/Area C_{FD} [pF/μm^2]	
				Measured	Calculated (C= $\frac{\epsilon A}{W}$) W = 50 µm
3331-19_West_2_2	48.40E+3, 10	≈ 200	29.67 ± 5.27	0.294 ± 0.006	0.1
3331-19_West_7_2	2.50E+5, 10		30.70 ± 2.86	0.823 ± 0.008	0.517
3331-16_North_2	48.40E+3, 10	≈ 150 - 200	26.03 ± 2.02	0.308 ± 0.004	0.1
3331-16_North_4	2.50E+5, 20		27.12 ± 3.79	0.963 ± 0.004	0.517
3331-16_North_7_1	2.50E+5, 10		27.94 ± 3.23	0.905 ± 0.004	0.517
3331-13_2	48.40E+3, 10	≈ 280	26.28 ± 4.55	0.293 ± 0.006	0.1
3331-13_4	2.50E+5, 20		28.19 ± 4.11	0.831 ± 0.006	0.517
3331-13_7	2.50E+5, 10		27.46 ± 3.14	0.863 ± 0.006	0.517
PIN diode: 3331-19_East_39_2	1.0E+6, 20	≈ 200	15.91 ± 1.28	2.830 ± 0.011	2.07

A summary of the electrical characterisation of the 50 µm thick LGAD is shown in table 5.2. Regardless of pixel size, the 3331-19 variant was fully depleted at ≈ 30 V, while the

other variants are depleted at a lower voltage ($\approx 26\,\mathrm{V}$ to $28\,\mathrm{V}$). This observation suggests that the V_{FD} depends on the gain implant doping concentration and not pixel size. In general, the measured breakdown voltages were 5 to 9 times higher than the V_{FD}. Thus, all these LGADs can be biassed at higher voltages to achieve higher gains. The V_{FD} in the 3331-16 variant are consistent with each other and indicate that the gain implant doping concentration for both is very close. The capacitance at full depletion (C_{FD}) appears larger than the capacitance calculated using equation 4.4. Assuming the whole bulk was fully depleted, this difference suggests that the depletion area was larger than the active pixel area, perhaps extended closer to the first guard ring.

The complicated iLGAD fabrication process and defects due to post-fabrication blunders result in iLGAD devices with electrical characteristics that deviate from the typical characteristics of p-n junction devices. In general, the iLGAD pad detector showed increased leakage current at a bias voltage of around 100 V, but the leakage current remains below 100 nA at bias voltages up to 250 V. The full depletion voltage measured on the iLGAD device is estimated at above 180 V. The CV curve of the iLGAD device also shows a double-drop characteristic. The first drop occurs at around 30 V bias voltage, understood to indicate the depletion of the multiplication layer. However, the nature of the second drop, which occurs around 170 V to 180 V, still needs to be fully understood, and requires further investigation.

5.2 Gain measurement in 50 µm thick LGAD

Pad detectors from the three 50 µm LGAD wafer variants with good IVs and CVs were distributed among LGAD collaboration members. A few were selected for gain and timing measurement at the University of Glasgow. The LGAD device is glued onto an aluminium box to shield it against RF interference. The high voltage is biassed from the top side, while the bottom side is in contact with the aluminium metal. The aluminium box be-

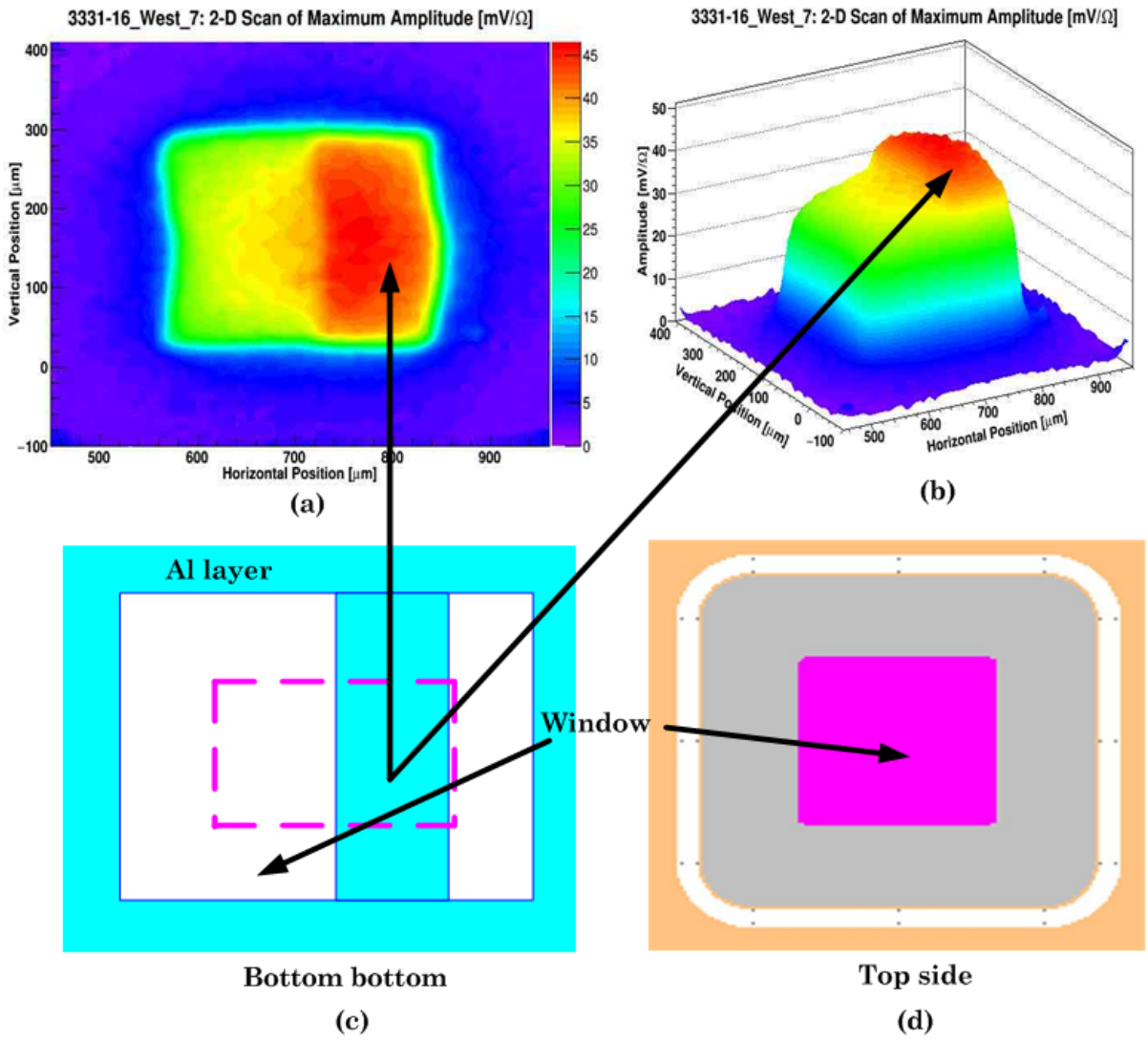

Figure 5.11: The 2D and 3D TCT responses with infrared laser (top) and the bottom and top metallisation layer (bottom) of the 0.5 × 0.5 mm² LGAD devices.

comes the ground reference. This assembly is called the Device Under Test (DUT) (see figure 4.6b), and it has a small window opening for laser irradiation on the top side. The multiplication layer is fabricated on the top side of the LGAD. Therefore, the laser must be able to penetrate beyond the multiplication layer in order for this LGAD to produce signal gain. Thus, this setup only makes gain measurements with long wavelength lasers such as the 1064 nm infrared.

A preliminary test on several LGAD devices uncovers that certain areas in the LGAD de-

vice produce high output signals. The 2D pixel response of the $0.5 \times 0.5\,\mathrm{mm}^2$ pixel, 20 µm JTE LGAD in figure 5.11a shows an example of this anomaly. Here it can be seen that the right section of the LGAD produces a high response. Upon investigation, the anomaly is understood to be due to the reflection of the infrared laser. An infrared photon produces ionisation tracks along its path as it transverses through the LGAD thickness, and it is reflected when it hits the aluminium layer at the bottom of the LGAD. The reflected infrared photon produces additional ionisation, thereby increasing the total response. As seen from the bottom side of the LGAD in figure 5.11c, the high response section coincides with the aluminium metallisation layer at the bottom side of the LGAD. This reflection must be avoided to obtain an accurate gain measurement. Therefore, a fine 2D raster scan is performed to find a reflection-free area before making a gain measurement. This position will be fixed for the duration of the gain measurement.

Figure 5.12 depicts an assortment of plots derived from the TCT voltage scan. The DUT's pulse is $\approx 4\,\mathrm{ns}$ delayed because the laser pulse travels a longer distance through the optical attenuator before reaching the DUT (see figure 5.12a). The measured charge as a function of bias voltage plot from the TCT voltage scan is depicted in figure 5.12b; the LGAD produces output once the gain layer starts depleting and then increases proportionally with bias voltage once the LGAD is fully depleted. The integral charge of the PIN device (figure 5.12c) rose quickly at low bias voltage and remained constant after it fully depleted. Throughout the TCT measurement, a slight variation in laser output was observed as a change in integral charge on the Beam Monitor (figure 5.12c). Laser output variation is minimised by using the normalised charge rather than the raw integral charge. The normalised charge as a function of the bias voltage is shown in figure 5.12d. As mentioned in the section 4.2.3, the gain was calculated as the ratio of the normalised charge LGAD to the PIN reference.

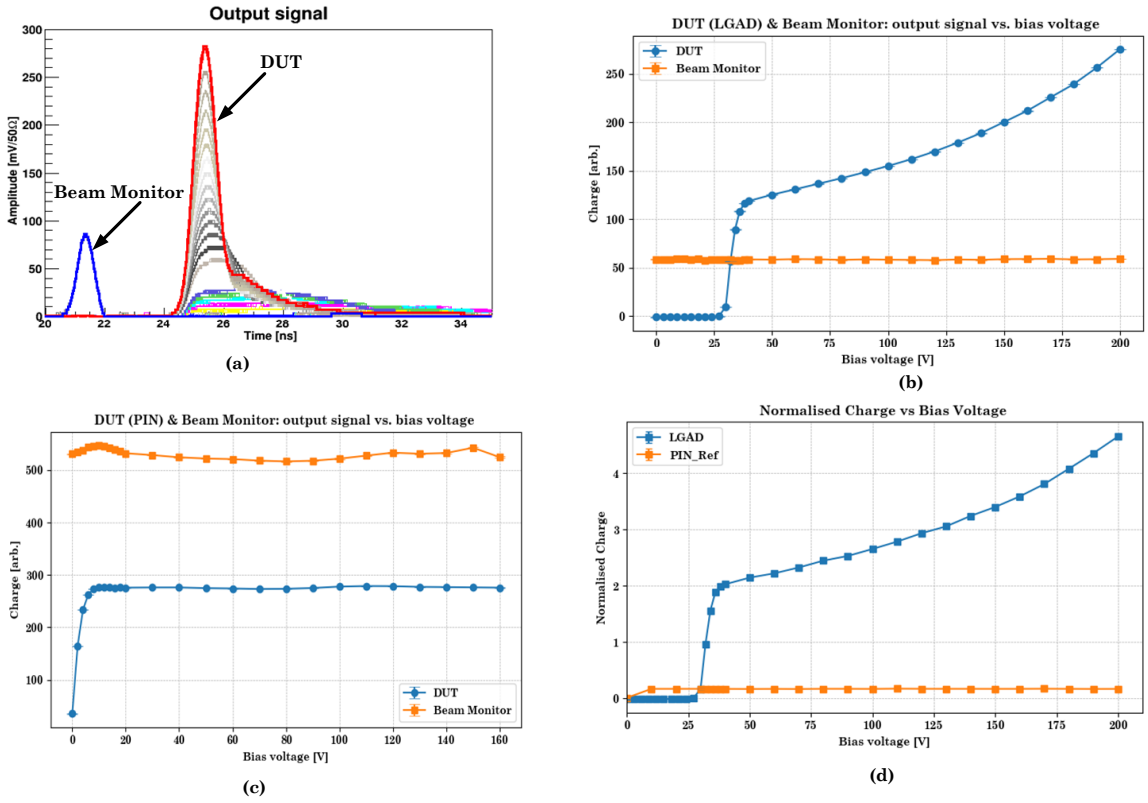

Figure 5.12: A collection of plots extracted from TCT_Voltage Scan. (a) The output signals of the DUT and Beam Monitor, (b) The integral charge of the DUT, (c) the integral charge of the PIN reference, and (d) the normalised charge.

5.2.1 Gain variations on implant dose and pixel size

The gain in LGAD devices was investigated as a function of doping concentrations by measuring gains in similar pixel sizes LGAD but with different gain implant doping concentrations. For this task, a pair of $0.5 \times 0.5\,\mathrm{mm}^2$ devices, each with JTE width 10 µm and 20 µm, were selected from the LGAD with high (3331-19) and intermediate (3331-16) gain implant doping concentrations. The influence of the doping concentration on the gain is shown in figure 5.13. The results are consistent with the theory as the LGADs with high doping concentration (3331-19) produce higher signal gain. Regardless of the width of the JTE, both devices from the 3331-19 show identical gain up to an applied bias voltage of 200 V. This observation suggests that the JTE's width has little effect on the gain in LGAD devices of this size. Unfortunately, no measurement was performed

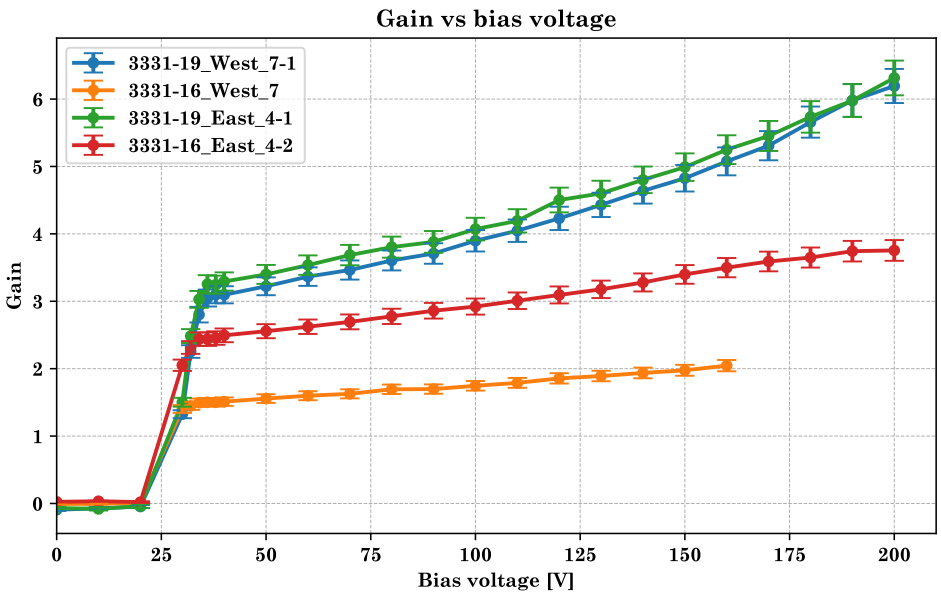

Figure 5.13: Gain in LGAD with pixel size of 0.5 × 0.5 mm^2 as a function of gain implant doping concentration. Both 3331-19 devices produced a consistent gain and were not affected by the JTE's width, whilst the signal gain in 3331-16 devices appeared JTE width dependent.

on the smaller pixel (0.22 × 0.22 mm^2) device from the 3331-16 and 3331-13 variants to corroborate this observation. It would be worth doing this measurement since the width of the JTE affects the gain in small pixel LGAD according to the study in [25].

Signal gain of a factor greater than 6 at an applied bias voltage of 200 V was obtained for both 3331-19 devices. The gain in the 3331-16 devices seems dependent on the pixel size, but further investigation found that the measurement in the 3331-16_East_4-2 device was flawed. The infrared laser was positioned in the LGAD area with infrared reflection issues. This finding explains why the gain in this device is one order of magnitude higher than the gain in 3331-16_West_7. The gain measurement in device 3331-16_West_7 stopped at 160 V because this device starts breaking down above this voltage. Nevertheless, plots in figure 5.13 are conclusive enough to infer that gain depends on the doping concentration. The gain in the 3331-13 variant is assumed to be much lower because the doping concentration is low in this variant. For this reason, this thesis does not investigate the gain in the 3331-13 variant.

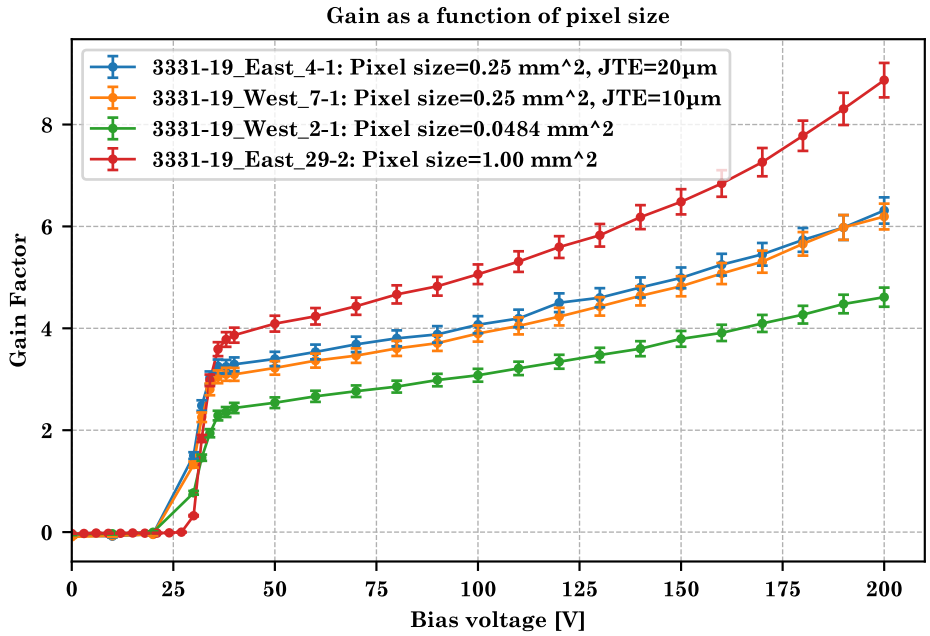

Figure 5.14: Gain in device 3331-19 as a function of pixel sizes. The size of the device influences signal gain where a larger pixel produces a higher signal gain.

The plot in figure 5.14 shows the gain variation as a function of the pixel sizes. This plot was derived from the gain measurement of four devices from devices with different pixel sizes from the 3331-19 variant. The gain varies significantly with pixel size, consistent with the small pixel effect described in [25]. At a bias voltage of 200 V, a gain of a factor around 8, 6 and 4 is measured for the $1.0 \times 1.0\,\mathrm{mm}^2$, $0.25\,\mathrm{mm}^2$, and $0.0484\,\mathrm{mm}^2$ devices.

5.2.2 Gain as a function of temperature

Temperature affects the gain in LGAD through the saturated velocity [82] and the impact ionisation rate, α. As the temperature drops, the saturation velocity rises. Hence, charge carriers travel greater distances at lower temperatures before experiencing lattice collisions. According to [83], the ionisation rate strongly depends on temperature and is greater at lower temperatures. The gain was measured using an infrared laser at 1064 nm wavelength. The absorption length of a photon at this wavelength is in the order of $\approx$ 1 mm [84]; thus, the infrared should traverses the entire 50 µm thickness. However, photon

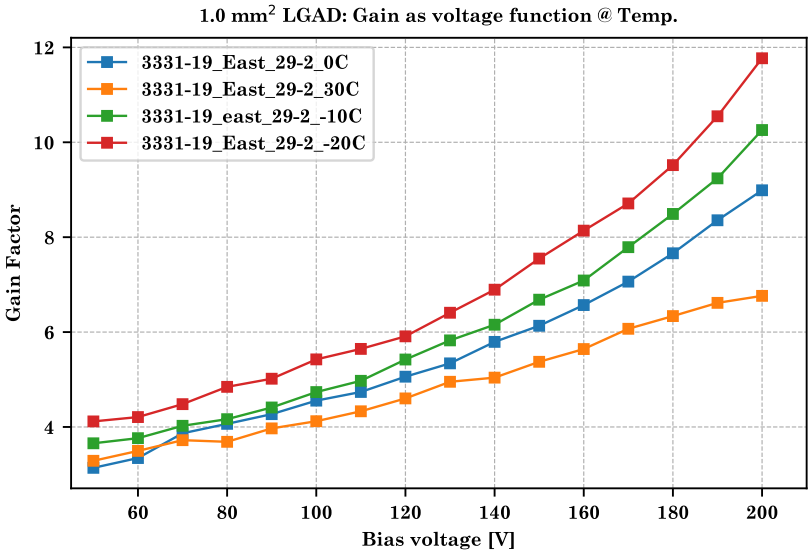

(a) Gain as a function of bias voltage at different temperatures.

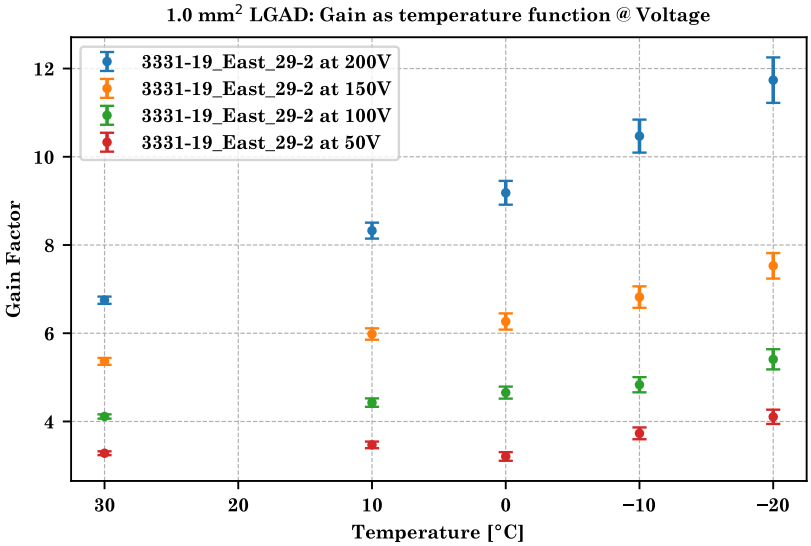

(b) Gain as a function of temperature at different bias voltages.

Figure 5.15: Gain variation in the 3331-19 LGAD variant as a function of temperatures and applied voltages. (a) Gain vs voltage for different temperatures, and (b) gain vs temperatures for different applied bias voltages

absorption is temperature-dependent, with absorption being lower at lower temperatures [85]. Therefore, the gain must be calculated using the LGAD and PIN reference charges measured at the same temperature. The 3331-19 variant has a significantly greater gain and is likely to show measurable gain after being subjected to neutron or proton radiation damage. So, only the devices from 3331-19 are chosen for the temperature-dependent gain

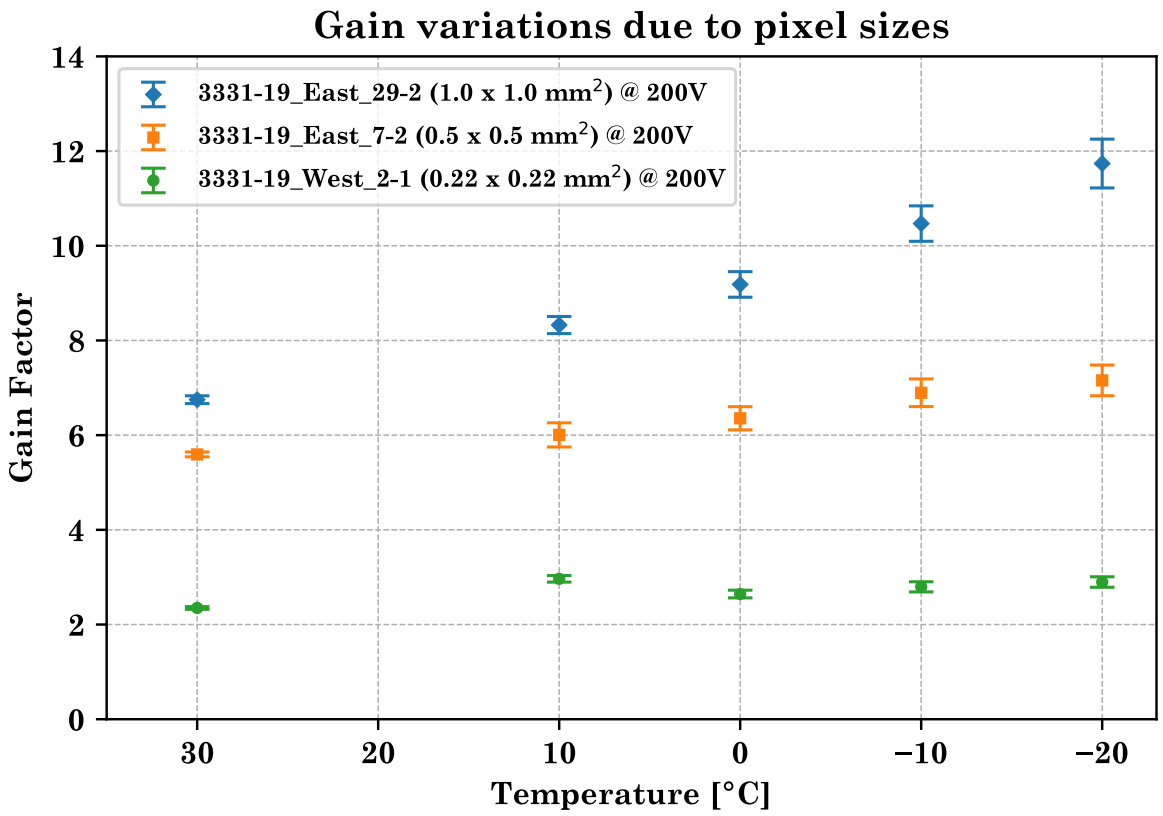

Figure 5.16: Gain as a function temperatures for devices with different active pixel size.

measurements.

Figure 5.15a and figure 5.15b show plots of gain as a function of bias voltages and temperatures for the 1.0 × 1.0 mm^2 device (3331-19_East_29-2). Both plots demonstrate temperature dependence, where the gain factor increases with decreasing temperature. The plot in figure 5.16 shows gain factors measured at an applied bias voltage of 200 V at temperatures of 30, 10, 0, -10, and -20 °C in the three LGAD devices of various pixel sizes from 3331-19 variant. The gain factor in the larger-pixel LGADs (1.0 mm^2 and 0.25 mm^2) shows a significant temperature dependence, but the gain factor in the smaller-pixel LGAD (0.0484 mm^2) does not change significantly. The plot in figure 5.16 also indicates that the size of the LGAD affects the gain factor, where larger-pixel LGAD exhibits a higher gain factor than the smaller-pixel LGAD.

Work in [24] and [25] explains how the pixel size affects the gain in the LGAD devices. According to this work, the width of the JTE reduces the fill factor in the LGAD device. Distortions in the electric field near the JTE structure cause electrons to move towards the JTE instead of the multiplication layer where the impact ionisation occurs. This effect is called *small pixel effect*, and it becomes severe for small pixel LGAD because the JTE and the multiplication layer are almost the same width. This effect causes the small-pixel LGAD device to produce less gain. Moreover, For the LGAD devices investigated here, the *reflection area* (see figure 5.11) is much closer to the centre of the pixel for the smaller-size LGAD. Therefore the laser has to be positioned slightly away from the centre of the pixel. This arrangement contributes further reduction of the gain measured in the small-pixel LGAD.

5.2.3 Summary of the gain measurement

Table 5.3: Result of gain measurement as a function of temperature for three devices from 3331-19 variant

Device ID	Pixel size [mm^2]	Gain at T = 30 °C	Gain at T = −20 °C	Increment ΔT = 50 °C [%]
3331-19_East_29-2	1.0 × 1.0	6.75 ± 0.09	11.74 ± 0.52	74
3331-19_East_7-2	0.5 × 0.5	5.59 ± 0.05	7.02 ± 0.13	26
3331-19_West_2-1	0.22 × 0.22	2.35 ± 0.03	3.14 ± 0.14	34

Table 5.3 summarises the result of the gain measurement at temperatures of 30, 10, 0, -10, and -20 °C on the 3331-19 LGAD devices. The gain in the LGAD devices shows temperature dependence, where the gain factor in the 1.0 mm^2 device increases ≈ 75 % for a variation of 50 °C. The JTE structure causes the LGAD device to produce a low fill factor; thus device's pixel size also affects the gain. These three devices were then sent to the University of Birmingham for irradiation with proton and neutron sources. Post-irradiation gain measurement, however, is beyond the scope of this thesis.

5.3 Chapter summary

The gain doping concentration in the multiplication region affects the electrical properties of the 50 µm thick LGADs. Higher doping concentrations increase the full depletion voltage, in line with Equation 2.19. While this enhances carrier multiplication due to a stronger electric field, it reduces the breakdown voltage. Thus, an optimal doping concentration balances the desired gain and sufficient breakdown voltage. In contrast, assessing similar effects in iLGADs has proven challenging due to their inconsistent performance, likely attributable to the complexities involved in their manufacturing processes.

In 50 µm thick pad LGADs, gain increases with higher bias voltages, and a higher doping concentration enhances achievable gain. The JTE structure acts as a dead region, thereby reducing the fill factor of an LGAD. Distortions in the electric field at the edges of the JTE attract electrons to this area instead of the multiplication region, leading to a decrease in overall gain. This effect is particularly pronounced in LGADs, where the multiplication width is comparable to the JTE width. Gain measurements show that the influence of the JTE is negligible in larger LGADs (1.0 mm × 1.0 mm), but studies have shown that it becomes more significant in smaller devices. Gain in the LGADs increases with decreasing temperature, a trend consistent with prediction in Subsection 2.1.4.

In summary, increasing the doping concentration enhances the gain in LGADs. However, this adjustment reduces their operational range. Operating LGADs at lower temperatures allows for achieving a higher gain.

CHAPTER 6

Characterisation of hybrid pixel detectors with XRF and radioisotopes

Two hybrid pixel detector prototypes have been developed in the past: 5 mm thick, 110 µm-pitch CZT, each bonded to Timepix and Timepix3 readout ASICs. Both detectors are fully characterised, and a considerable amount of γ-rays data were taken with these detectors, but their potential applications are yet to be explored. This chapter investigates the spectroscopic performance of both prototypes and explores their potential as detectors in a single-layer Compton camera system. Accurate energy calibration and the precise measurement of a signal's arrival time are crucial in Compton camera systems. The Timepix3(Timepix) measure incident particles' energy as ToT values, in which this quantity needs to be converted to energy units. The time-walk anomaly in Timepix3 introduces errors in the arrival time measurement. Therefore, hybrid pixel detectors utilising Timepix(Timpix3) as readouts require ToT calibration and time-walk correction.

This chapter describes the characterisation of the hybrid pixel detectors with XRF and radioisotope sources. Section 6.1 describes the materials and experiments setup, which

include the global ToT calibration of silicon sensor at the University of Glasgow and the per-pixel ToT calibration and time-walk correction of LGAD sensor at IEAP[1], Czech Technical University in Prague. Section 6.2 explains the analysis of the data. Section 6.3 discusses the global ToT calibration for silicon sensor, while Section 6.4, and Section 6.5 cover the per-pixel ToT calibration and the time-walk correction respectively, specifically for the LGAD sensors. The last section presents and discusses the spectroscopic performance of the two hybrid pixel detectors with CZT sensors.

6.1 Materials and experiment setup

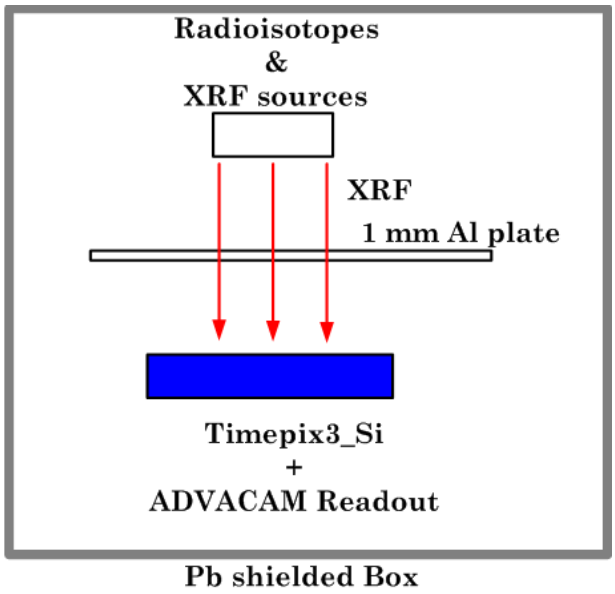

Figure 6.1: The experiment setup for ToT calibration at the University of Glasgow.

Figure 6.1 shows the experiment setup and materials used for the ToT calibration of hybrid pixel detectors at the University of Glasgow. The experiment is conducted inside a light-tight, lead-shielded enclosure to minimise background interference. Calibration sources used are 59.54 keV γ-rays and XRF photons produced through the excitation of several metal targets by the same γ-rays. Three hybrid pixel detectors listed in table 6.1 are used in the experiment. All measurements are acquired with the AdvaDAQ USB

[1]Institute of Experimental and Applied Physics, Czech Technical University in Prague, Husova 240/5, 110 00 Prague 1, Czech Republic. https://www.utef.cvut.cz/ieap

Table 6.1: Materials and the Timepix3 acquisition mode used for acquiring the data for ToT calibration.

XRF and Radioisotope sources	Energy [keV]	Hybrid pixel detector	Acquisition mode
XRF_Cu	8.05	Timepix3 + 300 µm thick, 55 µm-pitch silicon sensor (HV bias = 100 V	Event + iToT 10000 frames
XRF_Rb	13.40		
XRF_Mo	17.52	Timepix + 5 mm, 110 µm-pitch CZT (HV bias = −1100 V)	
XRF_Ag	22.16		
XRF_Ba	32.19		
XRF_Tb	44.48	Timepix3 + 5 mm, 110 µm-pitch CZT (HV bias = −1100 V)	
^{241}Am	59.54		

3.0-based readout interface and PIXet pro software, and the acquisitions are in Timepix3 Event + iToT mode with 10000 data frames for each calibration source. The hybrid pixel detector with silicon sensors is used to get training data for the global ToT calibration. The hybrid pixel detector with CZT sensors lacks the resolution to measure low energy photons. Therefore, only photons of energy above 20 keV are selected for evaluating the spectroscopic performance of the CZT detectors.

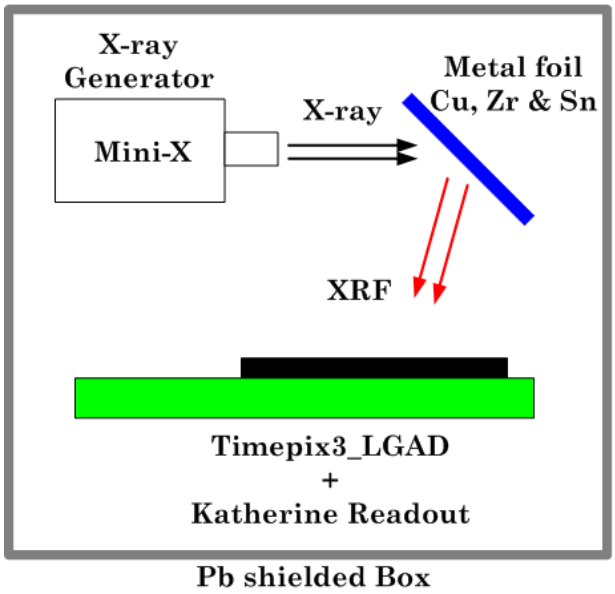

Figure 6.2: The experiment setup for per-pixel ToT calibration at IEAP.

Table 6.2: Calibration sources, acquisition parameters, readout system and calibration tools for the per-pixel energy calibration & time-walk correction

Calibration Sources		Energy[KeV]	Total hits for all pixels	Readout system, DAQ Software & Calibration tools
AMPTEK Mini-X tube V = 36 V, A = 100 µA	XRF_Cu	8.04	> 12 M	Readout: Katherine readout DAQ software: Burdaman Calibration tools: Katherine-Detector Tools for Timepix3
	XRF_Zr	15.77	> 12 M	
	XRF_Sn	25.71	> 40 M	
^{241}Am		59.54	> 80 M	

Per-pixel energy calibration and time-walk correction were carried out according to the procedures described in subsections 3.4 and 3.5 at IEAP, Czech Technical University in Prague. The experiment setup is shown in figure 6.2, where the acquisition is made with the Kathrine readout-Burdaman software[86], and the detector is a 250 µm thick, 110 µm-pitch LGAD bonded to Timepix3 readout ASICs. Table 6.2 shows the calibration sources and acquisition parameters used for the experiment. A portable X-ray device, the AMPTEK Mini-X[2], is used as an X-ray source to excite the XRF photons from metal targets.

The data acquisition procedure begins by taking the Timepix3 THL scan data (lower level threshold) for the three XRF sources using the Timepix3 DAC scan function. Katherine's readout system saves this data as comma-separated values (CSV) in the Burdaman software *log-folder*. The data must be renamed after completing the DAC scan because it will be overwritten when the next scan is performed. The THL scan data find the reference points for the THL to energy conversion and are used in the calibration coefficients extraction. The data acquisition for calibration and time-walk correction uses the same setup as the THL_scan. However, the acquisition is made in the data-driven, ToT + ToA mode for three XRF energies and the 59.54 keV γ-rays from ^{241}Am decay. The acquisition time is set to get enough statistics for the calibration, which is indicated by the number of pixel hits (see table 6.2).

[2]A portable X-ray device from AMPTEK Inc. (www.amptek.com)

6.2 Data analysis for ToT calibration and time-walk correction

Data from measurements in Glasgow were analysed using analysis scripts developed to process data acquired with the ADVACAM DAQ system. In contrast, data from measurements at IAEP is processed using analysis tools developed by IAEP. The following subsections describe the analysis methods used in both experiments.

6.2.1 Measurement at Glasgow

Data from XRF and radioisotopes measurements at the University of Glasgow are analysed by an analysis script that is based on Python 3 IDE implemented in *miniconda* distributed *Eclipse IDE* workspace or in the *VSCode* platform. The analysis script utilises various Python 3 *functions* and *classes* from the *medipix-analysis* GitLab repository that had been developed over the years to process Timepix(Timepix3) data acquired with the ADVACAM, AdvaDAQ and PIXet pro software. Data handling, clustering and processing were implemented mainly with *NumPy*, *Pandas* and *Scipy* packages. The *Matplotlib* is used for data visualisation and plotting, and the *LMFIT* [87] for regression and fitting.

Figure 6.3 shows a flow chart for analysing the hybrid pixel detector data using the said analysis script. The *MedipixFileOpener* function performs data handling and extracting the essential information (ToT, ToA, FToA, and pixel coordinates) and converts them into a list of Python dictionaries. These dictionaries are compiled into pseudo-frames and combined the pseudo-frames into a single super-frame of 256 $\times$ 256 matrices, dubbed *myFrames*. The basic pixel images, such as the raw pixel map or HitMap for binned frames, can be drawn directly from *myFrames*. The *ClusterProcessor/ClusteringEngine* calculates and combines the ToT value as the summed ToT of all pixels within the cluster. The centroid of the interaction is assigned to the pixel with the highest ToT value. The

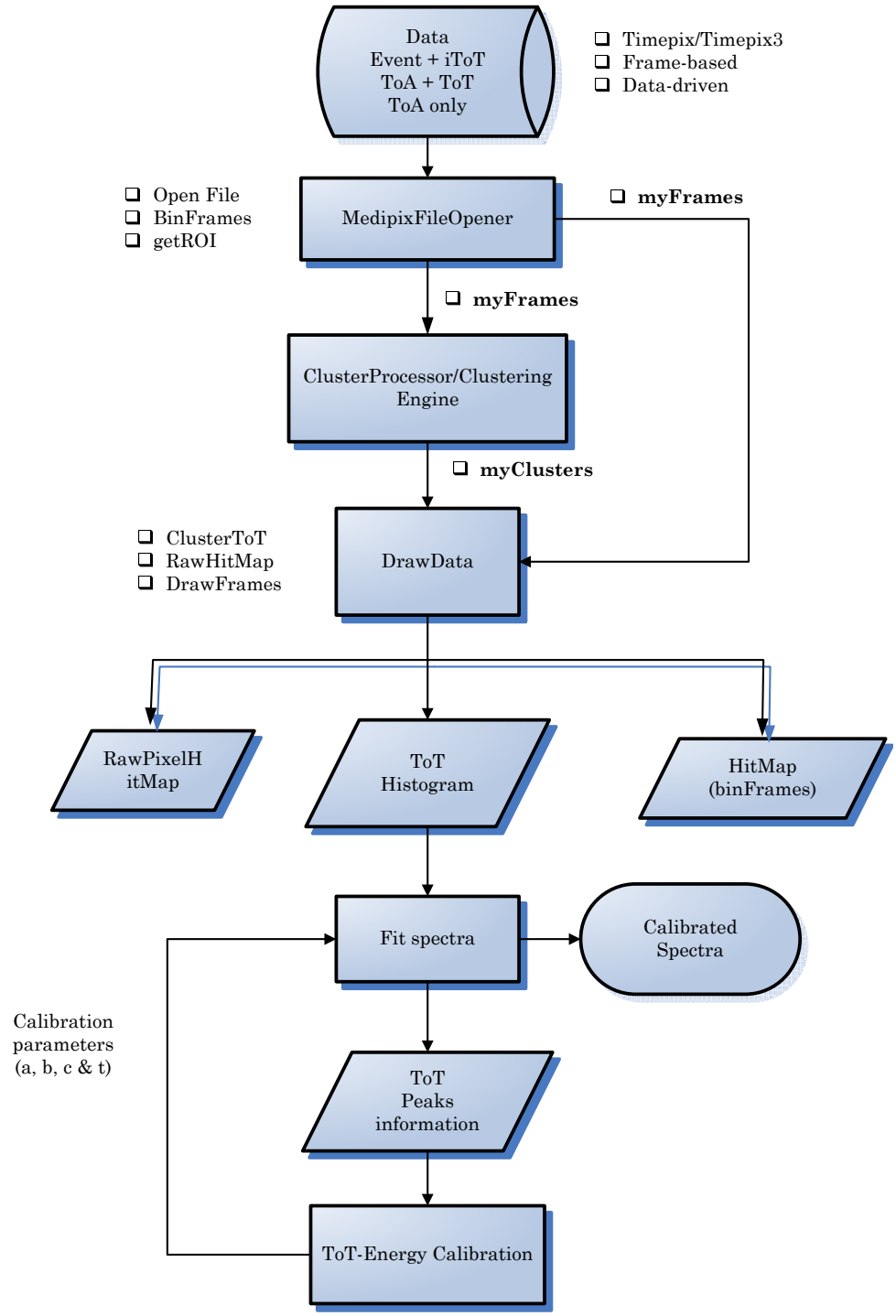

Figure 6.3: Flow chart of processing hybrid pixel detector data using the developed analysis code.

myCluster sorted the information (ToT, ToA, fToA and pixel coordinates) and saved it as a Python list called *myCluster*. The *DrawData* function plots the histogram of ToT, and a Gaussian fit extracts the spectral ToT of interest. The ToT calibration coefficients (*a, b,*

c, and t) are extracted from the plot of spectral ToT as a function of energy by surrogate function fit described in equation 3.1.

6.2.2 Per-pixel ToT calibration and time-walk correction

The *Katherine-Detector Tools for Timepix3* calibration tool was used to find the coefficients of the per-pixel ToT calibration and time-walk correction. The analysis begins by finding the corresponding XRFs peak energies from the THL_scan data. These peaks are used to obtain the THL to energy curve from the XRF peaks energy as a function of the THL plot. This curve links the Timepix3 THL value to the energy reference point, which becomes the arbitrary calibration point for the surrogate function fit during the coefficients extraction.

The single-pixel ToT peak for every calibration data is extracted via a Gaussian fit, and the single-pixel ToT peaks obtained from the said process are plotted as a function of their energy. The arbitrary calibration point is added to the plot, and a non-linear surrogate function fit extracts the single-pixel calibration coefficients (a, b, c, and t). The process is repeated to obtain the calibration coefficients for every pixel in the detector volume. The per-pixel ToT calibration process produces four separate plain text output files corresponding to the four calibration coefficients. The ^{241}Am data are used to obtain the time-walk correction coefficients (a, b, E_0, and d) described in equation 3.2. Only the cluster with a minimum size of 2 pixels and that carries energy between 29.2 – 30.50 keV are considered for the analysis. The energy calibration and the time-walk correction coefficients are saved as a plain text file (.txt) for future measurement.

6.3 Global ToT calibration

Figure 6.4 shows samples of ToT spectra acquired from the calibration sources. The XRF peaks are mostly distinguishable for fitting except for the XRF peak of Rubidium (Rb) due

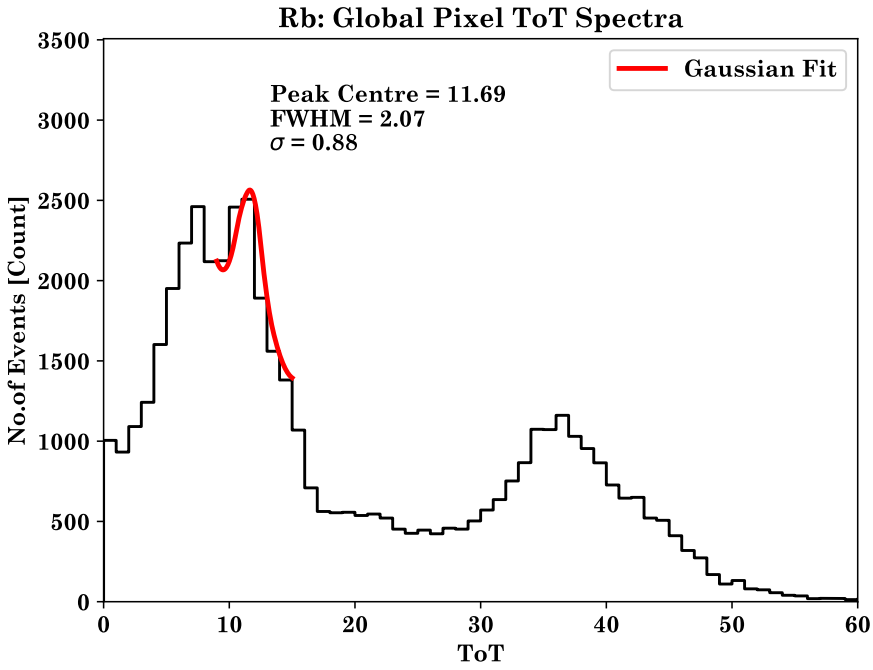

(a)

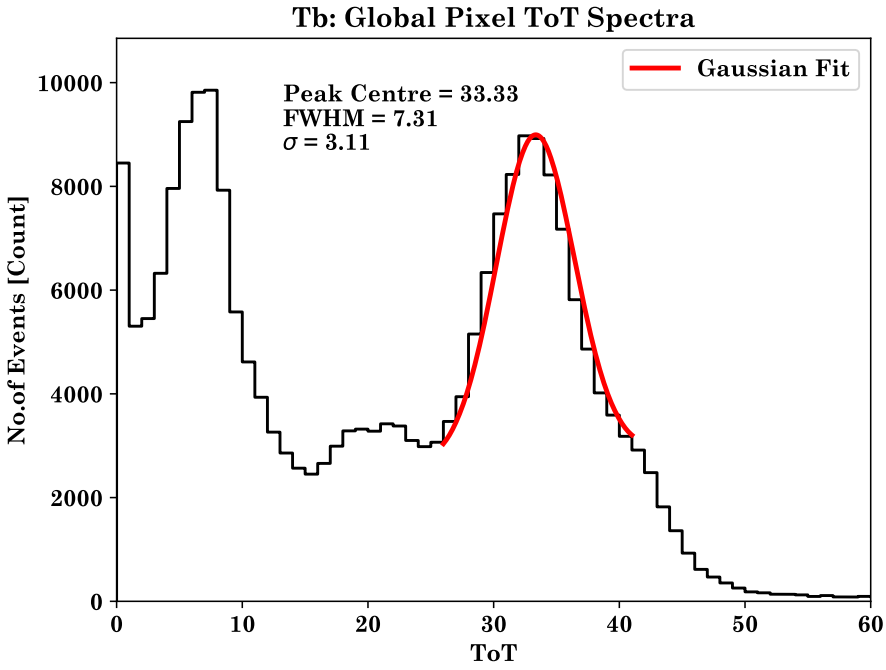

(b)

Figure 6.4: Global pixel ToT spectra of (a) XRF_Rb and (b) XRF_Tb obtained with the Timepix3_Si. The peak centre, FWHM and σ are all in ToT value.

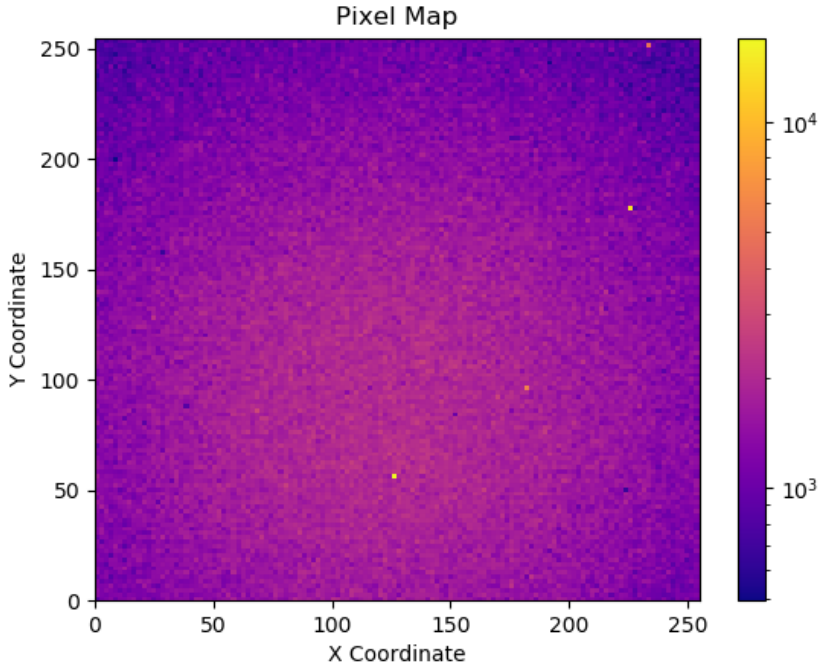

(a)

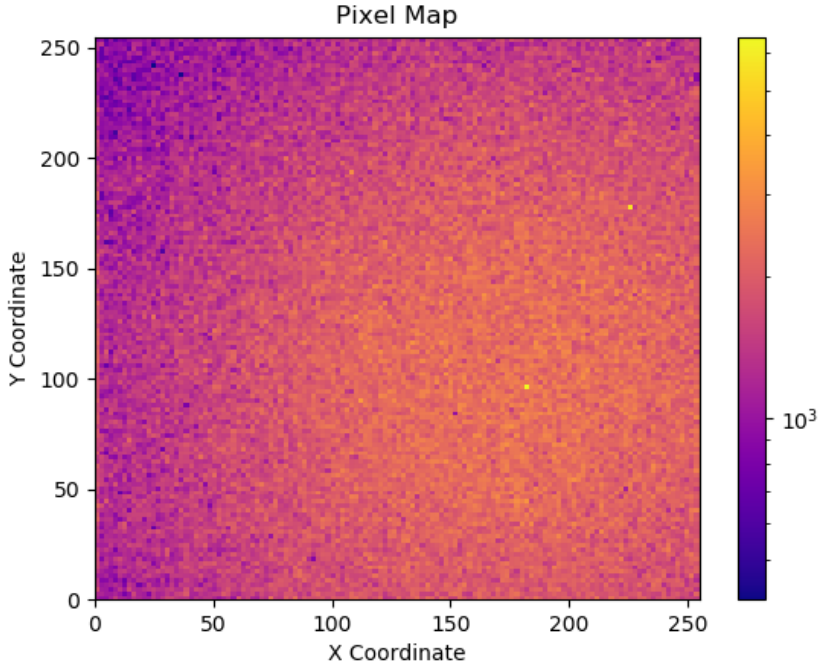

(b)

Figure 6.5: Comparison of recorded events for 10000 frames acquisition for XRF_Rb and XRF_Tb sources. (a) The average events for XRF_Rb $\approx 10^3$ counts, *and (b) average events for XRF_Tb* $\approx 10^5$ counts.

to the low photon yield of XRF_Rb and the finite resolution of the silicon sensors. Figure 6.5b shows the comparison of recorded events for 10000 frames acquisition for XRF_Rb and XRF_Tb. The recorded events for XRF_Rb are at least one-order magnitude lower than the XRF_Tb.

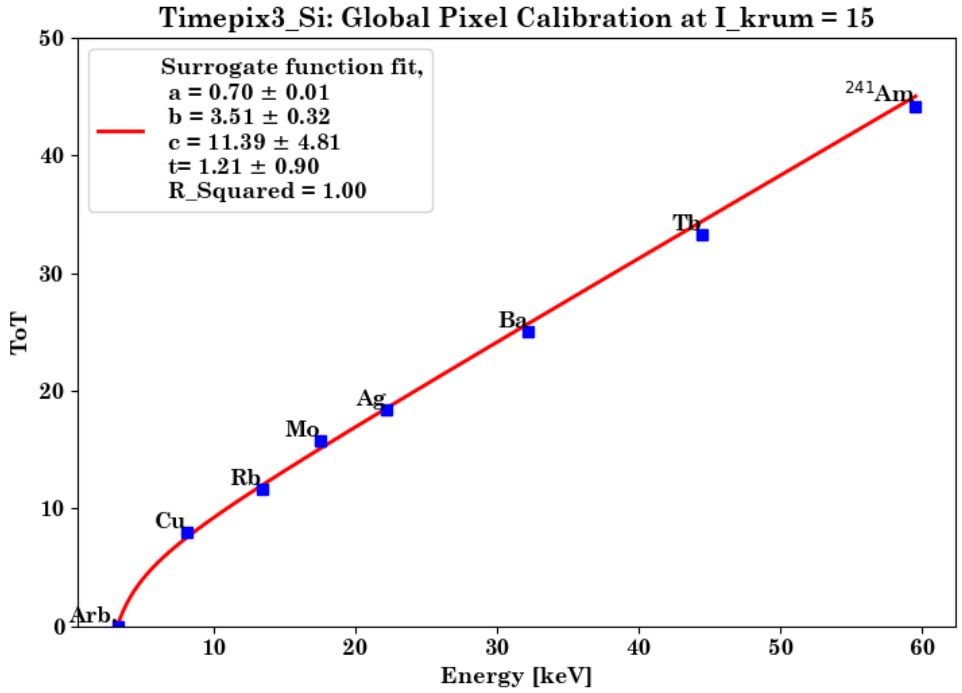

Figure 6.6: The global ToT calibration curve of the hybrid pixel detector with silicon sensors. The arbitary calibration point is set at 3.2 keV.

Table 6.3: Energy spectra of calibration sources measured with 55 µm*-pitch silicon sensor bonded to Timepix3 readout ASIC.*

Calibration Sources)	E [keV]	$E_{\text{measured}} \pm \sigma$ [keV]	**Deviation** [%]	**FWHM** [keV]	$\triangle E/E$ [%]
XRF_Cu	8.05	8.41 ± 1.45	4.47	2.99	36
XRF_Rb	13.40	13.26 ± 1.34	1.04	3.15	24
XRF_Mo	17.52	17.16 ± 2.10	2.05	4.96	28
XRF_Ag	22.16	21.19 ± 3.54	0.14	8.34	27
XRF_Ba	32.19	31.33 ± 4.27	2.67	10.05	32
XRF_Tb	44.48	43.29 ± 4.43	2.68	10.43	24
^{241}Am	59.54	58.73 ± 5.11	1.36	12.03	20

An arbitrary calibration point is introduced to ensure the fitting function (Equation 3.1) operates correctly, aligning with the energy equivalent of the globally set threshold level (THL) value. The THL is constrained by the combined contributions of the Timepix3 read-

out ASIC's minimum detectable charge (500 e^-) and ToT resolution (600 e^-), resulting in $\approx$ 2.83 keV (FWHM). The THL value obtained from the Timepix3 DAC scan function is $\approx$ 3.2 keV, close to the expected theoretical limit. The calibration curve in Figure 6.6 depicts a satisfactory agreement between the data and the fitting function. The extracted coefficients are then applied to spectra to obtain the equivalent energy in eV units.

Table 6.3 presents the energy spectra measurements conducted using a globally calibrated silicon sensor with a 55 µm-pitch and 256 $\times$ 256 pixels bonded to a Timepix3 readout ASIC. While the measured energies demonstrated a commendable deviation of less than 5 % from expected values, several critical limitations were identified. The Timepix3's ToT resolution of 2.16 keV (600 e^-) proved inadequate for distinguishing between closely spaced peaks, resulting in spectral overlap. This limitation was particularly pronounced in the case of the XRF_Ba, where the $K_{\alpha 1}$ (32.19 keV) and $K_{\alpha 2}$ (31.82 keV) transitions, with their respective emission probabilities of 88 % and 97 %[88], coalesced into a single, broadened peak. The initial assumption of using solely the $K_{\alpha 1}$ energies as reference points was an oversimplification, neglecting the significant contribution of $K_{\alpha 2}$. As evident from Figure 6.5a, the XRF_Rb exhibited low photon counts, leading to poor counting statistics and subsequent difficulties in peak fitting. This anomaly resulted in an artificially enhanced energy resolution that likely misrepresents the detector's true capabilities. Conversely, the XRF_Ba displayed a degraded resolution due to peak overlap.The FWHM was measured at 2.99 keV for 8.05 keV XRF_Cu and 12.03 keV for 59.54 keV ^{241}Am γ-rays. At 59.54 keV, the Fano-limited FWHM was about 345 eV (F=0.1 and E_i =3.62 keV). Given that the detector is from a reputable manufacturer, charge collection issues were assumed negligible, making electronic noise (from Timepix3 and sensor leakage current) the dominant contributor, with a calculated ($\mathrm{FWHM}_{noise} = \sqrt{\mathrm{FWHM}^2_{Total} - \mathrm{FWHM}^2_{Fano}} \approx 12.02$ keV.

The initial data collection of 10,000 frames in frame-based *Event + iToT* mode proved insufficient for per-pixel analysis, necessitating a modified approach. Instead of analysing

Table 6.4: Comparison between the global and per-region ToT peak centre of calibration sources in the55 µm-pitch silicon sensors bonded to Timepix3 readout ASIC.

		Per-region ToT Analysis	
Calibration Source	**Global ToT peak [ToT]**	**Mean ToT value [ToT]**	**Deviation from Global ToT [%]**
XRF_Cu	7.79	8.57 ± 0.99	14
XRF_Rb	11.69	7.94 ± 4.28	32
XRF_Mo	15.71	16.76 ± 2.69	6
XRF_Ag	18.51	19.29 ± 0.47	4
XRF_Ba	25.88	25.99 ± 0.52	3
XRF_Tb	33.33	43.83 ± 0.76	4
^{241}Am	44.18	46.81 ± 19.15	6

individual pixels, the 256 × 256 pixels were grouped into 16 × 16 blocks, each containing 256 pixels, resulting in 256 regions for analysis. Table 6.4 compares the per-region and global pixels' spectral peak (in ToT units). The analysis revealed small deviations (7 %) for XRF sources with high photon counts and the ^{241}Am. However, higher deviations were observed for XRF_Cu and XRF_Rb, attributed to insufficient data statistics leading to increased fitting errors.

The hybrid pixel detector with silicon sensors demonstrates reasonably good spectroscopic performance with measured $\sigma = 1.27$ keV at 8.05 keV XRF_Cu. This measurement employs global calibration, which assumes uniform pixel responses across the detector. However, this assumption is flawed due to inherent pixel-to-pixel variations. Additionally, the current method groups charge clusters based on size rather than ToA, potentially leading to misclassifying separate interaction events as single clusters, thus introducing energy measurement errors. For context, a previous study reported a superior σ of 0.9 keV for the same 8.05 keV XRF_Cu using a ToA-corrected, per-pixel calibrated system[69]. Unfortunately, the 10,000 data frames collected in this study were insufficient for implementing per-pixel calibration. Moreover, the frame-based *Event + iToT* acquisition mode proved impractical for calibration due to the generation of excessively large data files. Future work should utilise high-intensity photon sources and employ a data-driven acquisition mode to achieve optimal per-pixel calibration.

6.4 Per-pixel energy calibration (Timepix3 + 110 µm-pitch LGAD

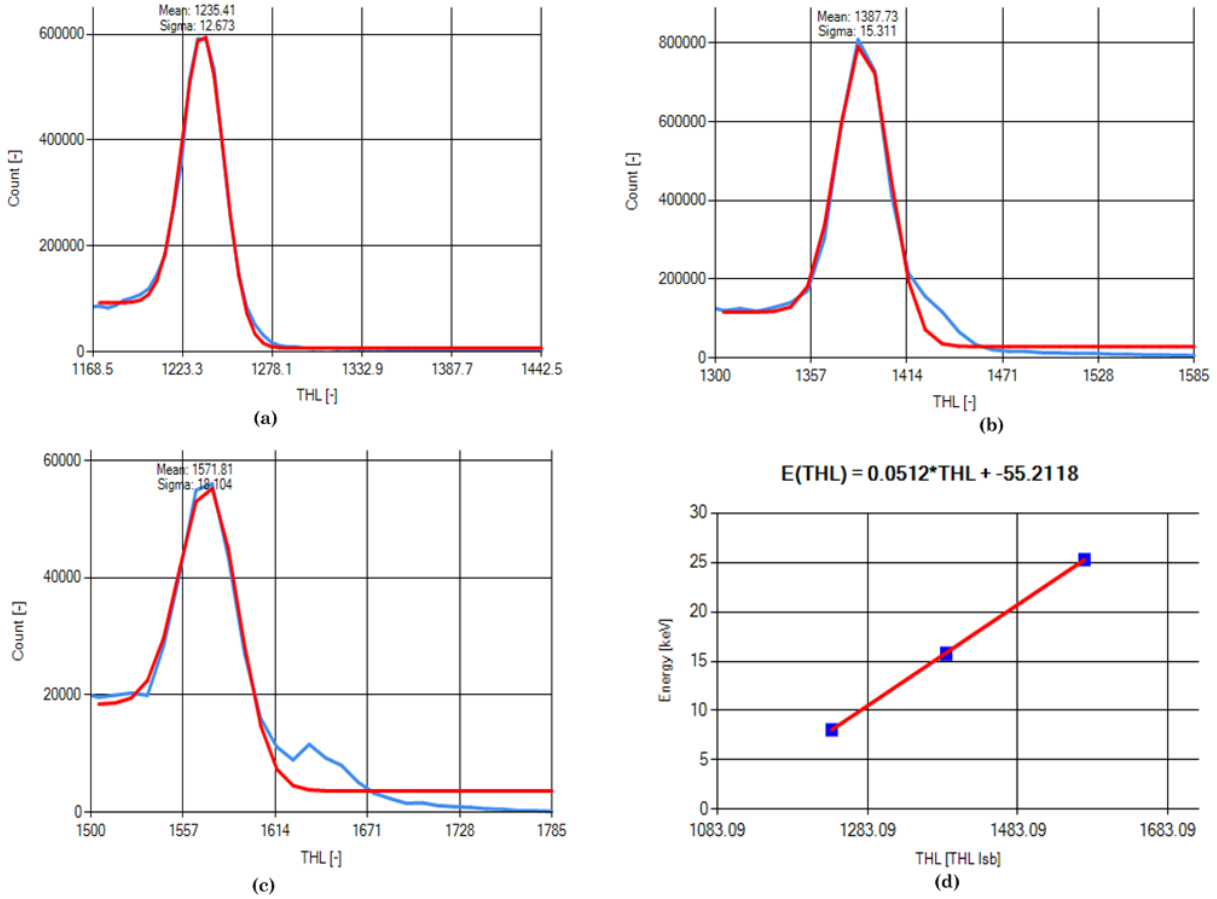

Figure 6.7: THL_scan peak and fitting for (a) XRF_Cu, (b) XRF_Zr, (c) XRF_Sn, and (d) the THL–Energy calibration curve.

The three XRFs peaks obtained from the THL_scan with the Timepix3 DAC scan function are shown in Fig. 6.7. The corresponding mean THL peak values were extracted via Gaussian fit and plotted as a function of its energy. The THL – energy calibration curve (see Fig. 6.7d) is used to find the energy equivalent to the THL obtained from the threshold equalisation. From the curve, the energy corresponding to THL (E_{THL}) = 1190 is 5.72 KeV. Figure 6.8 shows the single-pixel analysis at the pixel of interest (PoI) 128, 128 for four calibration sources. The four plots indicate that the calibration data provide adequate statistics for single-pixel ToT analysis. A Gaussian fit extracted the single-pixel

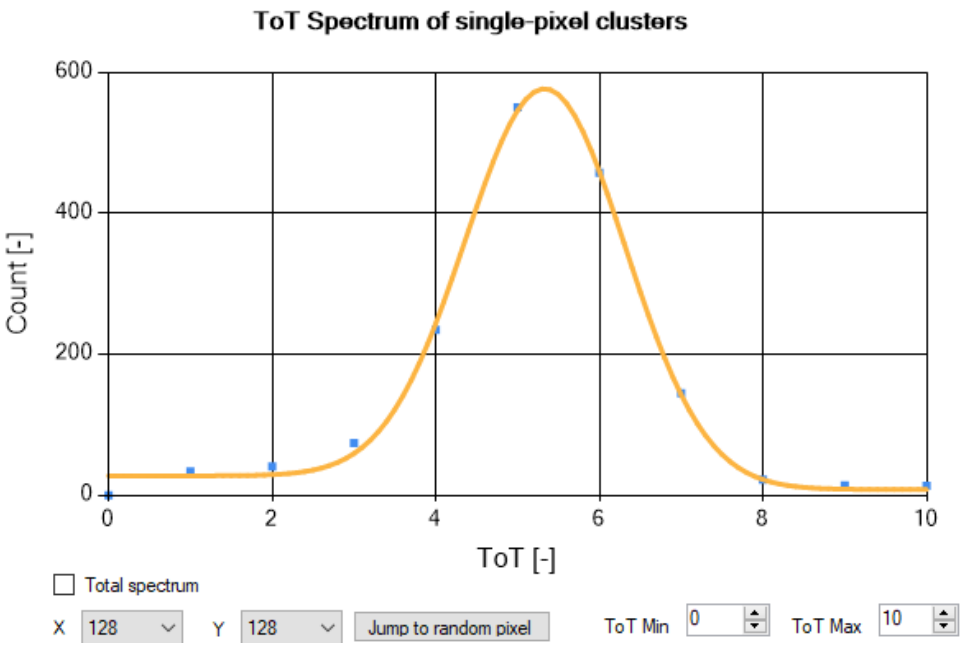

(a)

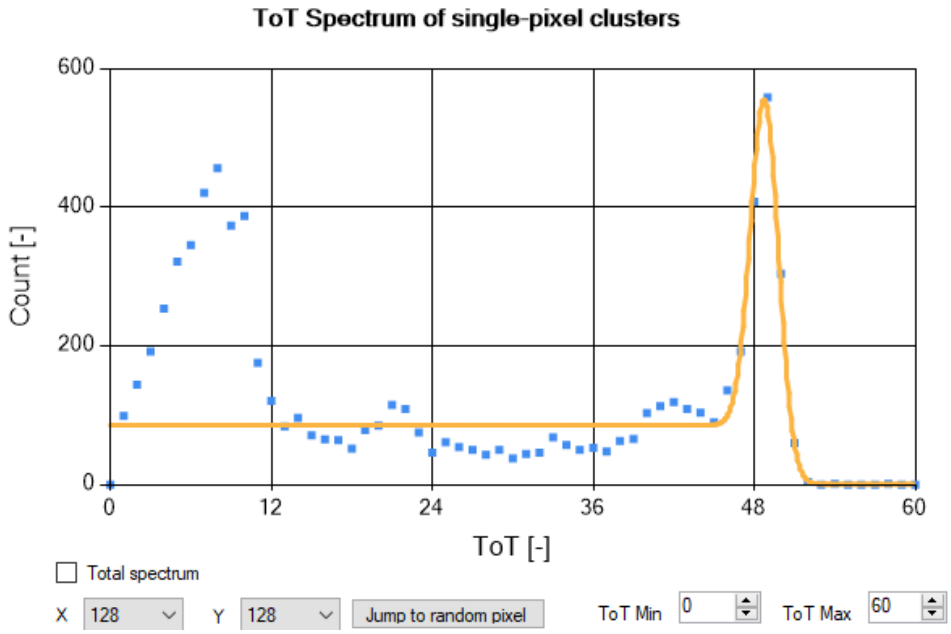

(b)

Figure 6.8: Single-pixel mean ToT spectra at PoI 128_128 for (a) XRF_Cu, and (b) 59.54 keV ^{241}Am.

mean ToT peak for each calibration point, and the process is repeated for each pixel in the entire detector.

The arbitrary calibration (E_{THL}, ToT = 0) is added into the single-pixel mean ToT peak

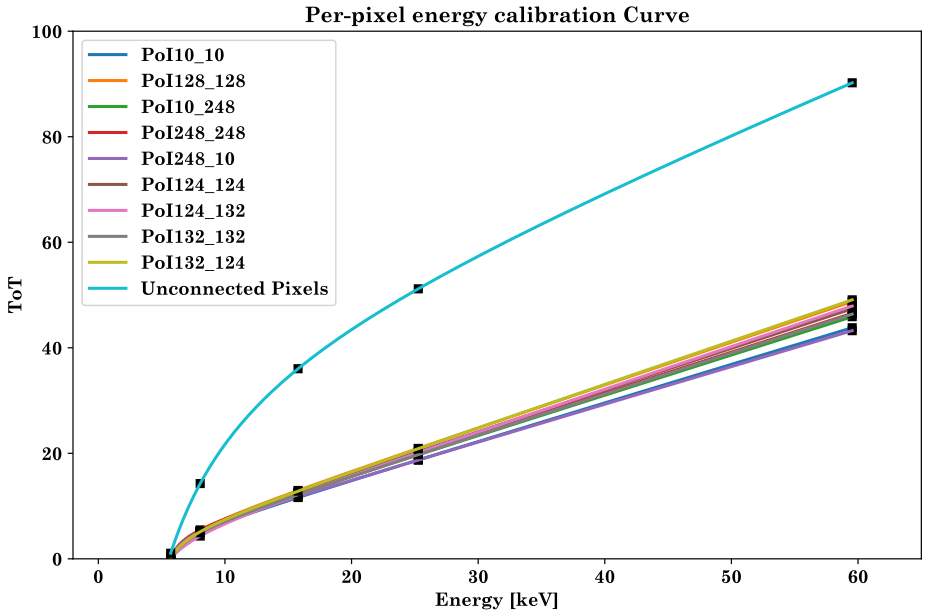

Figure 6.9: Per-pixel ToT—energy calibration for selected pixels

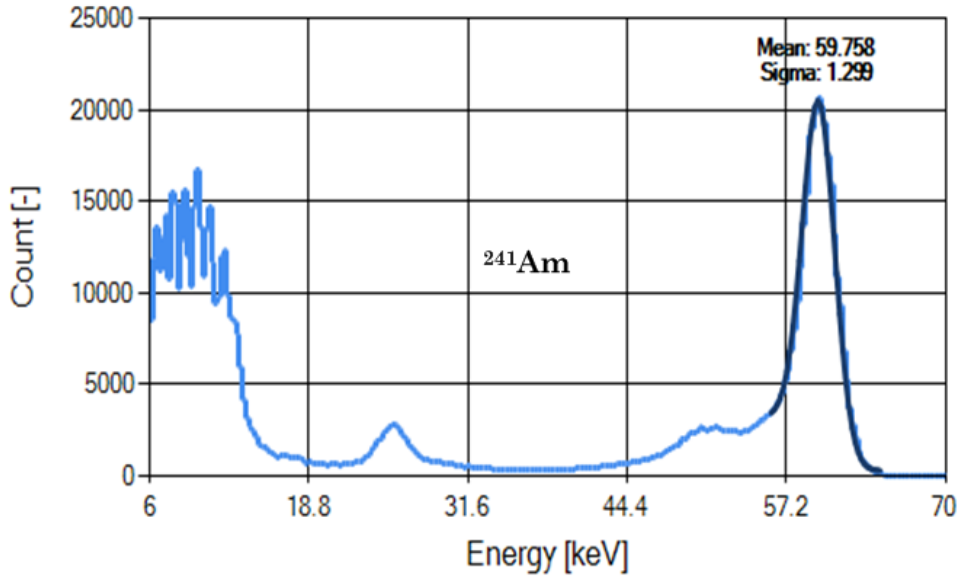

Figure 6.10: Energy spectrum of ^{241}Am obtained with per-pixel calibrated hybrid pixel detectors.

as a function of the energy plot. Then, the calibration coefficients were extracted for each pixel. Figure 6.9 shows the per-pixel ToT – energy calibration for selected pixels at the middle and edge of the detector whilst the extracted calibration coefficients are shown in Table 6.5. The Timepix3_LGAD is a 128 × 128 pixels; thus, the bump-bonding into the Timepix3 ASIC was done in every fourth pixel in the 2 × 2-pixel array. The

Table 6.5: The per-pixel ToT – Energy calibration coefficients for selected pixel at the middle and edge of the detector and the constant coefficient assigned to the unconnected pixel.

Pixel of Interest [POIX_Y]	Calibration Coefficients Energy = a·ToT + b - $\left[\frac{c}{\text{ToT} - t}\right]$			
	a	b	c	t
PoI10_10	0.726	0.676	5.756	4.498
PoI128_128	0.805	0.989	8.534	4.113
PoI10_248	0.759	0.798	5.384	4.641
PoI248_248	0.769	0.839	5.154	4.712
PoI248_10	0.711	1.006	5.294	4.645
PoI124_124	0.783	0.936	8.642	4.077
PoI124_132	0.801	0.455	12.585	3.175
PoI132_132	0.771	0.602	7.055	4.382
PoI132_124	0.816	0.647	8.069	4.164
Unconnected Pixel	0.967	37.148	271.543	-0.810

"Katherine-Detector Tools for Timepix3"calibration tools assign a constant calibration coefficient for the unconnected pixels—however, it not included in the final calibration file. A Small variation was observed in the calibration curves, and the calibration coefficient values from pixel to pixel indicate non-uniformity in the detector response, which is expected for a prototype detector. The energy spectra measured with a per-pixel calibrated Timepix3_LGAD shown in figure 6.10 show excellent agreement between theory and measurement.

6.5 Time-walk correction

Figure 6.11a shows the energy spectra of ^{241}Am with cluster sizes 2, 3 and 4. Spectra with cluster size 2 are dominant because the detector has a large pixel (110 µm-pitch). The plot of mean time difference as an energy function is shown in figure 6.11b. The time difference has an energy offset at around 5.72 keV, corresponding to the THL obtained during threshold equalisation. Table 6.6 shows the time-walk coefficient extracted via a non-linear fit with the fitting function described in equation 3.2.

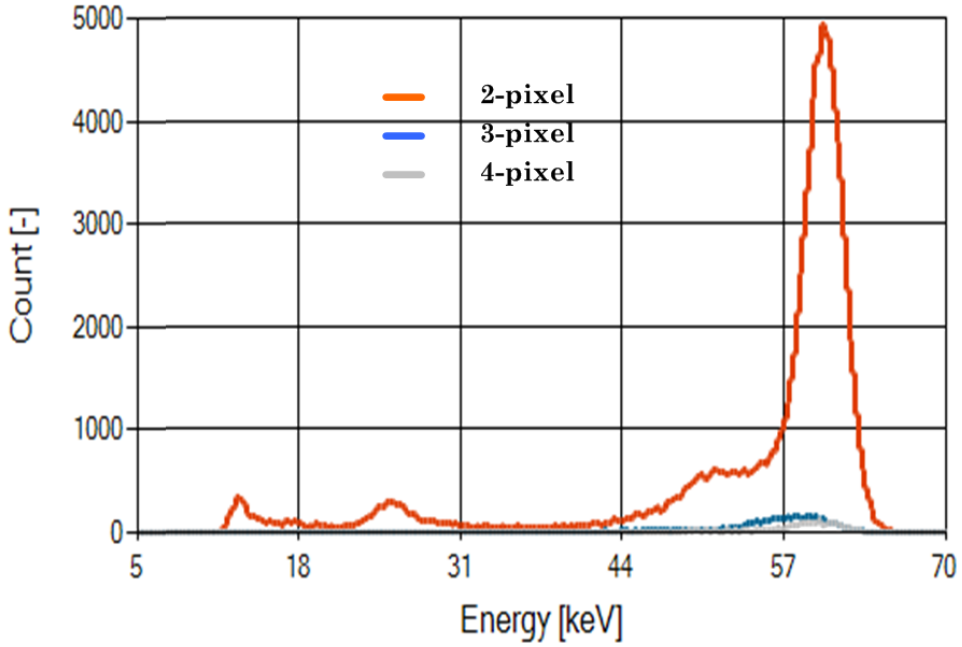

(a)

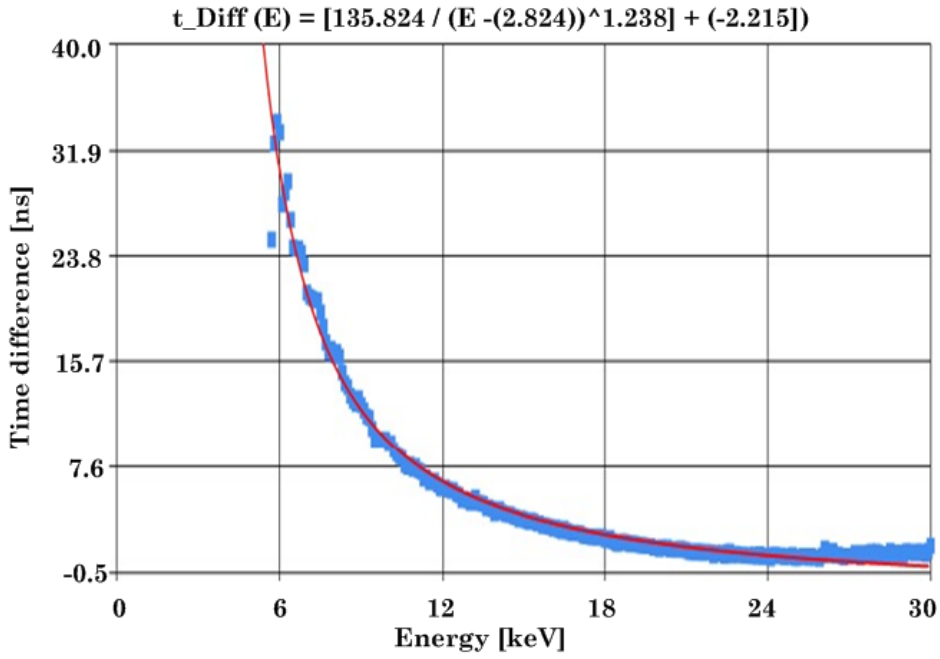

(b)

Figure 6.11: (a) Spectra of ^{241}Am with cluster size 2, 3 and 4. (b) Extraction of the time-walk coefficients from the time difference as a function of energy plot (red trace is the time-walk correction fit).

6.6 Analysis of data from 5 mm thick CZT detectors

The hybrid pixel detector with 5 mm thick, 110 µm-pitch CZT bonded to a Timepix read-out ASIC is calibrated in the same manner as described in section 6.3. However, the

Table 6.6: Time-walk coefficient

Time-walk coefficients, $\Delta T = \left[\frac{c}{(E-E_0)^d}\right] + \text{Offset}$	
c	99.121
E_0	3.528 keV
d	1.157
Offset	−2.013 ns

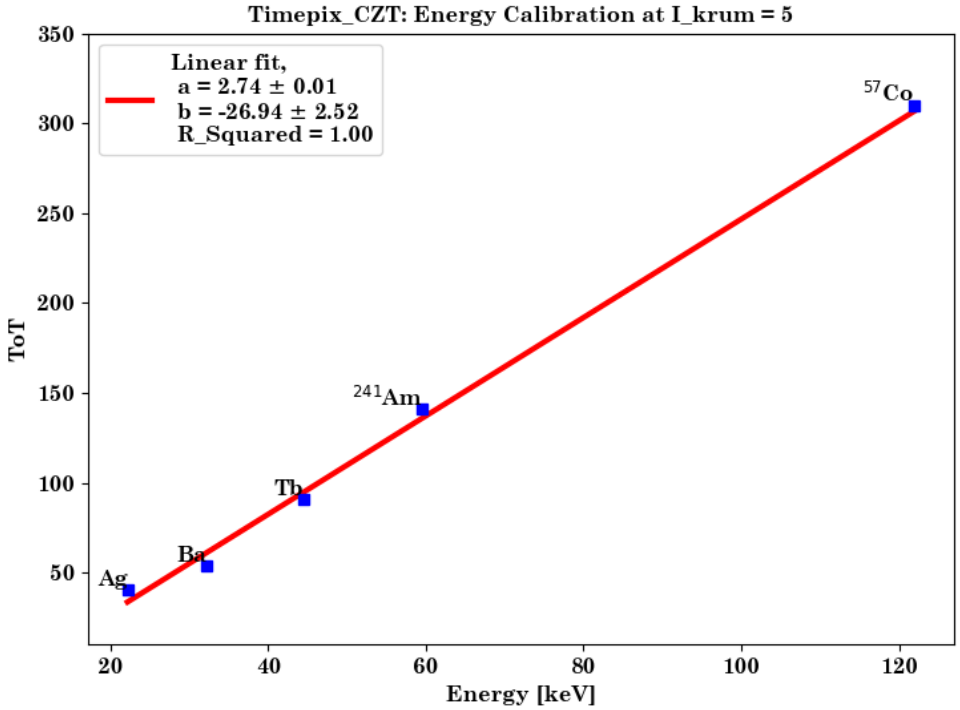

Figure 6.12: ToT–energy calibration curve for the Timepix_CZT.

Table 6.7: Energy spectra of calibration sources measured with the 5 mm *thick,* 110 µm*-pitch CZT bonded to Timepix readout ASIC.*

Source	***E*** **[keV]**	$\boldsymbol{E}_{\text{measured}}$ **[keV]**	**FWHM [keV])**	**△E/E [%]**
XRF_Ag	22.16	25.29 ± 0.19	11.84	47
XRF_Ba	32.19	29.95 ± 0.11	13.09	44
XRF_Tb	44.48	43.78 ± 0.18	17.26	39
^{241}Am	59.54	60.52 ± 0.27	17.86	30
^{57}Co	122.00	123.62 ± 0.14	30.20	24
^{137}Cs	661.70	666.37 ± 0.36	54.38	8

calibration coefficients are extracted by a linear fit since all calibration points are in the linear region of the calibration curve. Figure 6.12 shows the ToT–energy calibration curve

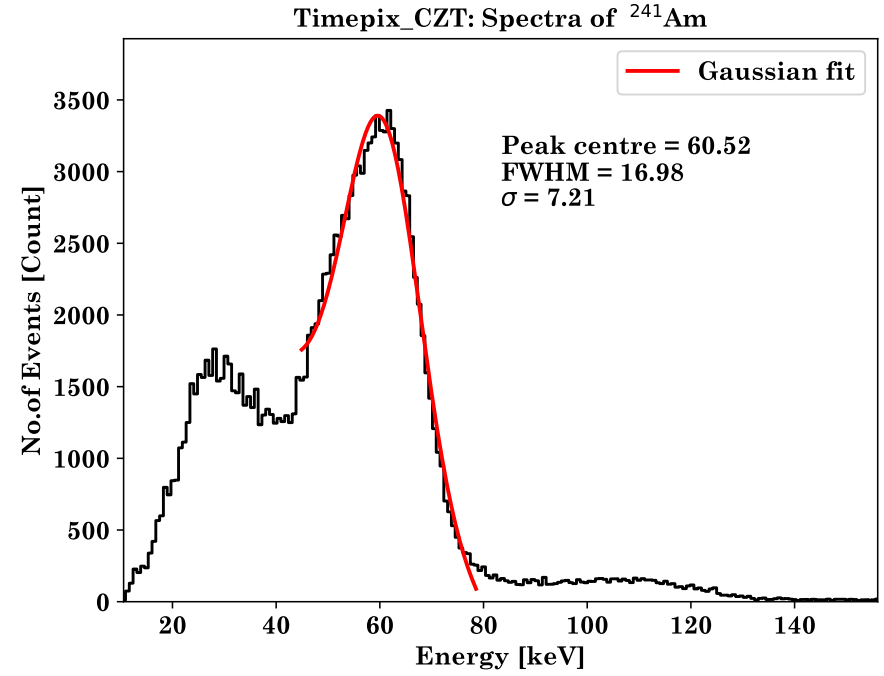

(a)

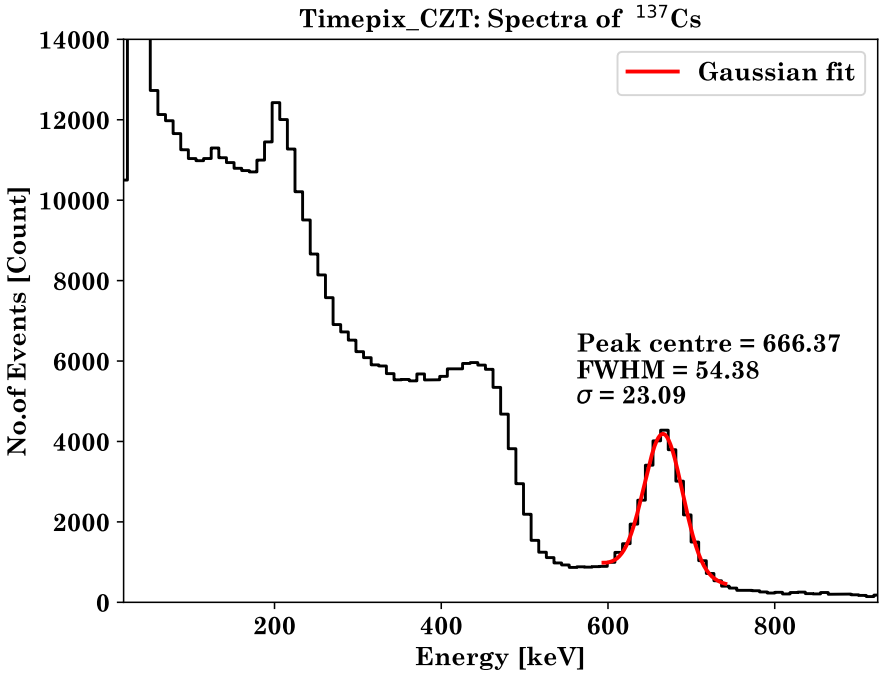

(b)

Figure 6.13: A collection of energy spectra obtained with a calibrated 5 mm *thick CZT bonded to Timepix readout ASIC. (a)* ^{241}*Am, and (b)* ^{137}*Cs.*

and the extracted calibration coefficients. A good agreement between data and fit was obtained for this analysis. Figure 6.13 shows the energy-calibrated spectra of XRF and radioisotopes measured with this detector. The calibration was also verified to be valid for photons with higher energy (see ^{137}Cs spectra in figure 6.13b). Spectroscopic measurement results are presented in Table 6.7. Measured energies are within 1 % of expected values, except for XRF_Ag and XRF_Ba, where CZT's finite resolution barely resolved the low-energy spectral peaks. The energy resolution at 661.7 keV ^{137}Cs) is approximately 8 %.

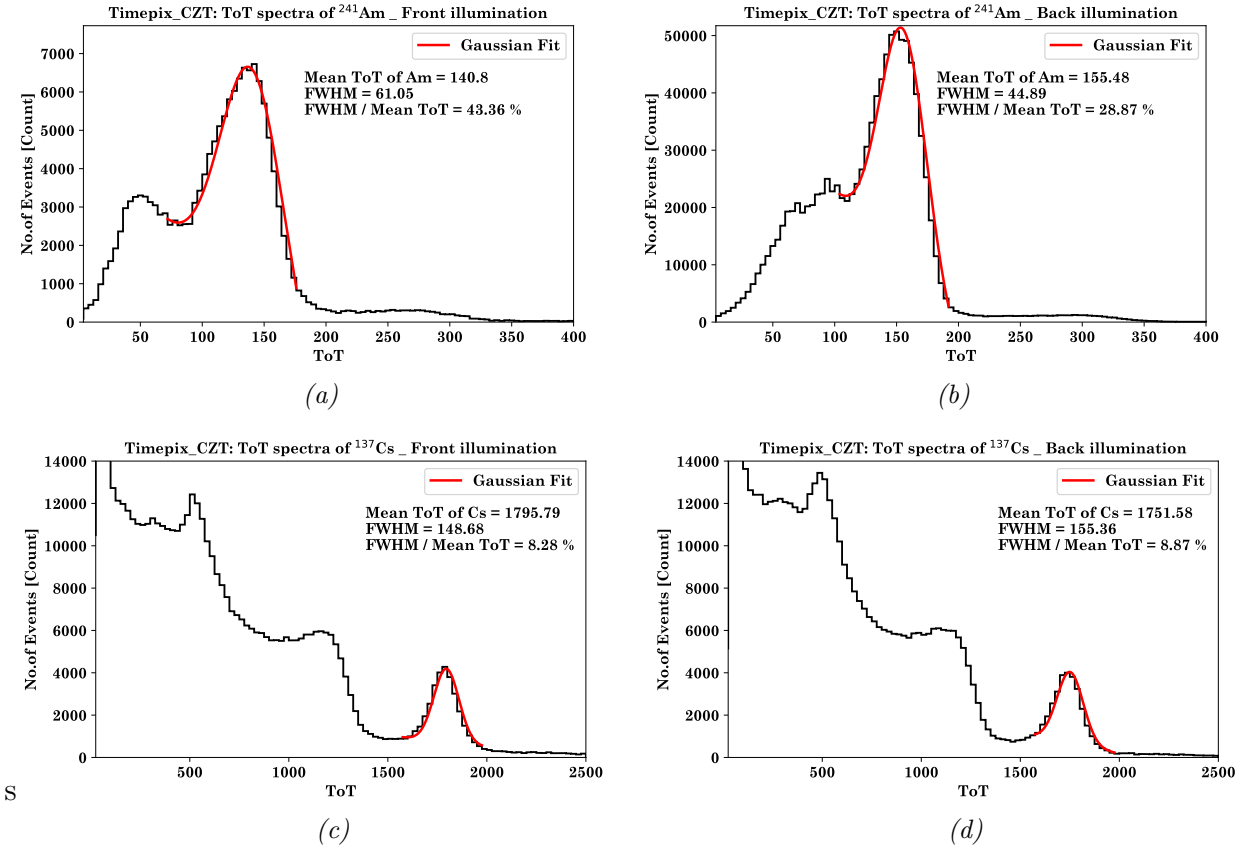

Figure 6.14: Effect of the depth of interaction on the ToT spectra.

The extent to which photons interact is crucial in enhancing spectral resolution. Low-energy photons produce smaller clusters much closer to the surface of the detector. Suppose these charge clusters are closer to the collector electrode. In that case, they will experience a reduced charge spread during their migration towards the electrode, increasing spectral resolution and vice versa if they are produced far from the collector electrode.

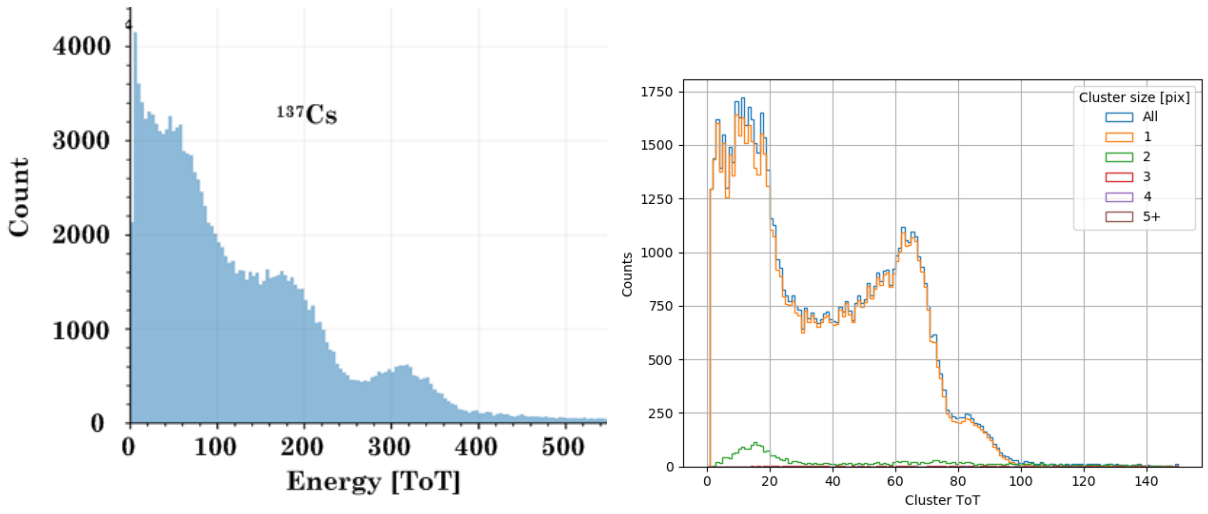

(a) *(b)*

Figure 6.15: ToT spectra acquired with the 5 mm *thick CZT bonded to Timepix3 readout ASIC from previous experiments in 2018. (a) ToT spectrum of* 661.70 keV ^{137}*Cs, and (b) ToT spectra of* 44.48 keV *XRF_Tb.*

Rear illumination of 59.54 keV ^{241}Am produces better spectral resolution (see figure 6.14a and figure 6.14b). The collecting electrodes for this detector are at the bottom, so rear illumination produces charge clusters closer to the collecting electrodes. As shown in figure 6.14c and figure 6.14d, the illumination orientation has little effect on the spectral resolution for the high-energy 661.70 keV ^{137}Cs case. High-energy photon penetrates deeper into the detector, producing larger charge clusters along its path. Charge clusters experience the same degree of charge spread regardless of illumination orientation and do not affect spectral resolution.

The 5 mm, 110 µm-pitch CZT bonded to Timepix3 experienced significant degradation and was rendered inoperable during a subsequent series of experiments conducted in 2020. Figure 6.15 shows two spectra of 661.70 keV ^{137}Cs, and 44.48 keV XRF_Tb from previous measurements in 2018. As seen from these two spectra, this hybrid pixel detector has already produced suboptimal spectral resolution since its inception. The spectroscopic performance of this hybrid pixel detector was unexpected, considering the advanced technological capabilities of the Timepix3 ASIC. Therefore, the CZT sensor is the primary

factor contributing to the suboptimal performance.

6.7 Chapter summary

This chapter delves into the characterisation of hybrid pixel detectors using XRFs and radioisotopes, specifically examining silicon, LGAD, and CZT sensors bonded to Timepix and Timepix3 readout ASICs. The global ToT to Energy calibration for the silicon sensor demonstrated commendable results, achieving an FWHM of 12.02 keV at 59.54 keV. Nonetheless, the calibration sources available at the University of Glasgow yielded low photon counts, rendering them inadequate for per-pixel ToT calibration and time-walk correction. The frame-based *Event + iToT* mode was found to be inefficient due to the production of excessively large data files. Conversely, using high-yield sources and data-driven mode, successful implementation of per-pixel ToT calibration and time-walk correction was achieved with LGAD sensors.

The 5 mm thick, 110 µm-pitch CZT sensor bonded to the Timepix readout ASIC exhibited promising spectroscopic performance, achieving an 8 % energy resolution at 661.7 keV. However, a comparable CZT sensor paired with the Timepix3 readout ASIC showed significant performance degradation. An in-depth analysis of the spectroscopic capabilities of both CZT detectors concluded that they are unsuitable for single-layer Compton cameras: the CZT sensor bonded to the Timepix readout ASIC lacks the capability for simultaneous energy and precise event detection, while the other displayed inferior spectroscopic performance.

CHAPTER 7

Characterisation of LGAD & iLGAD with micro-focus synchrotron beam

The University of Glasgow and Micron Semiconductor Ltd produced two prototypes of hybrid pixel detectors with 200 µm thick LGAD and 250 µm thick iLGAD detectors. These detectors have been fabricated with various pixel pitches of 55, 110, and 220 µm and are bonded to a Timepix3 readout ASICs. These hybrid pixel detector prototypes were tested with a micro-focused synchrotron beam at the Beamline B16 facility at the Diamond Light Source (DLS) in 2019 and 2021. The two synchrotron beam tests were performed to study the signal gain and pixel response of two prototypes. This chapter describes the synchrotron test beam setup and discusses the outcomes of the tests.

7.1 The LGAD/iLGAD hybrid pixel detectors and test beam setup

The hybrid pixel detector with LGAD sensor, conceived in [24], is a pixelated LGAD with a JTE structure bonded to Timepix3 ASIC. The first synchrotron beam test cam-

Table 7.1: The specifications of the hybrid pixel detectors, the types of test performed, and the Timepix3 acquisition setup used during the synchrotron beam test.

Device ID: **Timepix3_LGAD**	**Specifications** **[Pixel size, JTE width]**	**Tests performed** **E= 15 KeV, Focus ≈ 2 μm (FWHM)**	**Timepix3 acquisition setup**
C04-W0031	110 μm, 10 μm	1. Line scan (a) Middle pixel: PoI (127, 127) (b) Control pixel: PoI (5, 5)	Acquisition: ToT + ToA, Data-driven Readout: AdvaDAQ TPX3 USB3.0
F06-W0031	110 μm, 20 μm	2. Voltage scan @ PoI (127, 127)	
D04-W0031	55 μm, 5 μm	3. 2D scan @ PoI (127, 127)	
Device ID: **Timepix3_iLGAD**	**Specifications** **[Pixel size, Gain Doping]**	**Tests performed** **E= 15 KeV, Focus ≈ 2 μm (FWHM)**	
C10-W0018	55 μm, PIN Device	1. Line scan (a) Middle pixel: PoI (128, 128) (b) Control pixel @ Edge pixel: PoI (253, 128)	
I11-W0068	55 μm, 1.2e+13 cm^{-3}	2. Voltage scan @ PoI (128, 128)	
F08-W0068	110 μm, 1.1e+13 cm^{-3}	3. 2D scan	
L07-W0068	220 μm, 1.1e+13 cm^{-3}		

paign conducted in 2019 involved three Timpix3_LGADs with different pixel sizes and JTE widths (see Table 7.1). A total of 9 × 9 control pixels, which are pixels without gain, are fabricated at the bottom-left corner of the detector. These control pixels are used as a reference to evaluate the pixel response and signal gain in these detectors. Pixel (127, 127) is selected as the pixel of interest (PoI) for testing the pixel with gain and pixel (5, 5) is the control pixel.

The second synchrotron test beam campaign in the year 2021 involved three hybrid pixel detectors with iLGAD sensors of 55, 110 and 220 µm pixel pitches. In this detector, the control pixels are fabricated around the edges. The pixel in the middle (128, 128) and a group of pixels around the pixel edges are selected as the PoIs to assess the gain in these hybrid pixel detectors. This prototype is the first hybrid pixel detector of its kind that combines a Timepix3 readout ASIC with a highly pixelated iLGAD sensor. The iLGAD sensor is also the first iteration of iLGAD produced by Micron Semiconductor Ltd. Therefore, much information regarding the behaviour of a highly pixelated iLGAD has yet to be understood. Furthermore, the control pixel fabricated around the edge of the sensor might not function as expected. A Hybrid pixel detector with a 55 µm-pitch standard silicon sensor (C10-W0068) is included in the second beam test as a reference to study the pixel response of the Timepix3_iLGADs.

Three types of tests were performed in both synchrotron test campaigns: the *Line Scan*, *Voltage Scan*, and *2D Scan*. These scans are the synchrotron tests beam scan procedures described in section 4.3. Data are taken with the AdvaDAQ TPX3 USB3.0[1] readout in data-driven ToT + ToA mode. However, only the ToT data were analysed to evaluate the pixel response and gain of the LGAD/iLGAD hybrid pixel detectors.

7.2 Pixel response and gain in hybrid pixel detector with LGAD

This section presents the result of the synchrotron test beam conducted on the hybrid pixel detector with LGAD sensors. The analysis is divided into three subsections. The first subsection presents and discusses the analysis of the *Line Scan*, *Voltage Scan* and *2D Scan* on the 110 µm-pitch, 10 µm wide JTE device (C04-W0031). The second subsection evaluates the effect of the JTE width by comparing the result obtained from the 110 µm-pitch devices with 10 µm and 20 µm JTE (C04-W0031 and C06-W0031). The last subsection investigates the gain in the hybrid pixel detector with 55 µm-pitch LGAD.

7.2.1 Device C04-W0031: 110 µm-pitch + 10 µm JTE

Figure 7.1 shows the evolution of the ToT pixel response as a function of bias voltages across three PoIs with gain at the middle of the C04-W0031 device. The PoIs produce an output signal as early as −50 V bias voltage, but signal with gains are demonstrated after the bias voltage reaches −150 V. As seen from the plots, the ToT pixel response increases with voltages. This trait demonstrates a typical characteristic of a functional LGAD device. The plot in figure 7.2 shows the ToT pixel response at −350 V bias voltage across three PoIs in control pixel area. In this case, the synchrotron beam is scanned from the pixel without gain (PoI_5_5) across the pixel with gain (PoI_5_7) to the of another

[1]Timepix3 readout system from ADVACAM, https://advacam.com/

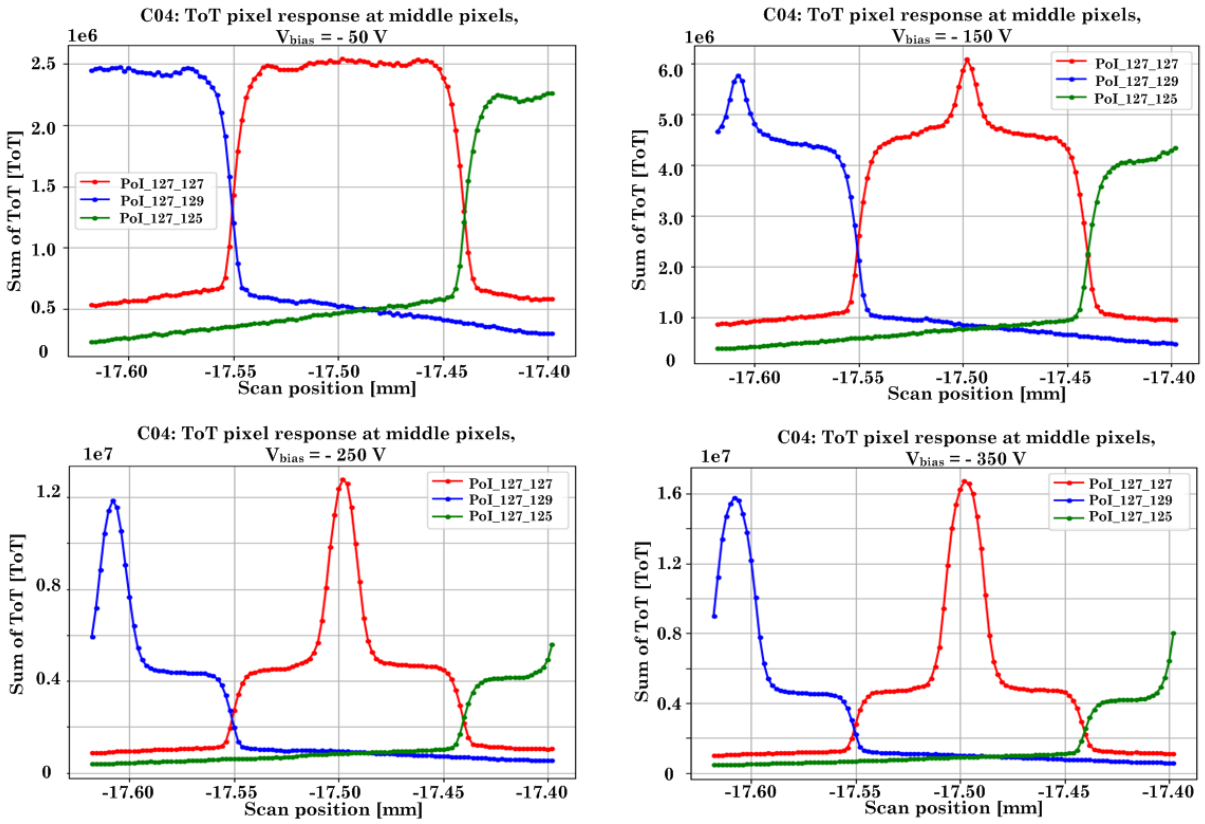

Figure 7.1: ToT pixel response across 3 PoIs at the middle of the C04-W0031 for -50, -150, -200 and −350 V bias voltages.

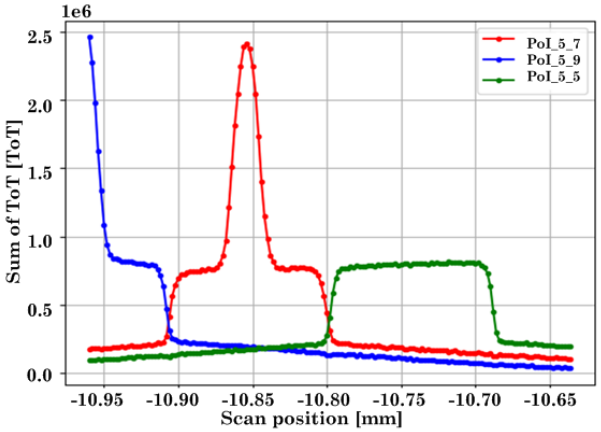

Figure 7.2: ToT pixel response across 3 PoIs from the control pixel (PoI_5_5) to the pixels with gain (PoI_5_7 & PoI_5_9) at a bias voltage of −350 V.

pixel with gain (PoI_5_9). This plot shows a better graphical visualisation of the signal gain in this device. The pixel without gain (PoI_5_5) shows a step function-like response, a typical pixel response of a silicon detector without signal gain. The transition of the pixel response is not sharp like a true step function response because the pixel response

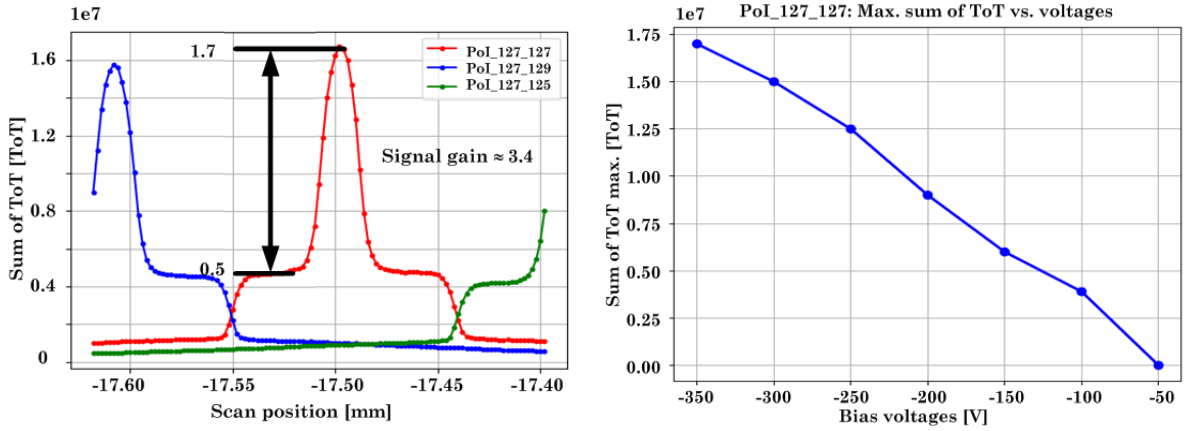

(a) *(b)*

Figure 7.3: (a) ToT pixel response at a bias voltage of −350 V across 3 PoIs at the middle of the device C04-W0031 and (b) the maximum sum of ToT value as a function of bias voltages at PoI_127_127.

is a convolution product of a step function (square pixel) and a Gaussian function (synchrotron with a finite beam size). The Pixels with gain in PoI_5_7 and PoI_5_9 show a significant increase in pixel response, demonstrating signal gain.

All three pixels with gain at the middle of the C04-W0031 in figure 7.3a exhibit high pixel responses in the central pixel area. The signal gain estimated from the ToT pixel response of device C04-W0031 is ≈ 3.4. The plot of the maximum value of the sum of ToT in PoI_127_127 as a function of the bias voltage in figure 7.3b shows a linear relationship between the gain and bias voltage, indicates a fully functional LGAD device. The high pixel response is only demonstrated in the central area of the pixel, indicates that the pixel has a low fill factor. However, this characteristic is expected and fully understood from previous studies in [24, 25].

Figure 7.4 shows the ToT spectrum at PoI (5, 5) for different beam positions. The spectral peaks due to the 3rd harmonic component of the beam are visible in the PoI (5, 5) regardless of the beam positions. This observation indicates that a 3rd harmonic halo with significant intensity is present. The halo spreads to a few hundred microns because it is

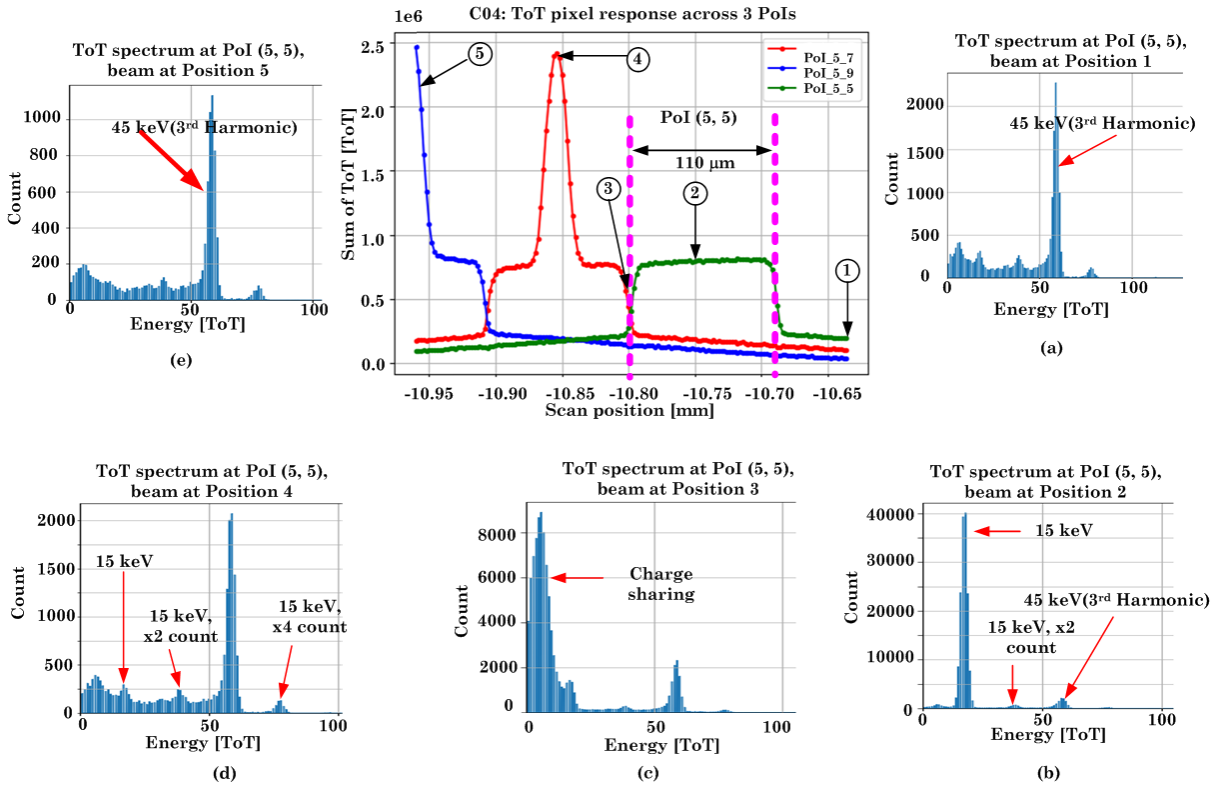

Figure 7.4: ToT spectra at PoI (5, 5) as a function of beam positions.

shown from figure 7.4 (d) that the 3rd harmonic peak is present in PoI (5, 5) despite the beam being positioned ≈ 160 µm from the PoI. As seen in figure 7.4 (a) and figure 7.4 (b), the intensity of the 3rd harmonic is ≈ $\frac{1}{20}$ of fundamental beam energy intensity when the beam is 55 µm away from the PoI.

The origin of the 3rd harmonic is not fully understood. However, two probable explanations exist for the presence of significant intensity of 3rd harmonic in the synchrotron beam during this test beam. First, the 3rd harmonic with reasonably low intensity is present in the beam and adding the 5 mm Al attenuator elevates the ratio of the 3rd harmonic intensity to fundamental energy. The 3rd harmonic intensity might still be reasonably low, but device C04-W0031 is a 110 µm-pitch, which is less affected by the charge spread and thus shows better resolution. The second explanation could be that the beam has a significant intensity of 3rd harmonic due to the beam configuration setup used during the test beam.

The beam intensity is still quite high despite being attenuated with 5 mm Al, as multiple low-intensity peaks due to signal pile-up are still visible in the ToT spectrum. The ToT spectrum of PoI(5, 5) for the beam at the pixel intersection in figure 7.4c shows inter-pixel charge sharing. However, this behaviour is expected in any pixel detectors. Figure 7.4d shows several low-intensity peaks corresponding to 15 keV as well as spectral peaks due to double and quadruple pile-ups in the PoI (5, 5) spectrum when the beam is positioned at the neighbouring pixel (PoI (5, 7)). This observation indicates charge generated in PoI (5, 7) is being diffused into PoI (5, 5).

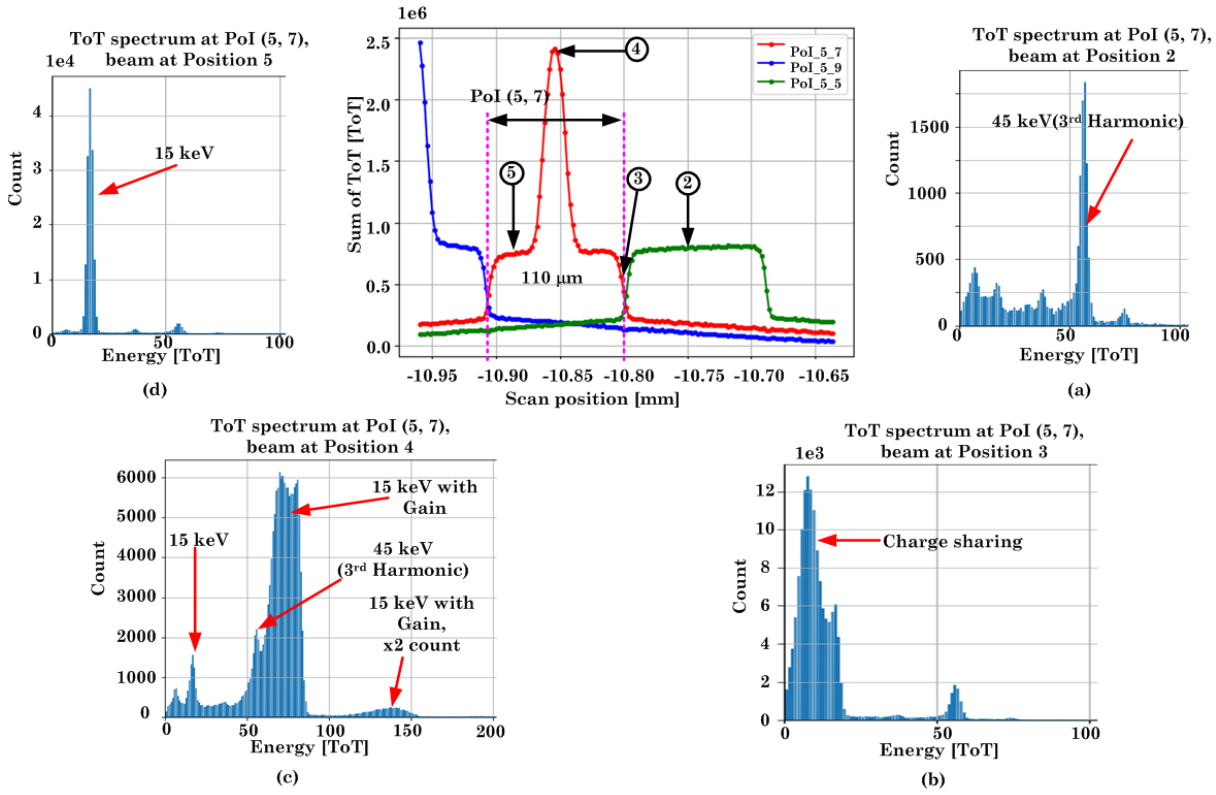

Figure 7.5: ToT spectra at PoI (5, 7) as a function of beam positions.

Figure 7.5 shows four ToT spectra of the pixel with gain, PoI (5, 7) corresponding to the signal capture for four beam positions. Pixels with and without gain produce identical ToT spectra when the beam is positioned outside the PoIs. The spectral peak due to 3rd harmonics and evidence of inter-pixel charge sharing are also observed in PoI (5, 7).

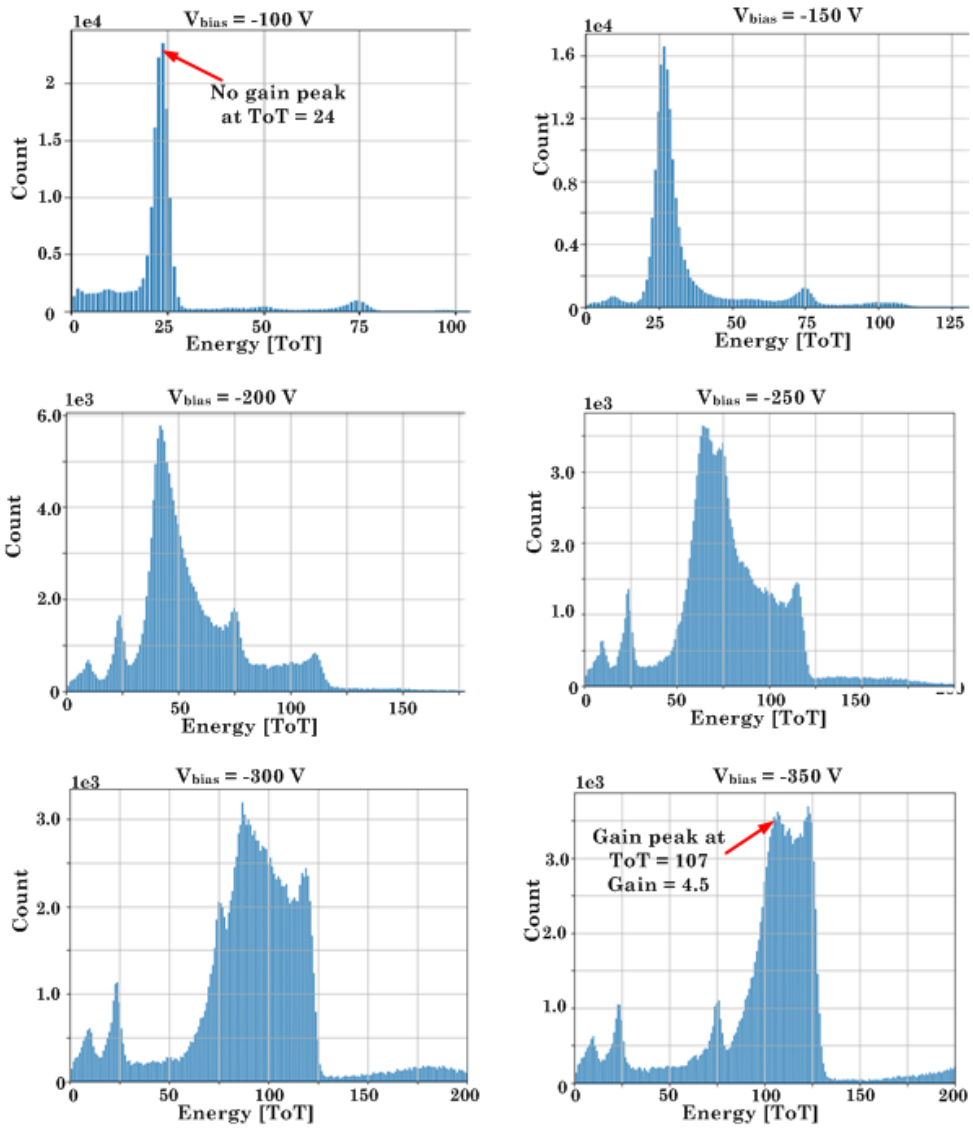

Figure 7.6: The evolution of ToT spectrum at the middle pixel, PoI(127, 127) as a function of bias voltages.

Figure 7.5c shows the ToT spectrum at PoI (5, 7) when the beam is in the centre of the pixel with gain. Two low-intensity peaks correspond to the fundamental energy, and 3rd harmonics are visible. PoI (5, 7) produces a broad ToT spectral peak corresponding to the fundamental energy with gain at around 60 ToT to 80 ToT. The broad peak indicates energy resolution degradation due to non-uniform gain in the multiplication region.

Figure 7.6 shows the evolution of the ToT spectrum of the pixel with gain at the middle pixel, PoI (127, 127) as a function of the bias voltage. The pixel is under-depleted at a bias

voltage of $-100\,\mathrm{V}$ and behaves like typical PIN silicon detectors. The PoI produces an output signal without gain with a spectral peak corresponding to the 15 keV synchrotron beam at $\approx 24\,\mathrm{ToT}$. The depletion region surpasses the multiplication layer at a bias voltage of $-150\,\mathrm{V}$, and the pixel starts to produce a signal with a small gain. This small gain shifted the spectral ToT peak to slightly greater than 25 ToT. The spectral ToT peak continues shifting to higher ToT values as bias voltage increases, and the ToT spectral peak is at $\approx 107\,\mathrm{ToT}$ when the pixel is fully depleted at a bias voltage of $-350\,\mathrm{V}$. This spectral peak shift corresponds to a gain factor of $\frac{107}{24} \approx 4.5$. The spectra at PoI(127,127) at $-350\,\mathrm{V}$ has an identical shape to the spectra at PoI(5, 7) in Figure 7.5(c).

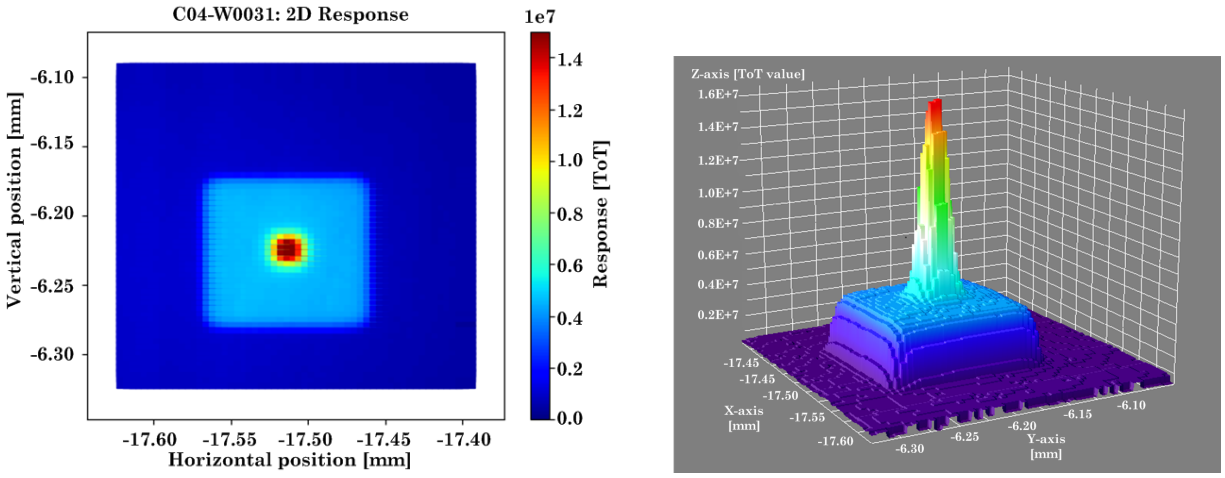

(a) *(b)*

Figure 7.7: A 2D view (a) and (b) 3D view of the ToT pixel response of the pixel with gain at PoI(127, 127).

The anomalies observed in the ToT spectra in Figures 7.5c and Figure 7.6 can be elucidated by the gain profile shown in the 2D scan in Figure 7.7b. The 110 µm-pitch LGAD has a narrow cusp spire gain profile with a base radius of $< 20\,\mu\mathrm{m}$, centred around the centre of the pixel. This observation is consistent with the TCAD simulation of gain in LGADs conducted in [25] shown in Figure 7.8a. Such profile is understood due to the distortion of electric field lines around the JTEs, causing the gain to vary based on the interaction position: electrons created in the centre experience maximum gain, those slightly outside experience reduced gain, and those far from the centre end up in the JTEs with no gain.

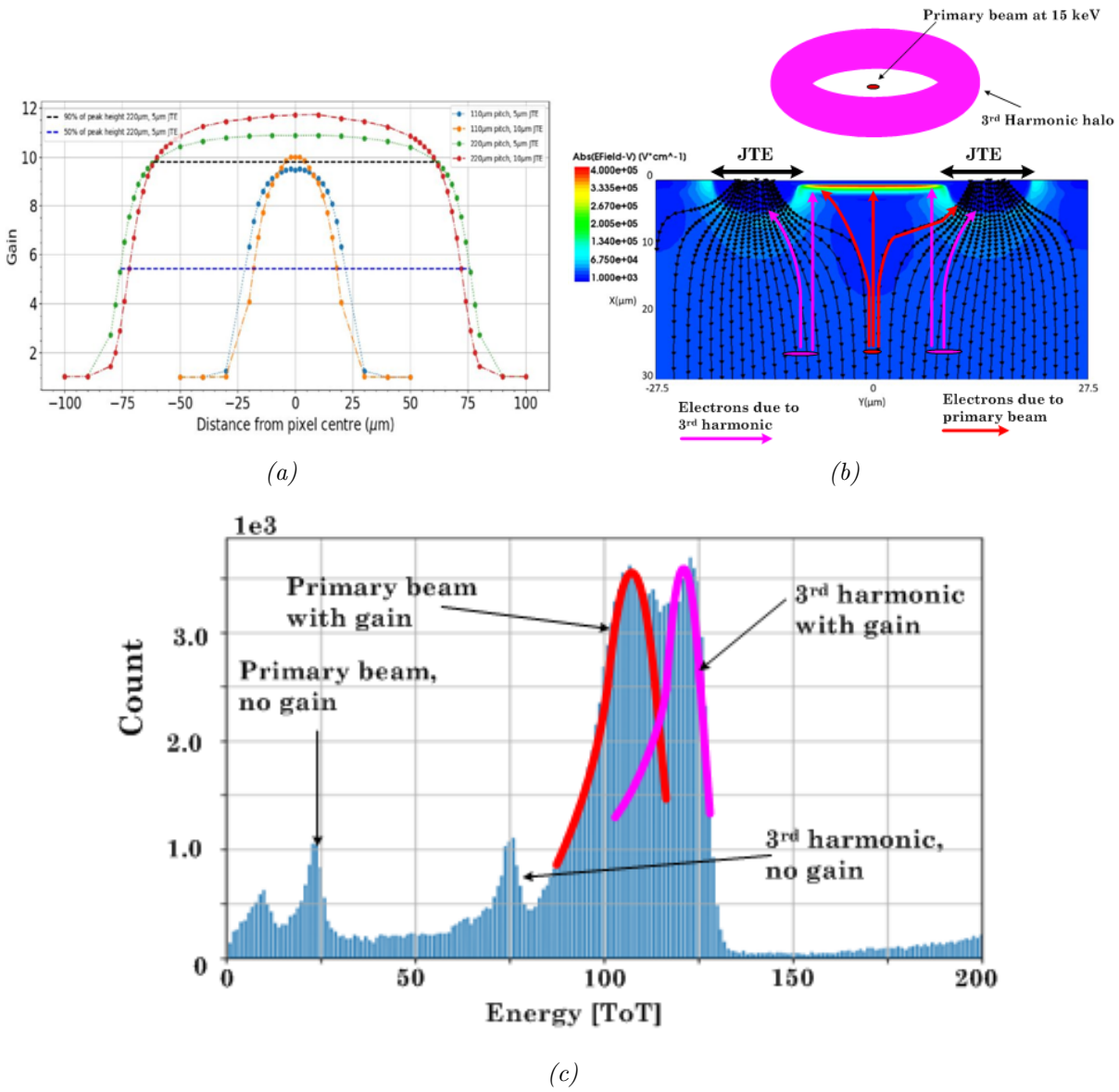

(a) *(b)* *(c)*

Figure 7.8: Understanding the anomaly in the ToT spectra at PoI (5, 7) and PoI (127, 127). (a) TCAD simulation of gain in LGADs [25], (b) Movement of electrons due to primary beam and 3rd harmonic under electric field in an LGAD with a JTE structure (plot adapted from [25] and (b) the explanation of the ToT spectra seen at centre of PoI (5, 7) and PoI (127, 127) at $-350\,\mathrm{V}$.

This explains the 15 keV spectrum with gain, which has a low-energy tail and peaking at ≈ 107 ToT, as well as the spectrum without gain, peaking at ≈ 25 ToT. Additionally, the synchrotron beam has a 3rd harmonic halo which generates electrons in the edges of the gain area and also in the no-gain area (see Figure 7.8b). This explains the presence of 3rd harmonic spectra both with gain (peaking at ≈ 120 ToT) and without gain (≈ 75 ToT). The complex spectral shape observed in Figure 7.8c is thus a composite of the overlapping

15 keV beam with gain and the 3rd harmonic peak with some gain.

7.2.2 Influence of JTE widths on gain and fill factor

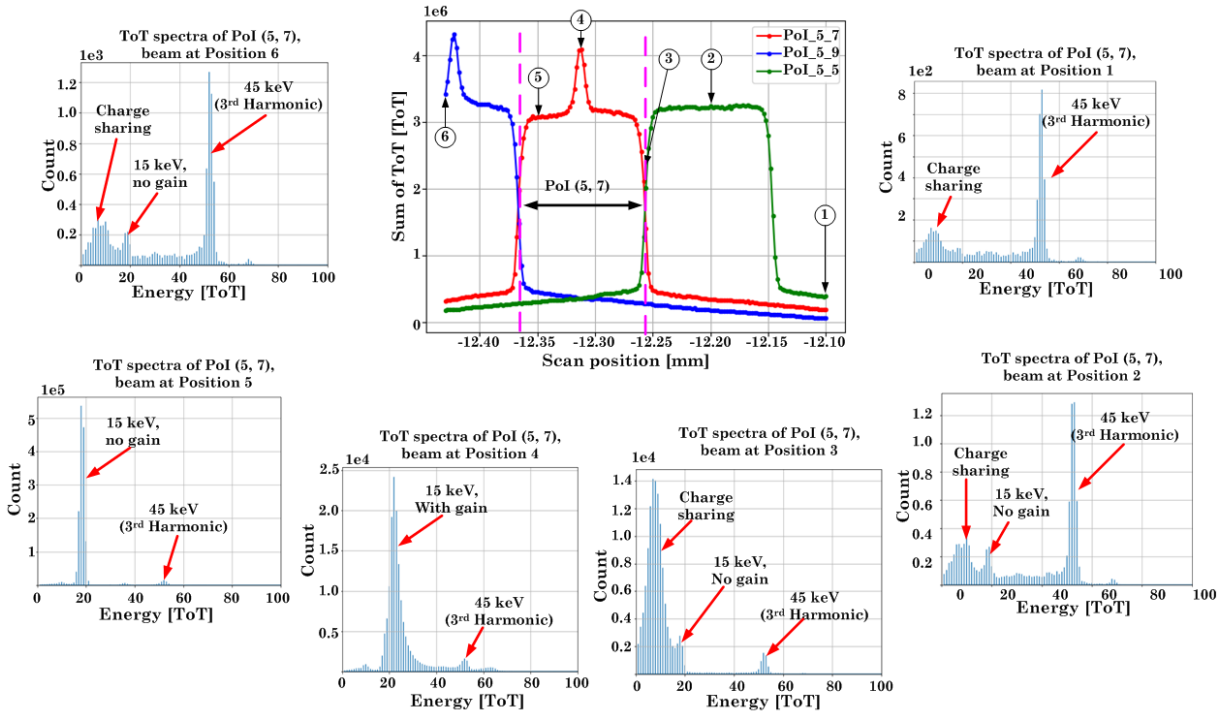

Figure 7.9: ToT pixel response across three PoIs and ToT spectra at PoI (5, 7) for 6 different beam positions in the F06-W0031 device.

Figure 7.9 shows the ToT pixel response across three PoIs: PoI (5,5), PoI (5,7), and PoI (5,9) and the ToT spectra at PoI (5,7) for 6 different beam positions in the hybrid pixel detector with 110 µm-pitch, 20 µm JTE LGAD, device F06-W0031. The F06-W0031 shared charge sharing and diffusion characteristics and identical pixel response as device C04-W0031 (10 μm JTE). However device F06-W0031 with a wider 20 µm JTE produces a much lower signal gain.

The comparison of pixel response across three PoIs in figure 7.10 and the 2D pixel response in figure 7.11 for two similar pixel-pitch LGAD with different JTE widths show that the width of the JTE affects the signal gain of LGAD detectors. The JTE width reduces the signal gain of an LGAD detector. The C04-W0031 with a narrow 10 µm JTE produces a signal gain of a factor ≈ 3.4 at a bias voltage of -350 V, while the F06-W0031 produces

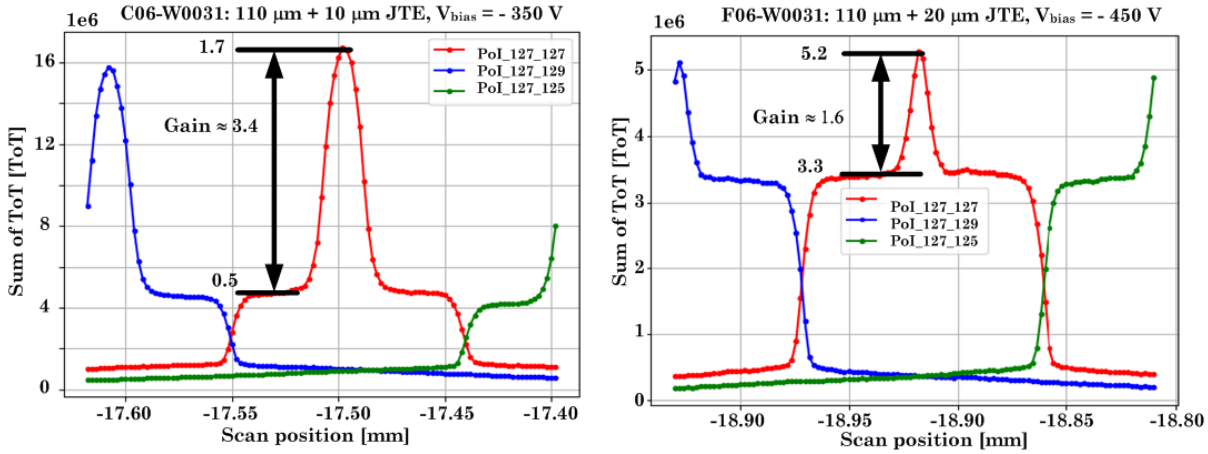

(a) Pixel response across three PoIs in device C04-W0031 (JTE = 10 µm).

(b) Pixel response across three PoIs in device F06-W0031 (JTE = 20 µm).

Figure 7.10: The influence of the JTE width on the signal gain in LGAD detectors.

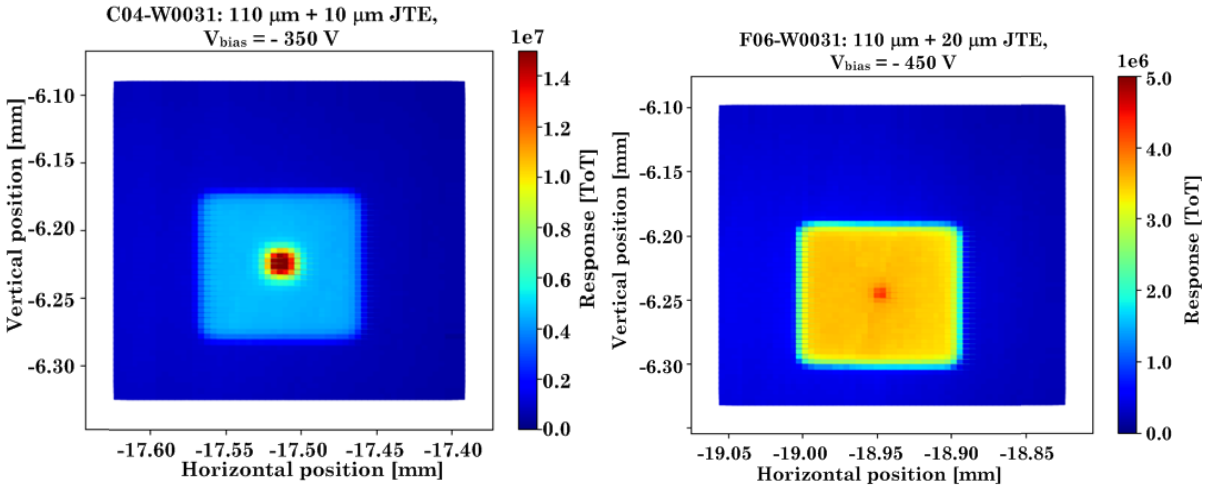

(a) 2D ToT pixel response of the C04-W0031.

(b) 2D ToT pixel response of the F06-W0031.

Figure 7.11: The influence of the JTE width on the fill factor in LGAD detectors.

a much lower signal gain of ≈ 1.6 despite being biassed at a much higher voltage. A further reduction in the fill factor was also observed for the Timepix3_LGAD with wider JTE.

The gain mechanism in LGAD explains the influence of the JTE width on the gain and fill factor. Charge multiplication via impact ionisation of electrons occurs in the multiplication layer where the electric field is ≈ 10^5 V/cm or higher [80]. The LGAD in its pixelated form constitutes the multiplication region and pixel border, where the pixel border is formed by the JTE and isolating structures such as a p-stop or p-spray. The JTE is added

around the pixel edges to suppress the electric field around this area while keeping the high electric field in the multiplication layer. The JTE structure prevents the LGAD from premature breakdown and enables a much higher voltage operation. The pixel border is a no-gain region which reduces the fill factor in LGAD devices—the fill factor increases with pixel size for a fixed pixel border width. The electric field lines in the LGAD are distorted toward the JTE structures, creating a non-uniform electric field [25]. The electric field lines are the pathway for the electrons as they drift towards the cathode. Therefore, most electrons are directed to the JTE instead of the multiplication region where the charge multiplication occurs. Increasing JTE width reduces the fill factor and ultimately decreases the gain.

7.2.3 Gain in small pixel LGAD

ToT pixel responses across three pixels with gain and control pixels in the hybrid pixel detector with a 55 µm-pitch LGAD (device D04-W0031) in figure 7.12a indicates that this device does not produce any significant signal gain. Similarly, the 2D ToT pixel response in the pixel with gain, PoI (127, 127) in figure 7.12b shows a flat response. Both observations validate the prediction in [24, 25], where the fill factor in the 55 µm-pitch LGAD is zero. The width of the multiplication region in the 55 µm-pitch LGAD is around 26 µm, which is almost the same width as the pixel border (JTE =5 µm + p-spray = 19 µm) [25]. Thus, all electrons are collected in the JTE, and the LGAD produces unity gain.

7.2.4 Timepix3_LGAD test beam summary

Beamline B16 produces a synchrotron beam of such high intensity that it induces multiple signal pile-ups at the hybrid pixel detector under test output. Therefore a beam attenuator was used to reduce the beam intensity and find a balanced acquisition parameter which allows high pixel hits within a short acquisition time while keeping the signal pile-up to a reasonable level. The maximum Al attenuator thickness of 5 mm was used throughout the test beam because this was the best option to proceed with the test beam. A small number

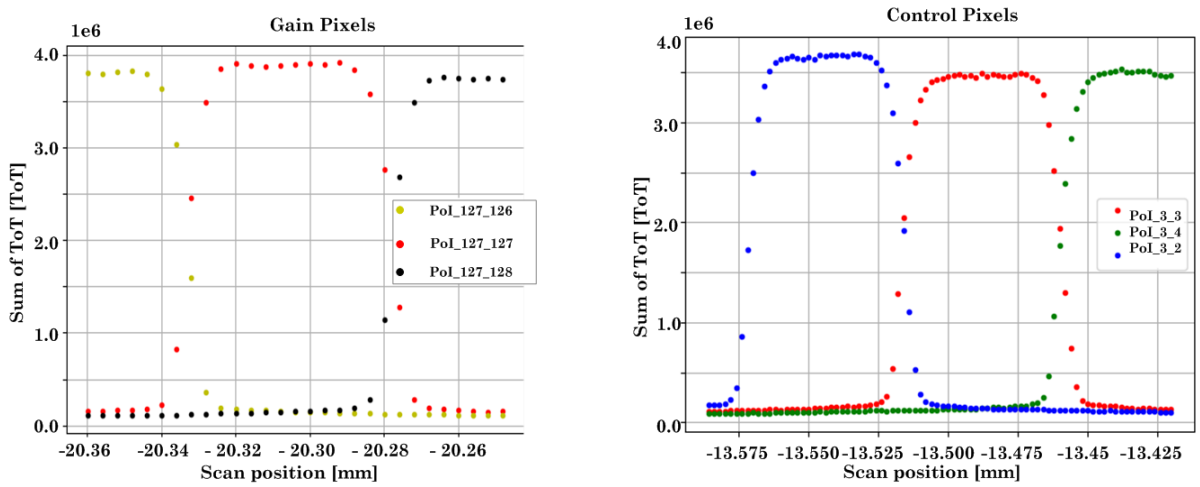

(a) ToT pixel response across three pixels with gain and control pixels in the small-pixel Timepix3_LGAD (pixel-pitch = 55 µm)

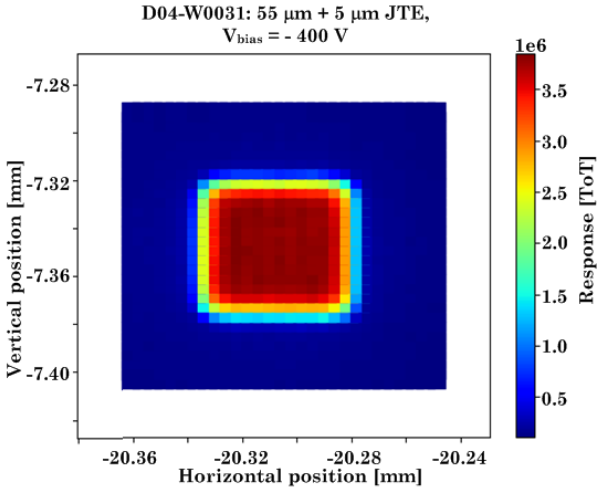

(b)

Figure 7.12: (a) ToT pixel responses across 3 PoIs at -400 V bias voltage for pixels with the multiplication implant (right) and pixels without multiplication implant (left). (b) The 2D ToT pixel response of the D04-W0031.

of signal pile-ups were present, but overall, it did not affect the integrity and quality of the data. The major issue during the test beam was the presence of the 3rd harmonic halo in the synchrotron beam. This beam artefact introduced interference in the pixel response, making it hard to understand the pixel behaviour.

The hybrid pixel detector with a 110 µm-pitch LGAD detector produced signal gains of ≈ 4.8 at a bias voltage of −350 V. The JTE width affects the signal gain and the fill factor in LGAD devices; increasing the width reduces the gain and the fill factor. This hybrid pixel

detector with LGAD detectors also showed the typical behaviour of pixelated detectors where reasonable pixel-to-pixel charge sharing and diffusion are normally present. The pixel-to-pixel charge sharing was not an issue for particle physics experiments because the centroid finding algorithm was already established. On the other hand, charge sharing may introduce a blurring effect in imaging applications. The hybrid pixel detector with a 55 µm-pitch LGAD did not produce signal gain, but this behaviour was expected and fully understood.

7.3 Pixel response and gain in hybrid pixel detector with iLGAD

This section describes the data analysis of the second synchrotron beam test campaign at the Beamline B16, Diamond Light Source facility, involving hybrid pixel detectors with iLGAD sensors in July 2021. The analysis is divided into three subsections. The first subsection examines the Al attenuator thickness's effect and finds a balanced acquisition setup for the test beam. The effect of beam size, threshold and charge sharing on pixel response is also investigated in this subsection because this effect was not considered during the previous beam test. The hybrid pixel detector with a standard PIN silicon sensor (device C10-W0068) is used in the study because it produces a well-understood pixel response. Moreover, the pixel response of such a hybrid pixel detector can be utilised as a reference to study the pixel response of a hybrid pixel detector with a similar-pitch iLGAD.

The second subsection presents a comprehensive analysis of the synchrotron beam test on the hybrid pixel detector with a 55 µm-pitch iLGAD (see device I11-W0068 in Table 7.1). Analysis includes the pixel responses at the edge and middle pixels, signal's gain evaluation and pixel response uniformity. The last subsection presents the findings from the synchrotron test beam on the 110 and 220 μm pixels Timepix3_iLGAD. Key analysis findings are presented, discussed and summarised.

7.3.1 Al attenuation and threshold study

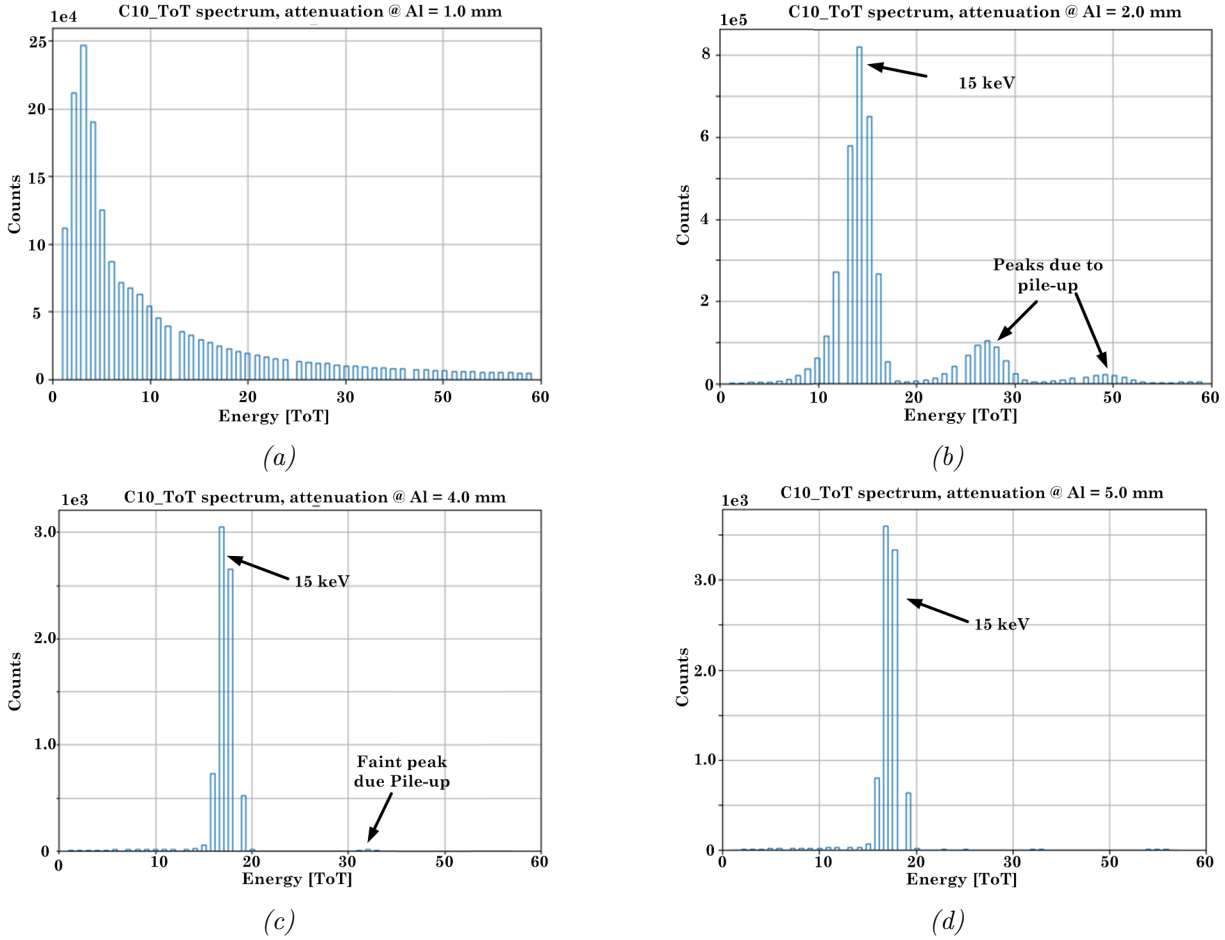

Figure 7.13: ToT spectra at PoI (128, 128) from the C10-W0068 device acquired with Al attenuator thickness of 1.0, 2.0, 4.0, and 5.0 mm *.*

Figure 7.13 shows how beam attenuation affects the single-pixel ToT spectrum of the standard PIN silicon detector (device C10-W0068). The PoI has a continuous spectrum at 1.0 mm Al attenuation because the high beam intensity causes many signal pile-ups. Increasing the Al attenuator thickness to 2.0 mm reduced the beam intensity and the number of signal pile-ups. Therefore, the PoI produces a distinct but broad spectral peak at 16 ToT corresponds to the 15 keV synchrotron beam. The PoI produces a much better ToT spectral peak at around 16 ToT to 17 ToT for Al attenuator thicknesses of 4.0 mm and 5.0 mm. However, a few double pile-ups are still faintly visible when 4.0 mm was used. So, the 5.0 mm Al attenuator is chosen for the test beam because this setting gives the

best attenuation and a balanced acquisition parameter. The 3rd harmonic peak is absent in the ToT spectrum for all Al attenuator thicknesses.

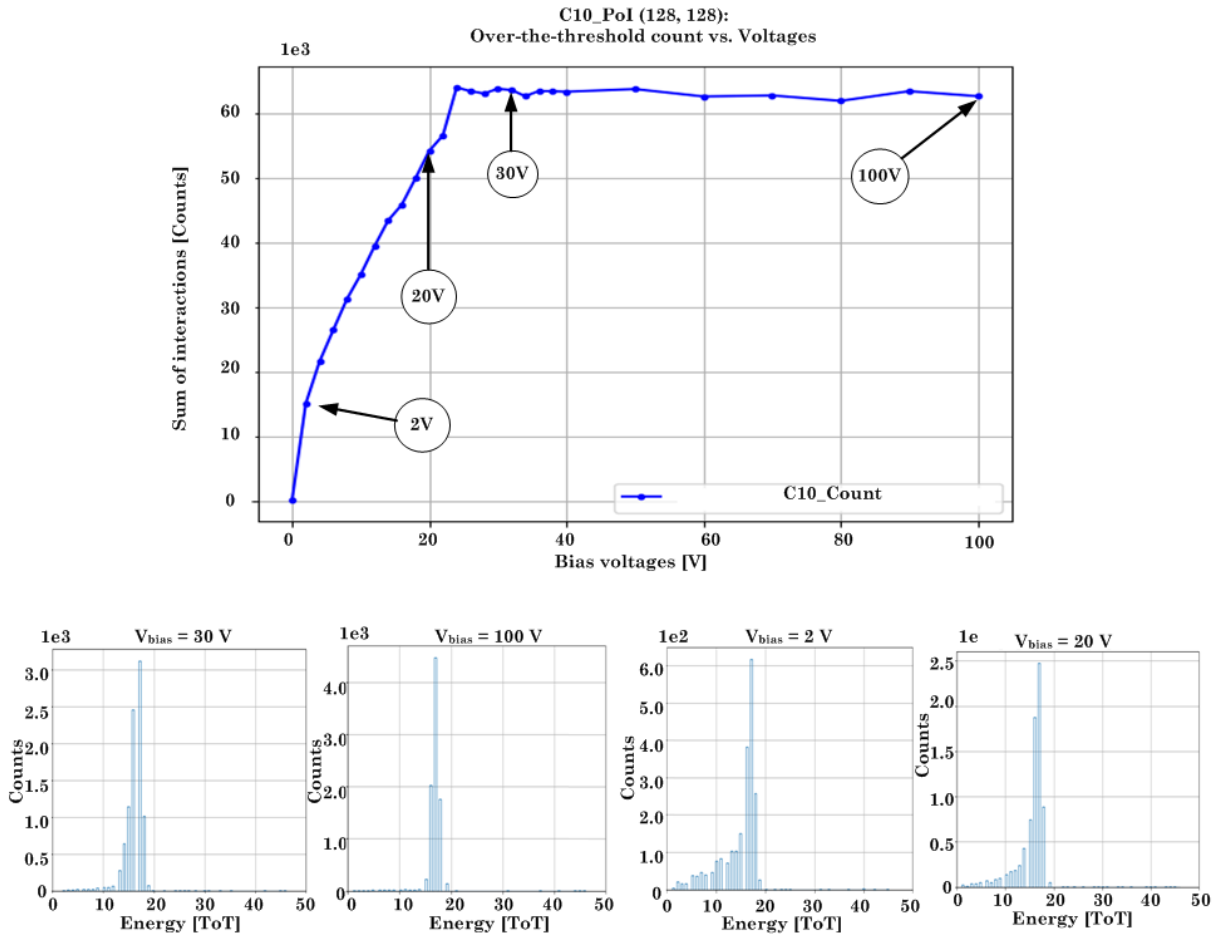

Figure 7.14: Sum of interactions and ToT spectra as voltage function for the Timepix3_Si at PoI (128, 128).

Figure 7.14 shows the over-the-threshold count pixel response as a function of bias voltages (left) and the ToT spectrum at 2, 20, 30 and 100 V in the PoI (128, 128). The pixel starts producing signals as early as 2 V bias but only achieves full depletion at bias voltage > 24 V. The pixel produces a broad ToT spectral peak with a tailing at the lower energy region when the pixel is under-depleted (2 V) or on the verge of depletion (24 V) states. The broad peak and tailing in the spectrum indicate energy resolution degradation due to partial charge collection. The spectral resolution improved, and the tailing gradually diminished once the pixel entered full depletion. The spectral resolution at 100 V because

the pixel achieves full charge collection due to a much stronger electric field.

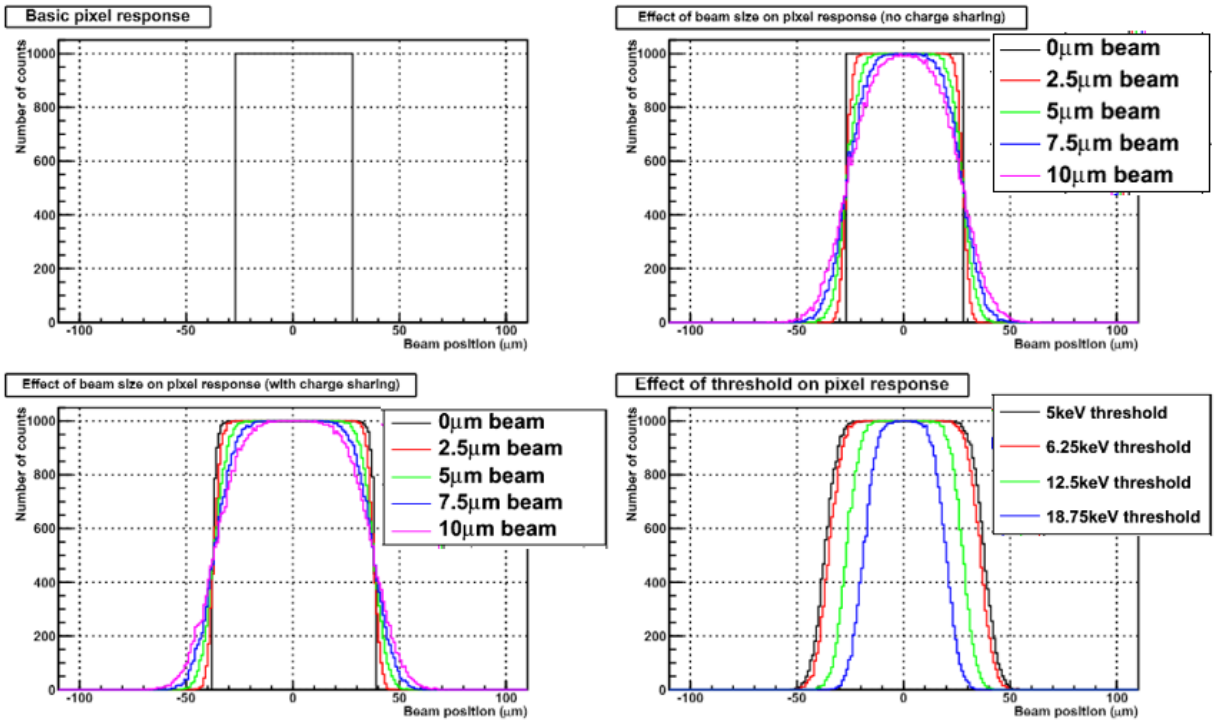

Figure 7.15: Pixel response simulation to evaluate the effect of beam size, charge sharing and threshold on the pixel response.

A pixel response simulation was conducted before the test beam to understand the effect of beam size, threshold and charge sharing on the pixel response. The response of a square pixel and synchrotron beam is simulated by convoluting a step function with a Gaussian function. The effects of beam size, charge sharing and threshold were simulated by varying the width of the Gaussian and step functions. The simulated responses are shown in figure 7.15 and show that the beam size only affects the pixel response's *shape*. On the other hand, both charge sharing and threshold affect the pixel response's *width* but not the *shape*.

Figure 7.16 shows the over-the-threshold count and ToT pixel responses across three PoIs for the C10-W0068 device and the ToT spectra at PoI (128, 128) for three different beam positions; beam at outside of the pixel (position 3), beam in the inter-pixel (position 2)

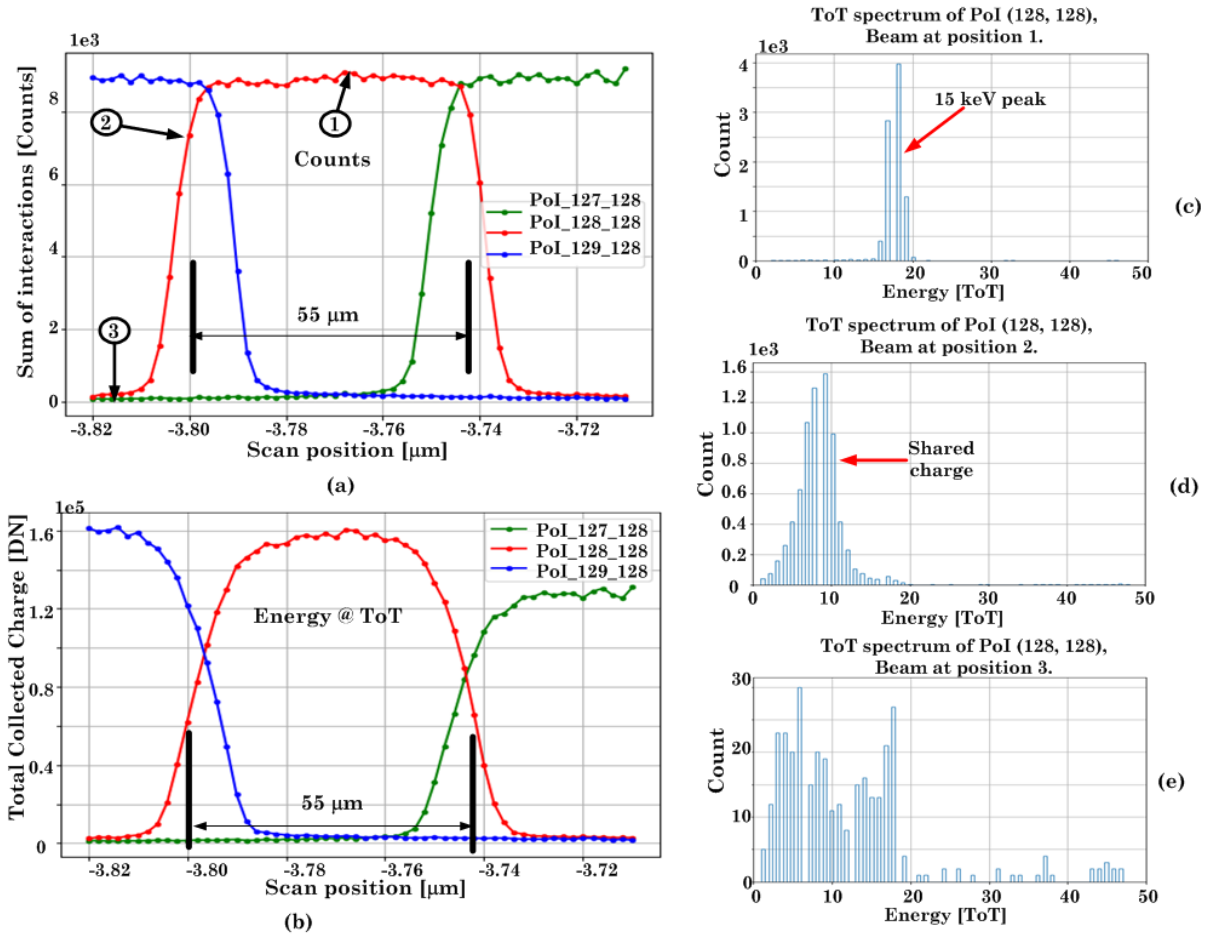

Figure 7.16: Line Scan across three PoIs for the Timepix3_Si. Plots of Sum of interactions and collected charge as a function of scan position (a & b) and the ToT spectra of PoI (128, 128) for three beam position (c, d, & e).

and beam in the middle of the PoI (position 1). The over-the-threshold count response in figure 7.16a appears wider than the effective pixel size due to the combined effect of charge sharing and threshold. A prominent ToT spectral peak corresponding to the 15 keV at ≈ 18 ToT is produced when the beam is at Position 1 (see figure 7.16c). A reasonable charge sharing is observed when the beam is at the inter-pixel area and negligible residual signal when the beam is outside the PoI (see figure 7.16d). These characteristics are expected for typical hybrid pixel detectors. As shown in figure 7.17, the hybrid pixel detector with a standard PIN silicon sensor (C10-W0068) produces a uniform 2D pixel response.

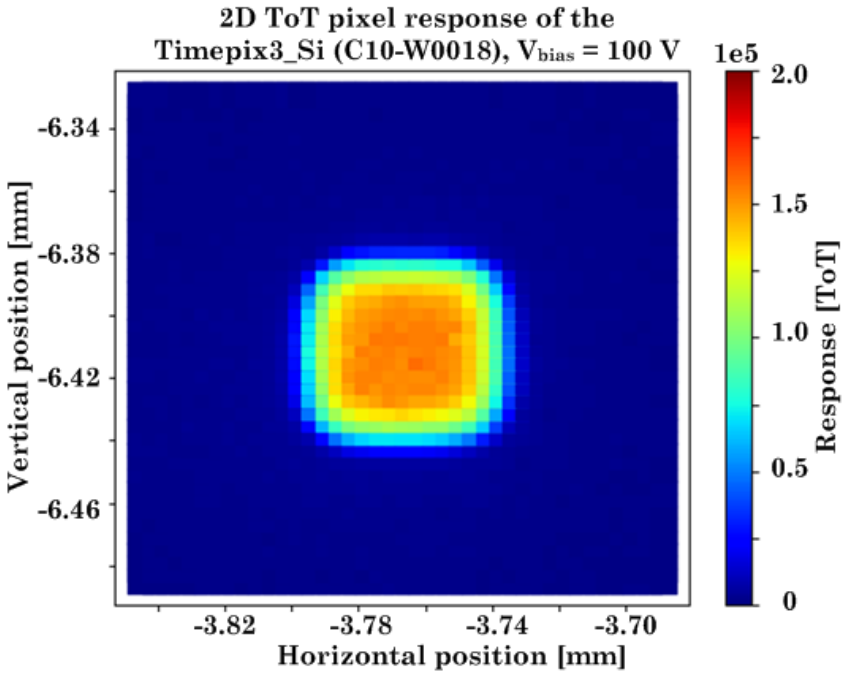

Figure 7.17: 2D ToT response map of the C10 device.

7.3.2 Pixel response and gain in a 55 µm-pitch iLGAD (device I11-W0018)

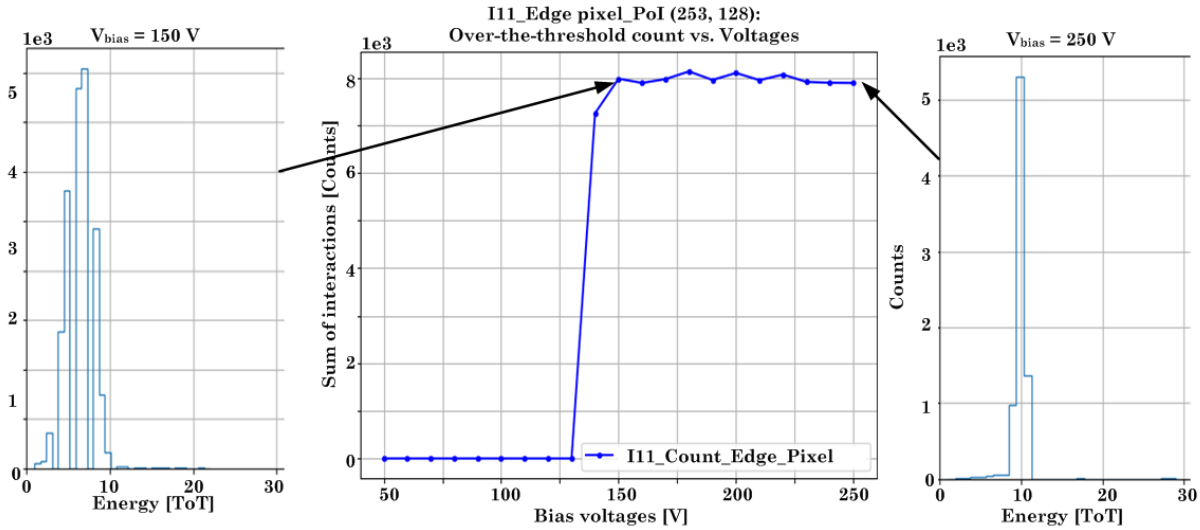

Figure 7.18: Voltage Scan pixel response and the ToT spectra at the edge pixel, PoI (253, 128)

Figure 7.18 shows the over-the-threshold pixel response of the PoI (235, 128), the control pixel of the hybrid pixel detector with a 55 µm-pitch iLGAD (device I11-W0018) as a

function of bias voltages. The control pixel shows no signal above the threshold until the bias voltage reaches around 140 V. This PoI shows a typical characteristic of a PIN silicon detectors which only functions when fully depleted. The control pixel is fully depleted at a bias voltage higher than 150 V. A substantial voltage is required to fully deplete this device because the substrate is a high-resistivity ($\approx$ 10 kΩ), 250 µm thick silicon. Moreover, the depletion starts from the top section (bias voltage connection) to the collecting pixel at the bottom. Therefore, the bulk must be fully depleted for the pixel to function. ToT spectra at the edge of depletion (150 V) and fully depleted (250 V) indicate that no signal gain is produced in this pixel.

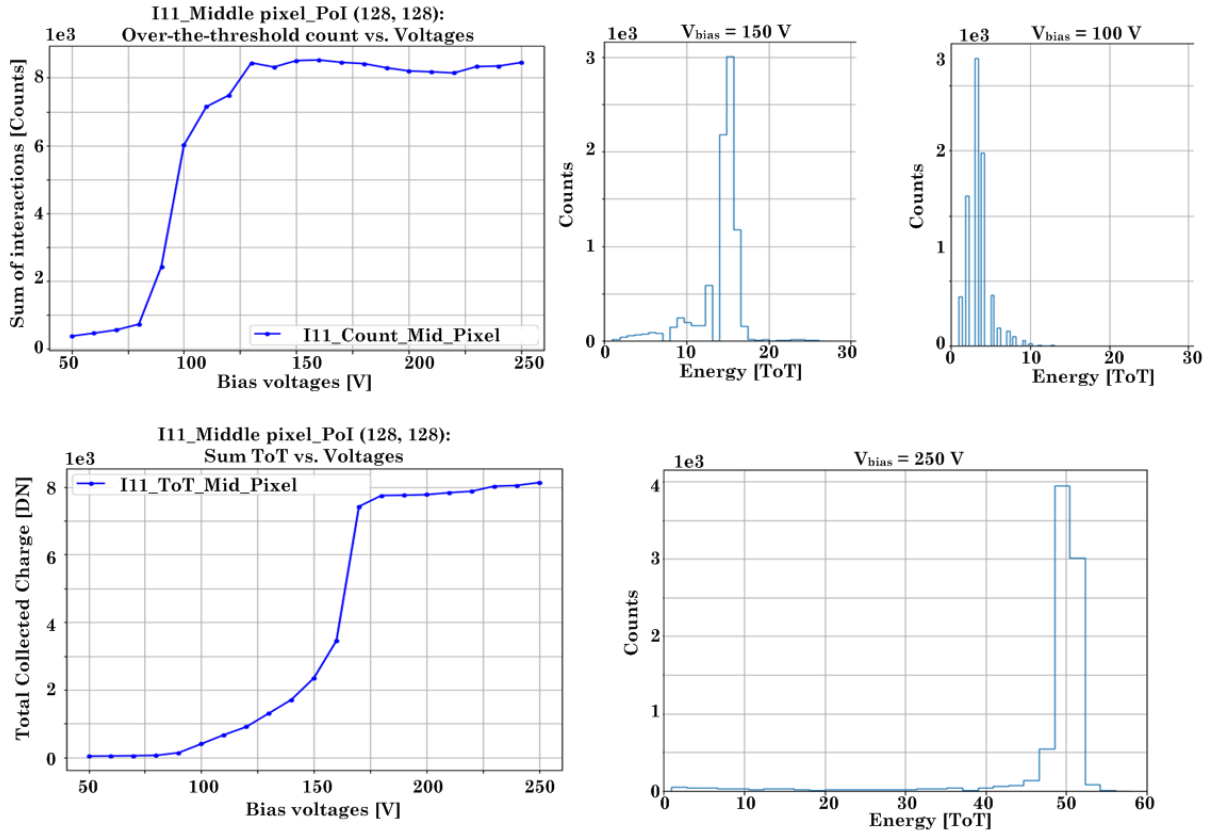

Figure 7.19: Voltage Scan pixel response and the ToT spectra at the middle pixel, PoI (128, 128)

As shown from the over-the-threshold and ToT pixel responses on the left side of figure 7.19, the pixel with gain, PoI (128, 128) is already producing an output signal at a bias voltage of $\approx$ 80 V. This observation shows a typical characteristic of an LGAD sensor

where a signal is produced once the multiplication layer is fully depleted. In this case, the multiplication layer is fully depleted at a bias voltage above 80 V. The three ToT spectra graphs on the right side of figure 7.19 show the ToT spectral for 100, 150 and 250 V bias voltages. The PoI demonstrates a significant spectral peak shift as a function of bias voltages (16 ToT at 150 V to 50 ToT at 250 V). This trait indicates a typical behaviour of a fuly functional LGAD detectors.

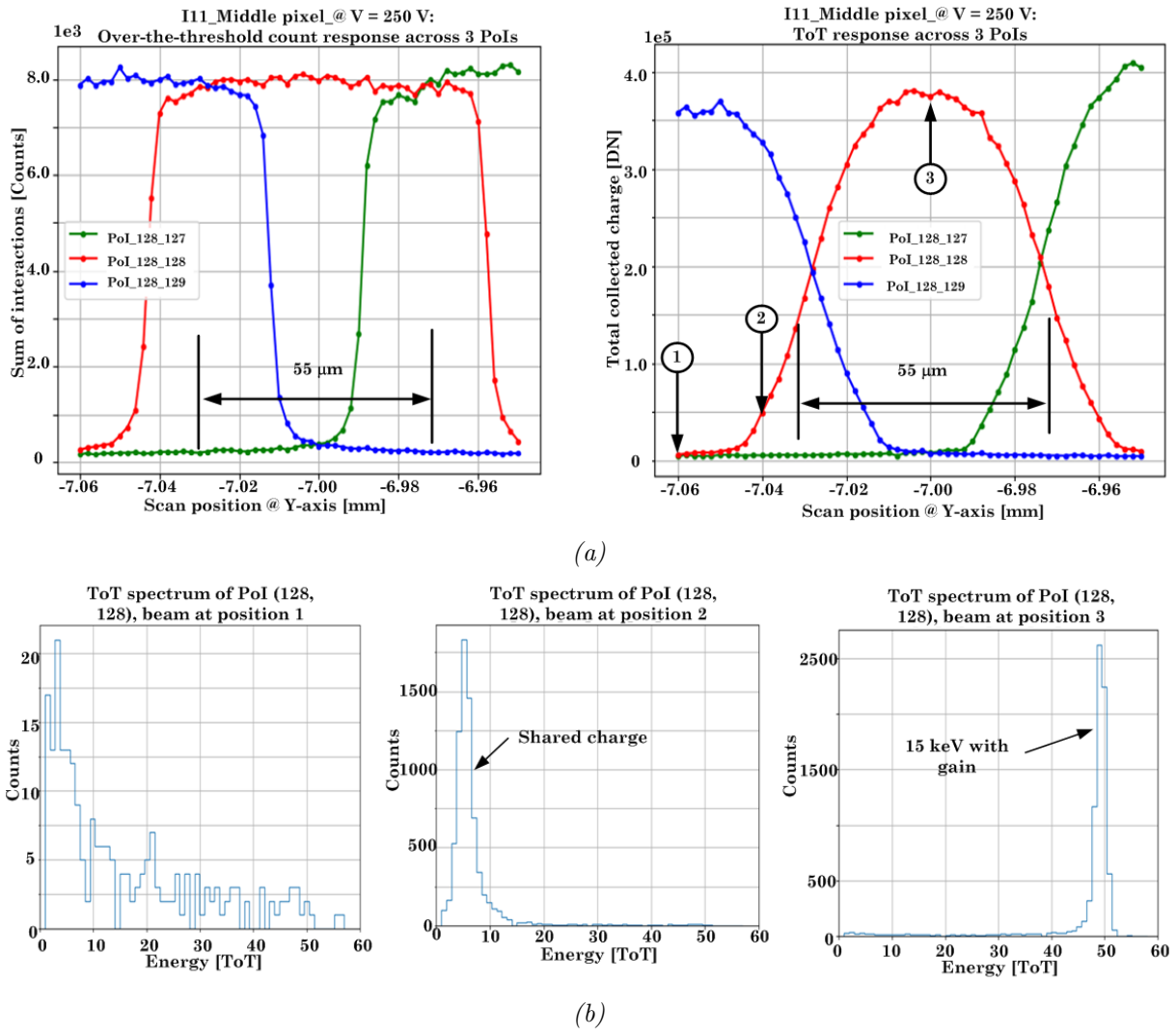

Figure 7.20: Line Scan at 250 V bias voltage over three PoIs in the middle of the I11 device. (a) Over-the-threshold count and sum of ToT responses and (b) the ToT spectra of PoI (128, 128) for beams at outside the PoI, at the inter-pixel and at the middle of the PoI

Figure 7.20a shows the *Line Scan* the over-the-threshold count and the sum of ToT pixel re-

sponses of the middle pixel (pixel with gain) at -250 V bias voltage. The over-the-threshold count pixel response conforms to a step function response. However, the response appears outspread over the pixel width due to the combined effect of threshold setting and charge sharing. The ToT spectra of the PoI (128, 128) in figure 7.20b support this assumption, where a substantial charge sharing is observed when the beam is in the inter-pixel area. A spectral ToT peaking around $\approx$ 49 ToT is obtained at 250 V when the beam is in the centre of the PoI.

Figure 7.21 shows the evolution of the ToT pixel response across 6 PoIs at the edge pixel for various bias voltages. The scan covers 3 PoIs without the multiplication implant (PoI_128_254, PoI_128_253 & PoI_128_251) and 3 PoIs with the multiplication implant (PoI_128_251, PoI_128_250 & PoI_128_249). No signals were observed in the pixels without the multiplication implant until the bias voltage reached -150 V. On the other hand, signals were observed as early as 125 V bias voltage for the pixel with the multiplication implant. An intriguing anomaly occurs at the border of pixels without multiplication implants and pixels with implants. When the pixel was sub-depleted (V_{bias} = 150 V), the response of the PoI pixel without the multiplication implant appears spread towards the pixel with the multiplication implant. The spread gradually diminishes as the bias voltage increases but did not vanish fully.

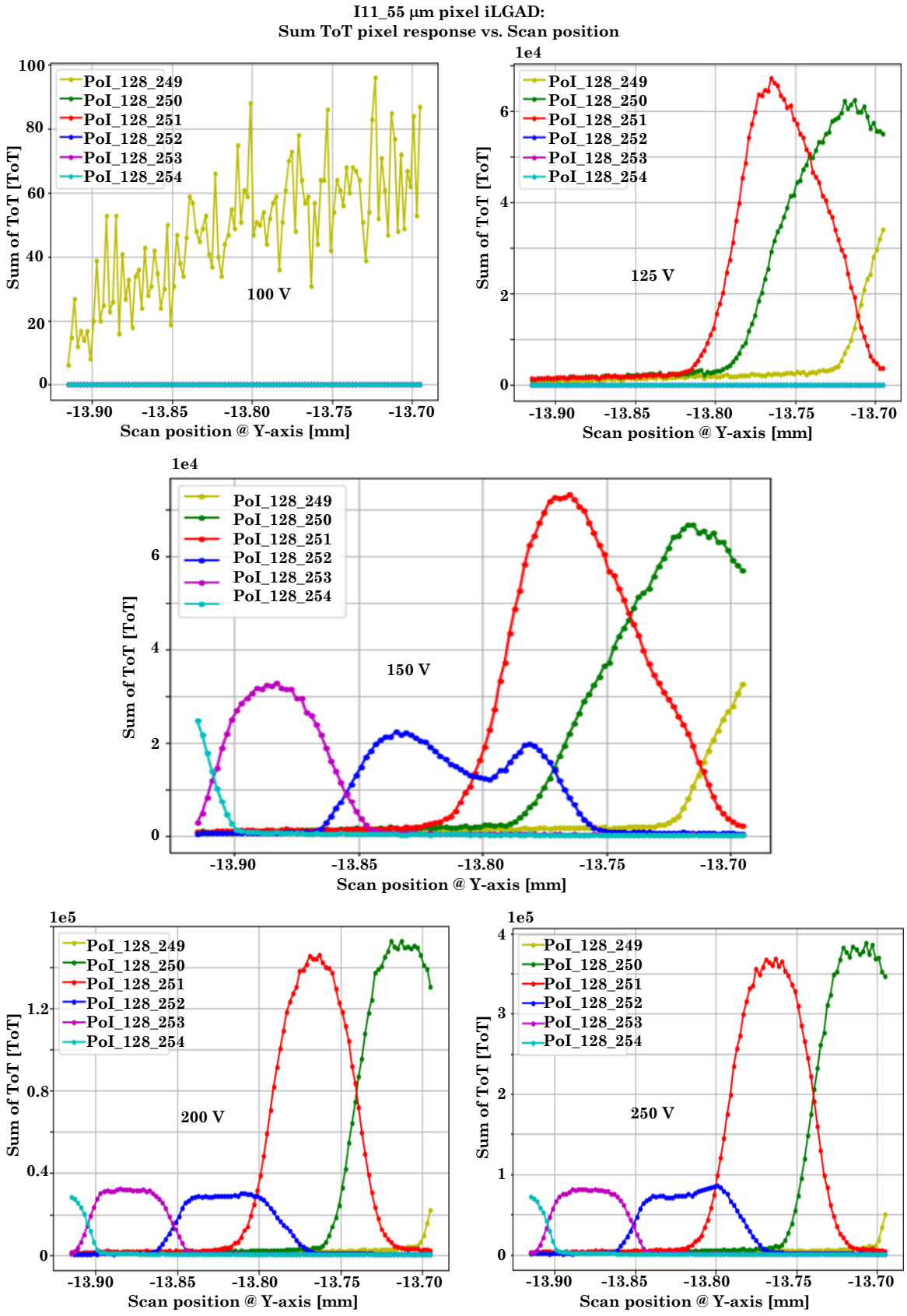

Figure 7.21: The evolution of the ToT pixel response across 6 PoI at the edge pixel of the I11-W0068 as a function of bias voltage.

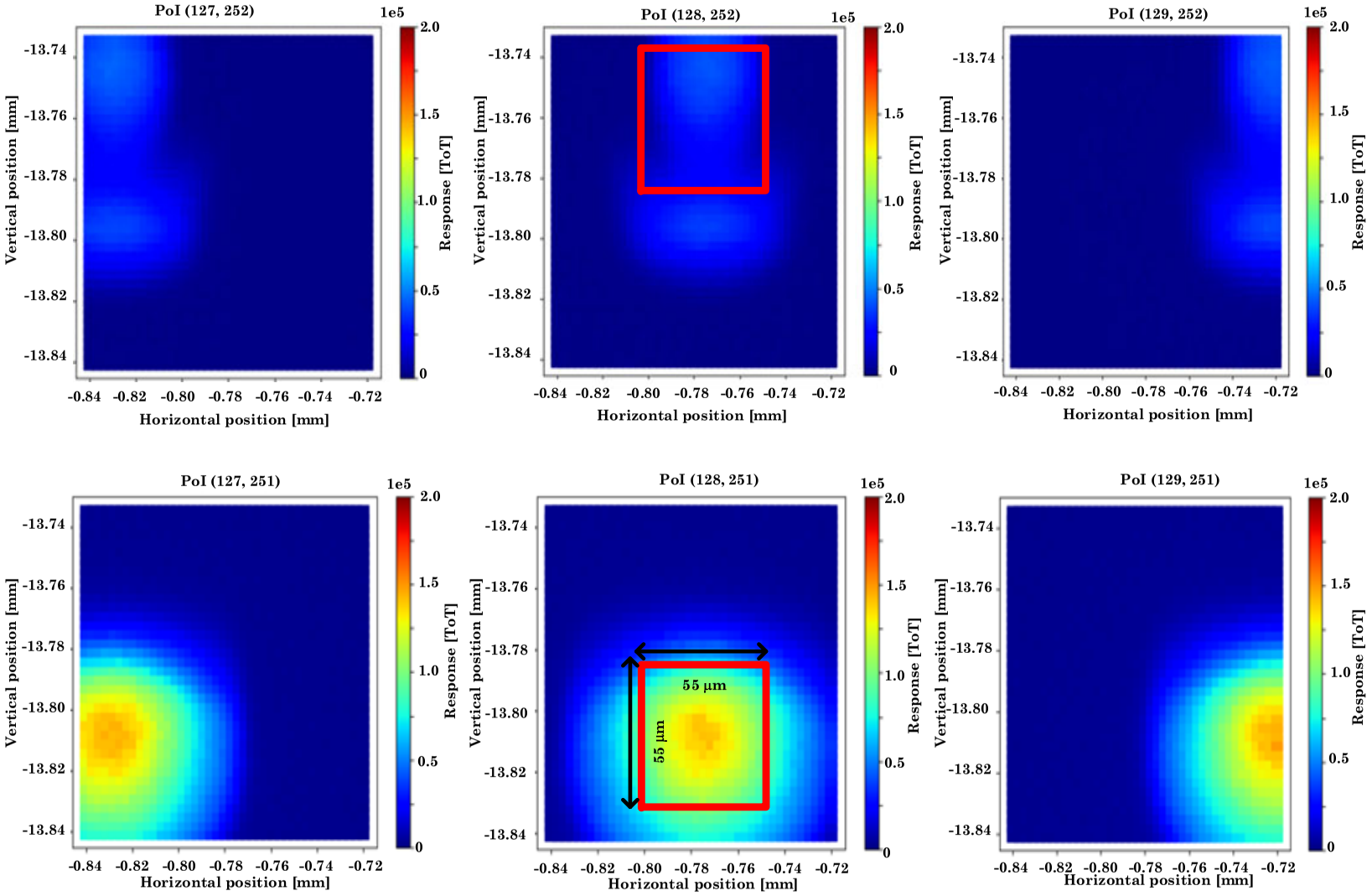

Figure 7.22: 2D sum of the ToT pixel response across two PoIs of I11 at 150 V bias voltage. Read square indicates pixel area.

The 2D pixel response at 150 V in figure 7.22 gives a clearer graphical visualisation of the anomaly. As shown in figure 7.22 (Top row - middle), charges generated in PoI without gain, PoI (128, 252) are diffused towards the pixel with gain, PoI (128, 251). The charge diffusion distorts the pixel response of the PoI without gain. This anomaly is not fully understood. However, it may be related to the vast differences in the electric field between these two pixels. The PoI with gain has a stronger electric field between the two because it has a multiplication implant layer. However, a comprehensive study of the electric field profile in the border region is necessary to corroborate this assumption. The PoI with gain (iLGAD) produces a round instead of a square pixel response when the pixel is on the verge of depletion states (see figure 7.22 - bottom row). This observation indicates that the iLGAD must be fully depleted for fully operational.

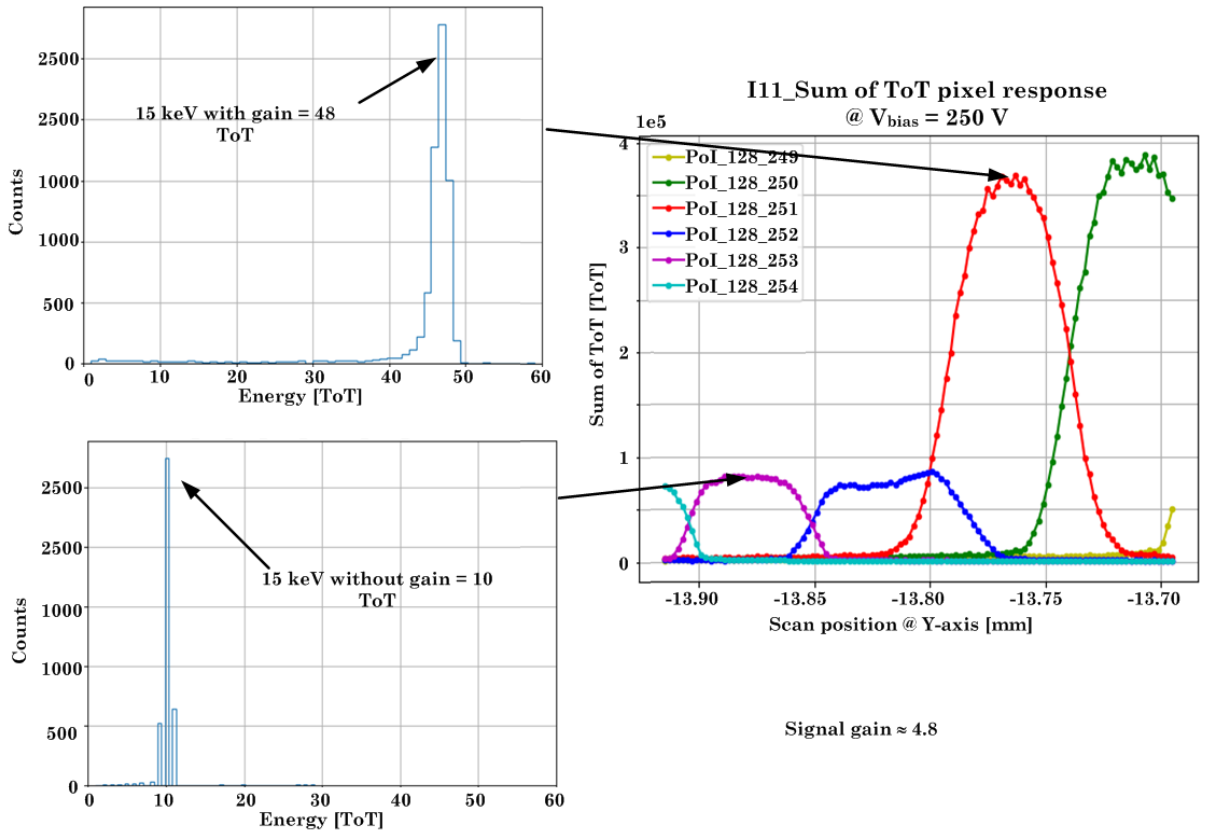

Figure 7.23: The estimated signal gain in the hybrid pixel detector with a 55 µm-pitch iLGAD (I11-W0068 device).

Figure 7.23 shows the ToT pixel response of the I11 device and the ToT spectra for the PoIs with and without gain. The significant increase in the pixel response seen in the PoI with gain and also the significant shift in the ToT spectral peak (see figure 7.23 (left)) show the demonstration of signal gain in small-pixel iLGAD device. Moreover, the uniform increase in the pixel response of the PoI with gain (PoI_128_251) indicates that this device exhibits a significantly large fill factor. The signal gain extracted from the single-pixel response of a PoI with gain in device I11-W0068 at a bias voltage of 250 V is ≈ 4.8.

7.3.3 Pixel response and gain in 110 and 220 µm-pitch iLGADs

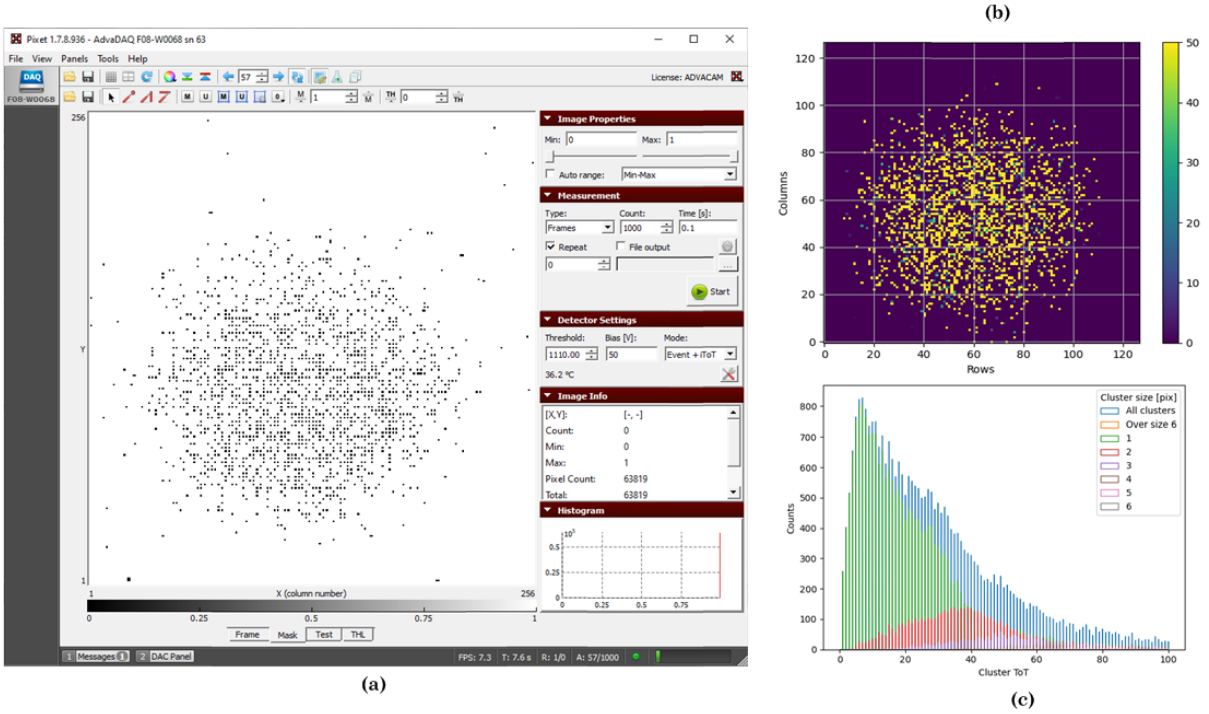

Figure 7.24: Laboratory test of the F08-W0068.(a) Threshold setup, (b) flat panel image of XRF_Tb, and (c) ToT spectrum of XRF_Tb.

Noisy pixels concentrated in the middle of the sensor were observed during the threshold equalisation (see figure 7.24a). Hence, a high threshold level was used on this device to get meaningful data. ToT spectrum from the laboratory test with XRF_Tb shows a broad continuous spectrum without any prominent spectral peak. Based on the preliminary test, it was expected that the hybrid pixel detector with a 110 µm-pitch iLGAD (device F08-

W0068) would perform poorly.

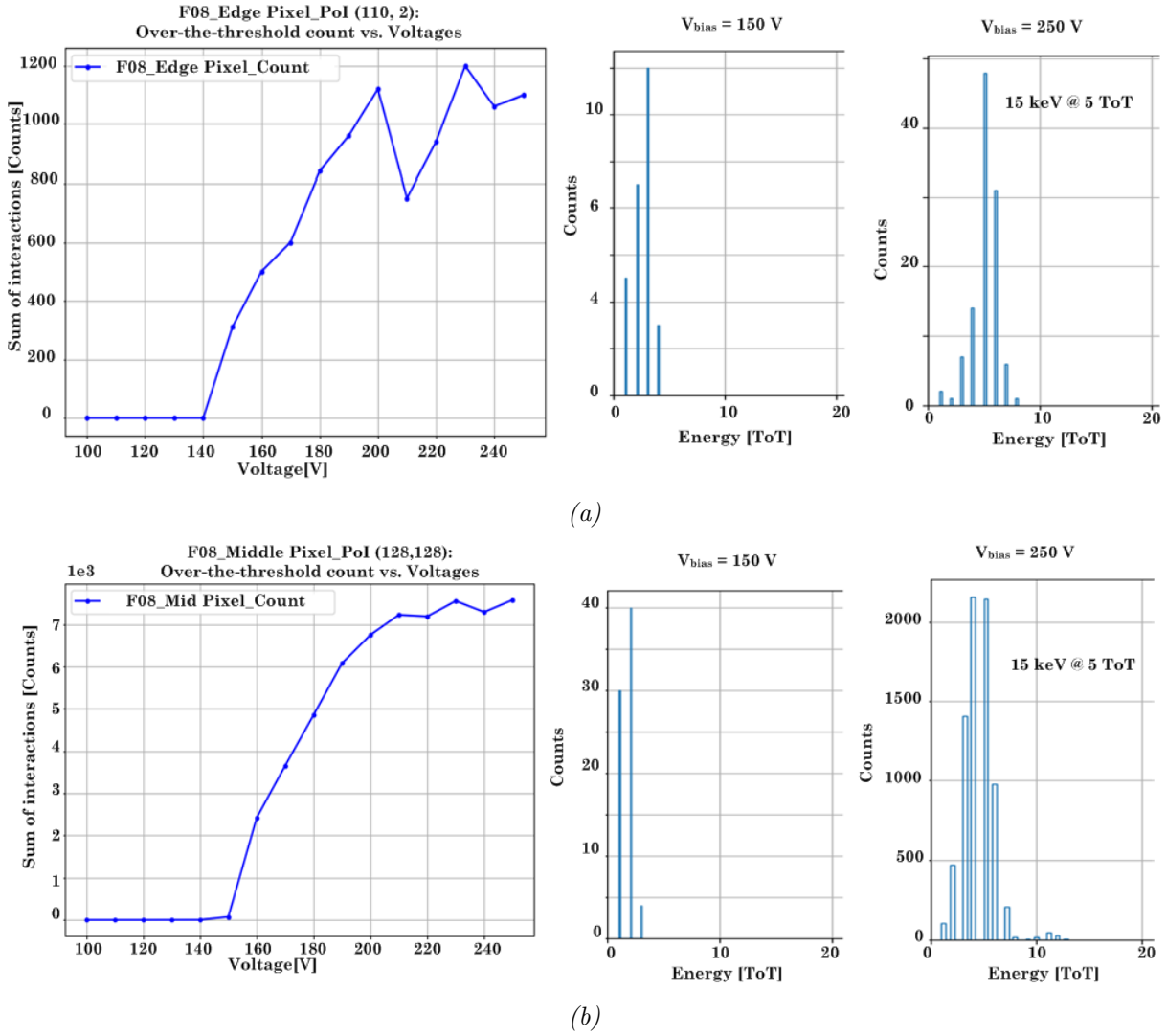

Figure 7.25: Sum of interactions as a function of bias voltages and the ToT spectra at 150V and 250V for (a) no-gain pixel (edge pixel) and (b) pixel with gain (centre pixel)

The performance of device F08-W0068 was inconsistent during the test beam. Multiple scans at several pixel coordinates were performed to find the best PoI for conducting the subsequent synchrotron test beam. The signal noise level was also high, so a higher threshold level was applied to get reliable data. Over-the-threshold count pixel response as a function of the bias voltages at the edge pixel, PoI (110, 2) in figure 7.25a shows a reduced count value due to a higher applied threshold. There was a momentary plunge in pixel response around the 200 230V region for unknown reasons. Apart from this, there were no

significant changes in the ToT spectra for the 150 V and 250 V bias voltages, indicating that the device produces little or no signal gain.

The *Line Scan* pixel response for multiple scan positions along the Y-pixels in figure 7.26 demonstrates the inconsistent performance of device F08-W0068, where the summed ToT pixel response varied greatly from one pixel to the next. Pixel response across 6 PoI in 5 different Y-pixel positions shows no response in pixels without the multiplication implant and irregular pixel response in pixels with the multiplication implant. Along Y-pixels 144 and 188, very non-uniform signal gains were observed (see figure 7.26a & figure 7.26d). Pixel response along Y-pixel 155 in figure 7.26b shows a broader pixel response (width $\approx$ 2 pixels) in PoI (7, 155), whereas signals in PoI (5, 155) and PoI (9, 155) were missing. Meanwhile, along Y-pixel 168, only pixels adjacent to control pixels show signal response (see figure 7.26c (c)), a similar response was observed along Y-pixel 213 in figure 7.26e albeit with a narrower pixel response.

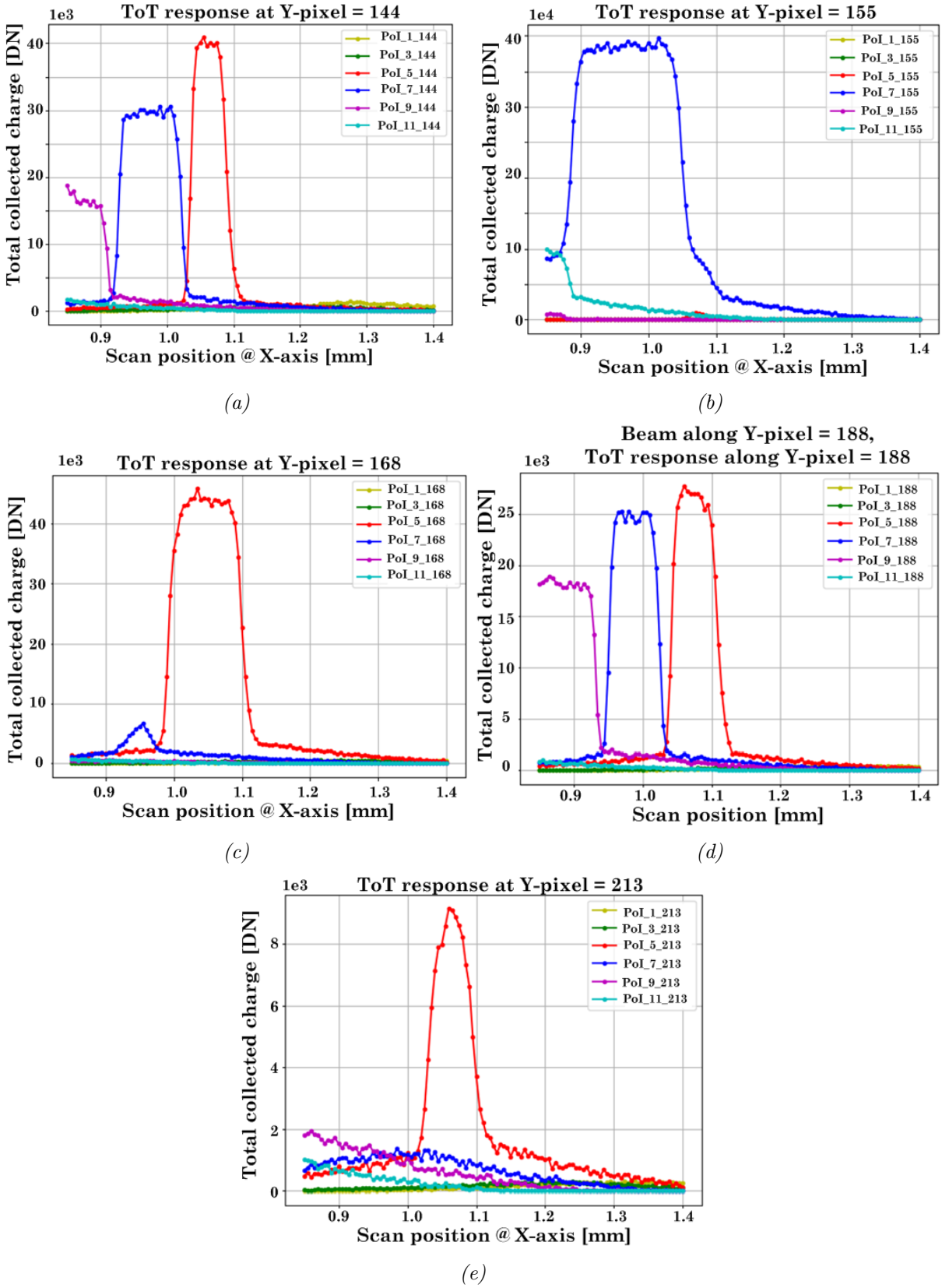

Figure 7.26: Variations of theLine scan sum of ToT pixel responses across 6 PoIs for various scan coordinates, $V_{\text{bias}} = 250\,V$.

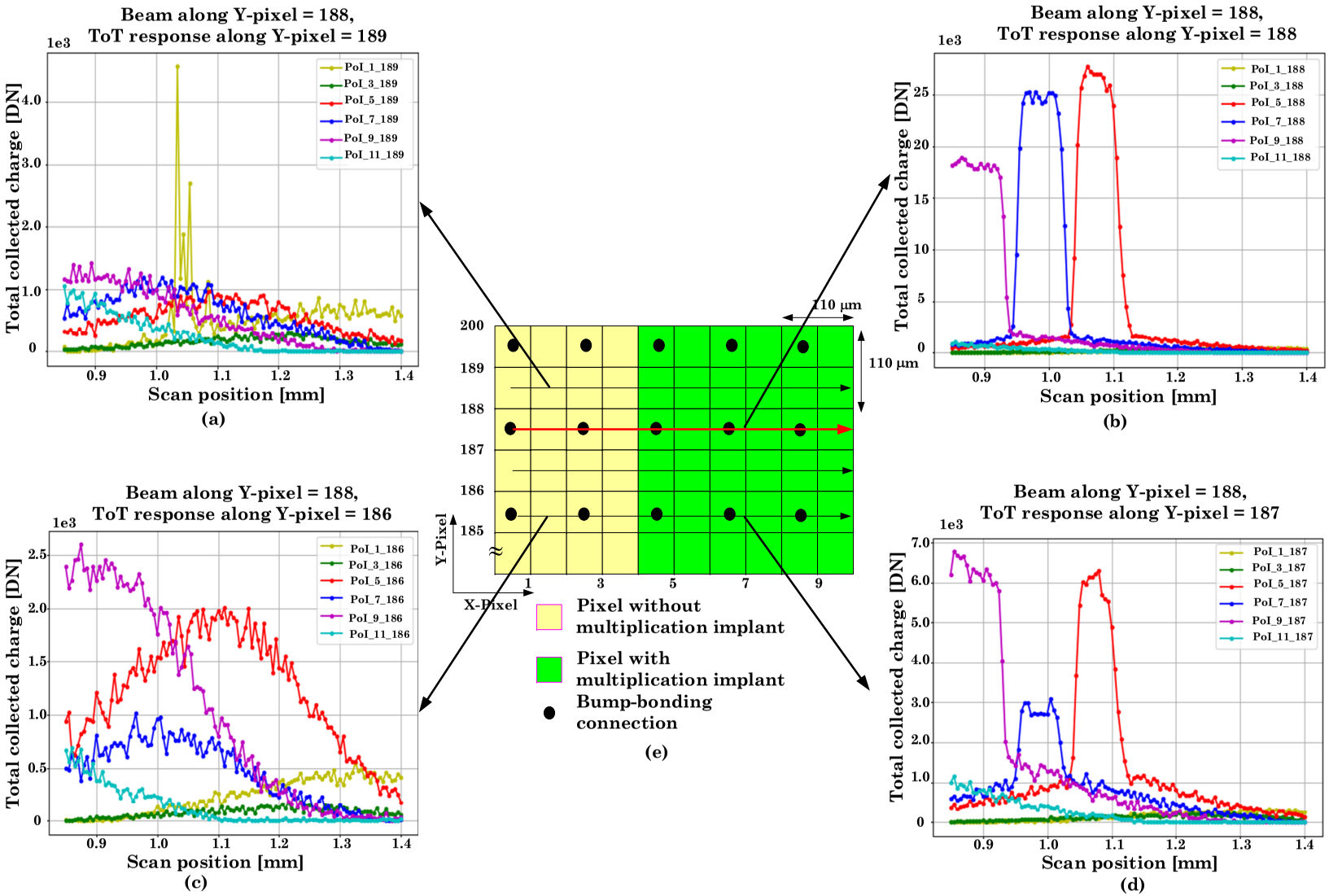

Figure 7.27: Induced signal in the neighbouring unconnected pixel.

The synchrotron test beam on device F08-W0068 uncovers a significant charge induced in the adjacent not only in the connected pixels but also in the unconnected pixels. Figure 7.27 shows the summed ToT pixel responses across 6 PoIs in 3 adjacents Timepix3 pixel arrays when the beam was scanned along the Y-pixel 188. Device F08-W0068 is a 110 µm-pitch, so the bump-bonding connections with the Timepix3 pixels are along Y-pixels 188 and 186, while Y-pixels 189 and 187 are unconnected. As shown in figure 7.27a, there were little signals along Y-pixel 189, above the PoIs where the beam was scanned. However, huge signals were observed in the pixels below, along the Y-pixel 187 (see figure 7.27d), implying that a significant amount of charges were induced in the adjacent unconnected pixels. This trait is odd because there should not be any signals in these unconnected pixels. A significant pixel response was also observed along the Y-pixel 186 (connected pixels), two pixels below the scanned pixels, implying charges were induced as far as the neighbouring connected pixels.

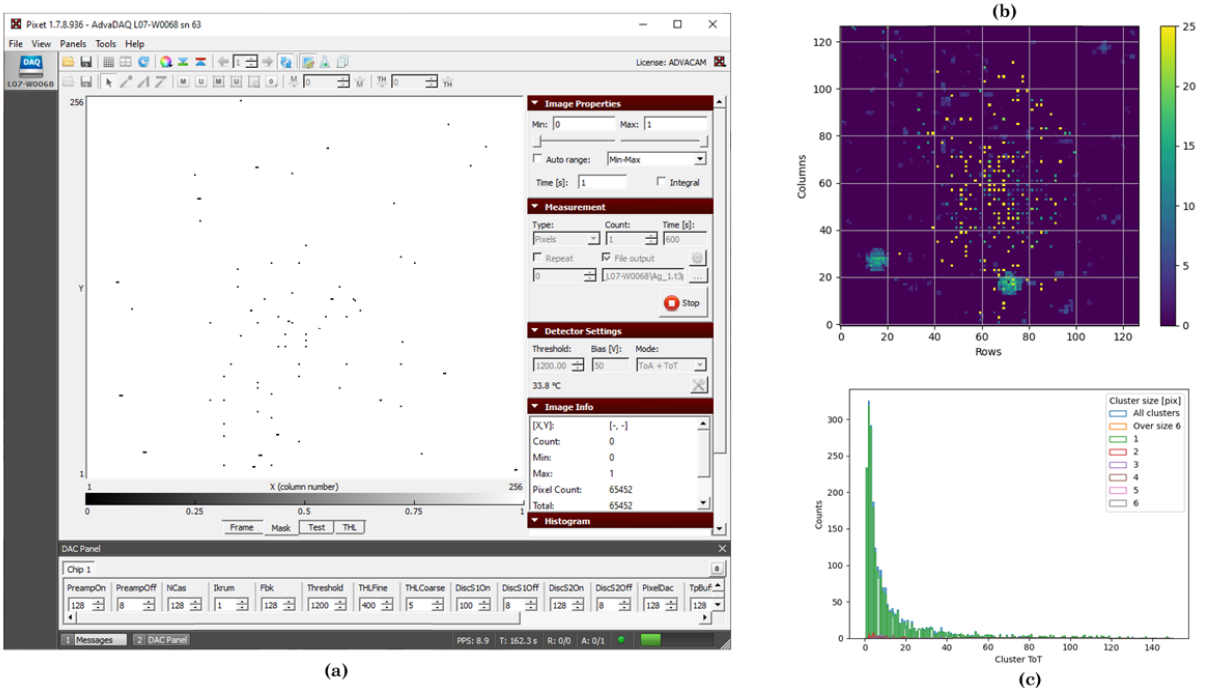

Figure 7.28: Laboratory test of the L07-W0068.(a) Threshold setup, (b) flat panel image of XRF_Tb, and (c) ToT spectrum of XRF_Tb.

A similar pixel behaviour was also observed during the preliminary laboratory testing of

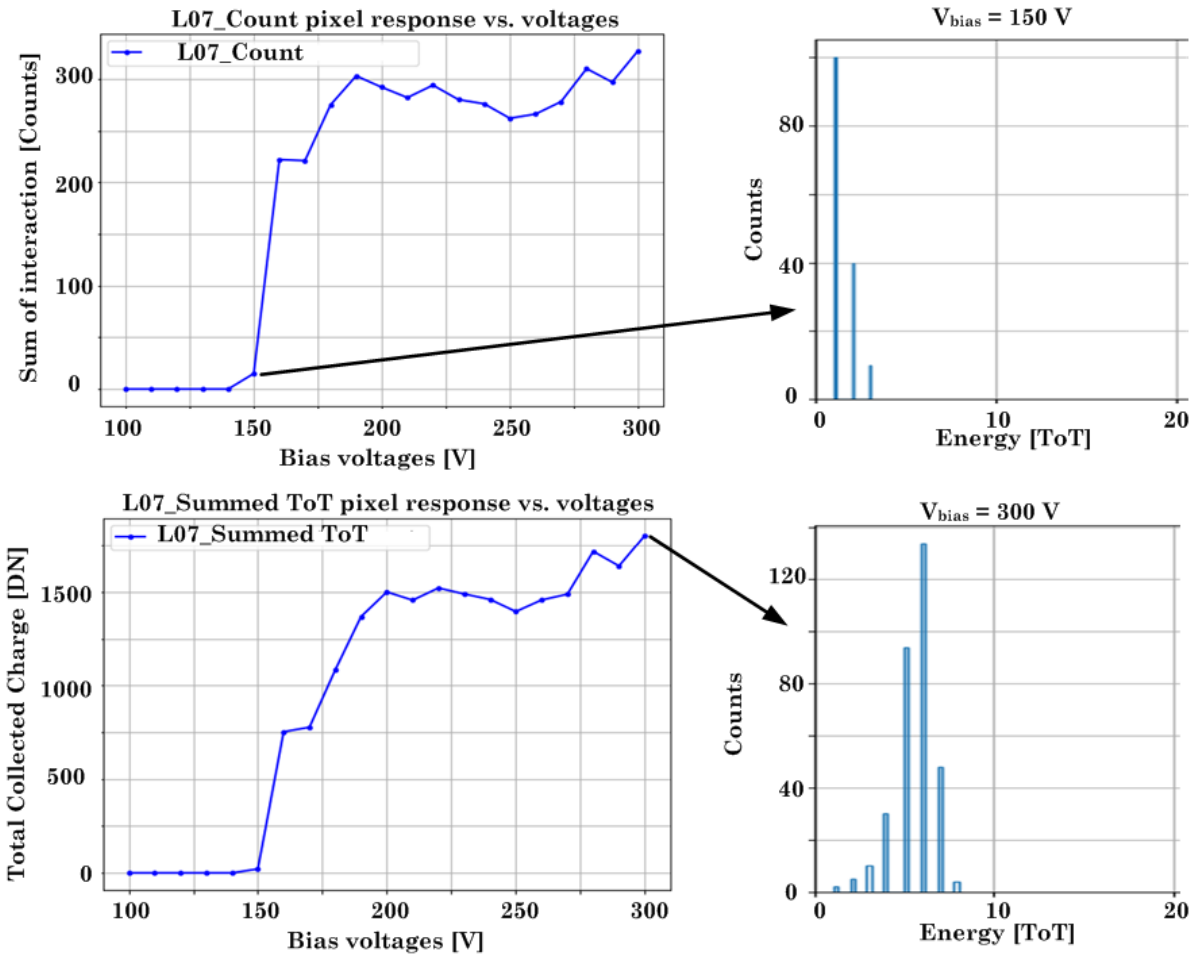

Figure 7.29: The pixel response of the centre pixel of the L07 device as a function of bias voltages (right) and the ToT spectrum at bias voltages of 150 V and 250 V.

the hybrid pixel detector with a 220 µm-pitch iLGAD (device L07-W0068). A large chunk of noisy pixels was observed in the centre column during the threshold optimisation (see figure 7.28a). A high threshold level was also applied to this device, and many pixels were masked to be operational. The flat panel image of XRF_Tb exposure in figure 7.28b shows two blobs of noisy pixel clusters (greenish colour) apart from the small XRF_Tb generated charge cluster scattered in the middle area. As shown in figure 7.28c, no prominent peak of the XRF_Tb was observed in the ToT spectrum.

The performance of device L07-W0068 are fared much worse than device F08-W0068. Multiple scans at several pixel coordinates were performed, but finding a reliable PoI for

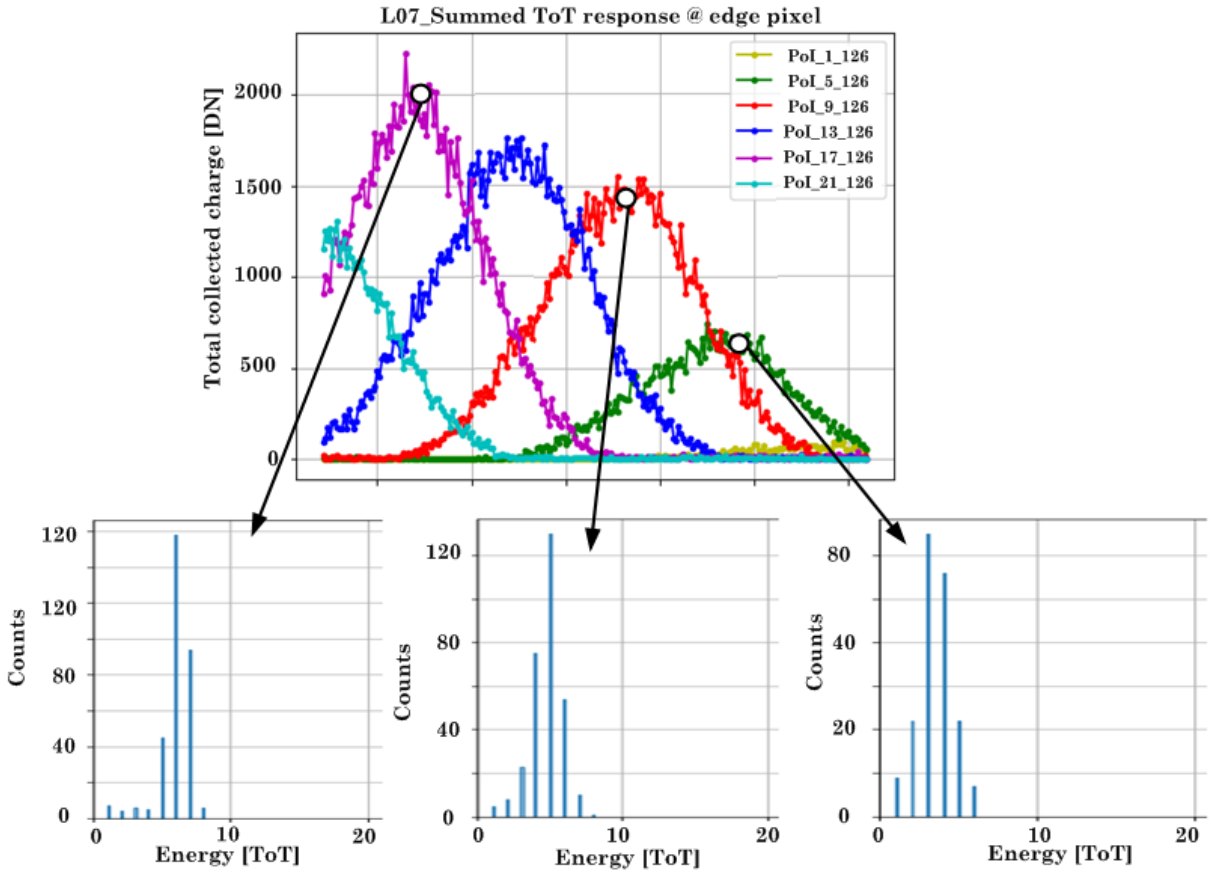

Figure 7.30: The pixel response of the L07 device across 6 PoIs at the edge pixel at 250 V bias voltage and the respective ToT spectra at the 3 PoIs.

proceeding with the test beam was challenging. Figure 7.29 shows the sample of the pixel response as a function of bias voltages obtained from the reliable pixel in the centre of the device. The over-the-threshold count and the summed ToT pixel responses show a decrease in the number of detected events, due to the application of a higher threshold value in this particular measurement. There was no significant shift in the ToT spectrum for 150 V and 300 V bias voltages, indicating this device produces either small or no signal gain. Figure 7.30 shows the summed ToT pixel response across 6 PoIs along the Y-pixel 126 and the ToT spectra of the PoIs with gain and control pixels. PoI_1_26, PoI_5_126 and PoI_9_126 are the three control pixels, and the other 3 PoIs are the pixels with gain. The pixel closer to the edge, PoI_1_126 appears unresponsive, while other PoIs produce overspread pixel response. It could be because the PoI_1_126 is dead or being masked. There are no significant difference in the pixel response between the PoI with gain, PoI_17_126 and

control pixel, PoI_9_126. Also, the spectral ToT of PoI_9_126 and PoI_17_126 are almost identical. Both observations, indicate that this device produces little or no signal gain.

7.3.4 Timepix3_iLGAD test beam summary

The synchrotron beam test on the hybrid pixel detector with a standard silicon detectors provides valuable understanding of how the Timepix3 threshold setting and beam attenuation affect the pixel response. The beam quality during the second synchrotron beam test was much better, where the 3rd harmonic was absent. Signal gain in the a small pixel iLGAD had been demonstrated. Device I11-W0018 which a hybrid pixel detector with a 55 µm-pitch iLGAD produced signal gains of ≈ 4.8 at a bias voltage of 250 V. Moreover, this device also showed a significantly large fill factor of $> 80\,\%$. Performance of the two hybrid pixel detectors with larger pitches iLGAD were inconsistent and sub-standard. It was difficult to identify what went wrong with these larger pixel iLGADs. The overall production yield of the iLGADs was very low; only 3 out of 20 iLGADs were responsive enough, and only one device (I11-W0068) performed as expected.

7.4 Chapter summary

This chapter comprehensively analyses LGAD and iLGAD technologies, employing a 2 µm focused, 15 keV mono-energetic synchrotron beam across two test beam campaigns. The 2019 study on traditional LGADs yielded crucial findings: gain initiation occurred above -50V for the 200 µm thick LGAD, optimal performance was obtained in 110 µm-pitch, 10 µm wide JTE devices with a gain of 3.4 at -350 V, and no observable gain was noted in 55 µm-pitch LGADs. The JTE width significantly impacted the gain and fill factor, with a 20 µm JTE width resulting in about 52 % gain reduction compared to their 10 µm wide JTE counterpart. A notable third harmonic halo in the synchrotron beam complicated the data analysis.

The 2022 campaign, focusing on iLGADs, demonstrated marked improvements, particularly in 55 µm-pitch devices, achieving a gain factor of 4.8 and a fill factor exceeding 80 %. Importantly, the third harmonic observed in the first campaign was absent, facilitating clearer data interpretation. This advancement addresses the fill factor limitations of traditional LGADs, especially at smaller pitches. However, larger-pitch iLGADs showed suboptimal performance, and the production yield of the iLGADs was poor, with only 3 out of 20 units being responsive due to the complexity of their fabrication process, which involves double-sided processing.

CHAPTER 8

Single-layer Compton camera (SLCC) with 1 mm thick CdTe

This chapter describes the application of hybrid pixel detectors with high-Z semiconductor sensors as detectors for a single-layer Compton camera (SLCC). The hybrid pixel detector used in this work is 1 mm thick, 256 × 256 with 55 µm-pitch CdTe sensors bonded to a Timepix3 readout ASIC. The discussion is confined to the Compton camera system based on the Timepix3 readout ASIC and high-Z semiconductor sensors. It includes a brief introduction to the two-layer and single-layer configurations, the kinematics of the Compton camera, the classification of valid Compton events, and image reconstruction. The remaining section presents the implementation of an SLCC with 1 mm CdTe bonded to Timepix3 readout ASIC. The experiment setup and data processing are explained, and the result will be discussed.

8.1 The Compton Camera

Compton camera detectors include scintillator-based detectors, semiconductor detectors like silicon, germanium, CdTe or CZT, or a combination of scintillator/semiconductor or

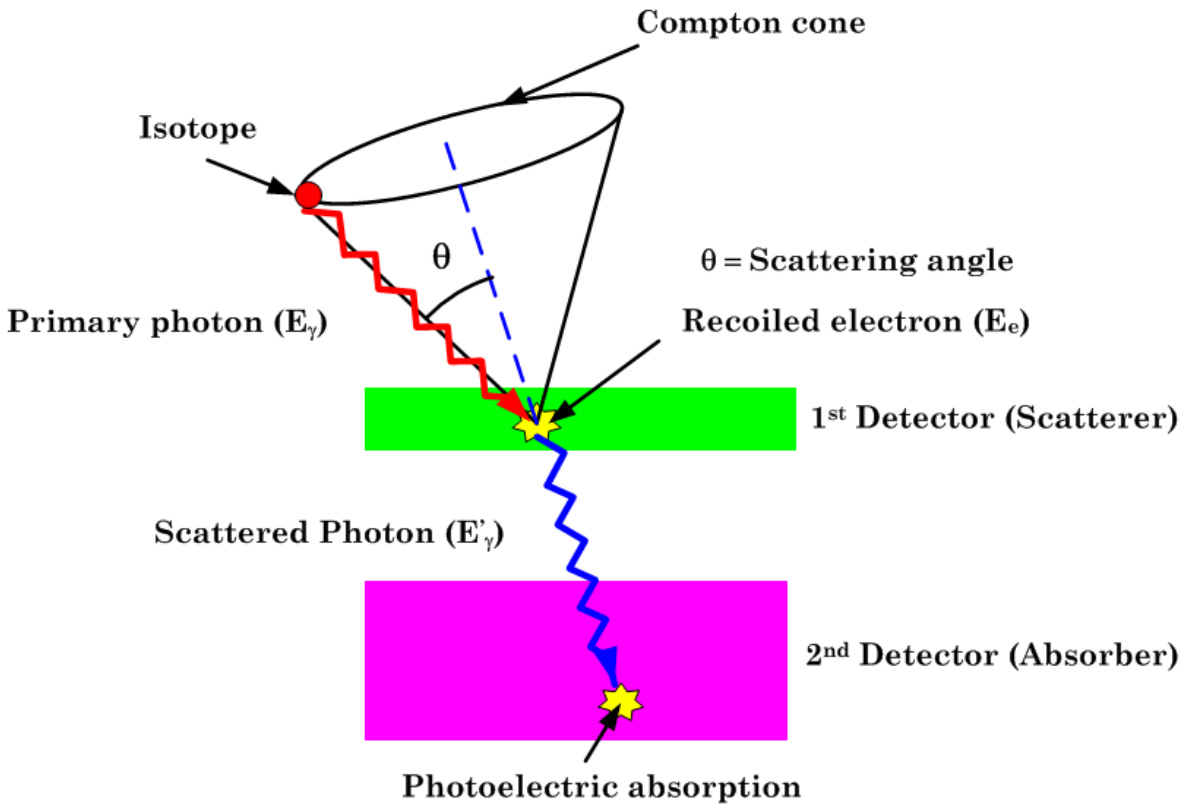

Figure 8.1: An illustration of a conventional Compton camera system using two detectors.

semiconductor/semiconductor detectors [89]. Scintillator-based detectors are widely used due to their high light output and relatively low cost but their angular, energy and spatial resolution are lower than semiconductor detectors. Thallium-doped sodium iodide (NaI(Tl)) and thallium-doped caesium iodide (CsI(Tl)) are among the popular scintillator detectors for Compton cameras. However, newer scintillators such as cerium-doped gadolinium aluminium gallium garnet (Ce:GAGG) and cerium-doped lanthanum bromide (Ce:$LaBr_3$) have gained more interest in recent years due to their high density, high light outputs, fast signal and better resolution[90, 91]. Scintillator detectors are commonly paired with photomultiplier tubes (PMTs), which limit their spatial resolution. However, a smaller pixelation was made available recently due to the introduction of multipixel photon counters (MPPCs). Silicon detectors, while offering excellent energy resolution and charge collection efficiency, are limited by their low atomic number, making them less effective for high-energy γ-ray detection. Germanium detectors, particularly high-purity

germanium (HPGe) detectors, provide superior energy resolution but require cryogenic cooling, which adds complexity and cost to the system.

A typical Compton camera has two detector systems (see figure 8.1). The Compton scattering occurs in the first detector, called the *scatterer*, where the recoil electrons deposit their energies. The scattered photons that escaped the first detector are absorbed and deposit their energies through the photoelectric effect in the second detector. Therefore, the second detector is the *absorber*. Both detectors register the Compton pairs events (recoil electron & photoelectric absorption) and the 2D coordinates of the events. The scattering angle θ is an important parameter in the Compton camera system, which came from the Compton equation (equation 2.28). A vector line connecting the absorption to the scattering coordinates for each Compton pair generates a cone axis with an angle given by the scattering angle θ. The cone axis is then converted into a conical surface called the *Compton cone* (see figure 8.1), and the intersections of many Compton cones reveal the origin of the incident photons. The Compton camera can also identify the radioisotope that produces the incident photons since the sum of energy from recoil electrons and the scattered photon equals the incident photon energy.

8.1.1 Kinematics of Compton camera

The Compton scattering is the dominant interaction process for incident photons with an intermediate energy range for any Z of absorber material (see figure 8.2). The probability of Compton scattering per atom occurring in an absorber depends on the number of electrons available as targets, and it increases linearly with Z. The angular distribution of the scattered photon for a differential cross section $\frac{d\sigma}{d\Omega}$ according to the Klein-Nishina formula is defined as

$$\frac{d\sigma}{d\Omega} = \frac{r_e^2}{2}\left(\frac{E'_\gamma}{E_\gamma}\right)^2\left(\frac{E_\gamma}{E'_\gamma} + \frac{E'_\gamma}{E_\gamma} - \sin^2\theta\right), \tag{8.1}$$

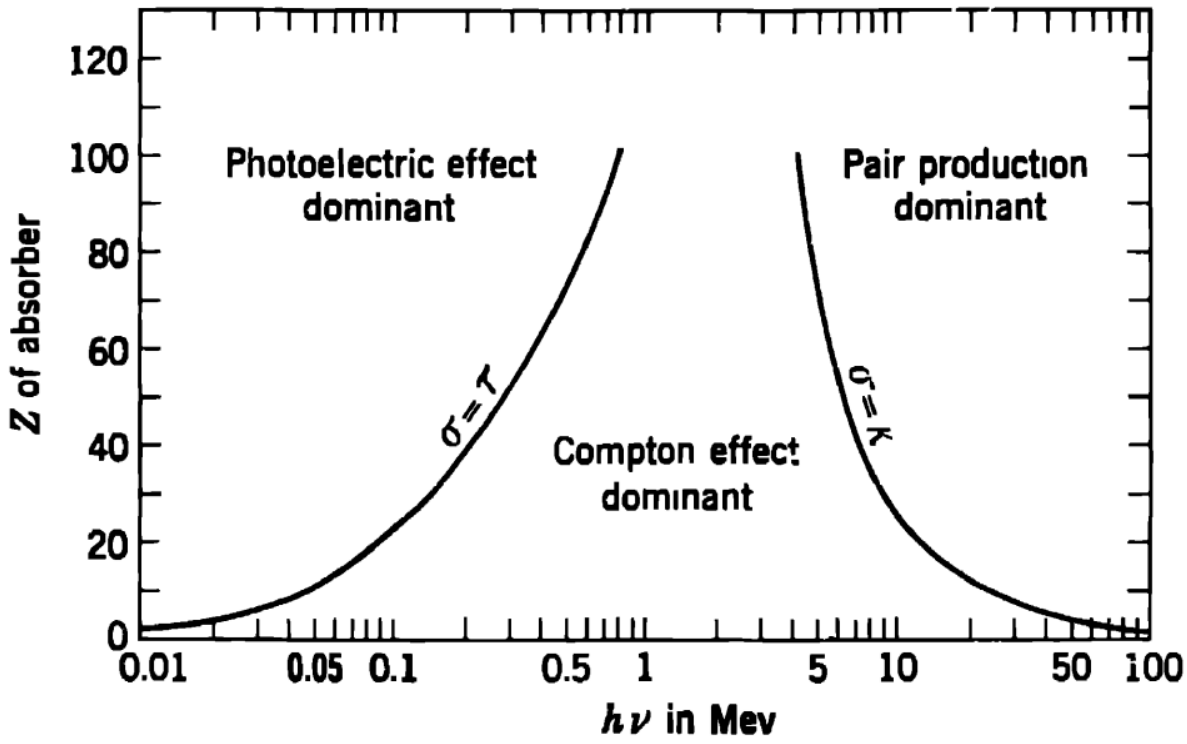

Figure 8.2: The dominant photons interaction process in material [92].

where $r_e = \dfrac{e^2}{m_e c^2}$ (2.8×10^{-13} cm) is the classical electron radius, while E_γ, and E'_γ are the incident and scattered photons.

The imaging principle of a Compton camera relies upon the Compton scattering angle, rearranging equation 2.28 gives the scattering angle θ

$$\theta = \arccos\left[1 - m_e c^2 \left(\frac{1}{E_2} - \frac{1}{E_1 + E_2}\right)\right], \tag{8.2}$$

where $m_e c^2 = 511\,\text{keV}$ is the electron rest mass energy whilst E_1, E_2 are the deposition energies of the recoil electron and scattered photon, respectively. The incident photon energy E_0 is the sum of E_1 and E_2 ($E_0 = E_1 + E_2$). The range for θ in equation 8.2 is from 0 to π with two extreme cases: maximum energy transfer to the recoil electron at $\theta = \pi$ and minimum when $\theta = 0$. A polar plot showing the number of photons scattered into a unit solid angle for a given incident photon energy in figure 8.3 indicates a strong tendency for the forward scattering to occur at higher incident photon energy.

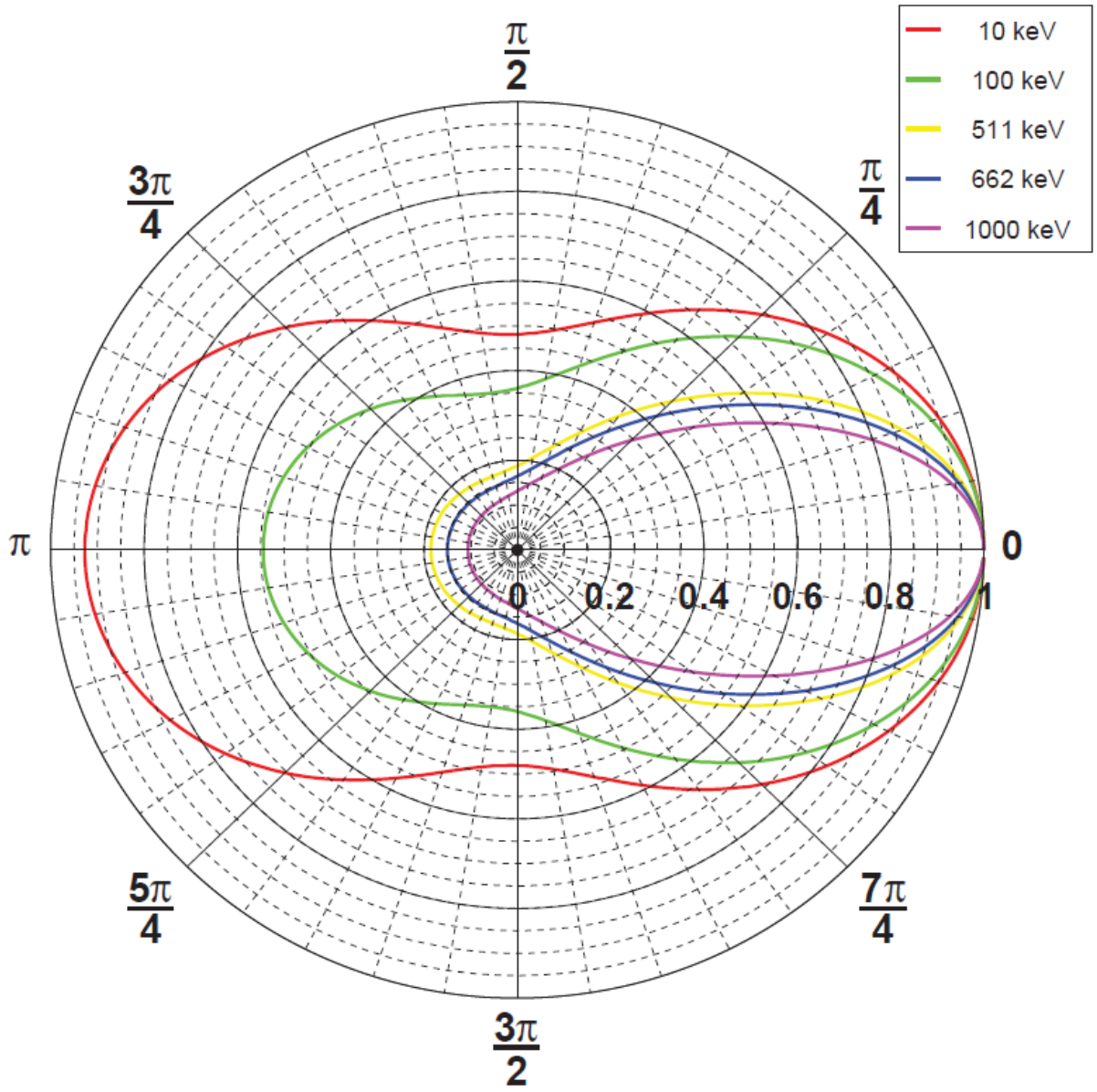

Figure 8.3: A polar plot showing photons scattered into a unit solid angle at the scattering angle θ obtained using the Klein-Nishina formula [93].

8.2 The single-Layer Compton camera

The work in [94] demonstrates a two-layer Compton camera based on Timepix3 readout ASIC. This system comprises a 1 mm thick silicon as the scatterer and a 1 mm thick CdTe as the absorber. Each sensor is bonded to a separate Timepix3 readout ASIC and operated in synchronised time mode. Only forward scattering is considered in this system, where the recoil electrons and scattered photons are captured in the silicon and CdTe,

respectively. The Compton cones are generated from two sets of 3D coordinates (x, y, z) obtained from both detectors. The lateral coordinates (x, y) are obtained directly from the hybrid pixel detectors pixels, while the depth coordinate, z, is assumed as the vertical distance between the silicon and the CdTe sensors.

The same group demonstrates a novel approach to the Compton camera with a single hybrid pixel detector called the *single-layer Compton camera* (SLCC) [26]. This work uses a 2 mm thick CdTe sensor bonded to Timepix3 Readout ASIC for their SLCC system. The lateral coordinates are obtained in the same manner as in the two-layer Compton Camera system. However, the vertical depth is determined using the charge collection time difference between the Compton pair event. In this system, the conversion of charge collection time to depth is calibrated using the cosmic muon track. The 1.56 ns resolution of ToA in the Timepix3 allows precise determination of the charge collection time and simultaneous detection of γ-ray interactions of various energies that occur in the multiple positions inside the detector volume. For this reason, the hybrid pixel detector based on the Timepix3 readout ASIC is the new state-of-the-art detector for the Compton camera system.

A small-pixel Compton camera with a single CZT or CdTe detector offers high spatial and energy resolution while operating at room temperature. Its compact size and sensitivity are ideal for constrained environments, such as intraoperative medical imaging or space telescopes. The enhanced energy resolution improves gamma-ray discrimination and image contrast, while room-temperature operation simplifies deployment for field applications in environmental monitoring, astrophysics, and homeland security.

8.2.1 Selection of Compton event

In Timepix3, the interactions due to the same photon are clustered based on the clustering time interval defined in the clustering algorithm. The clustering time interval equals the full-length charge collection time (FLCC), the time required for the electrons to drift the whole detector's thickness. The FLCC is related to the carriers' mobility and detector's thickness, as well as the bias voltage and is defined as:

$$FLCC = \frac{d}{v_e} = \frac{d^2}{\mu_e V_{bias}} \tag{8.3}$$

Alternatively, the FLCC can be calibrated experimentally by measuring the collection time of a MIP (cosmic muons) in the sensor [26].

Figure 8.4 shows three scenarios where Compton scattering may occur in the SLCC system. Only the forward scattering (see figure 8.4 (a)) is considered following the convention used in a two-layer system. More importantly, the backward scattering (figure 8.4 (b)) has to be removed since this event will produce a mirrored image as opposed to the real image. The flow chart in figure 8.5 describes the criteria and energy cuts for selecting the valid Compton event and the cone reconstruction. Events comprising two interactions acquired within the specified FLCC are stored as Python lists called the *Time Coincidence Group*. The candidate for a valid Compton event is selected from this group by imposing several criteria and energy cuts. Selecting a valid Compton event is crucial for image reconstruction in the SLCC system. Only events comprising two interactions are considered as candidates for a valid Compton event. An energy cut is applied to all events in the *Time Coincidence Group* to select the interactions with summed energy within the range of the incident photon energy ($\Sigma E = E_\gamma \pm \Delta E/E$).

The CdTe detector generates an XRF line due to k_α of Cadmium and Tellurium at around

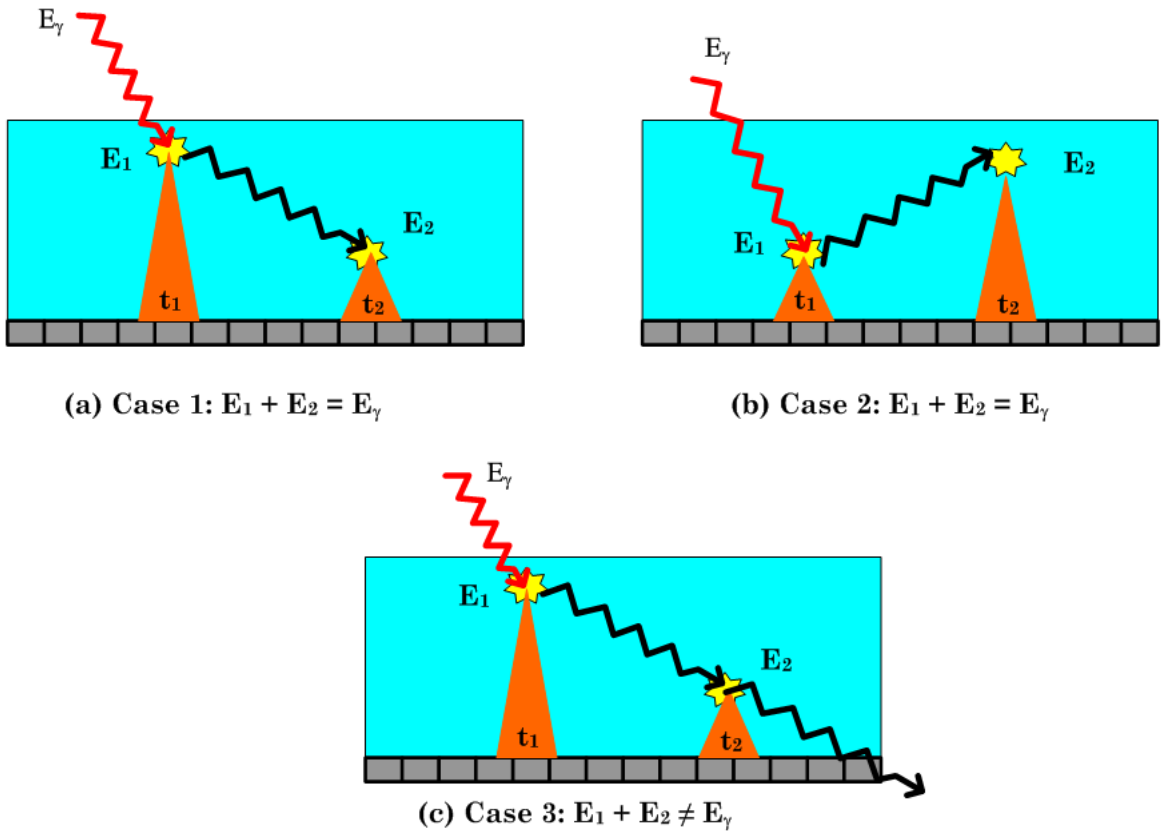

Figure 8.4: Three possible scenarios for Compton events to occur in a single-layer Compton camera. (a) Case 1 is a valid event, (b) Case 2 is an inverse coincidence event and is discarded, and (c) Case 3 is invalid event since $E_1 + E_2 \neq E_\gamma$.

22 keV. The XRF is a byproduct of the photoelectric absorption, which is also two interactions that coincide within the specified FLCC and could be mistaken as a valid Compton event. If not filtered, this event becomes dominant, and the final image will always be in the centre of the projected plane. The XRF events are filtered by applying another energy cut where any interactions with energies within the XRF energy range ($E = E_{XRF} \pm \Delta E/E$) are excluded. The next step of the selection process is identifying the interaction that belongs to recoil electrons (E_1) and the scattered photons (E_2). The Compton edge $\left(E_{CE} = \frac{E_\gamma}{\left(1 + \frac{m_e c^2}{E_\gamma}\right)} \right)$ is used as cut-off energy for identification. If an interaction has energy below the E_{CE}, it is assigned as the recoil electron interaction (E_1) and vice-versa. Interactions that pass the criteria and energy cuts are stored as Python lists called the *Valid Compton Event*. The next stage of the image reconstruction pro-

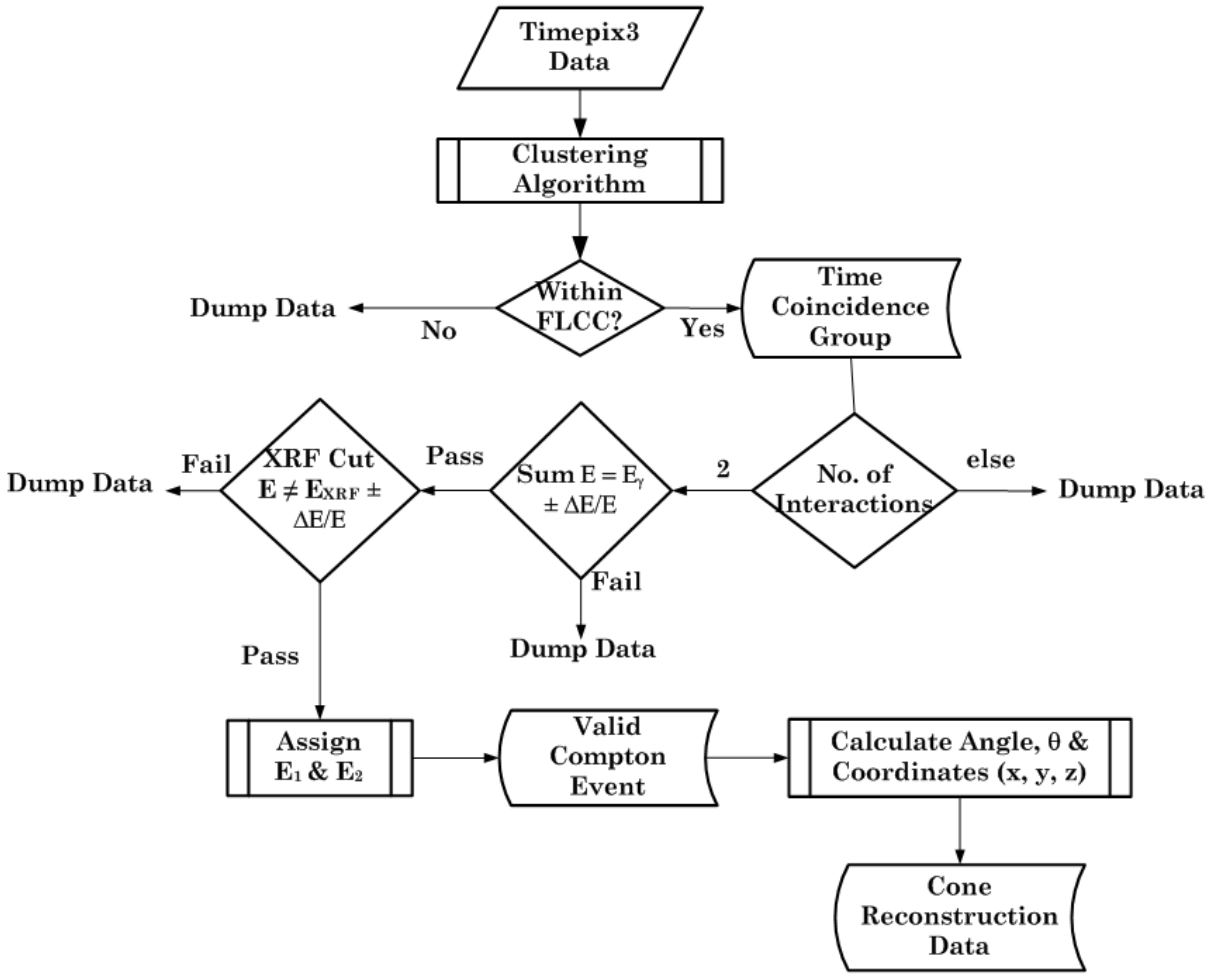

Figure 8.5: The flow-chart of classifying the valid Compton event in the SLCC system.

cess is assigning the 3D coordinates of the interactions deemed as *Valid Compton Event* and obtaining the Compton scattering angle. This process is described in the subsequent subsection.

8.2.2 3D coordinates and scattering angle

The valid Compton event is a two-interaction pair due to recoil electron and scattered photon. Henceforth, the interaction due to recoil electrons and scattered photons will be called *scattering* and *absorption* hits to simplify the naming convention. Individual hit contains data of ToA, energy, and 2D pixel coordinates (ToA, E, x, y). The only missing information is the z-coordinate, which is related to the depth of the interaction. The depth difference $d_{diff.}$ is obtained from the charge collection time difference τ_{ctd}, which is

the difference in ToA between the scattering and absorption hits and is calculated as

$$d_{diff.} = d\left[\frac{\tau_{ctd}}{FLCC}\right] \tag{8.4}$$

.

The depth difference represents the difference in the z-axis between the scattering and absorption hits, which is not an absolute value. In this work, the scattering is assumed to occur at the detector's surface ($z = 0$), and the absorption hit is at z = -1$*d_{diff.}$. The hybrid pixel detector produces 2D (x, y) coordinates in pixel values, not physical length. The pixel values of the respective x and y coordinates are converted into physical lengths by multiplying the pixel value by the detector's pixel pitch, in this case, 55 µm. Now, the individual hit is assigned its energy and 3D coordinates. The only missing information required for the cone projection is the scattering angle θ. The Compton scattering angle is calculated using equation 8.2 with the energy of the scattering and absorption hits. Assigning the 3D coordinate and obtaining the scattering angle is repeated and logged for all found *Valid Compton Events* and saved as the *Cone Reconstruction Data*. The process of projecting the Compton image on the projection plane is described in the following subsection.

8.2.3 Cone projection

The intersection of the Compton cone is solved using the vector algebra adapted from the work in [95]. Figure 8.6 shows the geometrical representation of the hits coordinates, the Compton cone, the vertical distance to the projection plane Z_L, and the two vectors connecting the hits coordinates. The vector line $\vec{d}$ connects the absorption hits to the scattering hit, whilst the second vector $\vec{u}$ connects the scattering hit to variable point (x, y, z) on the Compton cone.

The Compton cone formed by these hit points is the scalar product of the two vectors.

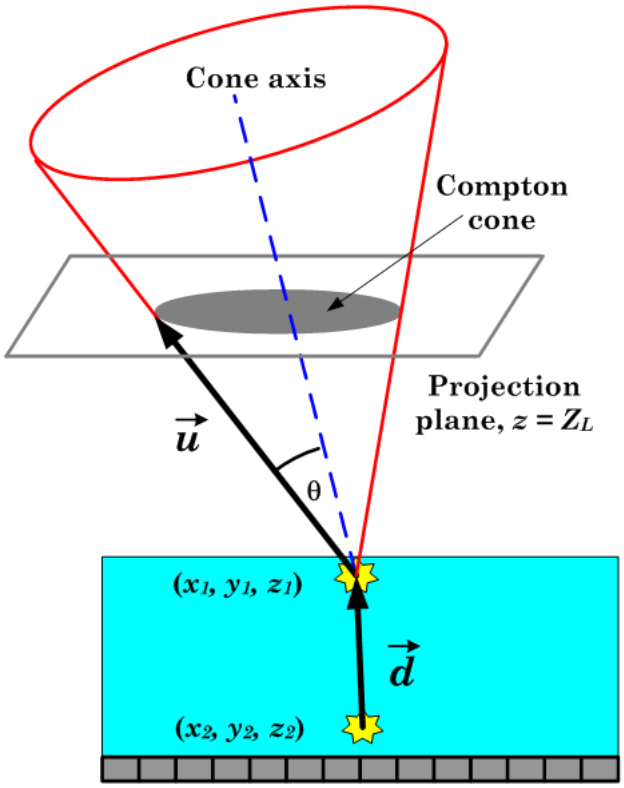

Figure 8.6: Projection of Compton cone on an image plane

These vectors are defined as

$$\vec{u} = (x - x_1, y - y_1, z - z_1) \tag{8.5}$$

and

$$\vec{d} = (x_1 - x_2, y_1 - y_2, z_1 - z_2)\,. \tag{8.6}$$

The scalar product representing the Compton cone is

$$\vec{u} \cdot \vec{d} = |\vec{u}||\vec{d}|\cos\theta. \tag{8.7}$$

Squaring equation 8.7 yields,

$$\left(\vec{u} \cdot \vec{d}\right)^2 = (\vec{u} \cdot \vec{u})\left(\vec{d} \cdot \vec{d}\right)\cos^2\theta = 0, \tag{8.8}$$

and by taking into account the $z = Z_L$, the scalar product becomes:

$$\begin{aligned}\vec{u}\cdot\vec{d} = &\ (x-x_1)(x_1-x_2)\\ &+(y-y_1)(y_1-y_2)\\ &+(Z_L-z_1)(z_1-z_2),\end{aligned} \tag{8.9}$$

which leads to the following:

$$\vec{u}\cdot\vec{d} = x(x_1-x_2)+y(y_1-y_2)+CC \tag{8.10}$$

where CC is equal to

$$CC = x_1(x_2-x_1)+y_1(y_2-y_1)+(Z_L-z_1)(z_1-z_2). \tag{8.11}$$

Similarly $\vec{u}\cdot\vec{u}$ and $\vec{d}\cdot\vec{d}$ can be expressed as

$$\begin{aligned}\vec{u}\cdot\vec{u} &= (x-x_1)^2+(y-y_1)^2+(Z_L-z_1)^2\\ \vec{d}\cdot\vec{d} &= (x_1-x_2)^2+(y_1-y_2)^2+(z_1-z_2)^2.\end{aligned} \tag{8.12}$$

Equation 8.8 can be expressed into a second-order quadratic equation as:

$$\begin{aligned}&\left(\vec{u}\cdot\vec{d}\right)^2-(\vec{u}\cdot\vec{u})\left(\vec{d}\cdot\vec{d}\right)\cos^2\theta =\\ &Ax^2+Bxy+Cy^2+Dx+Ey+F=0,\end{aligned} \tag{8.13}$$

where the set of coefficients A, B, C, D, E, F are defined for each interaction with:

$$\begin{aligned}A &= (x_1-x_2)^2-d^2\cos^2\theta\\ B &= 2(x_1-x_2)(y_1-y_2)\\ C &= (y_1-y_2)-d^2\cos^2\theta\\ D &= 2(x_1-x_2)CC+2x_1d^2\cos^2\theta\\ E &= 2(y_1-y_2)CC+2y_1d^2\cos^2\theta\\ F &= CC^2-\left[x_1^2+y_1^2+(Z_L-z_1)^2\right]d^2\cos^2\theta.\end{aligned} \tag{8.14}$$

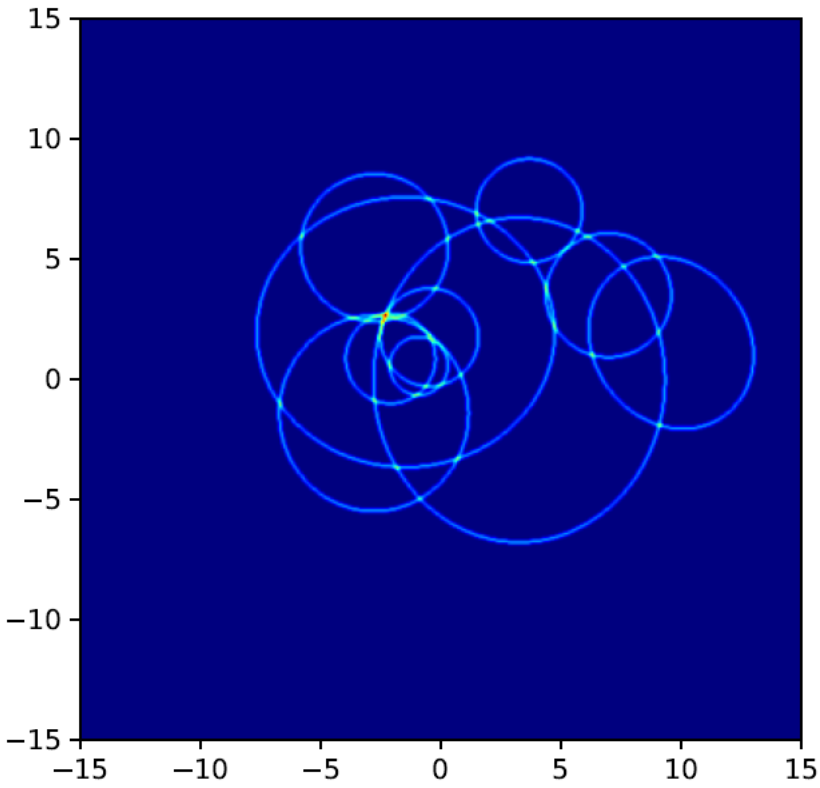

Figure 8.7: An example of a conic section on the projection plane

Solving equation 8.13 for a given scattering and absorption hits points gives a conic section representing the intersection between the Compton cone and the projection plane. An example of a conic section is shown in figure 8.7, and iterating the projection for each Compton event produces an image revealing the incident photon's origin.

8.3 Proof of concept: Single-layer Compton camera with 1 mm thick CdTe

An SLCC based on the hybrid pixel detector with 2 mm thick, pixelated CdTe bonded to a Timepix3 readout ASIC was introduced recently [26]. The implementation is possible due to the superior ToA time resolution (1.56 ns) of the Timepix3 readout ASIC, allowing precise measurement of the time difference between the two Compton events. It was decided to implement a similar setup using a 5 mm CZT bonded to Timepix3 readout ASIC. A thicker CZT sensor would have extended the capability of the Compton camera

for applications that utilise higher energy photons (> 500 keV). Unfortunately, this plan was never materialised because the hybrid pixel detector with 5 mm thick CZT produced by the University of Glasgow tested in Chapter 6 performed beyond acceptable (see section ??). The experiment is conducted at IEAP[1], Czech Technical University in Prague, Czech Republic because the hybrid pixel detector of such type is unavailable at the University of Glasgow.

8.3.1 Data acquisition and pre-processing

Table 8.1: Specification of the Timepix3_CdTe hybrid and the isotope used for the demonstration of a single-layer Compton camera

Hybrid Pixel Detector	Readout Electronics & DAQ software	Detector Specifications	Isotope
Timepix3 + CdTe	Katherine Readout & Burdaman software Communication: Gigabyte Ethernet	No. of Pixel : 256 × 256 Pixel Pitch: 55 μm Bias Voltage = -300 V Thickness = 1 mm	Co - 57 E = 122 KeV

Figure 8.8: The Katherine readout electronics used to acquire the data [86].

Table 8.1 shows the specifications of the Hybrid Pixel Detector, the readout system and the radioisotope used in this work. The hybrid pixel detector is 1 mm thick, 256 × 256 with 55 µm-pitch CdTe bonded to a Timepix3 readout ASIC. The data are acquired in Timepix3's data-driven mode with the Katherine readout and Burdaman Software (see figure 8.8). The ^{57}Co with photo-peak energy of 122 keV is chosen because this energy

[1]Institute of Experimental and Applied Physics, http://www.utef.cvut.cz/ieap

is within the energy range of the isotope used in medical imaging (e.g. radioisotope Tc-99m at 140 keV). Moreover, this was the only radioisotope with sufficient activity in the institute during the experiment. The photoelectric effect is expected to be the dominant interaction in CdTe in this energy range. However, a reasonable amount of Compton scattering events would also be produced. The acquisition time per measurement is set at 180 s with 20 measurements (total = 3600 s) for the *EXP 1* (figure 8.9a) and 10 measurements (total = 1800 s) for the *EXP 2* (figure 8.9b).

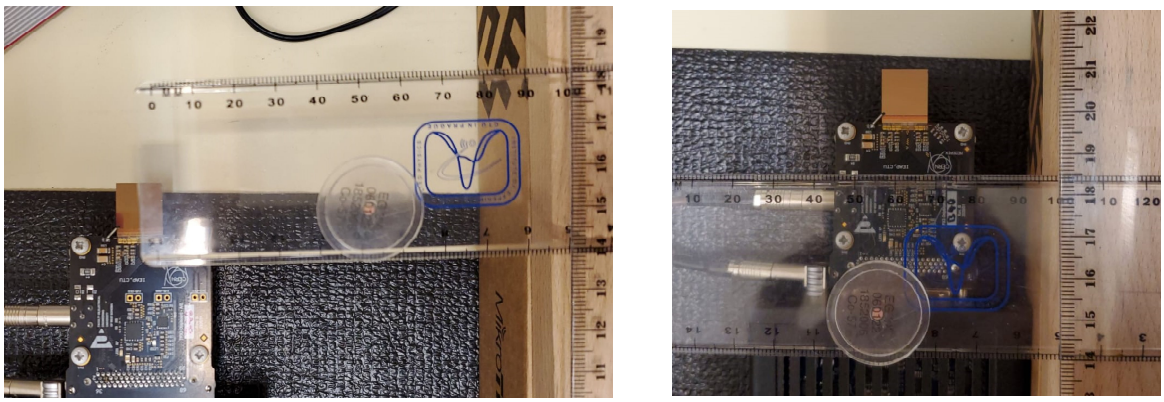

(a) Source positioned at x-axis EXP 1. *(b) Source positioned at y-axis EXP 2.*

Figure 8.9: The experiment setup for acquiring the SLCC data. (a) The ^{57}Co is positioned at 5 cm to the left of the detector, and (b) The ^{57}Co is positioned at 5 cm bottom of the detector.

Two pre-processing steps are required before proceeding with the SLCC's image reconstruction. First, the individual 180 s data from both experiments must be

(i) Clustered following the pre-set charge clustering limit.

(ii) Calibrated for energy (ToT) and corrected for time-walk (ToA).

(iii) Compensated the time delay in the ToA due to the intrinsic column delay in Timepix3 architecture (16-phase delay correction)

then the data are combined into a single 3600 s data file. This pre-processing is accomplished using the *Multifile Clustering* software developed by IEAP. The SLCC is realised using the *ComptonCamera.py*, a bespoke code based on the Python 3 IDE that uses the

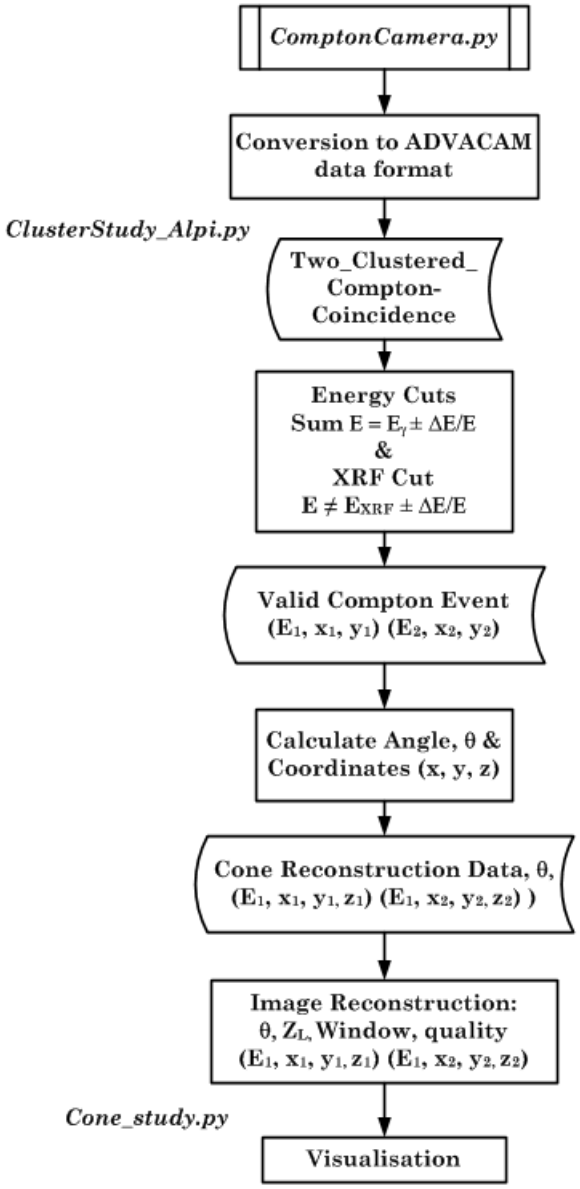

Figure 8.10: The flow-chart describing data processing in the SLCC system with the Compton-Camera.py bespoke Python IDE code.

input file of ADVACAM's PIXet Pro data format. The second pre-processing step is converting the Burdaman software-acquired data to ADVACAM's PIXet Pro data format. The data conversion is not trivial since both formats share an identical Timepix3 data structure; the only difference is the header file section.

8.3.2 Data processing

The *ComptonCamera.py* utilised *Numpy*, *Pandas*, *SciPy*, and *Matplotlib* packages for data handling, processing and visualisation. The data flow is shown in figure 8.10, where the data is first converted to the ADVACAM data format. The *ClusterStudy_Alpi.py* function selects the candidate for the Compton event from the two Compton coincidence clusters and implements the energy cuts and other criteria to find the valid Compton events. It also assigns the scattering and absorption hits with physical 3D coordinates and calculates the scattering angle of the respective hits.

The SLCC image reconstruction is handled by a function called *cone_study.py*. This function takes argument inputs from the cone reconstruction data and three more inputs, the vertical source to detector distance Z_L, *window*, and *quality*. The *window* and *quality* inputs define the dimension of the projection plane and image quality. This function calculates the solution for the vector algebra coefficients in equation 8.14 and performs the cone projection. The output of this process is a 2D matrix of the cone intersections on the projection plane. A filtered back projection with a Gaussian filter produces the final SLCC image.

8.4 Results and discussion

Table 8.2 shows the analysis of the number of interactions in the two experiments before and after implementing the Compton selection algorithm. The hybrid pixel detector with 1 mm thick CdTe manages to detect many interactions during the 3600 s and 1800 s acquisitions. The total interactions recorded for EXP 1 and EXP 2 are $\approx$ 5.2 Mhits and 3.6 Mhits, respectively. However, less than 0.2 % (EXP 1 = 8283 & EXP 2 = 7823) of the events are pair interactions that coincide within the specified FLCC, in this case 32 ns. It was expected that these interactions are mostly from the photoelectric absorption (^{57}Co energy = 122 keV & Z_{CdTe} = 48). Only $\approx$ 11 % of the pair interactions pass the energy

cuts criterion. It was found that the energy cuts criteria are insufficient to exclude the XRF contribution. Another criterion is introduced where the 2D-pixel distance is used to filter the XRF-induced interactions.

Table 8.2: Analysis of the number of interactions detected in the two experiments.

	No. of Interactions	
	EXP 1: Source at left-side (5 cm)	EXP 2: Source at bottom-side (5 cm)
Total Interactions	5179128	3577144
Coincidence within FLCC	8283	7823
Valid Compton Event	938	872
Cone Reconstruction Data	590	574

Figure 8.11a show the energy spectra of the ^{57}Co. The ^{57}Co photo-peak energy E_{Photo} is around 123.97 ± 8.46 keV, whereas the XRF peak is around 21.86 ± 6.00 keV. The energy resolution $\Delta E/E$ (FWHM) at the respective peaks are used as the range of the energy cut to select the valid Compton event. The spectral distribution of the pair interactions after passing the energy cut and scattering criteria are shown in figure 8.11b and figure 8.11c. The projected SLCC image produced with this algorithm is shown in figure 8.11d; the image is projected in the middle of the plane. The XRF event is also two interactions that coincide with the FLCC and can be mistaken as a valid Compton event. If this event is not excluded, it becomes dominant, and the projected image will always be at the plane's centre. The energy cut alone is insufficient to filter the XRF event. In addition to the energy cuts, there are two crucial criteria to obtain an accurate image projection in SLCC:

(i). Proper θ selection: $0 < \theta\ (rad.) < 1.0$.

(ii). Sizeable distance between the Compton pairs: 2D-pixel distance $\geq$ 15 pixels.

The θ selection criterion ensures the scattering event occurs on the top (forward scattering), and the sizeable 2D-pixel distance between the pair interactions is necessary to filter the XRF-induced interactions. The 2D-pixel distance is calculated as follows:

$$\text{2D pixel distance} = \sqrt{(x_1 - x_2)^2 + (y_1 - y_2)^2}, \tag{8.15}$$

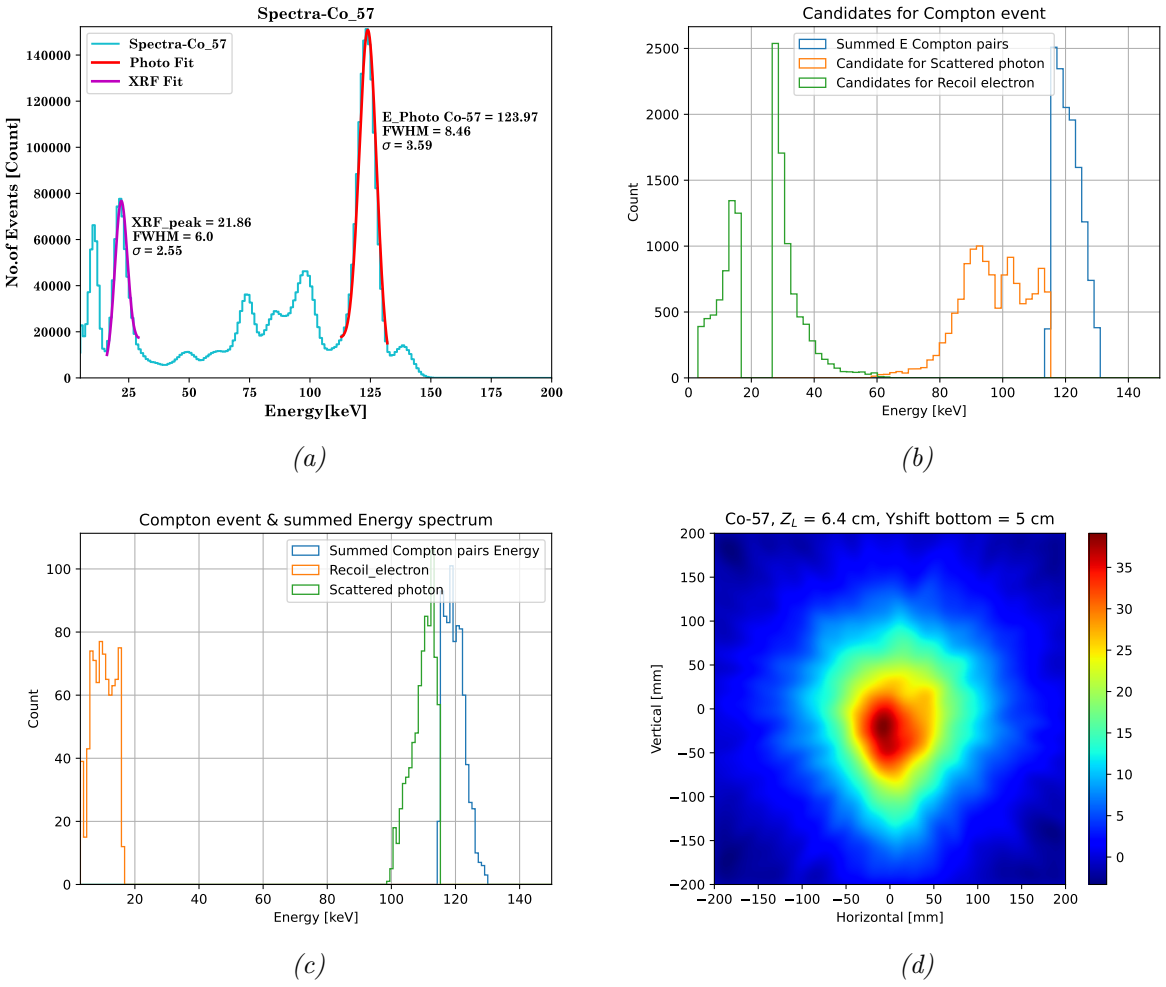

Figure 8.11: Energy spectra of the (a) ^{57}Co, (b) the Compton pair candidates and their summed energy, and (c) the valid Compton event after selection only the forward scattering. (a) The projected image of the valid Compton event.

where the (x_1, y_1) and (x_2, y_2) are the pixel coordinates of the scattering and absorption hits, respectively. The total interactions after applying criteria (i) and (ii) are 590 for *EXP 1* and 574 for *EXP 2*. The spectral distribution of valid Compton event in figure 8.2 indicates that events with energy from ≈ 20 - 100 keV are from the backward scattering.

Figure 8.12 shows the images of the Compton cone projections from the two experiments described in 8.3.1. The projected image's lack of sharpness is due to two major factors:

(i) Fewer data available for the cone projection.

(ii) Uncertainty in the θ measurement.

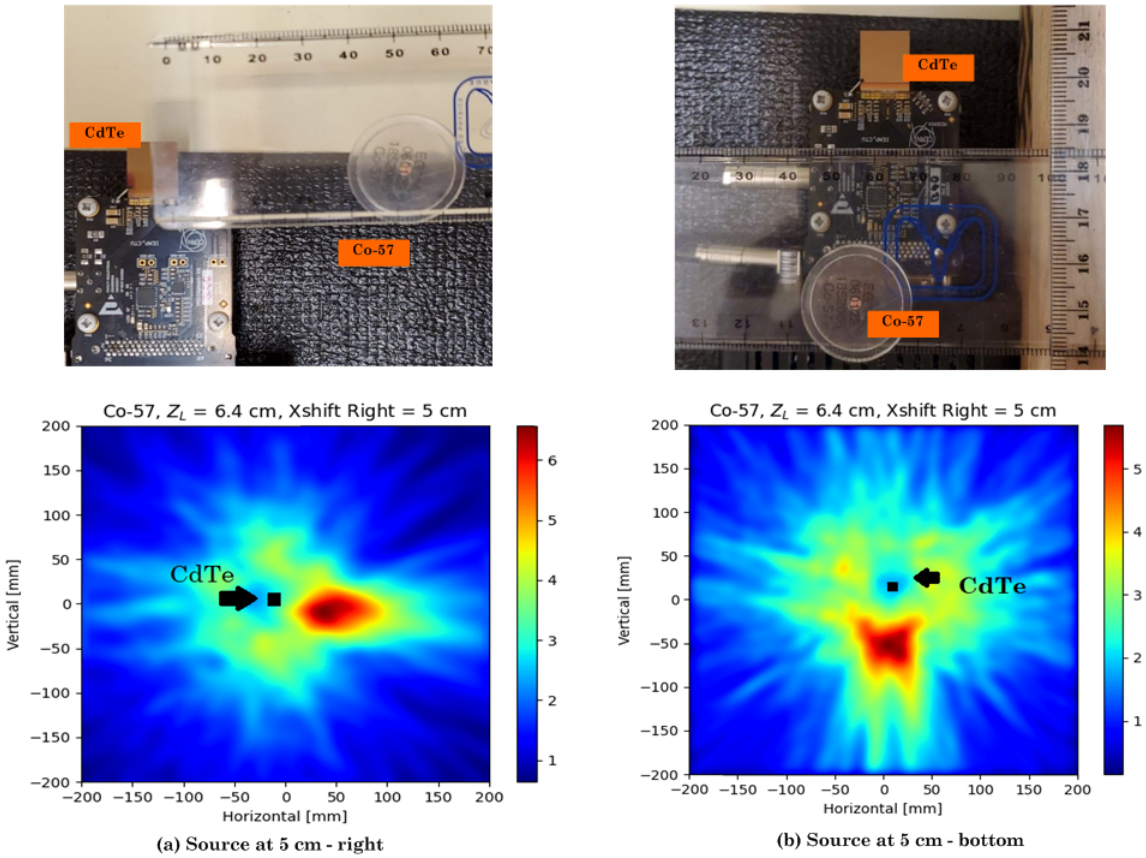

Figure 8.12: Demonstration of image shift in a single-layer Compton camera (SLCC) with 1 mm *thick CdTe bonded to Timepix3 readout ASIC. (a) The projected image with source at* 5 cm *to the left and (b) projected image with source at* 5 cm *to the bottom of the detector.*

The number of recorded interactions in a detector is closely related to the measurement time and source activities. Therefore, a longer measurement time would have increased the valid Compton event data statistics. A thicker CdTe would also improve the valid Compton event data statistics because the number of scattered Compton photons that escape the detector will be reduced.

The uncertainty in the θ measurement in Compton camera depends on the detector's spatial and energy resolutions and the Doppler broadening effect [96]. The spatial resolution affects the direction of the back-projection cone axis and generates the divergence between the measured scattering angle and the actual scattering angle. The divergence uncertainty is related to the distance between the isotope and the detector, which is higher than 6° for a 55 µm spatial resolution and 5 cm isotope-detector distance [96]. In this work, inter-

action's centroid is assumed to be the pixel with the highest energy value, which is not the real interaction point and adds to the uncertainty in the θ measurement. Work in [97] demonstrates an improvement in measurement by adopting the electron track algorithm to determine the interaction point.

The energy resolution and Doppler broadening affect the accuracy of the energy measurement. The hybrid pixel detector is biassed with internal bias supply from the Katherine readout (max at -300 V) because external bias supply was not available during the measurements. The -300 V bias is suboptimal for this detector since it is specified for optimal resolution at -500 V. The θ described in equation 8.2 is the Compton scattering angle for the target electron assumed at rest. This assumption is oversimplified since the photons interact with *moving* electrons *bound* to atoms. Interaction of photons with the non-rest electrons target leads to a broadening in the energy spectra for the scattering and absorption hits called the *Doppler broadening effect* [98]. The Doppler broadening effect is significant for low-energy incident photons, which adds to the uncertainty of the scattering and absorption hits energy measurements.

A thicker CZT detector would enhance the performance of an SLCC by increasing its efficiency in detecting photons. This improvement stems from the thicker CZT's greater stopping power, which allows it to absorb more high-energy photons. Furthermore, the increased depth of interaction contributes to enhanced scattering angle measurement, as it provides more accurate data on the position of photon interactions within the detector. As a result, the camera's sensitivity and resolution are heightened, enabling more precise imaging and better localisation of photon sources. The increased detection efficiency also reduces the required exposure time for accurate imaging, making the device more effective for various applications such as medical imaging, astrophysics, and security scanning.

The image reconstruction algorithm is an essential aspect of a Compton camera sys-

tem. Most Compton camera systems use a numerical or combined numerical-Monte Carlo methods-based reconstruction algorithm to improve image quality [96, 99–101]. However, the emphasis on the reconstruction algorithm is beyond the scope of this work. The source origin is sufficiently pinpointed in both projected images in the two experiments. Hence, the proof of concept of SLCC using a 1 mm thick CdTe bonded to Timepix3 readout ASIC is demonstrated.

CHAPTER 9

Conclusion & outlook

9.1 Conclusion

In this thesis: the characterisation of LGAD and iLGAD pad devices; the data analysis of Hybrid pixel detectors with various sensors (PIN silicon, CZT & LGAD) irradiated with XRF and γ-ray sources; demonstration of a single-layer Compton camera with a thinner CdTe-based hybrid pixel detector; and synchrotron beam test of hybrid pixel detectors with LGAD and iLGAD sensors have been presented.

The electrical characterisation of the 50 µm thick LGAD and 250 µm thick iLGAD were presented in section 5.1. Depending on the doping concentrations, the breakdown and full depletion voltages measured at room temperature for the 50 µm thick LGAD were ranged from 150 V to 280 V and 26 V to 30 V, respectively. These LGADs can therefore be operated 5 to 9 times higher than their full depletion voltage. Only a few iLGAD pad devices produced acceptable IV and CV characteristics. These devices showed no indication of breaking down as the leakage current remains below 100 nA at a bias voltage of 250 V. Their CV curve shows a double-drop characteristic, first at around 30 V, which

was understood as the depletion of the multiplication layer and another at around 170 V to 180 V. The full depletion voltage in the 250 µm thick iLGAD was estimated at around 180 V. These iLGAD pad devices were the first iterations of iLGADs produced by Micron Semiconductors Ltd. Hence, a low production yield was anticipated, as the fabrication of an iLGAD was complicated because it involved double-sided processing.

The gain measurement in the 50 µm thick LGAD was presented in section 5.2. This device produced a temperature-dependent gain, and due to the inherent limitations of the LGAD, its gain was also affected by the device's pixel sizes and the width of the JTE. A larger LGAD device attains higher gain at a lower temperature. A larger LGAD device achieves higher gains at lower temperatures. At a bias voltage of 250 V, the signal gain in the larger pixel LGADs ($1.0 \times 1.0\,\mathrm{mm}^2$) is a factor 7 at 30 °C and rose to a factor of 12 at −20 °C. This gain shift represents a 71 % gain increase for 50 °C changes in temperature. The LGADs whose gains were measured were then sent for neutron irradiations at the University of Birmingham, and post-irradiation gain measurements are currently ongoing at both institutions.

The data presented in this thesis was analysed using Python 3 IDE-based analysis scripts described in section 6.2.1. The analysis scripts updated and consolidated previously developed processing scripts compatible with ADVACAM's PIXet Pro software data format. It had been successfully used to analyse the data from XRFs, radioisotopes, and synchrotron test beams and process the image projection in the single-layer Compton camera system. The first per-pixel ToT calibration and time-walk correction in the hybrid pixel detector with the LGAD sensor were demonstrated in sections 6.4 and 6.5. Two hybrid pixel detectors with 5 mm thick CZT were explored for a single-layer Compton camera system in section 6.6. The 5 mm CZT bonded to the Timepix readout ASIC demonstrates a good spectroscopic resolution of FWHM = 8 % at 662 keV. However, the 10 ns time of arrival resolution of the Timepix readout ASIC was too slow for a single-layer Compton camera.

The 5 mm thick CZT bonded to Timepix3 readout ASIC fared much worse and can not be used as a single-layer Compton camera system detector.

The synchrotron beam test of two hybrid pixel detectors with LGAD and iLGAD sensors was presented in chapter 7. The small pixel LGAD (55 µm-pitch) that was bonded to Timepix3 readout ASIC did not produce any signal gain, confirming the *small pixel effect* predicted in the previous simulation in [24, 25]. The width of the JTE affects the signal gain in LGAD devices. The hybrid pixel detector with 110 µm-pitch, 10 µm wide JTE LGAD was found to have a signal gain of 3.4 but reduced to 1.6 for a similar-pitch LGAD with 20 µm wide JTE. The signal gain in the hybrid pixel detector with a small pixel iLGAD sensor was also measured. Most importantly, the small pixel iLGAD shows a significantly large fill factor of $> 80\,\%$. The hybrid pixel detector with 55 µm-pitch iLGAD sensor demonstrates a signal gain of around 4.8 at a bias voltage of -250 V. The multiplication layer and the collecting pixel were fabricated on the opposite side in an iLGAD. Hence, this device must be fully depleted to be operational.

The plan to utilise the hybrid pixel detectors with 5 mm thick CZT produced by the University of Glasgow in a single-layer Compton camera system was changed as both detectors were found unfit for this application. Instead, a hybrid pixel detector with 1 mm CdTe sensor was used for the demonstration of a single-layer Compton camera, which is presented in chapter 8. Due to the thinness of the CdTe sensor used, only a limited number of valid Compton events were obtained in the 3600 s measurement of the 122 keV γ-rays. Most detected events were from photoelectric absorptions or XRFs from Cd and Te atomic transitions. Filtering out the events not from Compton scattering events was key to the successful implementation of SLCC, which was previously addressed this issue by using the different process's cut-off energies as selection criteria. However, the cut-off energy criteria alone cannot completely filter out the XRF events. XRF events typically occur within a short range in the CdTe volume. The measurements presented in chapter

8 found that segregating Compton events based on their 2D pixel distances improves the XRF event filtering. With a 2D pixel distance of more than 20 pixels being adequate enough to filter out the XRF events in 1 mm thick, 55 µm-pitch CdTe.

9.2 Outlook and future work

The thin 50 µm LGAD pad devices have been irradiated with neutrons at the University of Birmingham. Post-irradiation gain and timing resolution studies must be conducted promptly to establish whether this technology is viable for the High Granularity Timing Detector (HGTD) in the ATLAS phase-II upgrade. The temperature control setup for the TCT measurement at the University of Glasgow must be improved to get consistent and reproducible measurements, especially at very low temperatures. Additionally, the edge-TCT must be implemented into the existing TCT setup to study the electric field profiles across the pixel and pixel-to-pixel gap in the thin LGAD and iLGAD devices.

The gains in small-pixel iLGAD devices have been measured, but unfortunately, the fabrication of this device involves a complex process that leads to a low production yield. Work is underway to produce a new variant of LGADs with a large fill factor which is easier to fabricate, called the Trench-Isolated LGAD (TI-LGAD). Multiple sizes of TI-LGAD pad devices and pixelated TI-LGAD with pitches of 55, 110 and 220 µm will be produced. These devices are expected to be fully characterised by similar techniques to the ones described in this thesis.

A new CZT crystal with fewer defects and superior spectroscopic performance called the *High Flux* CZT produced by Redlen Technologies has become available. Hybrid pixel detectors based on a thicker pixelated High Flux CZT bonded to Timepix3 or, even better, Timepix4 readout ASICs would be the ideal candidate as detectors for a single-layer

Compton camera. The CZT semiconductors are known to have higher γ-ray absorption and are more tolerant to polarisation than the CdTe. Furthermore, increasing the thickness of a CZT detector enables capturing more valid Compton events within a reduced exposure time.

Appendices

APPENDIX A

List of Acronyms

ASIC Application Specific Integrated Circuit

CdTe Cadmium Telluride

CZT Cadmium Zinc Telluride

LGAD Low Gain Avalanche Detector

JTE Junction Termination Extension

iLGAD Inverse Low Gain Avalanche Detector

TI-LGAD Trench Isolated Low Gain Avalanche Detector

AC-LGAD AC-coupled Low Gain Avalanche Detector

TCT Transient Current Technique

SLCC Single-Layer Compton Camera

MSM Metal-Semiconductor-Metal

MIP Minimum Ionising Particle

CCE Charge Collection Efficiency

FWHM Full-Width Half-Maximum

PSA Pulse Shaping Amplifier

FEE Front-end Electronics

ENC Equivalent Noise Charge

SNR Signal-to-Noise Ratio

IV Current-Voltage

CV Capacitance-Voltage

DUT Device Under Test

ToT Time over Threshold

ToA Time of Arrival

THL Threshold

DAC Digital-to-Analogue Converter

ADC Analogue-to-Digital Converter

CMOS Complementary Metal-Oxide Semiconductor

XRF X-ray Fluorescence

PPE Particle Physics Experimental Group

PoI Point of Interest

FLCC Full length Charge Collection

Bibliography

[1] M Campbell. "Electronics for Pixel Detectors". In: (2001). DOI: 10.5170/CERN-2001-005.11. URL: http://cds.cern.ch/record/528415.

[2] Rafael Ballabriga, Michael Campbell, and Xavier Llopart. "Asic developments for radiation imaging applications: The medipix and timepix family". In: *Nuclear Instruments and Methods in Physics Research Section A: Accelerators, Spectrometers, Detectors and Associated Equipment* 878 (2018). Radiation Imaging Techniques and Applications, pp. 10–23. ISSN: 0168-9002. DOI: https://doi.org/10.1016/j.nima.2017.07.029. URL: http://www.sciencedirect.com/science/article/pii/S0168900217307714.

[3] T Poikela et al. "Timepix3: a 65K channel hybrid pixel readout chip with simultaneous ToA/ToT and sparse readout". In: *Journal of Instrumentation* 9.05 (May 2014), pp. C05013–C05013. DOI: 10.1088/1748-0221/9/05/c05013. URL: https://doi.org/10.1088%2F1748-0221%2F9%2F05%2Fc05013.

[4] E Frojdh, M Campbell, M De Gaspari, et al. "Timepix3: first measurements and characterization of a hybrid-pixel detector working in event driven mode". In: *Journal of Instrumentation* 10.01 (Jan. 2015), pp. C01039–C01039. DOI: 10.1088/1748-0221/10/01/c01039. URL: https://doi.org/10.1088%2F1748-0221%2F10%2F01%2Fc01039.

[5] Tuomas Poikela et al. "The VeloPix ASIC". In: *JINST* 12.01 (2017), p. C01070. DOI: 10.1088/1748-0221/12/01/C01070.

[6] C. Granja et al. “Detection of fast neutrons with the pixel detector Timepix3”. In: *Journal of Instrumentation* 18.01 (Jan. 2023), P01003. DOI: 10.1088/1748-0221/18/01/P01003. URL: https://dx.doi.org/10.1088/1748-0221/18/01/P01003.

[7] Hubertus Bromberger et al. “Shot-by-shot 250 kHz 3D ion and MHz photoelectron imaging using Timepix3”. In: *Journal of Physics B: Atomic, Molecular and Optical Physics* 55.14 (June 2022), p. 144001. DOI: 10.1088/1361-6455/ac6b6b. URL: https://dx.doi.org/10.1088/1361-6455/ac6b6b.

[8] Joseph Bateman et al. “Testing the properties of Beam-Dose Monitors for VHEE-FLASH Radiation Theraphy”. In: *JACoW IPAC* 2022 (2022), pp. 3018–3021. DOI: 10.18429/JACoW-IPAC2022-THPOMS029. URL: https://cds.cern.ch/record/2845863.

[9] Cristina Oancea et al. “Out-of-field measurements and simulations of a proton pencil beam in a wide range of dose rates using a Timepix3 detector: Dose rate, flux and LET”. In: *Physica Medica* 106 (2023), p. 102529. ISSN: 1120-1797. DOI: https://doi.org/10.1016/j.ejmp.2023.102529. URL: https://www.sciencedirect.com/science/article/pii/S1120179723000066.

[10] Daniel Wood et al. “Ion Microscope Imaging Mass Spectrometry Using a Timepix3-Based Optical Camera”. In: *Journal of the American Society for Mass Spectrometry* 33.12 (2022). PMID: 36383767, pp. 2328–2332. DOI: 10.1021/jasms.2c00223. eprint: https://doi.org/10.1021/jasms.2c00223. URL: https://doi.org/10.1021/jasms.2c00223.

[11] Jeffrey P. Gambino, Shawn A. Adderly, and John U. Knickerbocker. “An overview of through-silicon-via technology and manufacturing challenges”. In: *Microelectronic Engineering* 135 (2015), pp. 73–106. ISSN: 0167-9317. DOI: https://doi.org/10.1016/j.mee.2014.10.019. URL: https://www.sciencedirect.com/science/article/pii/S0167931714004511.

[12] Katsuyuki Taguchi and Jan S. Iwanczyk. “Vision 20/20: Single photon counting x-ray detectors in medical imaging.” In: *Medical physics* 40 10 (2013), p. 100901.

[13] R. Ballabriga et al. “Review of hybrid pixel detector readout ASICs for spectroscopic X-ray imaging”. In: *Journal of Instrumentation* 11.01 (Jan. 2016), P01007. DOI: 10.1088/1748-0221/11/01/P01007. URL: https://dx.doi.org/10.1088/1748-0221/11/01/P01007.

[14] Erik H.M. Heijne. “History and future of radiation imaging with single quantum processing pixel detectors”. In: *Radiation Measurements* 140 (2021), p. 106436. ISSN: 1350-4487. DOI: https://doi.org/10.1016/j.radmeas.2020.106436. URL: https://www.sciencedirect.com/science/article/pii/S1350448720302146.

[15] M.P. Casado. “A High-Granularity Timing Detector for the ATLAS Phase-II upgrade”. In: *Nuclear Instruments and Methods in Physics Research Section A: Accelerators, Spectrometers, Detectors and Associated Equipment* 1032 (2022), p. 166628. ISSN: 0168-9002. DOI: https://doi.org/10.1016/j.nima.2022.166628. URL: https://www.sciencedirect.com/science/article/pii/S0168900222002005.

[16] Efrén Rodríguez Rodríguez. “Silicon vertex detector with timing for the Upgrade II of LHCb”. In: *Nuclear Instruments and Methods in Physics Research Section A: Accelerators, Spectrometers, Detectors and Associated Equipment* 1048 (2023), p. 167965. ISSN: 0168-9002. DOI: https://doi.org/10.1016/j.nima.2022.167965. URL: https://www.sciencedirect.com/science/article/pii/S0168900222012578.

[17] G. Pellegrini et al. “Technology developments and first measurements of Low Gain Avalanche Detectors (LGAD) for high energy physics applications”. English. In: *Nuclear instruments and methods in physics research. Section A, Accelerators, spectrometers, detectors and associated equipment* 765 (2014), pp. 12–16.

[18] Sofia Otero Ugobono. "Characterisation and Optimisation of Radiation-Tolerant Silicon Sensors with Intrinsic Gain. Caracterización e optimización de sensores de silicio con ganancia intrínseca resistentes á radiación". Presented 21 Nov 2018. PhD thesis. Santiago de Compostela U., July 2018. URL: https://cds.cern.ch/record/2649130.

[19] Maria del Mar Carulla Areste. "Thin LG AD timing detectors for the ATLAS experiment". presented 06 Jun 2019. PhD thesis. Barcelona, Autonoma U, 2019. DOI: 10803/667283. URL: http://cds.cern.ch/record/2694244.

[20] A. Bisht et al. "Development of LGAD sensors at FBK". In: *Nuclear Instruments and Methods in Physics Research Section A: Accelerators, Spectrometers, Detectors and Associated Equipment* 1039 (2022), p. 167018. ISSN: 0168-9002. DOI: https://doi.org/10.1016/j.nima.2022.167018. URL: https://www.sciencedirect.com/science/article/pii/S0168900222004430.

[21] F. Siviero, R. Arcidiacono, G. Borghi, et al. "Optimization of the gain layer design of ultra-fast silicon detectors". In: *Nuclear Instruments and Methods in Physics Research Section A: Accelerators, Spectrometers, Detectors and Associated Equipment* 1033 (2022), p. 166739. ISSN: 0168-9002. DOI: https://doi.org/10.1016/j.nima.2022.166739. URL: https://www.sciencedirect.com/science/article/pii/S0168900222002601.

[22] Sayaka Wada, Kyoji Ohnaru, et al. "Evaluation of characteristics of Hamamatsu low-gain avalanche detectors". In: *Nuclear Instruments and Methods in Physics Research Section A: Accelerators, Spectrometers, Detectors and Associated Equipment* 924 (2019). 11th International Hiroshima Symposium on Development and Application of Semiconductor Tracking Detectors, pp. 380–386. ISSN: 0168-9002. DOI: https://doi.org/10.1016/j.nima.2018.09.143. URL: https://www.sciencedirect.com/science/article/pii/S0168900218312993.

[23] G. D'Amen, W. Chen, C. De La Taille, et al. "First Characterization of AC-LGAD Sensors using a Readout ASIC". In: *2021 IEEE Nuclear Science Symposium and Medical Imaging Conference (NSS/MIC)*. 2021, pp. 1–6. DOI: 10.1109/NSS/MIC44867.2021.9875914.

[24] Neil Moffat. "Low gain avalanche detectors for particle physics and synchrotron applications". PhD thesis. University of Glasgow, 2020. URL: http://theses.gla.ac.uk/81281/.

[25] Neil Moffat and Richard Bates. "Simulation of the small pixel effect contributing to a low fill factor for pixellated Low Gain Avalanche Detectors (LGAD)". English. In: *Nuclear instruments & methods in physics research. Section A, Accelerators, spectrometers, detectors and associated equipment* 1018 (2021), p. 165746.

[26] D. Turecek et al. "Single layer Compton camera based on Timepix3 technology". In: *Journal of Instrumentation* 15.01 (Jan. 2020), pp. C01014–C01014. DOI: 10.1088/1748-0221/15/01/c01014. URL: https://doi.org/10.1088/1748-0221/15/01/c01014.

[27] S. Tsigaridas et al. "Characterisation of pixelated CdZnTe sensors using MAXIPIX". In: *Journal of Instrumentation* 14.12 (Dec. 2019), p. C12009. DOI: 10.1088/1748-0221/14/12/C12009. URL: https://dx.doi.org/10.1088/1748-0221/14/12/C12009.

[28] Stergios Tsigaridas et al. "Fabrication of Small-Pixel CdZnTe Sensors and Characterization with X-rays". In: *Sensors* 21.9 (2021). ISSN: 1424-8220. DOI: 10.3390/s21092932. URL: https://www.mdpi.com/1424-8220/21/9/2932.

[29] Matthew Charles Veale et al. "Characterization of the Uniformity of High-Flux CdZnTe Material". In: *Sensors* 20.10 (2020). ISSN: 1424-8220. DOI: 10.3390/s20102747. URL: https://www.mdpi.com/1424-8220/20/10/2747.

[30] Gerhard Lutz. *Semiconductor radiation detectors: device physics*. English. New York;Berlin; Springer, 2007. ISBN: 3540716793;9783540716792;

[31] Allan H. Johnston. *Reliability And Radiation Effects In Compound Semiconductors*. Singapore, SINGAPORE: World Scientific Publishing Company, 2010. ISBN: 9789814277112. URL: http://ebookcentral.proquest.com/lib/gla/detail.action?docID=731279.

[32] Glenn F. Knoll. *Radiation Detection and Measurement, 3rd ed.* 3rd edition. New York: John Wiley and Sons, 2000. ISBN: 978-0-471-07338-3, 978-0-471-07338-3.

[33] V. M. Zaletin and V. P. Varvaritsa. "Wide-bandgap compound semiconductors for X- or gamma-ray detectors". In: *Russian Microelectronics* 40.8 (Dec. 2011), pp. 543–552. ISSN: 1608-3415. DOI: 10.1134/S1063739711080208. URL: https://doi.org/10.1134/S1063739711080208.

[34] SD Sordo et al. "Progress in the Development of CdTe and CdZnTe Semiconductor Radiation Detectors for Astrophysical and Medical Applications". In: *Sensors* 9.5 (2009), pp. 3491–3526. DOI: doi:10.3390/s90503491.

[35] R. Devanathan et al. "Signal variance in gamma-ray detectors—A review". In: *Nuclear Instruments and Methods in Physics Research Section A: Accelerators, Spectrometers, Detectors and Associated Equipment* 565.2 (2006), pp. 637–649. ISSN: 0168-9002. DOI: https://doi.org/10.1016/j.nima.2006.05.085. URL: https://www.sciencedirect.com/science/article/pii/S0168900206009089.

[36] Alan Owens and A. Peacock. "Compound semiconductor radiation detectors". In: *Nuclear Instruments and Methods in Physics Research Section A: Accelerators, Spectrometers, Detectors and Associated Equipment* 531.1 (2004). Proceedings of the 5th International Workshop on Radiation Imaging Detectors, pp. 18–37. ISSN: 0168-9002. DOI: https://doi.org/10.1016/j.nima.2004.05.071. URL: https://www.sciencedirect.com/science/article/pii/S0168900204010575.

[37] Paul J Sellin. "Recent advances in compound semiconductor radiation detectors". In: *Nuclear Instruments and Methods in Physics Research Section A: Accelerators, Spectrometers, Detectors and Associated Equipment* 513.1 (2003). Proceedings of the 6th International Conference on Position-Sensitive Detectors, pp. 332–339. ISSN: 0168-9002. DOI: https://doi.org/10.1016/j.nima.2003.08.058. URL: https://www.sciencedirect.com/science/article/pii/S0168900203022836.

[38] M Niraula et al. "Stability issues of high-energy resolution diode type CdTe nuclear radiation detectors in a long-term operation". In: *Nuclear Instruments and Methods in Physics Research Section A: Accelerators, Spectrometers, Detectors and Associated Equipment* 491.1 (2002), pp. 168–175. ISSN: 0168-9002. DOI: https://doi.org/10.1016/S0168-9002(02)01175-0. URL: https://www.sciencedirect.com/science/article/pii/S0168900202011750.

[39] Lucio Cerrito. *Radiation and Detectors: Introduction to the Physics of Radiation and Detection Devices*. English. Cham: Springer International Publishing, 2017. ISBN: 3319531816;9783319531816;

[40] S. M. Sze. *Semiconductor devices: physics and technology*. English. 2nd. Hoboken, N.J: Wiley, 2002. ISBN: 0471333727;9780471333722;

[41] Helmuth Spieler and Oxford University Press. *Semiconductor detector systems*. English. Vol. 12;12.; Oxford: Oxford University Press, 2005. ISBN: 9780191713248;0191713244;

[42] D.R. Decker and C. N. Dunn. "Temperature dependence of carrier ionization rates and saturated velocities in silicon". In: *J. Electron.Mater.* 4 (3 1975), pp. 527–547. DOI: https://doi.org/10.1007/BF02666234.

[43] Karl Hecht. "Zum Mechanismus des lichtelektrischen Primärstromes in isolierenden Kristallen". In: *Zeitschrift für Physik* 77.3 (Mar. 1932), pp. 235–245. ISSN: 0044-3328. DOI: 10.1007/BF01338917. URL: https://doi.org/10.1007/BF01338917.

[44] Leonardo Rossi et al. *Pixel detectors: from fundamentals to applications*. Particle acceleration and detection. Berlin: Springer, 2006. DOI: 10.1007/3-540-28333-1. URL: http://cds.cern.ch/record/976471.

[45] R. Mulargia et al. "Temperature dependence of the response of ultra fast silicon detectors". In: *Journal of Instrumentation* 11.12 (Dec. 2016), pp. C12013–C12013. DOI: 10.1088/1748-0221/11/12/c12013. URL: https://doi.org/10.1088/1748-0221/11/12/c12013.

[46] Gabriele Giacomini. "LGAD-Based Silicon Sensors for 4D Detectors". In: *Sensors* 23.4 (2023). ISSN: 1424-8220. DOI: 10.3390/s23042132. URL: https://www.mdpi.com/1424-8220/23/4/2132.

[47] Umesh K. Mishra, Jasprit Singh, and SpringerLink (Online service). *Semiconductor device physics and design*. English. Dordrecht, The Netherlands: Springer, 2008. ISBN: 9781402064814;1402064810;

[48] Steven J. Bell. "Fabrication and characterisation of gold contacts on CdZnTe radiation detectors." PhD thesis. University of Surrey, 2015, p. 281.

[49] Claus Grupen et al. *Particle detectors*. English. 2nd. Vol. 26. Cambridge: Cambridge University Press, 2008. ISBN: 9780521840064;0521840066;

[50] S. Eidelman et al. "Review of Particle Physics". In: *Physics Letters B* 592 (2004), pp. 1+. URL: http://pdg.lbl.gov.

[51] U. Fano. "On the Theory of Ionization Yield of Radiations in Different Substances". In: *Phys. Rev.* 70 (1-2 July 1946), pp. 44–52. DOI: 10.1103/PhysRev.70.44. URL: https://link.aps.org/doi/10.1103/PhysRev.70.44.

[52] U. Fano. "Ionization Yield of Radiations. II. The Fluctuations of the Number of Ions". In: *Phys. Rev.* 72 (1 July 1947), pp. 26–29. DOI: 10.1103/PhysRev.72.26. URL: https://link.aps.org/doi/10.1103/PhysRev.72.26.

[53] W. Shockley. “Currents to Conductors Induced by a Moving Point Charge”. English. In: *Journal of applied physics* 9.10 (1938), pp. 635–636.

[54] Simon Ramo. “Currents induced by electron motion”. In: *Proceedings of the IRE* 27.9 (1939), pp. 584–585.

[55] V. Radeka. “LOW-NOISE TECHNIQUES IN DETECTORS”. In: *Annual review of nuclear and particle science* 38.1 (1988), pp. 217–277.

[56] Erik Fröjdh. “Hybrid pixel detectors : Characterization and optimization”. Vid tidpunkten för disputationen var följande delarbete opublicerat: delarbete 8 inskickat.At the time of the doctoral defence the following paper was unpublished: paper 8 submitted. PhD thesis. Mid Sweden University, Department of Electronics Design, 2015, p. 209. ISBN: 978-91-88025-37-1.

[57] Rafael Ballabriga. “The Design and Implementation in 0.13μm CMOS of an Algorithm Permitting Spectroscopic Imaging with High Spatial Resolution for Hybrid Pixel Detectors”. PhD thesis. Barcelona, Universitat Ramon Llull, 2009.

[58] V. Radeka. *Signal Processing for Particle Detectors: Datasheet from Landolt-Börnstein - Group I Elementary Particles, Nuclei and Atoms · Volume 21B1: “Detectors for Particles and Radiation. Part 1: Principles and Methods” in SpringerMaterials (https://doi.org/10.1007/978-3-642-03606-4_10)*. Ed. by C. W. Fabjan and H. Schopper. DOI: 10.1007/978-3-642-03606-4_10. URL: https://materials.springer.com/lb/docs/sm_lbs_978-3-642-03606-4_10.

[59] E. GATTI and PF MANFREDI. “PROCESSING THE SIGNALS FROM SOLID-STATE DETECTORS IN ELEMENTARY-PARTICLE PHYSICS”. English. In: *La rivista del Nuovo cimento* 9.1 (1986), pp. 1–146.

[60] S.R. Amendolia et al. “Test of a GaAs-based pixel device for digital mammography”. In: *Nuclear Instruments and Methods in Physics Research Section A: Accelerators, Spectrometers, Detectors and Associated Equipment* 460.1 (2001). Proc. 1st Int. Workshop on Radiation Imaging Detectors, pp. 50–54. ISSN:

0168-9002. DOI: https://doi.org/10.1016/S0168-9002(00)01095-0. URL: https://www.sciencedirect.com/science/article/pii/S0168900200010950.

[61] S Manolopoulos et al. "X-ray imaging with photon counting hybrid semiconductor pixel detectors". In: *Nuclear Instruments and Methods in Physics Research Section A: Accelerators, Spectrometers, Detectors and Associated Equipment* 434.1 (1999), pp. 38–43. ISSN: 0168-9002. DOI: https://doi.org/10.1016/S0168-9002(99)00430-1. URL: https://www.sciencedirect.com/science/article/pii/S0168900299004301.

[62] B Mikulec. "Single Photon Detection with Semiconductor Pixel Arrays for Medical Imaging Applications". CERN-THESIS-2000-021. PhD thesis. University of Vienna, Vienna, June 2000.

[63] Xavier Llopart Cudie. "Design and characterization of 64-K pixels chips working in single photon processing mode". CERN-THESIS-2007-062. PhD thesis. Mid Sweden U., Sundsvall, May 2007.

[64] X. Llopart et al. "Timepix, a 65k programmable pixel readout chip for arrival time, energy and/or photon counting measurements". In: *Nuclear Instruments and Methods in Physics Research Section A: Accelerators, Spectrometers, Detectors and Associated Equipment* 581.1 (2007). VCI 2007, pp. 485–494. ISSN: 0168-9002. DOI: https://doi.org/10.1016/j.nima.2007.08.079. URL: http://www.sciencedirect.com/science/article/pii/S0168900207017020.

[65] Xavier Llopart Cudie. *TIMEPIX Manual v1.0*. 2006.

[66] Xavier Llopart and Tuomas Poikela. *Timepix3 Manual v2.0*. 2015.

[67] M De Gaspari, J Alozy, R Ballabriga, et al. "Design of the analog front-end for the Timepix3 and Smallpix hybrid pixel detectors in 130 nm CMOS technology". In: *Journal of Instrumentation* 9.01 (Jan. 2014), pp. C01037–C01037. DOI: 10.1088/1748-0221/9/01/c01037. URL: https://doi.org/10.1088%2F1748-0221%2F9%2F01%2Fc01037.

[68] Tuomas Sakari Poikela. “Readout Architecture for Hybrid Pixel Readout Chips”. CERN-THESIS-2015-111. PhD thesis. University of Turku, Turun yliopisto, Finland, June 2015. URL: https://cds.cern.ch/record/2042198.

[69] D. Turecek, J. Jakubek, and P. Soukup. “USB 3.0 readout and time-walk correction method for Timepix3 detector”. In: *Journal of Instrumentation* 11.12 (Dec. 2016), pp. C12065–C12065. DOI: 10.1088/1748-0221/11/12/c12065. URL: https://doi.org/10.1088%2F1748-0221%2F11%2F12%2Fc12065.

[70] Jan Jakubek. “Precise energy calibration of pixel detector working in time-over-threshold mode”. In: *Nuclear Instruments and Methods in Physics Research Section A: Accelerators, Spectrometers, Detectors and Associated Equipment* 633 (2011). 11th International Workshop on Radiation Imaging Detectors (IWORID), S262–S266. ISSN: 0168-9002. DOI: https://doi.org/10.1016/j.nima.2010.06.183. URL: http://www.sciencedirect.com/science/article/pii/S0168900210013732.

[71] Jan Jakubek et al. “Pixel detectors for imaging with heavy charged particles”. In: *Nuclear Instruments and Methods in Physics Research Section A: Accelerators, Spectrometers, Detectors and Associated Equipment* 591.1 (2008). Radiation Imaging Detectors 2007, pp. 155–158. ISSN: 0168-9002. DOI: https://doi.org/10.1016/j.nima.2008.03.091. URL: http://www.sciencedirect.com/science/article/pii/S0168900208004245.

[72] Jan Jakubek. “Energy-sensitive X-ray radiography and charge sharing effect in pixelated detector”. In: *Nuclear Instruments and Methods in Physics Research Section A: Accelerators, Spectrometers, Detectors and Associated Equipment* 607.1 (2009). Radiation Imaging Detectors 2008, pp. 192–195. ISSN: 0168-9002. DOI: https://doi.org/10.1016/j.nima.2009.03.148. URL: http://www.sciencedirect.com/science/article/pii/S0168900209006408.

[73] M. Kroupa et al. “Techniques for precise energy calibration of particle pixel detectors”. In: *Review of Scientific Instruments* 88.3 (Mar. 2017), p. 033301. ISSN: 0034-6748. DOI: 10.1063/1.4978281. eprint: https://pubs.aip.org/aip/rsi/article-pdf/doi/10.1063/1.4978281/16076628/033301_1_online.pdf. URL: https://doi.org/10.1063/1.4978281.

[74] Laura Franconi. “Insertable B-Layer integration in the ATLAS experiment and development of future 3D silicon pixel sensors”. Presented 13 Apr 2018. PhD thesis. Oslo U, 2018. URL: https://cds.cern.ch/record/2313668.

[75] Gregor Kramberger. “Signal development in irradiated silicon detectors”. Presented 21 Jun 2001. PhD thesis. jubljana U, 2001. URL: http://cds.cern.ch/record/1390490.

[76] Gregor Kramberger. “Advanced Transient Current Technique Systems”. In: *PoS* Vertex2014 (2015), p. 032. DOI: 10.22323/1.227.0032.

[77] *B16-Beamline Layout*. https://www.diamond.ac.uk/Science/Research/Optics/B16/schematic.html. Accessed: 2022-12-02.

[78] *Beamline B16 Instruments*. https://www.diamond.ac.uk/Science/Research/Optics/B16.html. Accessed: 2022-12-02.

[79] Martin Berger et al. *XCOM: Photon Cross Section Database (version 1.2)*. en. 1999-01-01 1999.

[80] N. Moffat et al. “Low Gain Avalanche Detectors (LGAD) for particle physics and synchrotron applications”. In: *Journal of Instrumentation* 13.03 (Mar. 2018), pp. C03014–C03014. DOI: 10.1088/1748-0221/13/03/c03014. URL: https://doi.org/10.1088/1748-0221/13/03/c03014.

[81] Marco Petruzzo. "Fast timing detector developments for a LHCb Upgrade-II". In: (2018). URL: https://cds.cern.ch/record/2623703.

[82] Christian Scharf and Robert Klanner. "Measurement of the drift velocities of electrons and holes in high-ohmic silicon". In: *Nuclear Instruments & Methods in Physics Research Section A-accelerators Spectrometers Detectors and Associated Equipment* 799 (2015), pp. 81–89.

[83] C. R. Crowell and S. M. Sze. "TEMPERATURE DEPENDENCE OF AVALANCHE MULTIPLICATION IN SEMICONDUCTORS". In: *Applied Physics Letters* 9.6 (1966), pp. 242–244. DOI: 10.1063/1.1754731. URL: https://doi.org/10.1063/1.1754731.

[84] Hans-Günther Moser. "Silicon detector systems in high energy physics". In: *Progress in particle and nuclear physics* 63.1 (2009), pp. 186–237.

[85] Hieu T. Nguyen et al. "Temperature dependence of the band-band absorption coefficient in crystalline silicon from photoluminescence". In: *Journal of applied physics* 115.4 (2014), p. 043710.

[86] P. Burian et al. "Katherine: Ethernet Embedded Readout Interface for Timepix3". In: *Journal of Instrumentation* 12.11 (Nov. 2017), pp. C11001–C11001. DOI: 10.1088/1748-0221/12/11/c11001. URL: https://doi.org/10.1088%2F1748-0221%2F12%2F11%2Fc11001.

[87] Matthew Newville et al. *Lmfit: Non-Linear Least-Square Minimization and Curve-Fitting for Python*. Astrophysics Source Code Library, record ascl:1606.014. June 2016. ascl: 1606.014.

[88] R Deslattes et al. *X-ray Transition Energies (version 1.0)*. en. 2003-01-01 2003.

[89] Raj Kumar Parajuli et al. "Development and Applications of Compton Camera—A Review". In: *Sensors* 22.19 (2022). ISSN: 1424-8220. DOI: 10.3390/s22197374. URL: https://www.mdpi.com/1424-8220/22/19/7374.

[90] Kei Kamada et al. "Growth and scintillation properties of 3in. diameter Ce doped Gd3Ga3Al2O12 scintillation single crystal". In: *Journal of Crystal Growth* 452 (2016). ACCGE-20-OMVPE-17 (The 20th American Conference on Crystal Growth and Epitaxy in conjunction with the 17th US Biennial Workshop on Organometallic Vapor Phase Epitaxy, August 2-7, 2015, Big Sky, MT, USA), pp. 81–84. ISSN: 0022-0248. DOI: https://doi.org/10.1016/j.jcrysgro.2016.04.037. URL: https://www.sciencedirect.com/science/article/pii/S0022024816301774.

[91] Kei Kamada et al. "Composition Engineering in Cerium-Doped (Lu,Gd)3(Ga,Al)5O12 Single-Crystal Scintillators". In: *Crystal Growth & Design* 11.10 (2011), pp. 4484–4490. DOI: 10.1021/cg200694a. eprint: https://doi.org/10.1021/cg200694a. URL: https://doi.org/10.1021/cg200694a.

[92] R.D. Evans. *The Atomic Nucleus*. International series in pure and applied physics. McGraw-Hill, 1969. URL: https://books.google.com.my/books?id=xhVZAAAAYAAJ.

[93] Aya Kishimoto. "Study of ultra-compact Compton camera based on 3-D position sensitive scintillator for environmental and medical gamma-ray imaging". PhD thesis. Waseda University, 2016.

[94] D. Turecek et al. "Compton camera based on Timepix3 technology". In: *Journal of Instrumentation* 13.11 (Nov. 2018), pp. C11022–C11022. DOI: 10.1088/1748-0221/13/11/c11022. URL: https://doi.org/10.1088%2F1748-0221%2F13%2F11%2Fc11022.

[95] M. Zioga et al. "ComptonRec: Mastering conic sections for a direct 3D compton image reconstruction". In: *2015 IEEE Nuclear Science Symposium and Medical Imaging Conference (NSS/MIC)*. 2015, pp. 1–5. DOI: 10.1109/NSSMIC.2015.7582117.

[96] Chuanpeng Wu, Siyuan Zhang, and Liang Li. "An accurate probabilistic model with detector resolution and Doppler broadening correction in list-mode MLEM reconstruction for Compton camera". In: *Physics in Medicine & Biology* 67.12 (June 2022), p. 125017. DOI: 10.1088/1361-6560/ac73d2. URL: https://dx.doi.org/10.1088/1361-6560/ac73d2.

[97] Jiaxing Wen et al. "Optimization of Timepix3-based conventional Compton camera using electron track algorithm". In: *Nuclear Instruments and Methods in Physics Research Section A: Accelerators, Spectrometers, Detectors and Associated Equipment* 1021 (2022), p. 165954. ISSN: 0168-9002. DOI: https://doi.org/10.1016/j.nima.2021.165954. URL: https://www.sciencedirect.com/science/article/pii/S0168900221009086.

[98] Caesar E Ordonez, Alexander Bolozdynya, and Wei Chang. "Doppler broadening of energy spectra in Compton cameras". In: *1997 IEEE Nuclear Science Symposium Conference Record*. Vol. 2. IEEE. 1997, pp. 1361–1365.

[99] A. Gutierrez et al. "Progress towards a semiconductor Compton camera for prompt gamma imaging during proton beam therapy for range and dose verification". In: *Journal of Instrumentation* 13.01 (Jan. 2018), pp. C01036–C01036. DOI: 10.1088/1748-0221/13/01/c01036. URL: https://doi.org/10.1088/1748-0221/13/01/c01036.

[100] L.C. Parra. "Reconstruction of cone-beam projections from Compton scattered data". In: *IEEE Transactions on Nuclear Science* 47.4 (2000), pp. 1543–1550. DOI: 10.1109/23.873014.

[101] Enrique Muñoz et al. "A spectral reconstruction algorithm for two-plane Compton cameras". In: *Physics in Medicine & Biology* 65.2 (Jan. 2020), p. 025011. DOI: 10.1088/1361-6560/ab58ad. URL: https://doi.org/10.1088/1361-6560/ab58ad.